New theoretical concepts for designing oxide interfaces with exoticproperties for electronics and spintronics

Aysegül Begüm Koçak

▶ To cite this version:

Aysegül Begüm Koçak. New theoretical concepts for designing oxide interfaces with exoticproperties for electronics and spintronics. Mechanics of materials [physics.class-ph]. Université Grenoble Alpes; Université de Liège, 2017. English. NNT : 2017GREAI033 . tel-01687743

HAL Id: tel-01687743

https://theses.hal.science/tel-01687743

Submitted on 18 Jan 2018

Communauté
UNIVERSITÉ Grenoble Alpes

LIÈGE
université

THÈSE

Pour obtenir les grades de

DOCTEUR DE L'UNIVERSITE GRENOBLE ALPES et

DOCTEUR DE L'UNIVERSITE DE LIÈGE

préparée dans le cadre d'une cotutelle *entre l'Université Grenoble Alpes* et l'*Université de Liège*

Spécialité : **Materiaux**

Arrêté ministériel : le 6 janvier 2005 - 7 août 2006

Présentée par

Ayşegül Begüm KOÇAK

Thèse dirigée par **Marie-Bernadette LEPETIT**
codirigée par **Philippe GHOSEZ**

préparée au sein de l'Institut Néel et du Département de Physique
de l'Université de Liège

dans **l'École Doctorale Imep2 et l'Université de Liège**

Nouveaux concepts théoriques pour la conception d'interfaces d'oxydes avec des propriétés exotiques pour l'électronique et la spintronique

Thèse soutenue publiquement le **« 6 septembre 2017 »**,
devant le jury composé de :

Prof. Bernard MERCEY (Président)
Prof. Roberto DOVESI (Rapporteur)
Prof. Xavier ROCQUEFELTE (Rapporteur)
Dr. Eric BOUSQUET (Secrétaire pour l'Université de Liège)
Dr. Laurence MAGAUD (Membre)
Prof. Philippe GHOSEZ (Directeur de thèse)
Dr. Marie-Bernadette LEPETIT (Directrice de thèse)

I would like to dedicate this thesis to my spirit animal, ΨΨ . . .

Acknowledgements

I would like to express my deepest gratitude to my supervisors, Marie-Bernadette Lepetit and Philippe Ghosez for their guidance during my PhD.

I am very grateful to Julien Varignon who taught me the Crystal code and much more. Thanks for everything!

I would like to thank everyone whom I have shared the science/office/corridor/coffee/lunch/joy: Samuel Hanot, Sarah Gautier, Jordan Hervy, Henu Sharma, Elena Cannucia, Elisa Rebolini, Pablo Villar Arribi, Keith Gilmore, Luca De'Medici, Bruno Tomasello, Nicolás García, Andrew Geondzhian, Chloe Clear, Eric Bousquet, Jacques Villain, Jean-Pierre Gaspard, Philippe Nozières, Timothy Ziman, Dominique Bicout, Fabio Comin, Markus Holzmann, Patrick Bruno, Gabriele D'Avino, Can Yıldırım, Barış Malcıoğlu, Marco Di Gennaro, Zeila Zanolli, Matthieu Verstrate, Nick Bristowe.

I thank to my flatmates Carole Loable and Claudia Mokbel for everything. We shared a home and much more. The memories of watching Friends together while eating dinner in cold winter nights will always warm my heart. You made Grenoble home for me.

I would like to thank my folks from Turkey: Seda Sezen, Çağrı Dinçer, Gamze Alaçam, Çağdaş Polat. You made my Christmas and summer breaks a long, fresh breath.

I want to thank Fereydoon Taheri who never gave up believing in me. Even if our roads get apart, your place will always be unique.

I would like to thank Arzu Tuğçe Güler a.k.a. ATG for being the best friend of any kind: Smart, crazy, loveful, adventurous! We are gonna make an adventure out of this life.

I want to thank Clément Février who gave me the most selfless support. Without him, it could not be possible. Thank you for believing in me and being always there for me. Pizza night?

At last but not least, I would like to thank my family. They taught me love, courage and fight.

Abstract

This thesis theoretically studies structural and electronic properties of perovskite manganese oxide superlattices by means of ab-initio calculations.

Lanthanum manganese oxides, given with the generic formula $\mathrm{La_{1-x}A_xMnO_3}$ (LAMO) (A a divalent element), are an important class of perovskite manganese oxides due to their various exotic properties, such as giant and colossal magnetoresistance effect, rich phase diagrams with respect to doping, temperature or external fields, and intrinsic large Curie temperature. These properties can be exploited in many potential technological applications such as spin valves or spin injectors. Controlling the properties of these materials can be done through deposition as thin films or as building blocks in superlattices. When x = 1/3, bulk $\mathrm{La_{1-x}A_xMnO_3}$ is ferromagnetic and metallic due to the double-exchange mechanism in the Mn 3*d* shell. When Mn is in a mixed valence state, the eg orbitals ($d_{x^2-y^2}$ and d_{z^2}) are partially occupied, and can delocalize on neighboring Mn atoms only if the latter are ferromagnetically aligned. In very thin films, since the direction perpendicular to the substrate, $\vec{c}$, is only a few unit cell thick, only in-plane (*ab*) interactions are important for the thermodynamic properties. By acting on the LAMO layer geometry, one can thus maximize the $d_{x^2-y^2}$ orbital occupancy and increase the magnetic exchange and related Curie temperature.

Our aim was thus to design new materials with desired 3*d* orbital order so that to ensure desired magnetic properties.

In this thesis, we worked on two types of superlattices. The first one was made of two undoped antiferromagnetic manganese oxides $\mathrm{LaMnO_3}$ and $\mathrm{SrMnO_3}$, i.e. $\mathrm{[LaMnO_3]_n/[SrMnO_3]_m}$ superlattices. We investigated the magnetic ground state for different n and m values in order to explain suprising experimental results. The second type of superlattices is composed of metallic LAMO layers with alternated insulating layers. Indeed, the superlattices with metal-insulator interfaces have a great potential in spin valves applications. Thus, we first considered the ferromagnetic-metallic/ferroelectric-insulating $\mathrm{[LAMO]_3/[BTiO_3]_3}$ superlattices

(A = Sr or Ba, B = Ba or Pb) where the magnetic properties are reduced due to delocalization of d_{z^2} electrons at the interface from Mn to Ti. In such superlattices, we clarified the role of the polarization of the ferroelectric layers and the role of the antiferrodistortive motions in the manganite layers. In order to prevent the delocalization taking place at the interface, we designed another superlattice with metallic-insulator interface where we replaced the insulator ($BTiO_3$) with a simple oxide (BO); that is $[\mathrm{LAMO}]_{\mathrm{n}}/[\mathrm{BO}]_{\mathrm{p}}$ superlattices ($A = Sr$ or Ba, $B = Ba$, Sr or Mg and $n = 3$ or 6, $p = 6$ or 2). Within this new superlattice, we successully managed to promote $d_{x^2-y^2}$ orbital occupancies at the interfaces which ensures a large magnetic moment at the interfaces and an expected large Curie temperature. We also showed the weak correlation between electrical conductivity and orbital ordering.

Résumé

Au cours de cette thèse, nous avons étudiés théoriquement les propriétés structurelles et électroniques des super-réseaux d'oxyde de manganèse en structure perovskite au moyen de calculs ab initio.

Les oxydes de manganèse au lanthane, donnés avec la formule générique $\mathrm{La_{1-x}A_xMnO_3}$ (LAMO) (A un élément divalent), constituent une classe importante d'oxydes de manganèse en raison de leurs diverses propriétés, telles que l'effet de magnétorésistance colossale, leur riche diagramme de phase en fonction du dopage, de la température ou de champs externes, et leur grande température Curie. Ces propriétés peuvent être exploitées dans de nombreuses applications technologiques potentielles telles que les valves de spin ou les injecteurs de spin. Le contrôle des propriétés de ces matériaux peut se faire par dépôt sous forme de films minces ou comme blocs de construction dans des super-réseaux. Lorsque $x = 1/3$, le $\mathrm{La_{1-x}A_xMnO_3}$ massif est ferromagnétique et métallique grâce au mécanisme de double échange dans les electrons $3d$ de Mn. Lorsque Mn est dans un état de valence mixte, les orbitales eg ($d_{x^2-y^2}$ and d_z^2) sont partiellement occupées et peuvent se délocaliser sur les atomes de Mn voisins, seulement si ceux-ci sont alignés ferromagnétiquement. Dans des films très minces, puisque la direction perpendiculaire au substrat, $\vec{c}$, n'a que quelques cellules unitaires d'épaisseur, seules les interactions dans le plan (ab) sont importantes pour les propriétés thermodynamiques. En agissant sur la géométrie de la couche LAMO, on peut ainsi maximiser l'occupation de l'orbitales $d_{x^2-y^2}$ et augmenter l'échange magnétique et la température Curie associée.

Notre but était donc de concevoir de nouveaux matériaux avec un ordre orbital $3d$ spécifique afin d'assurer les propriétés magnétiques souhaitées.

Dans cette thèse, nous avons travaillé sur deux types de super-réseaux. Le premier était constitué de deux oxydes de manganèse antiferromagnétiques, non dopés, $\mathrm{LaMnO_3}$ et $\mathrm{SrMnO_3}$, c'est-à-dire des super-réseaux $\mathrm{[LaMnO_3]_n/[SrMnO_3]_m}$. Nous avons étudié

l'état fondamental magnétique pour différentes valeurs n et m afin d'expliquer les résultats expérimentaux surprenants. Le deuxième type de super-réseaux que nous avons étudiés est composé de couches métalliques LAMO en alternance avec des couches isolantes. En effet, les super-réseaux avec des interfaces métal-isolant ont un grand potentiel dans les applications de valves de spin. Ainsi, nous avons d'abord considéré des super-réseaux entre composés ferromagnétiques-métalliques et ferroélectriques-isolantes $[\mathrm{LAMO}]_3/[\mathrm{BTiO}_3]_3$ ((A = Sr ou Ba, B = Ba ou Pb). Dans ces super-réseaux, les propriétés magnétiques sont malheuresement réduites en raison de la délocalisation d'électrons d_{z^2} à l'interface entre Mn et Ti. Dans de tels super-réseaux , nous avons clarifié le rôle de la polarisation des couches ferroélectriques et le rôle des mouvements antiferrodistortifs dans les couches de manganite. Enfin, de manierè à éviter que la délocalisation ait lieu à l'interface, nous avons conçu un autre super-réseau avec interface métal-isolant dans lequel nous avons remplacé l'isolant (BTiO_3) par un oxyde simple (BO): $[\mathrm{LAMO}]_\mathrm{n}/[\mathrm{BO}]_\mathrm{p}$ superlattices (A = Sr ou Ba, B = Ba, Sr ou Mg et $n = 3$ ou 6, $p = 6$ ou 2). Dans ces nouveaux super-réseaux, nous avons réussi à promouvoir les occupations des orbitales $d_{x^2-y^2}$ dans les interfaces assurant un fort moment magnetique à l'interface et a priori une fort temperature de Curie. Nous avons également montré une faible corrélation entre la conductivité électrique et l'ordre orbitaire.

Table of contents

Preface

Everything that we have and surrounds our lives is made of something. Everything has a substance. If we take out the materials from our lives we are naked to this world. Materials and the way that we used them determined the level of our civilizations through history: The stone, the iron and the bronze ages. Not only for the practical purposes but also for the sake of art and aesthetics, humankind gave the greatest importance to the understanding of materials. For example, Egyptians were the earliest masters of gold beating. They were using very thin gold leafs between different layers of materials for decoration purposes. In Victorian era, engineering technologies developed with the use of materials, iron and steel. Today, what we got used to see in our daily lives like bridges, railways etc. were the creation of this development. The information age is brought by new advancements in the material technologies, such as silicon technology or thin-film technology. Thus, controlling the materials used in today's technology is of great importance for the scientists and engineers. Both scientist and engineers study the structures, physical and chemical properties of material substances.

To begin with, we can give the definition of a matter. Matter is anything that occupies space and has a mass. There are four states of matter observable in everyday life, i.e. solid, liquid, gas and plasma but under extreme situations such as low or high pressure or temperature there exist other states as well such as Bose-Einstein condenstate and quark-gluon plasma. Condensed matter physics deals with the properties of condensed phases of matter. The most common condensed phases are solids and liquids. The main approach of condensed matter physics is to measure material properties by experiments, along with the development of mathematical models in order to understand the physical behaviour of the material. Understanding the properties of a material comes naturally with the desire to control these properties for various purposes. A spotlight of condensed matter physics is on the transport and magnetic properties of the materials for technological devices, such as electronics and spintronics. Like our old wise Egyptian ancestors creating new compounds by thinly layering different materials, today, material scientists and physicists create novel artificial thin films to control the transport and magnetic properties of the material.

Thin films deposited on a substrate are widely used in many technological devices. To begin with examples, we can start with the compound semiconductor based devices. Light emitting diodes (LED), laser diodes (LD), solar cells and electronic devices, such as high electron mobility transistors (HEMT) and heterojunction bipolar transistors (HBT) require the deposition of thin epitaxial layers. These thin layers often have lower defect and impurity levels as compared to bulk materials. The invention of the first high-T_c superconducting $YBa_2Cu_3O_x$ (YBCO) thin films [1] opened a great new interest in the thin film community and in superconducting microwave devices. Magnetic recording/memory technology is also one of the most remarkable application of the thin film technology. Giant and colossal magnetoresistance features that some thin film materials exhibit have a great impact on the magnetic recording/memory technology. The miniaturization of magnetic devices opened a new research field loosely named “micromagnetic devices”. The basic micromagnetic device is built by the combination of a thin magnetic film with a planar coil. Possible applications are micropower supplies, microsensors and mobile communication handsets. Ferroelectric thin films are also demanded for nonvolatile memory devices (also named as FeRAMs, ferroelectric random access memories) due to their high-speed writing, low dissipation, power and high endurance. Due to the variety of technological devices that the thin films offer, there exist various techniques to prepare high-quality thin films such as molecular beam epitaxy (MBE), metal chemical vapour deposition (MOCVD) and pulsed laser deposition (PLD).

When materials are constructed as layers or films, thickness of these layers/films is significantly important to engineer their properties. A very thick film of a certain material can exhibit bulk-like properties whereas very thin layers can exhibit different properties. However, as it is hard to grow and use free-standing thin films, one needs to deposit them on another material, namely on a substrate. Thus, in a thin film environment, the solid is deposited on a substrate and experiences two interfaces: film-substrate interface and film-vacuum interface. In such a case, the properties are expected to be much more dependent of the interfacial effects. One challenge is to use the concepts of surface and interface physics in order to understand and control the properties of thin films. Interface physics is therefore embedded in the conventional condensed matter physics and it is truly correlated with other research field such as molecular physics or particle beam optics (See Figure 2). Surface and interface physics bring aspects for technological applications such as semiconductor technology or corrosion and surface protection. Understanding this field from both experimental and theoretical points of view is really important. On the one hand, there are a few fields in physics and chemistry that provide experimental methods and techniques to extract the surface and interface physics. On the other hand, in addition to experimental approaches, computer calculations is another important element. Indeed, nowadays accessible complex and large-scale computer calculations made it possible to deduce theoretical understanding of interface physics of thin films. In this thesis, we will study interfaces in heterostructures by means of computer calculations in order to obtain the physics of thin films. More precisely, we will study manganite-based superlattices at the atomic scale by means of ab-initio calculations.

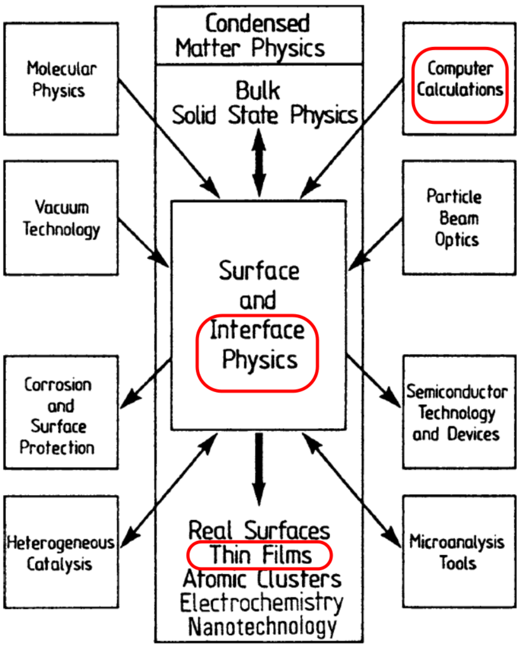

Fig. 1 Surface and Interface Physics correlated with a variety of research fields. In this thesis, we are particularly interested in Interface Physics of Thin Films at the computer calculations level. Picture taken from Ref. [2]

This thesis is organized as follows. In chapter 1, we give a very short review of solid state physics in order to introduce some basic concepts that are necessary to capture the physics of thin films. In the same chapter, we shortly talk about the thin films conceptually. In chapter 2, we give a review of CMR manganites and discuss their structural, electronic and magnetic properties. We will also give a short comparison of the properties of $\mathrm{La_{1-x}A_xMnO_3}$ bulk materials and thin films. The chapter 3 is devoted on the methodology that is used in this thesis. In chapter 4, we will give the results of $\mathrm{(LaMnO_3)_n - (SrMnO_3)_p}$ superlattices. In chapter 5, we provide the results of the superlattices of $\mathrm{(La_{2/3}A_{1/3}MnO_3)_3}$ with alternated perovskite layers. In chapter 6, we present the results of superlattices of $(La_{2/3}A_{1/3}MnO_3)_3$ with simple alkaline oxides. In chapter 6.4, we give our conclusions and future perspectives.

Préface

Tout ce que nous avons et qui entoure nos vie est fait de quelque chose. Tout a une substance. Si on sort les matériaux de nos vie, nous sommes nus face à ce monde. Matériaux et la manière dont nous les utilisons déterminent notre niveau de civilisation : L'age de pierre, de fer, de bronze. Non seulement pour des raisons pratiques mais mais aussi pour l'art et l'esthétisme, l'humanité donna la plus grande importance à la compréhension des matériaux. Par exemple, les égyptiens étaient les premiers maîtres à façonner l'or. Ils utilisaient des couches très minces d'or entre différentes couches de matériaux pour décorer. À l'époque victorienne, l'ingénierie technologique a développé l'utilisation de matériaux, fer et acier. Aujourd'hui, ce que nous sommes habitués à voir dans notre quotidien, comme les ponts, chemins de fer, etc. sont à l'origine de ces avancées. L'ère de l'information arrive avec des nouveaux avancement en technologie des matériaux, comme l'utilisation du silicone ou les films minces. Donc contrôler l'utilisation de matériaux dans la technologie actuelle est de grande importance pour les scientifiques et ingénieurs. Tous deux étudient les structures, les propriétés physiques et chimiques de la substances des matériaux.

Pour commencer, nous pouvons donner la définition de la matière. La matière est tout ce qui occupe l'espace et a un masse. Il y a quatre états de la matière que l'on peut observer dans la vie quotidienne, solide, liquide, gaz et plasma mais sous conditions extrêmes, comme forte ou basse pression ou température, il existe d'autres états comme le bien connu condensat de Bose-Einstein et le plasma de quak-gluon. La physique de la matière condensée s'attache à l'étude des propriétés des phases condensées de la matière. Les phases condensées les plus communes sont solide et liquide. L'approche principale de la physique de la matière condensée est de mesurer les propriétés des matériaux avec des expériences, ainsi que le développement de modèles mathématiques pour comprendre le comportement physique des matériaux. Comprendre les propriétés des matériaux vient naturellement avec le désir de contrôler ces propriétés pour différentes raisons. Un intérêt particulier de la physique de la matière condensée est donné propriétés de transport magnétiques des matériaux pour les appareils technologiques, tels que l'électronique ou la spintronique. Comme nous anciens sages ancêtre égyptiens, créer de nouveaux composés en superposant des couches minces de différents matériaux, aujourd'hui, les scientifiques des matériaux et les physiciens créent de nouveaux films minces pour contrôler le transport et les propriétés magnétiques des matériaux.

Les couches minces déposées sur un substrats sont largement utilisées dans différent appareils technologiques. Pour commencer avec des exemples, on peut commencer avec les appareils à base de semi-conducteurs. Diode électroluminescente (DEL), diode laser (DL), cellules solaires et appareils électroniques, tels que les transistors à haute mobilité d'électrons (HEMT) et transistor bipolaire à hétérojonction (HBT) ont besoin de dépôts de couches minces épitaxiales car ces couches minces ont souvent peu de défauts et un faible taux d'impureté comparé au matériau en vrac. L'invention du premier supraconducteur à haute température critique $YBa_2Cu_3O_x$ (YBCO) en couche mince [1] a ouvert un grand nouvel intérêt dans la communauté des films en couche minces et des appareils microonde supraconducteurs. La technologie d'enregistrement magnétique et de mémoire magnétique est aussi une des plus grandes applications remarquable de la technologie en couche mince. La propriété de magnétorésistance géante et colossale que certains matériaux en couches minces ont a un grand impact sur les technologie d'enregistrement et de mémoire magnétique. La miniaturisation des appareils magnétiques a ouvert un nouveau domaine domaine nommé "appareils micromagnétiques". Le plus basique appareil micromagnétique est construit en une combinaison de films minces magnétiques avec une bobine plane. Quelques possibles applications sont des alimentations micropower, microsensors et de communication mobile. Les films minces ferroélectique sont aussi prisés pour des appareils de mémoire non volatiles (aussi nommées FeRAMs, ferroelectric random access memories) à cause de leur rapide vitesse d'écriture, faible dissipation, puissance et haute endurance. Grâce à la diversité d'appareils technologiques qu'offrent des films minces, il existe différentes techniques pour préparer une diversité de films minces de haute qualité, comme l'épitaxie par jet moléculaire, le dépôt chimique en phase vapeur et l'ablation laser pulsé.

Quand les matériaux sont composés de couches ou films, l'épaisseur de ces couches/films est importante pour contrôler leurs propriétés. Un film épais d'un matériau donné peut avoir certains propriétés du matériau massif alors que des couches très minces peuvent avoir des propriétés très différentes. Cependant, comme il est difficile de faire pousser et d'utiliser des films minces autonome, nous devons les déposer sur un autre matériau, appelé substrat. Donc, dans un environnement de films minces, le solide est déposé sur un substrat et a deux interfaces : une interface film-substrat et film-vide. Dans ce cas, les propriétés seront plus plus dépendantes des effets d'interface. Un défis est d'utiliser les concepts de la physique des surfaces et interfaces pour comprendre et contrôler les propriétés des films minces. La physique des interfaces est donc incluses dans la physique de la matière condensée conventionnelle et est vraiment corrélée avec d'autres champs de recherche tels que la physique moléculaire ou l'optique du faisceau de particules (voir Figure 2). La physique des surfaces et interfaces apporte des aspects d'applications technologiques comme la technologie des semi-conducteurs ou corrosion et de protection de surface. Comprendre ce domaine d'un point de vue expérimental et théorique est vraiment très important. D'un côté, il y a quelques domaines en physique et chimie qui fournissent des méthodes expérimentales et des techniques pour extraire la physique des surfaces et interfaces. De l'autre, en plus des approches expérimentales, les calculs informatiques est un autre élément important. En effet, de nos jours, les calculs informatiques complexes et à haute échelle sont rendus accessibles et permettent de déduire une compréhension théorique des la physique des interfaces des films minces. Dans cette thèse, nous étudierons les interfaces dans les hétérostructures grâce à des calculs informatiques pour obtenir la physique des films minces. Plus précisément, nous étudierons les super réseaux à base de manganites à l'échelle atomique à l'aide de calculs ab-initio.

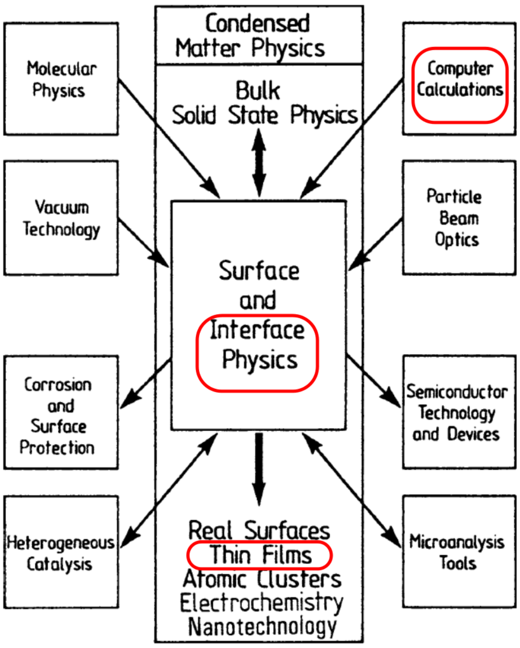

Fig. 2 Physique des surfaces et interfaces corrélée avec une diversité de domaines recherches. Dans cette thèse, nous sommes particulièrement intéressés par la physique des interfaces des films minces par des calculs informatiques. Image prise de Ref. [2]

Cette thèse est organisée de la manière suivante. Dans le chapitre 1, nous donnons une très courte revue de la physique du sole pour introduire quelques concepts basiques qui sont nécessaires pour la physique des films en couches minces. Dans le même chapitre, nous parlons brièvement des concepts de film mince. Dans le chapitre 2, nous donnons une revue de CMR manganites et discutons de leurs propriétés structurelles, électroniques et magnétiques. Nous donnons aussi une courte comparaison des propriétés de $\mathrm{La_{1-x}A_xMnO_3}$ materieaux massif et des couches minces. Le chapitre 3 est dédié à la méthodologie qui est utilisés dans cette thèse. Dans le chapitre 4, nous donnons les résultats pour $\mathrm{(LaMnO_3)_n - (SrMnO_3)_p}$ super réseaux. Dans le chapitre 5, nous fournissons les résultats pour les super réseaux de $\mathrm{(La_{2/3}A_{1/3}MnO_3)_3}$ avec des couches pérovskite alternées. Dans le chapitre 6, nous présentons les résultats des super réseaux de $\mathrm{(La_{2/3}A_{1/3}MnO_3)_3}$ avec les oxydes alcalines simple. Dans le chapitre 6.4, nous donnons nos conclusions et perspectives futures.

Chapter 1

Controlling the Matter

Contents

1.1 A very Short Review on Solids

Before describing thin-films and their place in today's technology, let us start with recalling some basics of solid materials. Some solid materials have a crystalline form, i.e. an ordered internal crystal structure. The crystal structure is a description of a periodic arrangement of atoms, ions or molecules in a crystalline material. The primitive unit cell, which contains the smallest group of particles that determines the repeating pattern, defines the symmetry and structure of the crystal lattice. The lengths of the principal axes of the unit cell and the angles between them are named as the lattice constants or lattice parameters. The crystal lattice is built by periodic translation of the unit cell along the axes. In three dimensions, all possible symmetric arrangements of particles in space is given using one of the seven crystal lattice systems. In these seven lattice systems, there are fourteen Bravais lattices. In figure 1.1, one can see the seven different lattice systems with the fourteen Bravais lattices. For example for the case of the orthorhombic lattice system, there exist four Bravais lattices; simple, base-centered, body-centered or face-centered. The rotations, reflections or translations of a crystal structure determine their symmetry operations and the set of these operations is named as the crystallographic point groups. There are 32 crystallographic points groups. The combination of crystallographic points groups with Bravais lattices constructs the notion of space groups in three dimensions. There are 230 space groups in three-dimensional space.

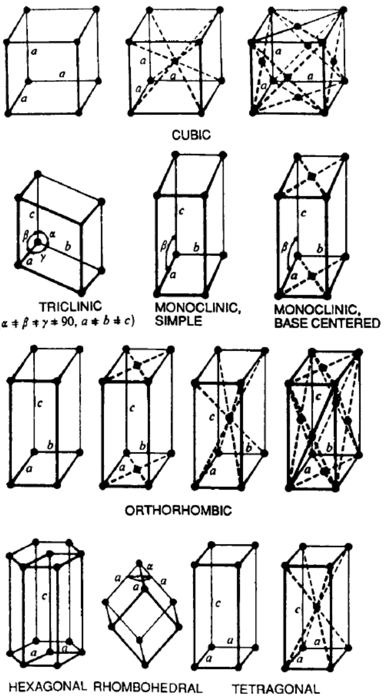

Fig. 1.1 The fourteen Bravais lattices. Picture taken from Ref. [3]

In order to determine the crystal lattice structure of a compound, there are different experimental diffraction techniques widely used: X-ray or electron or neutron diffractions on single crystals or powders. In X-ray diffraction technique, for example, the crystalline atoms are exposed to a beam of incident X-rays that diffracts into many specific directions. Particles in these techniques act as matter waves (i.e. wave-like). The de Broglie relation states the relation between the wavelength and the momentum, that is $\lambda = h/p$, where λ is the wavelength, h is the Planck's constant and p is the magnitude of momentum. The relation between the momentum p and the wavevector $\vec{k}$ is given by $p = [h/(2\pi)]\vec{k}$. Thus, it is convenient to define a k-space or reciprocal space in the momentum space that is related to real space. In real space, Bravais lattice is given with the mathematical formulation as $\vec{R} = n_1\vec{a}_1 + n_2\vec{a}_2 + n_3\vec{a}_3$ where $\vec{a}_1$, $\vec{a}_2$ and $\vec{a}_3$ are the primitive vectors and n_1, n_2 and n_3 are integers. The Fourier transform of Bravais lattice gives us the reciprocal lattice with $\vec{G} = m_1\vec{b}_1 + m_2\vec{b}_2 + m_3\vec{b}_3$ where $\vec{b}_1 = 2\pi\frac{\vec{a}_2\times\vec{a}_3}{\vec{a}_1\cdot(\vec{a}_2\times\vec{a}_3)}$, $\vec{b}_2 = 2\pi\frac{\vec{a}_3\times\vec{a}_1}{\vec{a}_2\cdot(\vec{a}_3\times\vec{a}_1)}$ and $\vec{b}_3 = 2\pi\frac{\vec{a}_1\times\vec{a}_2}{\vec{a}_3\cdot(\vec{a}_1\times\vec{a}_2)}$ are the primitive vectors and m_1, m_2 and m_3 are the Miller indices. Miller index is a notation tool to define crystal planes inside the lattice. One can also use similar indices to design the directions inside the lattice, i.e. direction indices. In figure 1.2, there are example crystal planes denoted with Miller indices and direction indices.

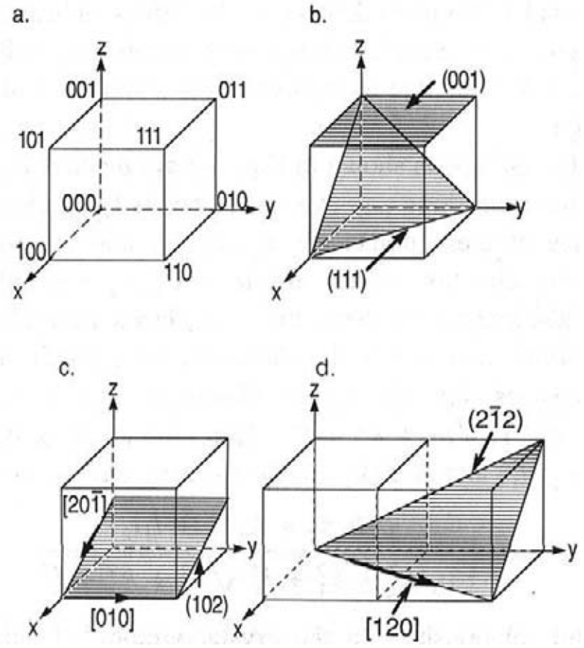

Fig. 1.2 (a) Coordinates of lattice sites; (b) Miller indices of planes; (c,d) Miller indices of planes and direction indices. Picture taken from Ref. [3]

Materials can be classified according to their bonding type into four classes: Metallic, ionic, covalent and van der Waals. Metallic bonding occurs in metals and alloys. In metals, the Fermi level electrons are rather delocalized and metallic bonding is relatively soft. Ionic bonding occurs due to electrostatic attraction between oppositely charged ions such as between metals and nonmetals. Covalent bonding is a chemical bond in which neighbouring atoms share electrons. The van der Waals type bonding occurs due to weak dispersion forces.

Materials can be classified according to their ability to conduct electricity into three classes: Conductors, semi-conductors, insulators. The distinction rises from the electronic dispersion curves. The energy band structures are schematically shown in figure 1.3 for metals, semiconductors and insulators. In metals, the Fermi level is in the middle of a band. In insulators, there are only fully occupied or fully empty bands. In semi-conductors, at 0 Kelvin, there are only fully occupied or fully empty bands but bands can be partially occupied at a finite temperature.

Materials can also be classified by their response to externally applied magnetic field. This classification is based on the strength of the response. Diamagnetism is a fundamental

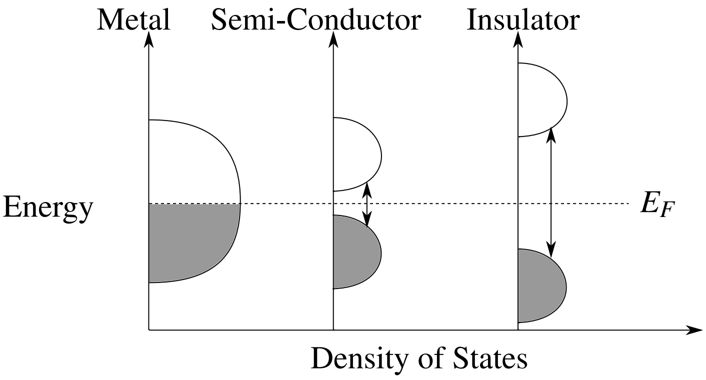

Fig. 1.3 Schematic band structure for metal, semi-conductor and insulator.

property that all materials exhibit initially though it is normally very weak. In a diamagnetic or non-magnetic material, atoms have no net magnetic moment. However, when a diamagnetic material is exposed to an applied magnetic field, non-cooperative orbital motions of electrons create small atomic currents which produce an induced magnetic field in the opposite direction of the applied field so that a negative magnetization is produced to compensate and the diamagnetic material is repelled. The response of a diamagnatic material to an applied field can be seen schematically in figure 1.4a. In a paramagnetic material, there

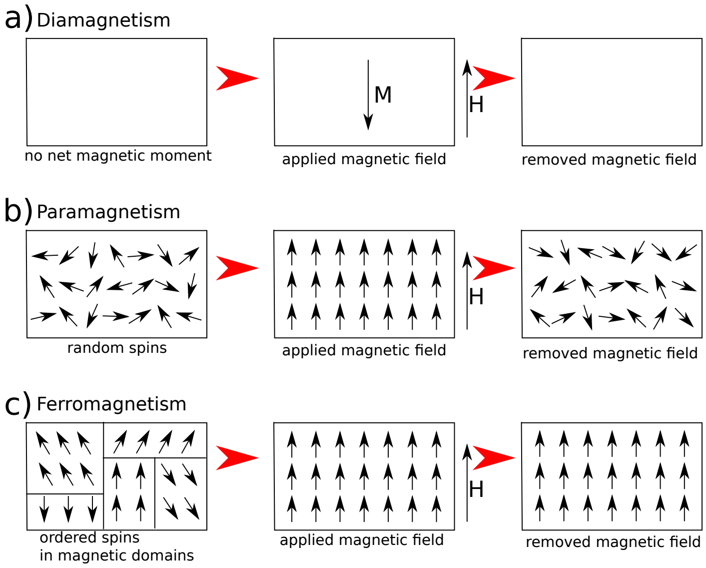

Fig. 1.4 Different responses of materials to an applied magnetic field: a) Diamagnetism b) Paramagnetism c) Ferromagnetism.

are some atoms with a net magnetic moment but the individual magnetic moments do no interact. However, in the presence of an applied magnetic field, the local magnetic moments align in the same direction of the applied field which induce a small magnetization. This magnetization disappears when the applied field is removed. This can be schematically seen in figure 1.4b. Unlike paramagnetic materials, the atomic spins in a ferromagnetic material strongly interact with each other and align in the same direction inside magnetic domains, even in the absence of an applied magnetic field. When there is an applied field the domain boundaries move and the atomic spins align along the applied field. This mechanism can be seen in figure 1.4c. There are two characteristics of ferromagnetic materials: i) Spontaneous magnetization, ii) Magnetic ordering temperature also known as the Curie temperature. The spontaneous magnetization is the net magnetization that the ferromagnetic material exhibits uniformly inside the volume in the absence of an applied magnetic field. At 0 K, the magnitude of the magnetization depends on the magnetic moments of the electrons. Saturation magnetization, M_s, on the other hand, is the maximum magnetization that can be obtained in a magnetic field $\mathrm{H_{sat}}$ which depends on the temperature. Thermal energy affects the exchange interactions in ferromagnetic materials. The Curie temperature T_c is the temperature above which ferromagnetic alignment breaks and there is a spin randomizing effect. Ferromagnetic materials can retain a memory of an applied magnetic field when the field is removed. This is known as hysteresis and the change of magnetization with respect to magnetic field is named as hysteresis loop. In figure 1.5, one can see an example of a ferromagnetic hysteresis loop.

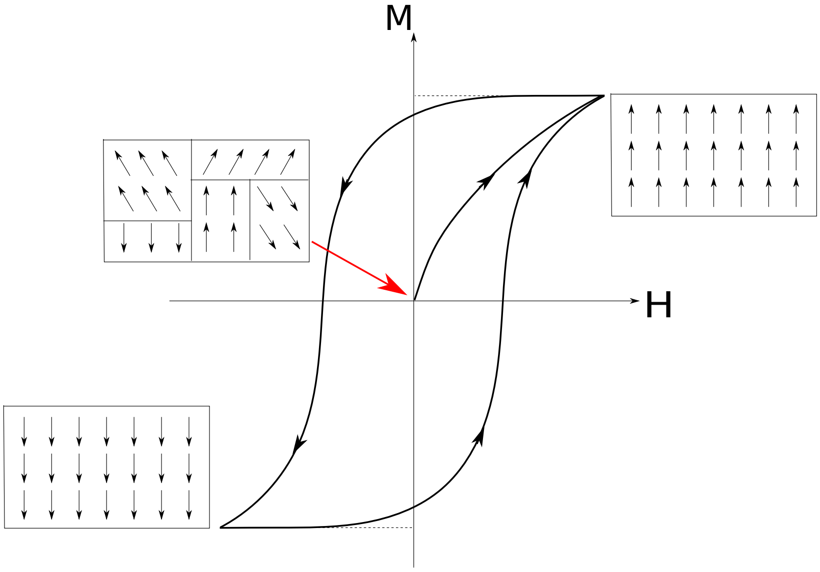

Fig. 1.5 Hysteresis Loop for a ferromagnetic material

In addition to paramagnetic and ferromagnetic materials, there are other type of magnetic materials, i.e. antiferromagnetic and ferrimagnetic. The schematical representation of magnetic materials are given in figure 1.6. In the absence of an applied field, when the magnetic moments/spins in a material align in opposite directions at neighbouring sites with the same amplitude then this material is an antiferromagnetic material. Thermal energy also affects the interactions inside an antiferromagnetic material. The Néel temperature T_N is the temperature above which the antiferromagnetic-paramagnetic transition takes place. When the magnetic moments align in opposite directions but have different amplitudes so that the net magnetic moment is non zero then this material is ferrimagnetic.

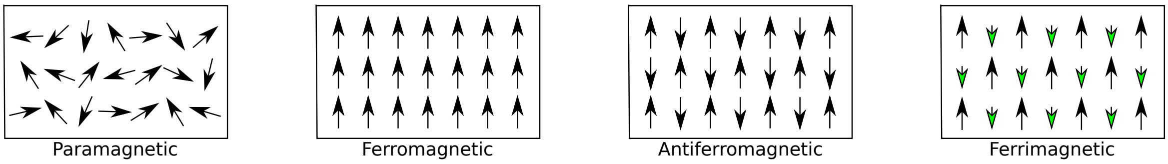
Paramagnetic Ferromagnetic Antiferromagnetic Ferrimagnetic

Fig. 1.6 Type of magnetic materials: Paramagnetic, Ferromagnetic, Antiferromagnetic, Ferrimagnetic

Materials can also be classified by their response to externally applied magnetic field. Insulators can be sub-classifed as well depending on their response to an applied electric field. When an electrical insulator can be polarized by an applied electric field and if this polarization is linearly proportional to the applied field, this is a dielectric material. (See the left figure 1.7.) The electrical charges inside the material volume do not flow like in a conductor but positive charges move toward the field direction and negative charges move in the opposite direction which results a dielectric polarization. Paraelectric materials exhibit an enhanced non-linear polarization to an applied field. (See the center figure 1.7.) When a material exhibit a spontaneous electric polarization that can be reversed by an external electric field, this material is named as ferroelectric. The prefix “ferro” is for an analogy to ferromagnetism as the ferroelectric materials exhibit a hysteresis loop which can be seen on the right in figure 1.7. Barium titanate $BaTiO_3$ is an example of ferroelectric insulator. This compound has a perovskite form where Ba atoms sit in the corner of the lattice, Ti atom is at the center and the oxygen atoms surround the Ti on the face-centers creating an octahedron. The spontaneous polarization is created by the ionic displacement inside volume when there is a non-centrosymmetric phase. The displacement of Ti with respect to surrounding oxygens create a dipole moment. The diagram of energy with respect to polarization, on the left in figure 1.8, reveals the double-well feature present in ferroelectric materials. There are at least two directions with equal energy minima for the system, each of them is associated to equal amplitudes but different orientations of the polarization. When there is an applied electric field, one direction of the polarization is preferred over the others so that the degeneracy is no longer active. When the applied field is applied in the opposite direction, the polarization switches to this direction. Figure 1.8 demonstrates the double-well

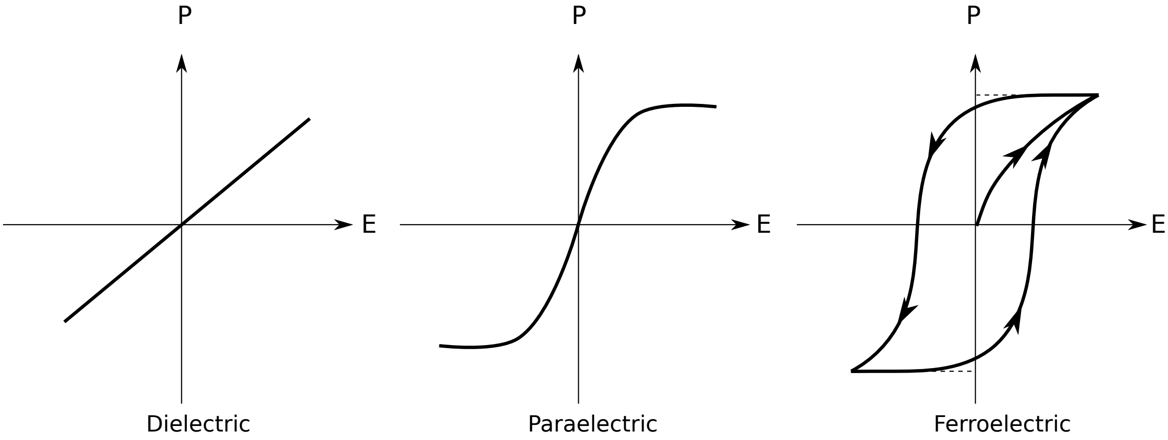

Fig. 1.7 Polarization vs Electric Field in dielectric, paraelectric and ferroelectric materials

potential and the hysteresis loop of a ferroelectric cubic perovskite material. One must note that there are also orthorhombic/rhombohedral lattice systems exhibiting ferroelectricity. Thus, the polarization can be in different directions rather than only two.

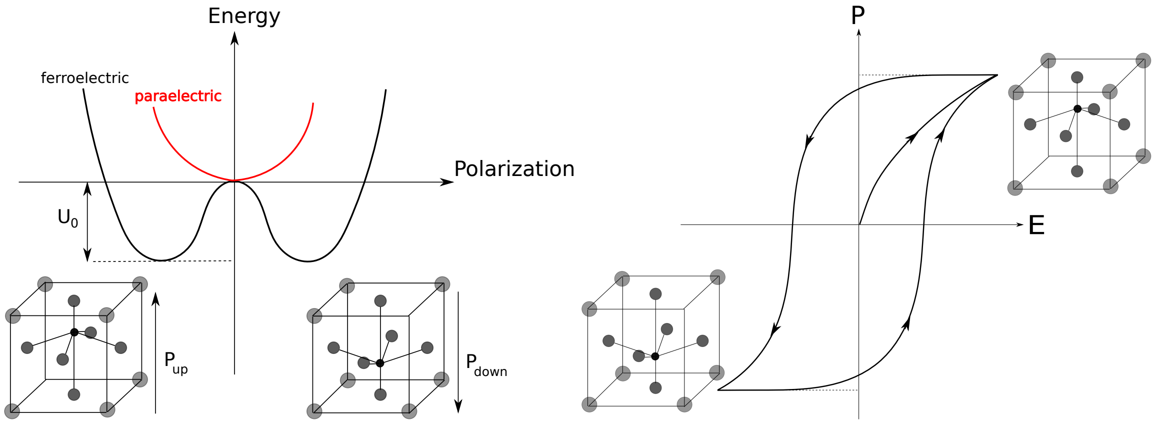

Fig. 1.8 Double-well potential and Hysteresis loop of a ferroelectric perovskite material.

Before finishing this short review of solids, we would like to shortly talk about the concepts of strain, stress and elasticity. Strain is a change in a solid in lattice parameters (length, angle, or volume) compared to its bulk values. Stress is the force per unit area that caused this change (for example, a force applied to the surface of the material). Elasticity is the measure of the deformation of the material when a stress is applied. Strain can be induced in a crystalline material by depositing on an another crystalline material (substrate). This is called as epitaxy.

As we gave the very essential background for the materials, now we can talk about how to control their properties. During this thesis we will focus on thin films and would like to dedicate the next section to a short introduction on the subject.

1.2 Thin Films

There has been always a great interest in the solids which have naturally layered-type structures such as the bulk clay minerals or cobaltates in battery. Solid materials can also be artificially layered as it is in thin films. Thin film is a material made of thin layers with a thickness ranging from few atoms to several micrometers. Thin films do usually not exist alone and they have to be deposited on a substrate material. The substrate material imposes its symmetry and lattice parameters by strain to the thin films. The thickness of the film plays a role on up to which unit cell the induced substrate symmetry and lattice parameters will be kept in the films. In a thin film environment, thin part (film) tries to adopt the thick part (substrate). Indeed, in thick films on a substrate only a few unit cells at the interface have the lattice properties and symmetry induced by the substrate. After these unit cells, the films behave as the bulk. In figure 1.9, on the left we give an illustration of a thin film structure deposited on a substrate. Here, a and b denote the lattice parameters of the substrate and c is the thickness of the thin film. On the right, we give an example of a thin film deposited on a substrate: $Pr_{0.5}Ca_{0.5}MnO_3$ thin film deposited on $SrTiO_3$ (STO) [4].

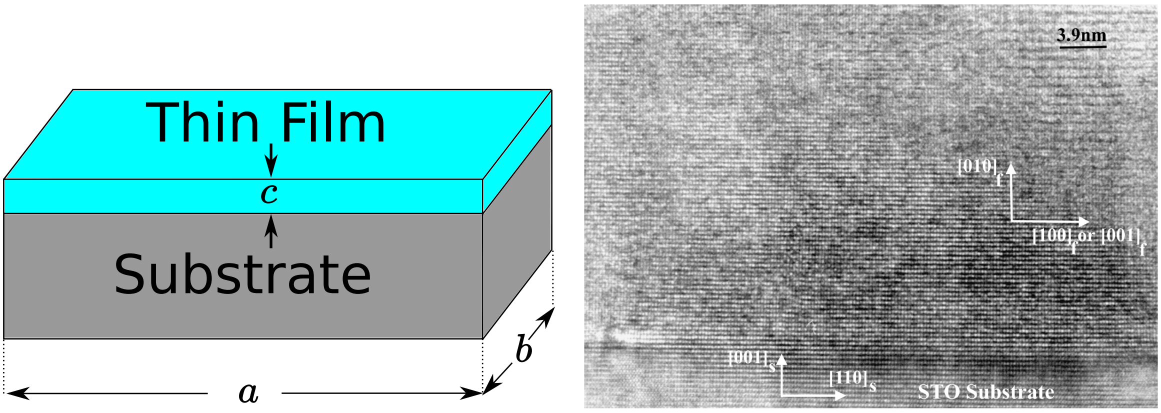

Fig. 1.9 (Left) An illustration of a thin film deposited on a substrate. (Right) A [010] cross section of $Pr_{0.5}Ca_{0.5}MnO_3$ thin film deposited on $SrTiO_3$ (STO) taken at room temperature. Picture taken from Ref. [4]

When two or more different materials are artificially layered together, a new structure, namely a heterostructure, is formed. Heterostructures cannot exist alone and they have to be deposited on a substrate material as well. Heterostructures are a variety of thin films. A heterostructure is named as a superlattice when it is a super periodic structure of layers. The thickness of one layer in a superlattice is generally a few nanometers. In figure 1.10, we give the schematical representation of an example of superlattice. Here, on a substrate material, the material A is layered thrice and the material B is layered four times, this repeats twice leading to a $[(A_3)/(B_4)]_2$ superlattice.

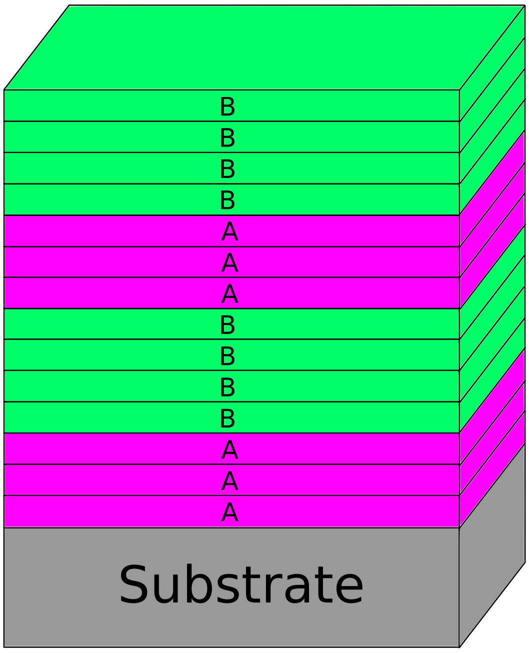

Fig. 1.10 Schematical picture of a superlattice: $[A_3/B_4]_2$

The properties of very thin heterostructures/superlattices are mainly determined by their surfaces and interfaces. In a solid heterostructure, an interface separates two solids while a surface of a solid is in fact a simple type of interface, at which the solid is in contact with the atmosphere or the vacuum. The properties of the heterostructure at the interfaces might differ significantly from the parent bulk materials. For example, when a metallic film is deposited on a semi-conductor, there exists a semi-conductor/metal interface and one can expect new phenomena to appear at the interface. From a more general point of view, in a solid compound, there are different degrees of freedom; that are spin, charge, orbital and lattice degrees of freedom. Tuning these different degrees of freedom is possible by creating interfaces which cause some effects such as symmetry breaking, charge transfer, strain, electrostatic coupling, frustration as illustrated in figure 1.11. Symmetry

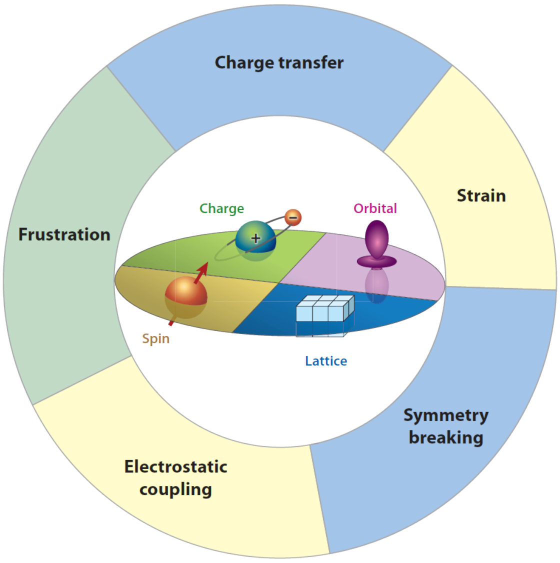

Fig. 1.11 Spin, charge, orbital and lattice at interfaces between different oxides can be modified through the effects of local symmetry breaking, charge transfer, electrostatic coupling, strain, and frustration. Picture from Ref. [5]

breaking at interfaces results with modification of the electronic and structural properties of heterostructure. Charge transfer between one material to another takes place if two interfacing materials have different chemical potentials. When two interfacing materials have different lattice parameters, epitaxial strain is produced at the interface which is a useful tool to control the lattice distortions and influence the electronic degrees of freedom so that alternative electronic and structural ground states can be stabilized. In a thin film environment, substrate induce strain effects on the thin film which modifies the latter's lattice parameters. When two polar materials are attached to each other, electrostatic interactions at the interface result in electrostatic coupling between the layers. When there is a competition between different interactions at the interface, frustration can take place resulting in new structural and electronic phases.

Most of the technological applications require thin films. Therefore, constructing such films and understanding their properties are vital. The material can exhibit quite different properties when it is built as thin films compared to the bulk form due to deposition conditions. In a thin film environment, two surfaces (substrate and thin film) are close to each other, where the former can impact on the latter's physical properties. This influence can lead to new phenomena appearing. Indeed, imposed strain effects by the substrate can stabilize different structures that do not appear under the classical conditions of pressure and temperature. For example, the metastable perovskite compounds $BiMnO_3$ and $YMnO_3$ cannot exist in bulk and can only be prepared under high pressure. However, these metastable phases can be synthesized as thin films via a pulser laser method [6, 7]. The dimensions of thin films are well defined and controllable. The thickness, for example, can be reduced to one unit cell. Thus, the deposition of ultrathin films or superlattices are possible. Reducing one dimension of a material makes the system an intermediate one between macro and molecular systems in which one can expect to investigate physical properties in microscopic scale. In addition, growing artificially multilayer structures and controlling the film orientations are possible in thin film technology which are essential for device applications. At last but not least, one can engineer the properties of some materials such as manganese oxides by using artificial superlattices. Indeed, it has been shown that stacking a magnetic layer $La_{0.7}A_{0.3}MnO_3$ (A = Sr, Ca or Ba) with an insulator such as $SrTiO_3$ can create exotic properties in the system [8–11]. For instance, in $La_{0.7}Ca_{0.3}MnO_3$, the magnetoresistance (MR) can be enhanced at low temperature and the metallic transition is supressed when the superlattice thickness is about 25 Å [10].

Since we would like to focus on manganite superlattices/thin films in this thesis, next chapter is dedicated to manganites. We will recall some fascinating features that manganites hold and explain structural, electronic and magnetic properties of manganites.

Chapter 2

Manganites

Contents

2.1 Why Manganites?

Ever since Jonker and Van Santen reported the existence of ferromagnetism in the mixed crystals of $LaMnO_3$-$AMnO_3$ (A = Sr, Ca or Ba) in 1950s [12], these doped manganese oxides, named as manganites, are under the spotlight of scientists. Indeed, manganites, given with the formulation $AMnO_3$, have been fascinating the scientists since then, due the opportunity to obtain large varieties of systems depending on the solid solution of the site A. Naturally, due to the potentiality for applications, a greater interest has been given into the class of manganites that exhibit large Curie temperature. The colossal magnetoresistance effect is another reason which makes the manganites desirable for applications. Lastly but most importantly, the manganites present rich phase diagrams in terms of both transport and magnetic properties depending on the concentration of the doping elements. Given all these interesting qualities, there have been a great amount of theoretical and experimental studies carried out and yet, even today there are still many things to exploit in manganites.

In 1950, Jonker and Van Santen discovered the dependence of the Curie temperature (T_c), saturation magnetization (M_s), and electrical resistivity (ρ) in various ferromagnetic doped $\mathrm{LaMnO_3}$ compounds [12, 13]. For the doping value $x \sim 0.35$, they showed that $\mathrm{La_{1-x}Sr_xMnO_3}$ is ferromagnetic and has a maximum Curie temperature of $T_c \sim 370K$, with a saturation magnetization of $M_s \sim 90G/g$, and a minimum electrical resistivity compared to the other doping values. (See Figure 2.1). Jonker and Van Santen stated that the ferromagnetic properties are the result of a strong $\mathrm{Mn^{3+} - Mn^{4+}}$ exchange interaction, combined with a weak $\mathrm{Mn^{3+} - Mn^{3+}}$ interaction and a negative $\mathrm{Mn^{4+} - Mn^{4+}}$ interaction. They also showed that the change of the Curie temperature in these materials cannot only be explained by the simple exchange interaction. Later studies showed that what determines the Curie temperature is not the distance between manganese atoms, but the $\mathrm{Mn - O - Mn}$ angle.

On the track of Jonker and Van Santen's steps, Volger's measurements on $\mathrm{La_{0.7}Sr_{0.3}MnO_3}$ showed that magnetism and electrical conductivity are correlated [14]. In 1951, Zener brought a theoretical explanation of the appearance of ferromagnetism by an effect called "double exchange mechanism" [15], which we will explain in details in this chapter. The double-exchange mechanism also explained the correlation between the electrical conduction and ferromagnetism in doped manganites, reported in Jonker and Van Santen's seminal paper [13]. In 1955, using neutron scattering techniques, Wollan and Koehler obtained a detailed characterization of the type of the magnetic orders for $\mathrm{La_{1-x}Ca_xMnO_3}$ and built the very first magnetic structure-based phase diagrams for manganites [16]. Their samples were purely ferromagnetic over a relatively narrow range of composition ($\mathrm{x} \sim 0.35$), showed simultaneous occurrence of ferromagnetic and antiferromagnetic phases in the ranges ($0 < \mathrm{x} < 0.25$) and ($0.40 < \mathrm{x} < 0.5$), and antiferromagnetic orders at $\mathrm{x} = 0$ and $x > 0.5$. During the same period, Jonker related the ferromagnetic and metallic phases of the manganites to lattice and crystal structure [17]. He stated that $\mathrm{LaMnO_3}$ is antiferromagnetic, but it could be ferromagnetic if the cubic perovskite structure, present at high temperatures, could be preserved at low temperature. He concluded that when the structure gets closer to a stable cubic structure, then the $\mathrm{Mn^{3+} - O^{2-} - Mn^{4+}}$ bonds are stronger and a stronger double exchange mechanism takes place. In 1969, Searle and Wang reported the magnetic field dependence of the resistivity for $\mathrm{La_{1-x}Pb_xMnO_3}$, and in particular the existence of a large magnetoresistance effect near the Curie temperature [18]. The magnitude of the magnetoresistance was reported to be 20% at room temperature, for $B = 1$ T [18].

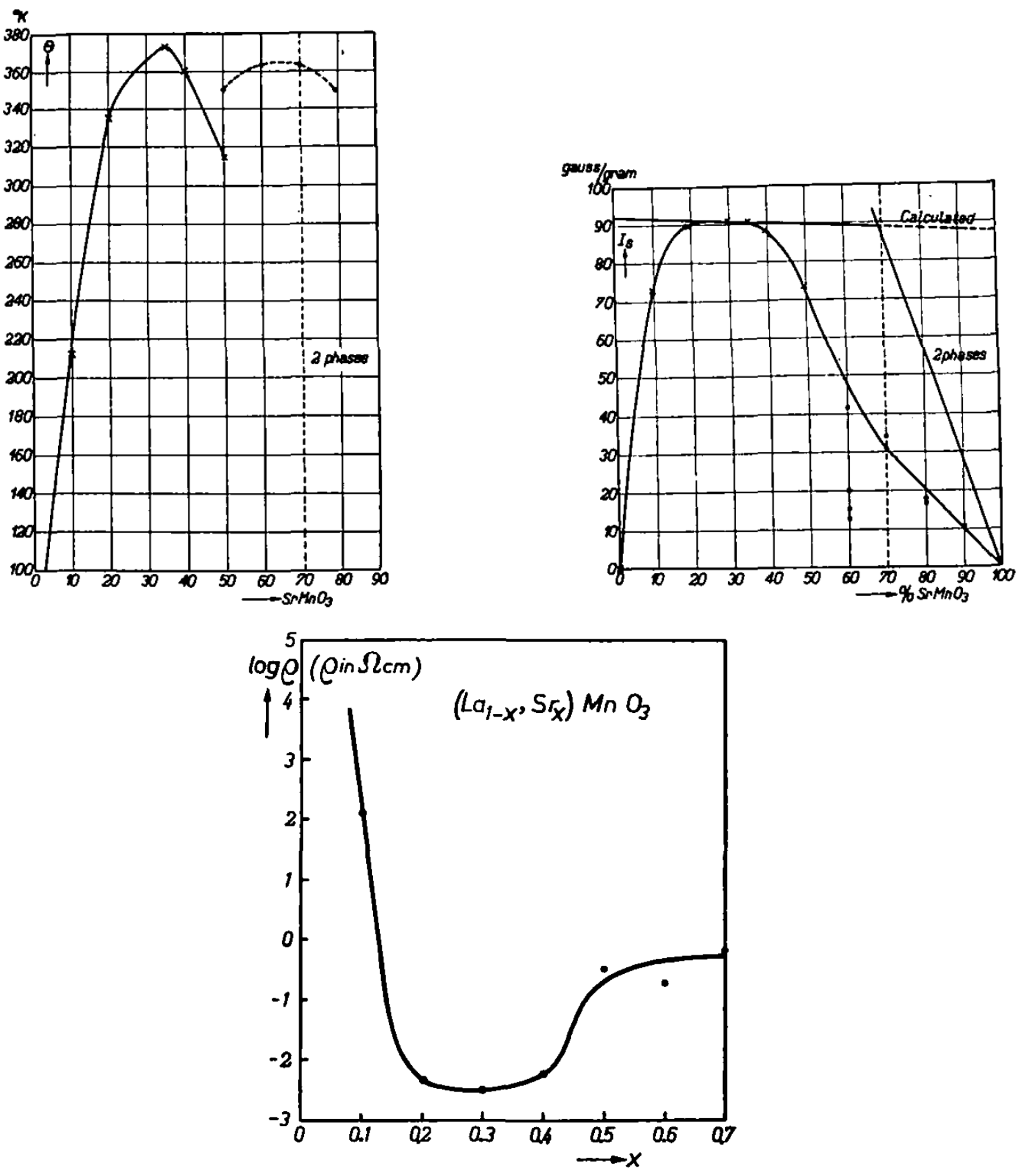

Fig. 2.1 Magnetic properties of $La_{1-x}Sr_xMnO_3$ with respect to Sr doping: (top left) Curie temperature $T_c(K)$, (top right) saturation magnetization M_s at 90 K (label “calculated” corresponds to the saturation magnetization calculated on the assumption that all $3d$ electrons in the mangenese ions contribute with their spins to the saturation magnetization), (bottom) resistivity ρ. (Picture taken from references [12, 13])

In 1988, the so-called “giant” magnetoresistance (GMR) was discovered in Fe/Cr superlattices [19, 20]. In these superlattices with thin Cr layers, A. Fert and P. Grünberg observed that the magnetoresistance is very large; indeed, for example the resistivity is reduced by a factor of 2 at $T = 4.2$ K and $B = 2$ T in Fe/Cr superlattice samples, with a Cr layer thickness of 9 Å [19]. This so-called GMR materials are made of metallic multilayers and heterogeneous films. The magnetoresistance values do typically range between $5 - 150\%$ in these compounds [21–25]. The interest in manganites was then triggered by the observation of similarly large magnetoresistance effects in $Nd_{0.5}Pb_{0.5}MnO_3$ [26] single crystal and in $La_{2/3}Ba_{1/3}MnO_3$ [27] thin films. Their resistivity as a function of an applied magnetic field is reported in figure 2.2, extracted from references [26, 27]. On the left, for different magnetic fields, the resistivity of the [110] direction cut from $Nd_{0.5}Pb_{0.5}MnO_3$ single crystal is given as a function of temperature for different external magnetic fields. The largest resistivity at zero field appears close to 185 K. Below 185 K, the resistivity decreases sharply, by two orders of magnitude. Between 190 K and 300 K, the resistivity declines. The largest negative magnetoresistance (MR) appears close to the peak in the zero-field resistivity, where the resistivity is reduced by two orders of magnitude. When the magnetic field increases, the peak in the resistivity get smaller and occurs at higher temperatures. In the case of $La_{2/3}Ba_{1/3}MnO_3$ ferromagnetic thin films, the resistivity measurements at room temperature [27] showed a large magnetoresistance of more than 60%, formulated as ($[\rho(0) - \rho(B)]/\rho(0)$ where $\rho(B)$ and $\rho(0)$ are the resistivities at magnetic field B and without field respectively) which can be seen on the right in figure 2.2. However, using the magnetoresistance formulation usually used for magnetic multilayers, which is $[\rho(B) - \rho(0)]/\rho(B)$, gives us the giant MR value 150%. From now on, the values given for magnetoresistance will be reported by taking into account the latter formulation. Later, in the $La_{0.67}Ca_{0.33}MnO_x$ thin films, the magnetoresistance effect is reported to be of 127000% at 77 K, B = 6 T [28, 29] (See figure 2.3). This huge magnetoresistance was called colossal magnetoresistance (CMR) since it is of three orders of magnitude larger than giant magnetoresistance (GMR). This large increase in magnetoresistance created a big impact in the field of manganites. Indeed, CMR effect offers tremendous potentials in the technologies of magnetic recording, spin-polarized electronics, sensors and etc.

In conventional ferromagnets spin is not coupled with the lattice. However, in CMR manganites, charge, spin, and lattice degrees of freedom are strongly coupled and these couplings give rise to a rich variety of physical phenomena. Thus, in order to understand the CMR effect, researchers enlarged their perspectives from the ferromagnetic metallic phase to the doping regions where there exist many different competing phases.

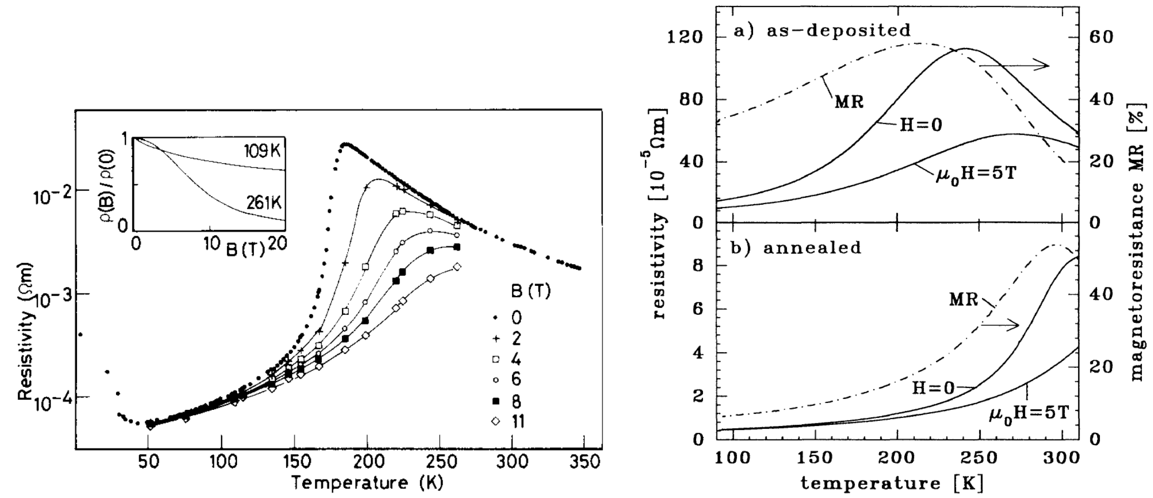

Fig. 2.2 (Left) The resistivity and magnetoresistance of $Nd_{0.5}Pb_{0.5}MnO_3$ single crystal from reference [26]. (Right) The resistivity and magnetoresistance of $La_{2/3}Ba_{1/3}MnO_3$ ferromagnetic thin films [27]

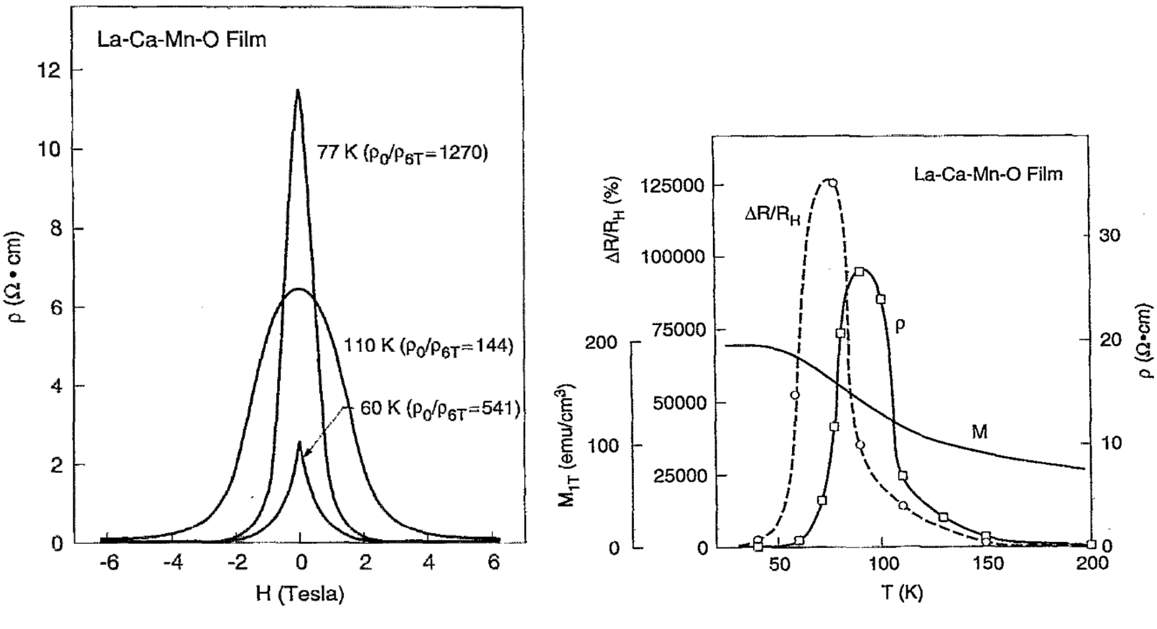

Fig. 2.3 (Left) Resistivity (ρ) vs. Magnetic Field (B = H) exhibits the colossal magnetoresistance behaviour about 127000% at 77 K. Picture taken from reference [28] (Right) Temperature dependence of magnetoresistance ($\Delta R/R = \Delta\rho/\rho$), resistivity ($\rho$) and magnetization (M). (Picture taken from reference [28])

Half-doped manganites are given with the generic formulation of $R_{1-x}A_xMnO_3$. Here, R is a trivalent element and A is a divalent alkaline element. Depending on the choice of R and A, the composition can exhibit a wide range of magnetic and electric phenomena, including ferromagnetic, antiferromagnetic, charge, and orbital ordering. In Figure 2.4 one can see the phase diagrams of $La_{1-x}Sr_xMnO_3$ (LSMO), $Nd_{1-x}Sr_xMnO_3$ (NSMO) and $Pr_{1-x}Ca_xMnO_3$ (PCMO) [30]. This figure pictures the variety of the systems that one can obtain in rare-earth manganites depending on the solid solutions of R and A. For example, LSMO is a ferromagnetic metal in the doping region $x = 0.3$, so is NSMO, whereas PCMO is a ferromagnetic insulator. Since $La_{1-x}Sr_xMnO_3$ has the largest T_c (370 K) among manganites and a large bandwidth, significant amount of attention and focus have been given to the study of these manganites. Thanks to this, the phase diagram of LSMO is the most complete phase diagram among all manganites [31]. (see figure 2.5) This diagram was obtained by the measurements of structural, magnetic, and transport properties on single crystals of LSMO within $0 \leq x \leq 0.85$ region. At low temperature, the system presents different magnetic orderings depending on the Sr concentration. In the doping region of $0.16 \leq x \leq 0.5$, LSMO is ferromagnetic below the Curie temperature. For $T < 200K$, between the doping values 0.5 and 0.6, the magnetic ground state is either canted (CA) metallic or a non-uniform phase-seperated (PS). For $0.6 \leq x \leq 0.7$ and $T < 200K$, LSMO is A-type antiferromagnetic

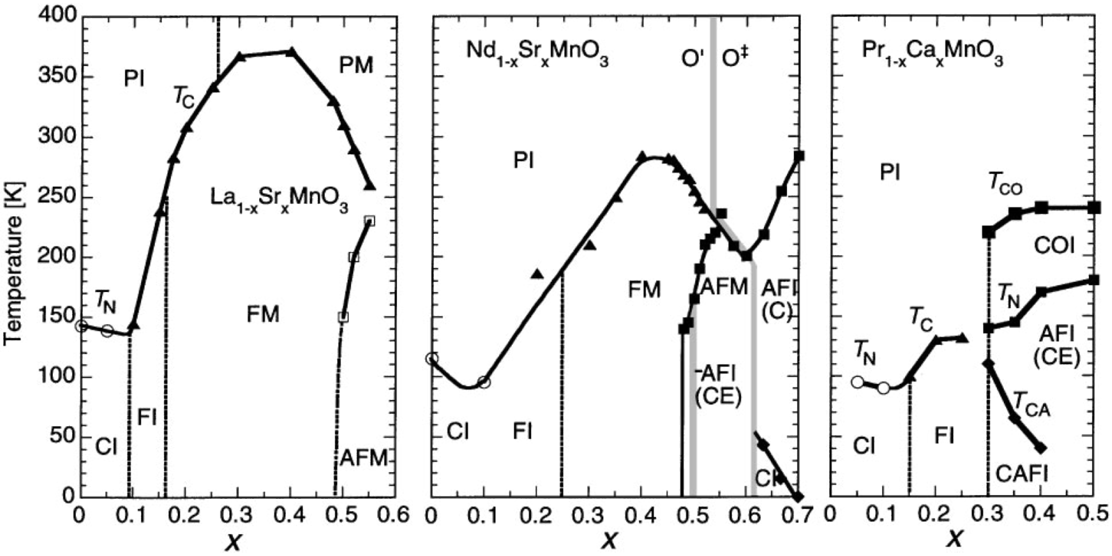

Fig. 2.4 The magnetic and electronic phase diagrams of $La_{1-x}Sr_xMnO_3$ (left), $Nd_{1-x}Sr_xMnO_3$ (center) and $Pr_{1-x}Ca_xMnO_3$ (right). The PI, PM and CI stand for the paramagnetic insulating, paramagnetic metallic and spin-canted insulating states, respectively. The FI, FM, and AFM denote the ferromagnetic insulating and ferromagnetic metallic, and antiferromagnetic (A-type) metallic states, respectively. (Picture taken from reference [30])

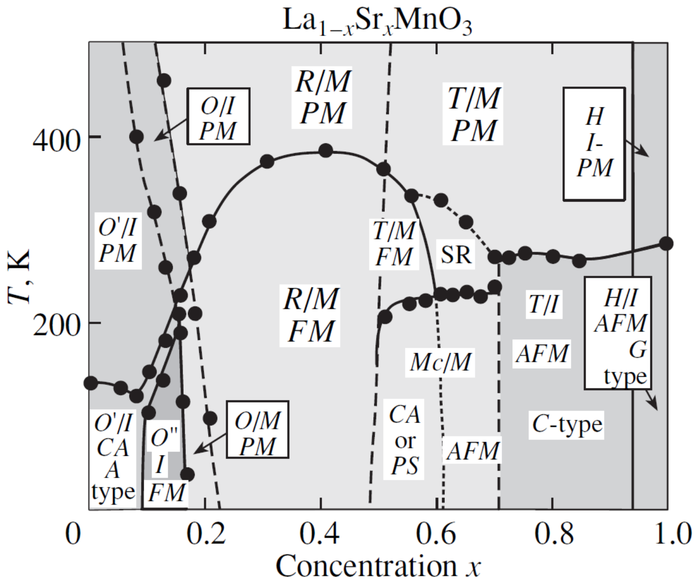

Fig. 2.5 Phase diagram of LSMO. Crystal Structures: O, O' and O'' refer to orthorhombic structures: T is tetragonal, Mc is monoclinic, H is hexagonal, R is rhombohedral. Magnetic structures: *PM* is paramagnetic, *FM* is ferromagnetic, *AFM* is antiferromagnetic, *CA* is canted antiferromagnetic. Electronic states: *PS* is phase separated, *I* is insulating and *M* is metallic. (Picture taken from Ref. [31])

metal. As Sr concentration increases, the phase transfers to C-type insulating AFM state. Lastly, for $x > 0.9$, it goes through its G-type insulating AFM phase.

For the LSMO, it was shown by Tokura *et al.* that the magnetoresistance effect is maximized in the doping region $x = 0.175$ which is the transition point from insulating to metallic states at low temperatures [32]. This magnetoresistance effect is pictured in figure 2.6. A large MR value around 90% is seen close to $T_c = 283K$. Such a large MR above T_c is the indication of an insulator-metal transition.

With applications in mind, one can wonder whether it is possible to control these fascinating properties of manganites. One way to do it is to deposite the manganites as thin films, so interface effects or strain engineering can take place. Thus, we choose to work with $\mathrm{La_{1-x}Sr_xMnO_3}$ ($x = 1/3$) (LSMO) thin films because both Mn^{3+} and Mn^{4+} coexist in the bulk LSMO and the Curie temperature of bulk LSMO as a function of hole doping is one of the highest ($\mathrm{T_c} \simeq 370$K). The question here is whether this Curie Temperature can be controlled and whether it can be increased. Let us first take a look on the general structure of manganites. Then later, in order to understand the behaviour and properties of LSMO, we shall recall the properties of the parent compounds.

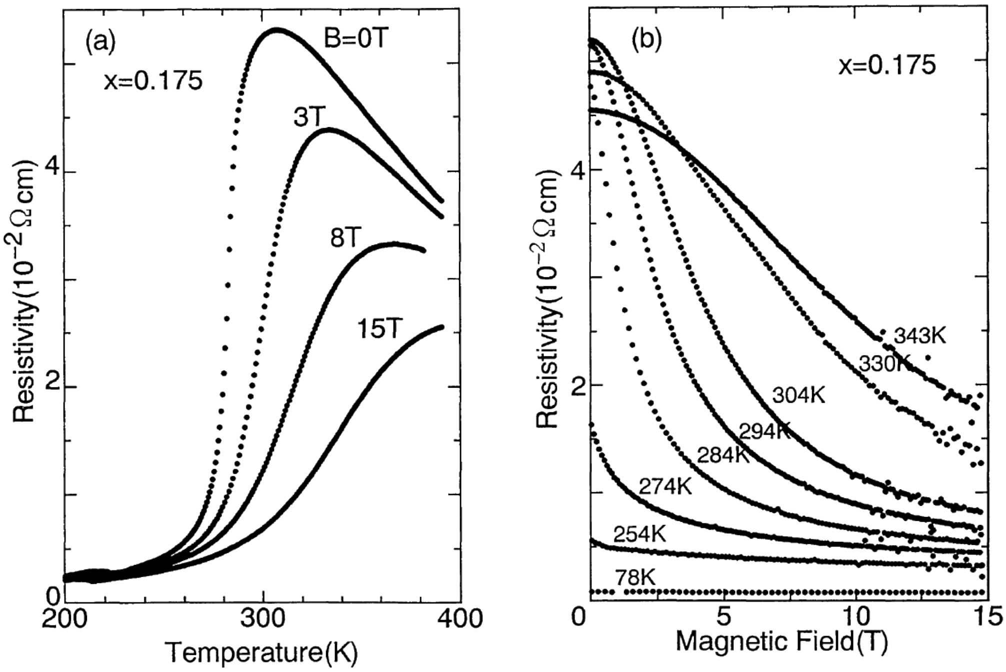

Fig. 2.6 Magnetoresistance in a $La_{0.825}Sr_{0.175}MnO_3$ crystal: (a) temperature dependence of the resistivity in various magnetic fields and (b) the magnetic field dependence of resistivity at various temperatures. (Picture taken from reference [32])

2.2 General Properties of CMR Manganites

2.2.1 Structure

The manganites, i.e. the compounds with $AMnO_3$ formula, where A is either a cation or a mixture of two or more of such elements, or vacancies, mostly crystallize at high temperature in the so-called cubic perovskite structure (space group $Pm\bar{3}m$) as shown at left in figure 2.7. The perovskite structure allows the system to be doped in a large variety on both A and Mn sites. In most of the cases, dopants on the A-site can form homogeneous solid solution. At low temperature, perovskites exhibit lattice distortions leading to symmetry breakings. One of very well known lattice distortion arises from the deformation of the MnO_6 octahedron and originates from a Jahn-Teller effect which we will explain later in this chapter. In the ideal $AMnO_3$ perovskite structure given at the left in figure 2.7, the mismatch between the equilibrium A – O and Mn – O bond lengths is given by a tolerance factor $\mathrm{t} = \frac{(\mathrm{A-O})}{\sqrt{2}(\mathrm{Mn-O})}$, which can be calculated from the sums of ionic radii obtained from X-ray diffraction at room temperature. This mismatch takes then the form of $t = \frac{r_A + r_O}{\sqrt{2}(r_{Mn} + r_O)}$. Here, r_A, r_{Mn} and r_O are the averaged ionic radii at sites A, Mn and O, respectively. t is called as the

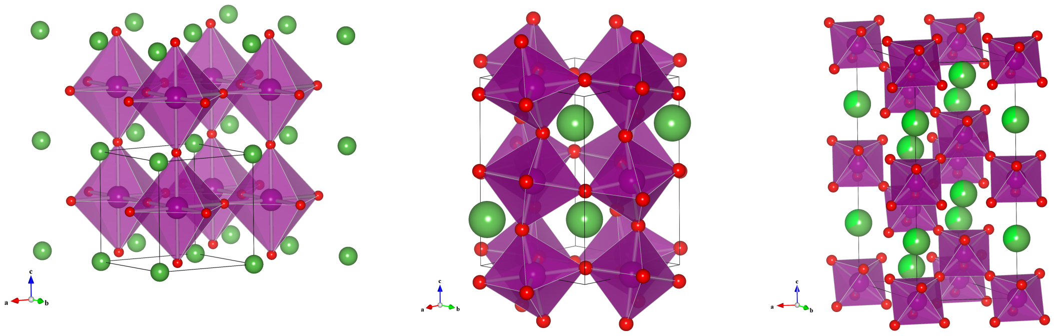

Fig. 2.7 (Left) Schematic picture of a cubic perovskite manganite. A cation sits at the corners. Mn is at the center of the unit cell. Oxygens are at the face centers and form an octahedron around Mn atom. Schematic distorted perovskite structures of manganite: orhorhombic (center) and rhombohedral (right)

Goldschmit's tolerance factor. When t is close to 1, the cubic perovskite structure is realized. As t decreases, the lattice structure transforms to the rhombohedral ($0.96 < t < 1$) and then to the orthorhombic ($t < 0.96$) structures in which the $Mn-O-Mn$ bond angle is also modified. On the other hand, when $t > 1$, which is the indication that the cation in the A-site is too large, the hexagonal perovskite structure appears. In hexagonal perovskite structures, the MnO_6 octahedra exhibit face-sharing and chain-formation along the $\vec{c}$ axis.

Taking into account the general perovskites with the formula ABO_3 let us briefly give examples of perovskites with varying t values. When $t > 1$, the structure adjusts through ferroelectric displacements in the perovskite, such as in $BaTiO_3$ ($A = Ba$, $B = Ti$). When $t < 1$, there are cooperative rotations of BO_6 octahedra around a cubic [001] axis, such as in $CaTiO_3$ ($A = Ca$, $B = Ti$) [33]. These cooperative rotations also adjust to $t < 1$ in some manganites such as $La_{0.7}Ba_{0.3}MnO_3$ at $T = 1.6$ K around a cubic axis [101] in orthorhombic space group (*Imma*) [34]. These rotations bend the $Mn-O-Mn$ bond angle from 180° to $180° - \alpha$ and as a consequence affect the magnetic interactions which takes place between Mn ions.

Hwang *et al.* studied the correlation between the Curie temperature and the average ionic radius of La site $\langle r_A \rangle$ in doped $LaMnO_3$ [35]. They found a decrease in T_c and a sharp increase in the magnetoresistance near the T_c for decreasing $\langle r_A \rangle$ values. They also noted that decreasing $\langle r_A \rangle$ values also reduces the $Mn-O-Mn$ bond angle and thereby the electron hopping matrix element between the Mn sites since the bond angle is the responsible parameter for electron hopping between Mn sites. Mahesh *et al.* also studied the same relation in rare-earth manganites and stated that ferromagnetic transition temperature T_c and insulator-metal transition temperature T_p increases with $\langle r_A \rangle$ [36]. In figure 2.8, one can see the temperature as a function the tolerance factor and as well as $\langle r_A \rangle$.

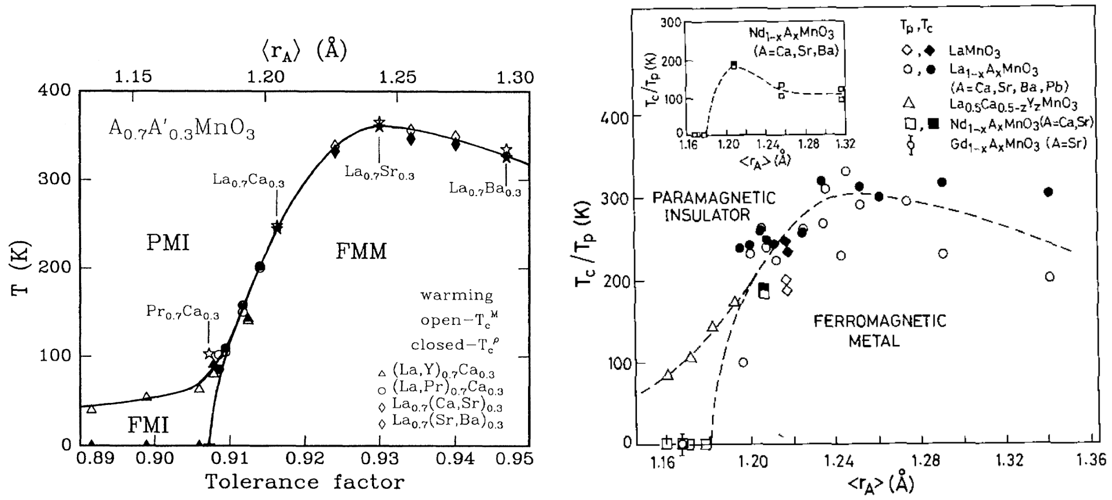

Fig. 2.8 (Left) Curie temperature as a function of tolerance factor for the system of $A_{0.7}A'_{0.3}MnO_3$ where A is a trivalent rare earth and A' is a divalent alkali earth ion. (Right) Curie temperature as a function of $\langle r_A \rangle$ for the system of $A_{1-x}A'_xMnO_3$. (Picture taken from references [35] (left) and [36] (right))

However, the electronic and magnetic properties of manganites depend not only on the tolerance factor or $\langle r_A \rangle$, but also on the size mismatch between the A-size cations defined by the variance $\sigma^2 = \sum_i y_i r_i^2 - r_A^2$, where r_i is the radius of each R^{3+} and D^{2+}, y_i is fractional occupations of the i ions, r_A is the average ionic radius of R^{3+} and D^{2+} [37–41]. The variance σ^2 determines the random distribution of the $Mn-O-Mn$ bonds. Rodriguez-Martinez *et al.* [37] studied the cation size and disorder effects in various rare earth manganites in the doping region $x = 0.3$. They pointed out that the metal-insulator transition temperature decreases as the variance σ^2 increases as one can see on the left in figure 2.9. They have proposed a fit to the linear region of this data in this figure with the relation: $T_m(\langle r_A \rangle, \sigma^2) = T_m(\langle r_A \rangle, 0) - p_1\sigma^2$. Here, $T_m(\langle r_A \rangle, 0)$ is an estimate of the ideal metal-insulator transition temperature if cation-size disorder were not present, i.e $\sigma^2 \to 0$ and p_1 is the slope of the fitting and gives the $Mn-O$ force constant. Damay et al. [38] also studied cation disorder and size effects upon magnetic transitions in various rare earth manganites in the doping region $x = 0.5$. They have used the same fitting procedure proposed by Rodriguez-Martinez *et al.* [37]. One can see on the right in figure 2.9 that the Curie temperature decreases as the variance σ^2 increases.

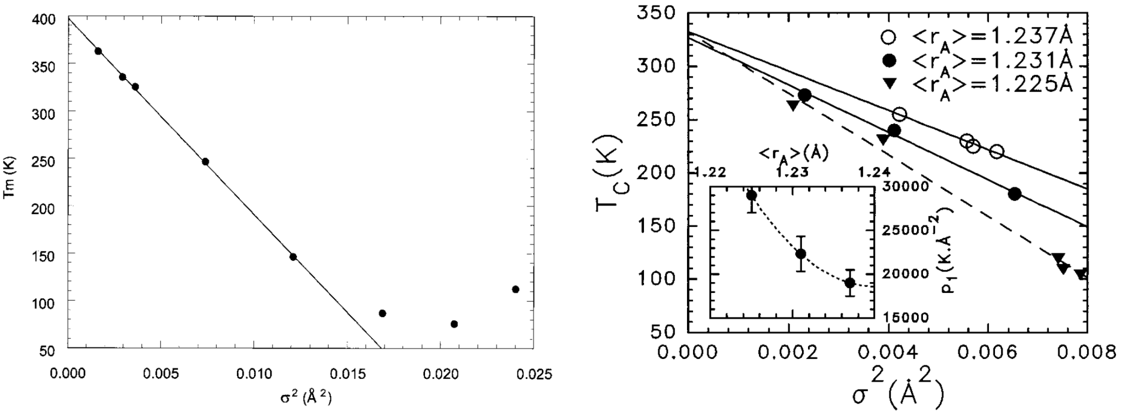

Fig. 2.9 (Left) The variation of the metal-insulator transition temperature from resistivity T_m with respect to the variance σ^2. (Right) The variation of the ferromagnetic-paramagnetic transition temperature T_c with respect to σ^2 at constant $\langle r_A \rangle$ for three series of compounds involving $\langle r_A \rangle = 1.237$ Å, $\langle r_A \rangle = 1.231$ Å, and $\langle r_A \rangle = 1.225$ Å. Inset: p_1 vs $\langle r_A \rangle$ for the three $\langle r_A \rangle$ values studied. (Picture taken from references [37] (left) and [38] (right))

2.2.1.1 Parent Compounds

One can classify the undoped manganites into two groups: $RMnO_3$ and $AMnO_3$. Here, R is a trivalent rare-earth atom and A is a divalent alkaline earth atom like Ca or Sr. Both $RMnO_3$ and $AMnO_3$ are antiferromagnetic insulators. Let us briefly take a look at the literature for the crystal structures and magnetic orderings of $LaMnO_3$ (La^{3+}), $CaMnO_3$ (Ca^{2+}), $BaMnO_3$ (Ba^{2+}) and $SrMnO_3$ (Sr^{2+}) on which we will base our study as mixed-manganites.

The study of lanthanum and calcium manganites are well visited since the mid 50ies. Wollan and Koehler stated that the magnetic ground state of $LaMnO_3$ is A-type antiferromagnetic (A-AFM) while $CaMnO_3$ is G-type antiferromagnetic (G-AFM) [16]. Yakel studied the structures of $LaMnO_3$ and $CaMnO_3$ compounds by means of X-ray powder diffraction at room temperature [42]. At low temperature, Yakel reported orthorhombic structure for $LaMnO_3$ and $CaMnO_3$ with a tolerance factor around 0.92. Elemans *et al.* studied mixed manganites $La_{1-x}Ba_xMnO_3$ and found the orthorhombic structure present with the space group *Pbnm* from X-ray and neutron diffractions at room temperature though this orthorhombic distortion becomes smaller with increasing x values [43]. Later, $CaMnO_3$ was reported to have an orthorhombic derivative (*Pbnm* space group) of the ideal cubic perovskite with nearly perfect octahedra [44–47]. Rodríguez-Carvajal *et al.* also studied $LaMnO_3$ by thermal analysis and high-resolution neutron-powder diffraction [48]. At room temperature, they obtained the orthorhombic phase with *Pbnm* space group with an antiferrodistortive orbital ordering which is due to the Jahn-Teller effect. Above 750 K, there is a structural phase transition where this Jahn-Teller effect disappears as well as the orbital ordering disappears. The crystal symmetry does not change with this transition but lattice becomes metrically cubic and MnO_6 octahedra becomes more ideal at high temperature. They finally reported that at 1010 K the phase transiton $Pbnm \rightarrow R\bar{3}c \rightarrow Pm\bar{3}m$ occurs due to steric-thermal effects.

In 1968, Syono *et al.* studied the phase stability of $BaMnO_3$ and $SrMnO_3$ compounds [49]. They showed that these two manganites have hexagonal perovskite-like structures. Indeed, at normal pressure $BaMnO_3$ has a two layered hexagonal structure ($2H$) while $SrMnO_3$ has a four layered hexagonal structure ($4H$) [50]. The hexagonal structures for $SrMnO_3$ and $BaMnO_3$ can be schematically seen in figure 2.10. $BaMnO_3$ with $2H$ hexagonal structure is stable below $1150°C$ [51] whereas $SrMnO_3$ hexagonal structure is stable in air below $1035°C$ with a cubic and a hexagonal perovskite structures [52, 53]. In 1988, by neutron diffraction measurements, Battle *et al.* [54] stated that $SrMnO_3$ is paramagnetic at room temperature and has a hexagonal structure with $P6_3/mmc$. Chamberland *et al.* [50] have proposed that the hexagonal $SrMnO_3$ has an antiferromagnetic ordering with Néel temperature $T_N = 350$ K but Battle *et al.* [54] reported a short-range antiferromagnetic coupling between Mn ions in face-sharing MnO_6 octahedra above $T_N = 278 \pm 5$ K. At 290 K, there is no long-range magnetic ordering. The hexagonal $SrMnO_3$ structure is stable up to about 1309 K above which it transforms to a cubic structure. [52] The high-temperature cubic $SrMnO_3$ survives as a metastable phase at low temperatures if quenched. This cubic $SrMnO_3$ has a G-type antiferromagnetic structure at low temperature [16]. Both the hexagonal and the cubic structures are semiconductors.

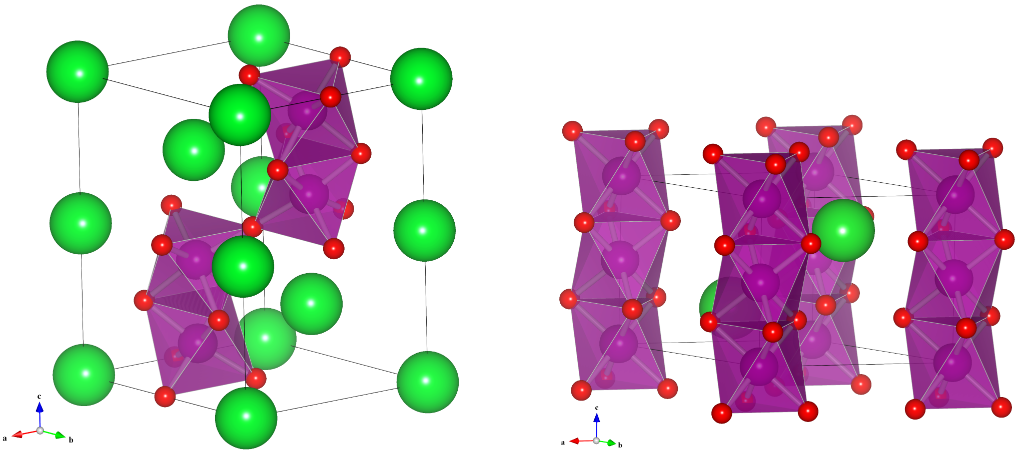

Fig. 2.10 Schematical picture for hexagonal perovskite structures: (left) the four layered hexagonal ($4H$-$P6_3/mmc$) for $SrMnO_3$, the two layered hexagonal ($2H$-$P6_3/mmc$) for $BaMnO_3$

For the crystal structures of mixed manganites, we can look back at the phase diagram of $La_{1-x}Sr_xMnO_3$ (LSMO) given in figure 2.5. One can see that LSMO is orthorhombic for small values of doping value x like the undoped $LaMnO_3$. When $0.2 < x < 0.5$, LSMO is rhombohedral. At low temperature, when $0.5 < x < 0.7$, LSMO is monoclinic. In the same interval it is tetragonal at high temperature. When x values approaches to 1, LSMO is hexagonal like $SrMnO_3$.

As we shortly described the crystal structures and magnetic orderings of the undoped manganites $LaMnO_3$, $CaMnO_3$, $BaMnO_3$, $SrMnO_3$ and $La_{1-x}Sr_xMnO_3$ now we would like to recall the electronic structure of the manganites.

2.2.2 Atomic Electronic Structure

Manganese (Mn) belongs to the family of transition metals. It has 25 electrons with the electronic configuration $1s^22s^22p^63s^23p^64s^23d^5$ in which there exist 7 valence electrons (2 valence electrons in the $4s$ shell and 5 valence electrons in the $3d$ shell). Let us first define the orbitals of the $3d$ shell, i.e. the magnetic orbitals. In figure 2.11, one can see the d orbitals: $d_{x^2-y^2}$, d_{z^2}, d_{xy}, d_{yz}, d_{xz}.

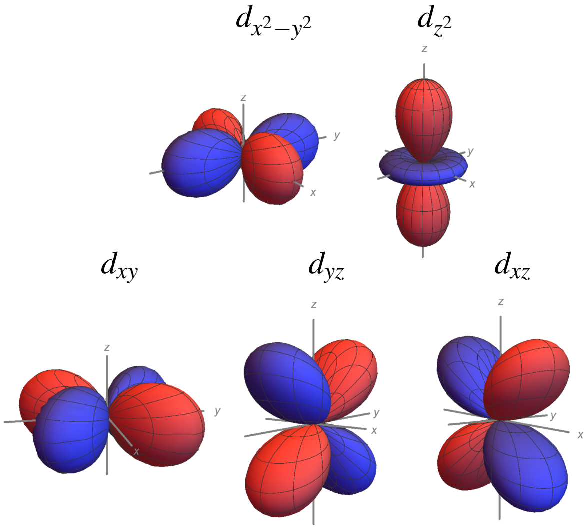

Fig. 2.11 Magnetic orbitals: Five orbitals of the $3d$ shell

2.2.2.1 Crystal-Field Splitting

In an isolated atom, these $3d$ orbitals of Mn would be degenerated. However, when manganese atoms are embedded in a specific crystal geometry, in a solid state system, Mn being positioned at the approximate center of an "octahedron", breaking of the orbital degeneracy takes place. In other words, the orbital degeneracy is removed by the presence of a crystal field and the $3d$ orbitals energies are split. One can schematically see in figure 2.12 that for an Mn atom embedded in a regular octahedron, the $3d$ orbitals are split into subsets e_g ($d_{x^2-y^2}$, d_{z^2}) and t_{2g} (d_{xy}, d_{yz}, d_{xz}), with the crystal field splitting energy Δ. Now, let us recall the notion of crystal field splitting and how exactly it takes place.

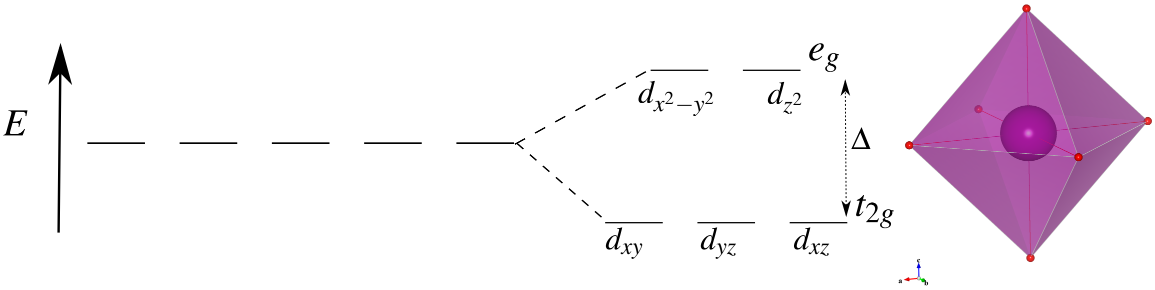

Fig. 2.12 Crystal Field Splitting of a regular octahedron. Five-fold degenerate atomic $3d$ levels split into lower t_{2g} (triply degenerate) and higher e_g (doubly degenerate) levels.

In an isolated, free ion, the one-electron potential $v_R(\vec{r})$ has a $O(3)$ symmetry (spherical symmetry) and it is invariant under any rotation. Thus, all one-electron states within a given shell ($3d$ shell in the Mn ion case) are degenerate. However, when the same ion is embedded inside a molecule or a solid, the one-electron potential $v_R(\vec{r})$ is expected to have a lower symmetry, thus the one-electron states of the the given shell will split. This symmetry reduction arises from crystal field; which has two components:

- Ionic Contribution: Coulomb potential generated by the surrounding charged ions (dominant in ionic crystals)

- Covalent Contribution: Ligand field due to the bonding with neighbours.

Ionic contribution is dominant when the crystal is perfectly ionic and the ions can be treated as point charges. Then, the one-electron potential can be given as

$$v_R(\vec{r}) = \sum_{\mu} \frac{q_\mu}{|\vec{A}_\mu - \vec{r}|} = v_0(r) + \sum_{\mu \neq 0} \frac{q_\mu}{|\vec{A}_\mu - \vec{r}|} = v_0(r) + v_c(\vec{r}) \tag{2.1}$$

where $\vec{A}_\mu$ are the position vectors of the ions and q_μ are the ion charges. $v_0(r)$ is the ionic central potential at the site $\vec{A}_0$ and has spherical symmetry. $v_c(\vec{r})$ is the "crystal field potential" at a given site $\vec{A}_0$ generated by all the surrounding ions in the crystal. For example, in the case of perovskite manganites, at the site of Mn, one can calculate the crystal field potential $v_c(\vec{r})$ generated by all the neighbouring oxygen ions (six oxygen ions) using the equation 2.1 and making Taylor expansion approximations. For perovskite structure, one can find that the crystal field potential $v_c(\vec{r})$ has an octahedral symmetry. Thus, the crystal field potential $v_c(\vec{r})$ lowers the Mn site symmetry from spherical to octahedral. As a consequence, it lifts the degeneracy of the shell. We will not present the details here (a detailed lecture on crystal field splitting can be found in the reference [55]), however, based on group theory, one can find how this splitting takes place (d shell splits into e_g ($d_{x^2-y^2}$ and d_{z^2}) and t_{2g} (d_{xy}, d_{yz} and d_{xz}) shells). In addition, in order to determine which orbital set is lower in energy, one can calculate the potential $v_c(\vec{r}) = v_{\text{oct}}(\vec{r})$ and find that the e_g states are higher in energy than t_{2g} states since the e_g electrons face toward the negative oxygen ions and therefore feel a larger Coulomb repulsion than the t_{2g} ones, the latter having its nodes directed between the negative oxygen ions. (See figure 2.13.) One must note that this result stands on the assumption of the first neighbours determining the crystal field. However, Coulomb repulsion

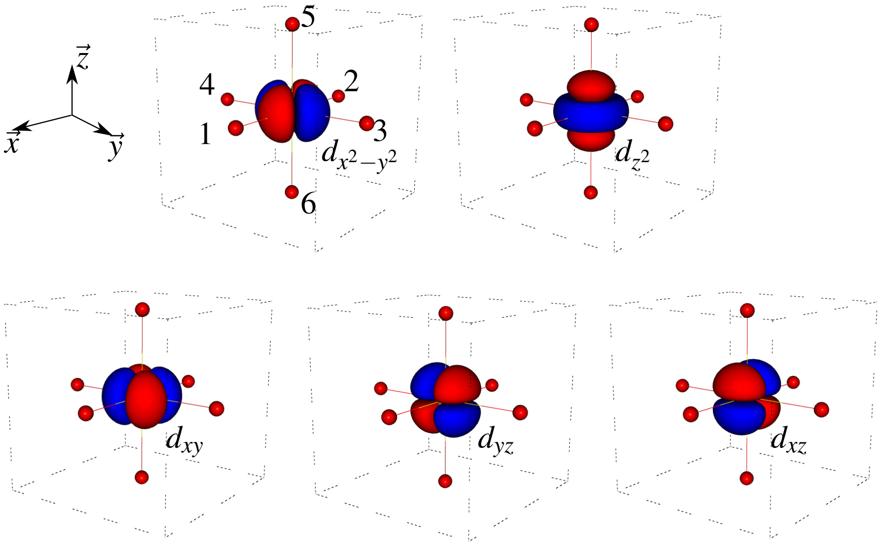

Fig. 2.13 d orbitals in an octahedral environment facing the negative oxygen ions

is a long-range interaction. Thus, in the same ionic system, at a given site, while the first neighbour interactions yielding an octahedron symmetry the further neighbour interactions can lower the symmetry of the site. Therefore, one should take into account all contributions of the splitting. Indeed, in many crystal systems, the point-charge model is not accurate and moreover, the crystal field has a large covalent contribution, i.e. ligand field.

Now, we would like to point out the role of the ligand field on the crystal field splitting. For this purpose, we will use the tight-binding theory. The Hamiltonian of a system for an octahedron can be given as

$$\hat{H} = \sum_{\sigma}\sum_{m}\varepsilon_{d_m} c^{\dagger}_{d_{m\sigma}} c_{d_{m\sigma}} + \varepsilon_p \sum_{\sigma}\sum_{n}\sum_{\mu} c^{\dagger}_{p_{n\sigma\mu}} c_{p_{n\sigma\mu}} + \sum_{\mu}\sum_{\sigma}\sum_{m}\sum_{n} t_{mn\mu}\left(c^{\dagger}_{d_{m\sigma}} c_{p_{n\sigma\mu}} + c^{\dagger}_{p_{n\sigma\mu}} c_{d_{m\sigma}}\right). \tag{2.2}$$

Here, m stands for the $3d$-orbitals of the Mn (i.e. d_{x-y^2}, d_{z^2}, d_{xy}, d_{yz} and d_{xz}) and n stands for the $2p$-orbitals of the O (i.e. p_x, p_y and p_z). μ is the number of the oxygens in the first coordination shell of the Mn (it is equal to 6 locally in an octahedron) and σ is for the spin-up or spin-down electron. Finally, the operator $c^{\dagger}_{d_{m\sigma}}$ creates a σ-electron in the orbital d_m while $c_{d_{m\sigma}}$ removes a σ-electron in the orbital d_m. Similarly, $c^{\dagger}_{p_{n\sigma\mu}}$ creates a σ-electron in the orbital p_n of the μth oxygen while $c_{p_{n\sigma\mu}}$ removes a σ-electron in the orbital p_n of the μth oxygen. $t_{mn\mu}$ is the hopping between d_m orbital of the Mn and p_n orbital of the μth oxygen.

We encounter two types of bonds between manganese $3d$ orbitals and oxygen $2p$ orbitals in the manganese octahedron environment. The σ bond takes place along the orbital axis which makes it the strongest bond among other types of bonds. The $d_{x^2-y^2}$ orbital has a σ-bond with p_x orbitals of the oxygens located along the $\vec{a}$ direction from the Mn and p_y orbitals of the oxygens located along the $\vec{b}$ direction from the Mn while the d_{z^2} orbital has also a σ-bond with p_x orbitals of the oxygens located along the $\vec{a}$ direction from the Mn, p_y orbitals of the oxygens located along the $\vec{b}$ direction from the Mn and p_z orbitals of the oxygens located along the $\vec{c}$ direction from the Mn. (See figure 2.14 (a).) The π-bond takes place between orbitals which share a nodal plane such as the d_{xy} orbital with p_x orbitals of the oxygens located along the $\vec{b}$ direction from Mn and p_y orbitals of the oxygens located along the $\vec{a}$ direction from the Mn; the d_{yz} orbital with p_y of the oxygens located along the $\vec{c}$ direction from the Mn and p_z orbitals of the oxygens located along the $\vec{b}$ direction from the Mn; the d_{xz} orbital with p_x orbitals of the oxygens located along the $\vec{c}$ direction from the Mn and p_z orbitals of the oxygens located along the $\vec{a}$ direction from the Mn. (See figure 2.14 (b).)

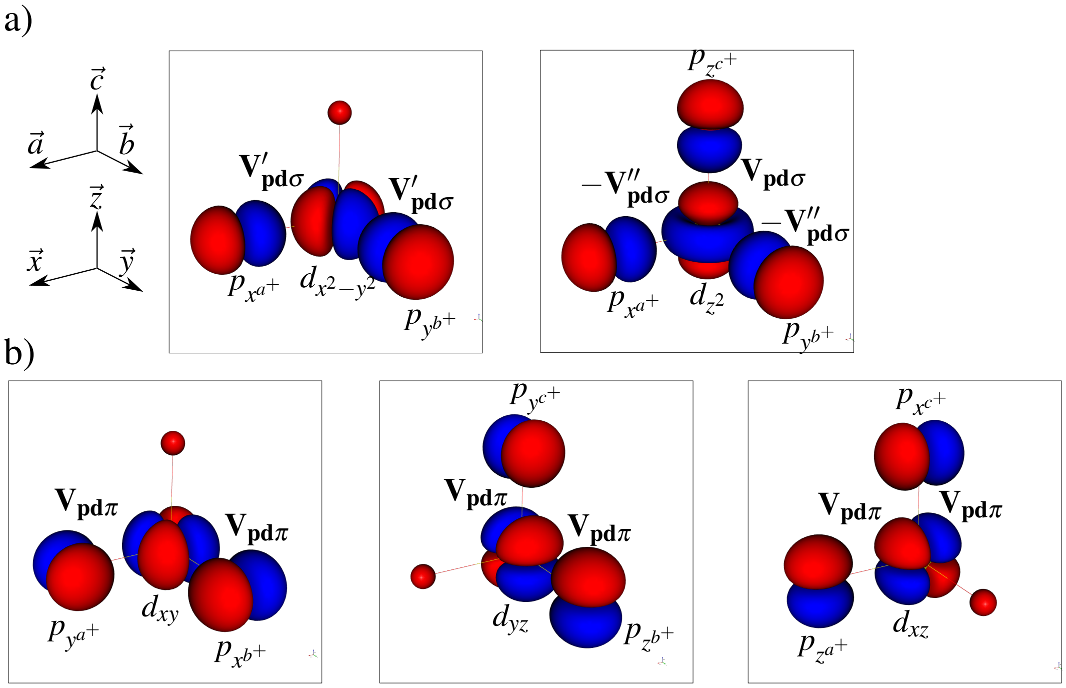

Fig. 2.14 Independent Slater-koster two-central integrals for p and d-orbitals. a) σ-type bonding: the bonding state is symmetrical with respect to rotations about the the bond axis. b) π-type bonding: the bond axis lies in a nodal plane.

Now we will build the tight-binding Hamiltonian matrix first for the basis of e_g orbitals of Mn and $2p$ orbitals of O. We can build the hopping integrals between the e_g and $2p$ orbitals by using the Slater-Koster parameter $V_{pd\sigma}$. For example, the hopping between $d_{x^2-y^2}$ and $p_{x^{a+}}$ is given by $t_{x^2-y^2 p_x 1} = V'_{pd\sigma} = \sqrt{3}V_{pd\sigma}/2$ and the hopping between d_{z^2} and $p_{x^{a+}}$ is given by $t_{z^2 p_x 1} = -V''_{pd\sigma} = -V_{pd\sigma}/2$. The hopping between d_{z^2} and $p_{z^{c+}}$ is given by $t_{z^2 p_z 5} = -V_{pd\sigma}$

The tight-binding Hamiltonian matrix for the e_g orbitals is given by:

$$H_{e_g} = \begin{array}{c} \begin{array}{cccccccc} |d_{x^2-y^2}\rangle & |d_{z^2}\rangle & |p_x^{a^+}\rangle & |p_x^{a^-}\rangle & |p_y^{b^+}\rangle & |p_y^{b^-}\rangle & |p_z^{c^+}\rangle & |p_z^{c^-}\rangle \end{array} \\ \left(\begin{array}{cc|cccccc} \varepsilon_{d_{x^2-y^2}} & 0 & \sqrt{3}V_{pd\sigma}/2 & -\sqrt{3}V_{pd\sigma}/2 & -\sqrt{3}V_{pd\sigma}/2 & \sqrt{3}V_{pd\sigma}/2 & 0 & 0 \\ 0 & \varepsilon_{d_{z^2}} & -V_{pd\sigma}/2 & V_{pd\sigma}/2 & -V_{pd\sigma}/2 & V_{pd\sigma}/2 & V_{pd\sigma} & -V_{pd\sigma} \\ \hline \sqrt{3}V_{pd\sigma}/2 & -V_{pd\sigma}/2 & \varepsilon_p & 0 & 0 & 0 & 0 & 0 \\ -\sqrt{3}V_{pd\sigma}/2 & V_{pd\sigma}/2 & 0 & \varepsilon_p & 0 & 0 & 0 & 0 \\ -\sqrt{3}V_{pd\sigma}/2 & -V_{pd\sigma}/2 & 0 & 0 & \varepsilon_p & 0 & 0 & 0 \\ \sqrt{3}V_{pd\sigma}/2 & V_{pd\sigma}/2 & 0 & 0 & 0 & \varepsilon_p & 0 & 0 \\ 0 & V_{pd\sigma} & 0 & 0 & 0 & 0 & \varepsilon_p & 0 \\ 0 & -V_{pd\sigma} & 0 & 0 & 0 & 0 & 0 & \varepsilon_p \end{array}\right) \end{array} \tag{2.3}$$

$$= \begin{pmatrix} H_{dd} & H_{dp} \\ H_{pd} & H_{pp} \end{pmatrix} \tag{2.4}$$

Here, $\varepsilon_p < \varepsilon_{d_{x^2-y^2}} = \varepsilon_{d_{z^2}} = \varepsilon_d$, and $\Delta_{pd} = \varepsilon_d - \varepsilon_p$ and $V_{pd\sigma} < 0$. As we have given the blocks in 2.4, we can use downfolding method to project out the non-interacting p-electrons and find an operator which acts only in d orbitals space e_g-like bands. Thus, using the resolvent of the matrix given in 2.4, we obtain the resolvent matrix;

$$R(\varepsilon, H_{e_g}) = (\varepsilon I - H_{e_g})^{-1} = \begin{pmatrix} \varepsilon - H_{dd} & H_{dp} \\ H_{pd} & \varepsilon - H_{pp} \end{pmatrix}^{-1}. \tag{2.5}$$

The first matrix element of the resolvent matrix will give us this energy-dependent operator: $H^{\varepsilon}_{e_g}$.

$$R_{00}(\varepsilon, H_{e_g}) = \left(\varepsilon - \underbrace{(H_{dd} + H_{dp}(\varepsilon - H_{pp})^{-1}H_{pd})}_{H^{\varepsilon}_{e_g}}\right)^{-1} \tag{2.6}$$

By downfolding, we also transformed the previous basis set to an energy-dependent basis set of $|d_{x^2-y^2}\rangle_{\varepsilon}$ and $|d_{z^2}\rangle_{\varepsilon}$, thus the energy-dependent e_g Hamiltonian in this energy-dependent basis is as follows:

$$H_{e_g}^{\varepsilon} = \begin{array}{ccc} |d_{x^2-y^2}\rangle_\varepsilon & |d_{z^2}\rangle_\varepsilon & \\ \left(\begin{array}{cc} \varepsilon_d + \frac{3V_{pd\sigma}^2}{\varepsilon-\varepsilon_p} & 0 \\ 0 & \varepsilon_d + \frac{3V_{pd\sigma}^2}{\varepsilon-\varepsilon_p} \end{array}\right) & \begin{array}{c} |d_{x^2-y^2}\rangle_\varepsilon \\ |d_{z^2}\rangle_\varepsilon \end{array} \end{array} \tag{2.7}$$

By setting $\varepsilon = \varepsilon_d$, one can find the eigenenergies of this matrix

$$\varepsilon_d' = \varepsilon_d + \frac{3V_{pd\sigma}^2}{\Delta_{pd}}.$$

We can do the same calculations for the t_{2g} orbitals as well. The Hamiltonian matrix on the basis of the metal t_{2g} orbitals and the oxygen p-orbitals coupled to the later, is given by the following:

$$H_{t_{2g}} = \begin{array}{ccc|cccccccccccc}
|d_{xy}\rangle & |d_{yz}\rangle & |d_{xz}\rangle & |p_x^{b^+}\rangle & |p_x^{b^-}\rangle & |p_x^{c^+}\rangle & |p_x^{c^-}\rangle & |p_y^{a^+}\rangle & |p_y^{a^-}\rangle & |p_y^{c^+}\rangle & |p_y^{c^-}\rangle & |p_z^{a^+}\rangle & |p_z^{a^-}\rangle & |p_z^{b^+}\rangle & |p_z^{b^-}\rangle \\
\varepsilon_{d_{xy}} & 0 & 0 & V_{pd\pi} & -V_{pd\pi} & 0 & 0 & V_{pd\pi} & -V_{pd\pi} & 0 & 0 & 0 & 0 & 0 & 0 \\
0 & \varepsilon_{d_{yz}} & 0 & 0 & 0 & 0 & 0 & 0 & 0 & V_{pd\pi} & -V_{pd\pi} & 0 & 0 & V_{pd\pi} & -V_{pd\pi} \\
0 & 0 & \varepsilon_{d_{xz}} & 0 & 0 & V_{pd\pi} & -V_{pd\pi} & 0 & 0 & 0 & 0 & V_{pd\pi} & -V_{pd\pi} & 0 & 0 \\
\hline
V_{pd\pi} & 0 & 0 & \varepsilon_p & 0 & 0 & 0 & 0 & 0 & 0 & 0 & 0 & 0 & 0 & 0 \\
-V_{pd\pi} & 0 & 0 & 0 & \varepsilon_p & 0 & 0 & 0 & 0 & 0 & 0 & 0 & 0 & 0 & 0 \\
0 & 0 & V_{pd\pi} & 0 & 0 & \varepsilon_p & 0 & 0 & 0 & 0 & 0 & 0 & 0 & 0 & 0 \\
0 & 0 & -V_{pd\pi} & 0 & 0 & 0 & \varepsilon_p & 0 & 0 & 0 & 0 & 0 & 0 & 0 & 0 \\
V_{pd\pi} & 0 & 0 & 0 & 0 & 0 & 0 & \varepsilon_p & 0 & 0 & 0 & 0 & 0 & 0 & 0 \\
-V_{pd\pi} & 0 & 0 & 0 & 0 & 0 & 0 & 0 & \varepsilon_p & 0 & 0 & 0 & 0 & 0 & 0 \\
0 & V_{pd\pi} & 0 & 0 & 0 & 0 & 0 & 0 & 0 & \varepsilon_p & 0 & 0 & 0 & 0 & 0 \\
0 & -V_{pd\pi} & 0 & 0 & 0 & 0 & 0 & 0 & 0 & 0 & \varepsilon_p & 0 & 0 & 0 & 0 \\
0 & 0 & V_{pd\pi} & 0 & 0 & 0 & 0 & 0 & 0 & 0 & 0 & \varepsilon_p & 0 & 0 & 0 \\
0 & 0 & -V_{pd\pi} & 0 & 0 & 0 & 0 & 0 & 0 & 0 & 0 & 0 & \varepsilon_p & 0 & 0 \\
0 & V_{pd\pi} & 0 & 0 & 0 & 0 & 0 & 0 & 0 & 0 & 0 & 0 & 0 & \varepsilon_p & 0 \\
0 & -V_{pd\pi} & 0 & 0 & 0 & 0 & 0 & 0 & 0 & 0 & 0 & 0 & 0 & 0 & \varepsilon_p
\end{array}$$

$$= \begin{pmatrix} H_{dd} & H_{dp} \\ H_{pd} & H_{pp} \end{pmatrix} \tag{2.8}$$

Using the resolvent of the matrix given in 2.8 we have the resolvent matrix;

$$R(\varepsilon, H_{t_{2g}}) = (\varepsilon I - H_{t_{2g}})^{-1} = \begin{pmatrix} \varepsilon - H_{dd} & H_{dp} \\ H_{pd} & \varepsilon - H_{pp} \end{pmatrix}^{-1} \tag{2.9}$$

The first element of the matrix gives us the energy-dependent operator which only acts on d-space.

$$R_{00}(\varepsilon,H_{t_{2g}}) = \left(\varepsilon - \underbrace{(H_{dd} + H_{dp}(\varepsilon - H_{pp})^{-1}H_{pd})}_{H^{\varepsilon}_{t_{2g}}}\right)^{-1} \tag{2.10}$$

We take $\varepsilon_{d_{xy}} = \varepsilon_{d_{yz}} = \varepsilon_{d_{xz}} = \varepsilon_d$. In the basis of energy-dependent basis set of $|d_{xy}\rangle_\varepsilon$, $|d_{yz}\rangle_\varepsilon$ and $|d_{xz}\rangle_\varepsilon$, the energy-dependent t_{2g} Hamiltonian is as follows;

$$H^{\varepsilon}_{t_{2g}} = \begin{array}{cc} \begin{array}{ccc} |d_{xy}\rangle_\varepsilon & |d_{yz}\rangle_\varepsilon & |d_{xz}\rangle_\varepsilon \end{array} & \\ \begin{pmatrix} \varepsilon_d + \frac{4V^2_{pd\pi}}{\varepsilon-\varepsilon_p} & 0 & 0 \\ 0 & \varepsilon_d + \frac{4V^2_{pd\pi}}{\varepsilon-\varepsilon_p} & 0 \\ 0 & 0 & \varepsilon_d + \frac{4V^2_{pd\pi}}{\varepsilon-\varepsilon_p} \end{pmatrix} & \begin{array}{c} |d_{xy}\rangle_\varepsilon \\ |d_{yz}\rangle_\varepsilon \\ |d_{xz}\rangle_\varepsilon \end{array} \end{array} \tag{2.11}$$

By setting $\varepsilon = \varepsilon_d$, one can find the eigenenergies of this matrix

$$\varepsilon''_d = \varepsilon_d + \frac{4V^2_{pd\pi}}{\Delta_{pd}}$$

Finally, the covalent contribution in the $3d$-shell crystal field splitting can be given by

$$\Delta \sim \varepsilon'_d - \varepsilon''_d = 3\frac{V^2_{pd\sigma}}{\Delta_{pd}} - 4\frac{V^2_{pd\pi}}{\Delta_{pd}} > 0. \tag{2.12}$$

We have shown that the e_g orbitals are higher in energy compared to the t_{2g} ones since the σ bonds are stronger than π bonds.

At this point, one should also recall the notion of "*High Spin configuration*" and "*Low Spin configuration*. According to the Hund's rule, for a given electronic configuration with degenerate orbitals, the spin value is maximized. This means that, in a degenerated set of orbitals, electrons must first singly occupy all orbitals with the same spin, before filling in pairs. For instance, for a system of five d electrons in an octahedron environment, there are two possibilities:

- "*High Spin configuration*": All five d electrons occupy singly all d orbitals with the energy $E = -10J_{ab} + 10U_{ab} + 2\Delta$ where J_{ab} is the Hund's exchange energy, U_{ab} is interorbital Coulomb repulsion energy and Δ is the crystal field splitting energy (See figure 2.15 a)).

- "*Low spin configuration*": Three electrons will first fill t_{2g} level with the same spins and then the two electrons will be paired in t_{2g} level again with the energy $E = -4J_{ab} + 8U_{ab} + 2U_{aa}$ where J_{ab} is the Hund exchange energy, U_{ab} is interorbital Coulomb repulsion energy and U_{aa} is the intraorbital Coulomb repulsion energy (See figure 2.15 b)).

Thus, noting that $U_{aa} \simeq U_{ab} + 2J_{ab}$, one can find the conditions for the spin configuration of such system. If $\Delta < 5J_{ab}$ then *High Spin configuration* takes place whereas if $\Delta > 5J_{ab}$ *Low Spin configuration* takes place.

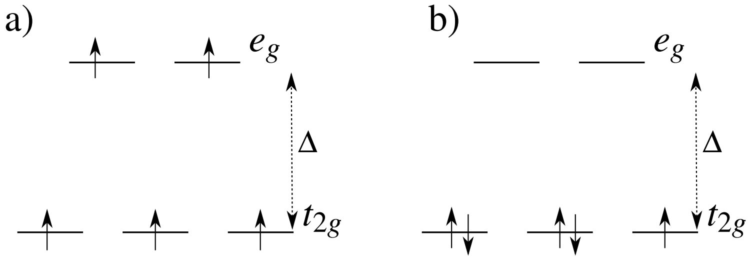

Fig. 2.15 a) "*high spin configuration*" b) "*low spin configuration*"

Before finishing the section on the crystal field splitting, we would like to give the density of states and band structure of an ideal cubic perovskite $LaMnO_3$ (space group *Pm*3*m*) obtained by a single-point non-magnetic calculation within B1WC hybrid functional [56] with CRYSTAL code [57] in figure 2.16. Through this figure, one can easily see the effect of the splitting of the 3*d* orbitals. The bands issued from the t_{2g} orbitals (in green) lie down under the Fermi level whereas the bands issued from the e_g orbitals (in red) are above the Fermi level. One can also depict from band structure along the path $\Gamma - \mathrm{R}$ that the e_g orbitals are doubly-degenerated and the t_{2g} orbitals are triply-degenerated.

2.2.2.2 Jahn-Teller Distortion

Let us assume a physical system consisting of a large number of particles; that is nuclei and electrons. The time-independent Schrödinger equation, that is $\hat{\mathrm{H}}\Psi = \mathbf{E}\Psi$, describes stationary states of such a system. Here, $\hat{\mathrm{H}}$ is the Hamiltonian operator and $\mathbf{E}$ is the energy of the state Ψ. The Born-Oppenheimer approximation helps us to write the system many-body

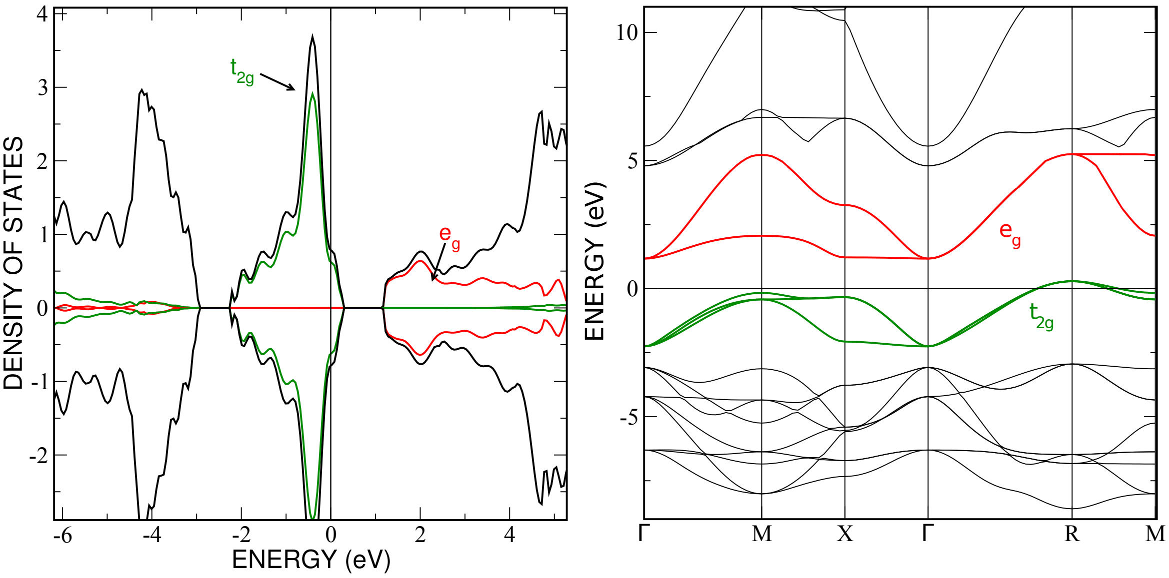

Fig. 2.16 Density of states (left) and band structure (right) of an ideal cubic perovskite LaMnO$_3$ (Space group $Pm\bar{3}m$). The bands issued from the e_g orbitals are in red, the bands issued from the t_{2g} orbitals are in green. The special points in the band structure are $\Gamma = (0,0,0)$, $\mathrm{M} = (\pi/\mathrm{a}, \pi/\mathrm{a}, 0)$, $\mathrm{X} = (\pi/\mathrm{a}, 0, 0)$, $\mathrm{R} = (\pi/\mathrm{a}, \pi/\mathrm{a}, \pi/\mathrm{a})$

wave function Ψ as a product of a many-body electron wave function ψ and a many-body nuclei wave function ϕ:

$$\Psi(\{\vec{r}\};\{\vec{R}\}) = \psi(\{\vec{r}\})_{\{\vec{R}\}}\,\phi(\{\vec{R}\}),$$

where $\{\vec{r}\}$ and $\{\vec{R}\}$ are respectively the ensemble of the position vectors of the electons and the nuclei. Thus, the Hamiltonian operator can be split into two operators as well:

$$\begin{aligned}\hat{H}_{el}(\{\vec{r}\})_{\{\vec{R}\}} &= \hat{T}_e(\{\vec{r}\}) + \hat{V}_{eN}(\{\vec{r}\})_{\{\vec{R}\}} + \hat{V}_{ee}(\{\vec{r}\}) + \hat{V}_{NN} \\ \hat{H}_{nucl}(\{\vec{R}\}) &= \hat{T}_N(\{\vec{R}\}) + E(\{\vec{R}\})\end{aligned}$$

Here, $\hat{T}_e$ and $\hat{T}_N$ are kinetic energy operators for electrons and nuclei. $\hat{V}_{eN}$, $\hat{V}_{ee}$ and V_{NN} are the potential energy operators for electron-nuclei, electron-electron and nuclei-nuclei, respectively. The time-independent Schrödinger equation, $\hat{\mathrm{H}}\Psi = \mathbf{E}\Psi$ also splits into:

$$\begin{aligned}\hat{H}_{el}\,\psi(\{\vec{r}\})_{\{\vec{R}\}} &= E(\{\vec{R}\})\,\psi(\{\vec{r}\})_{\{\vec{R}\}} \\ \hat{H}_{nucl}\,\phi(\{\vec{R}\}) &= \mathbf{E}\,\phi(\{\vec{R}\})\end{aligned}$$

Let us assume that, for a given system defined by $\{\vec{r}\}$ and $\{\vec{R}\}$, we have solved the electronic eigenvalue problem defined by $\hat{H}_{el}$. Let us also assume that $\{\vec{R}\} = \{\vec{R}^0\}$ defines a crystal structure whose electronic ground state is degenerated. Thus, one will wonder whether this crystal structure, that $\{\vec{R}^0\}$ defines, is stable. According to the Jahn-Teller theorem [58], such a system is not stable and any non-linear system with a degenerate electronic ground state will undergo some symmetry breaking by removing the symmetry constraint on the wave-functions to lower the energy and remove the electronic degeneracy. This electronic instability will drive lattice distortions. These distortions are named "Jahn-Teller distortion", and the reason behind it is the coupling between the electrons and the nuclei when occurring locally as on a single ion. Jahn-Teller distortion is mostly seen when transition metals happen to be in octahedral environments, but it can be observed in tetrahedral compounds as well.

As stated before, in an octahedral environment, the five d atomic orbitals are split into two degenerate sets: e_g and t_{2g}. When the system has a degenerate electronic ground state (partially filled e_g or t_{2g} orbitals), it will distort to remove this degeneracy and lower its energy. In octahedral environments, one way to remove the degeneracy is either by elongation or compression along one direction. The effects of elongation or compression are determined by the overlap between the transition metal and ligand orbitals.

Now, let us take a deeper look on how the Jahn-Teller effect takes place with the insight given in the references [55, 59]. Let us take a system in an equilibrium structure, $\{\vec{R}^0\}$ with degenerate electronic ground states. The ground state energy is labelled as $E(\{\vec{R}^0\})$ with the degeneracy $d > 1$. For the simplicity, we take this energy as zero energy. The corresponding degenerate electronic many-body wavefunctions are $\psi_j(\{\vec{r}\})_{\{\vec{R}\}}$, $j = 1, \cdots, d$. Since $E(\{\vec{R}\})$ acts as a potential for the nuclei Hamiltonian we can label $\hat{U}_N = E(\{\vec{R}\})$. This potential is also called Born-Oppenheimer potential energy surface and in the system under our consideration there are d Born-Oppenheimer energy surfaces. The energy surfaces close to $\{\vec{R}^0\}$ can be classified in two classes:

- Renner-Teller section: The equilibrium structure, $\{R^0\}$ is a stationary point for all d surfaces ($\vec{\nabla}\hat{U}_N(\{\vec{R}^0\}) = \vec{0}$).

- Jahn-Teller section: The equilibrium structure, $\{R^0\}$ is not a stationary point for at least some of the surfaces ($\vec{\nabla}\hat{U}_N(\{\vec{R}^0\}) \neq \vec{0}$ at least in some direction).

One can expand $\hat{U}_N$ around equilibrium structure $\{\vec{R}^0\}$ by assuming $\{\vec{R}^0\}$ is a stationary point and find;

$$\hat{H}_{\mathrm{nucl}} = \hat{T}_N + \underbrace{\sum_I \sum_\nu \left[\frac{\partial \hat{U}_N}{\partial u_{I\nu}}\right]_{|\{\vec{R}^0\}} u_{I\nu}}_{=0} + \underbrace{\frac{1}{2}\sum_I \sum_\nu \sum_{I'} \sum_{\nu'} \left[\frac{\partial^2 \hat{U}_N}{\partial u_{I\nu}\partial u_{I'\nu'}}\right]_{|\{\vec{R}^0\}} u_{I\nu}\, u_{I'\nu'}}_{\hat{U}_N^{\mathrm{PH}}} + \cdots \tag{2.13}$$

where $\vec{u}_I = \vec{R}_I - \vec{R}_I^0$ is the displacement vector for the atoms with respect to their equilibrium position. Here, I and I' are indexes for atoms and $\mu = x, y, z$ are the cartesian coordinates. Thus, one can write

$$\hat{H}_{\mathrm{nucl}} \sim \hat{T}_N + \hat{U}_N^{\mathrm{PH}}.$$

This Hamiltonian gives the phonon dispersions in a crystal. Going back to the cases where $\vec{\nabla}\hat{U}_N(\{\vec{R}^0\}) \neq \vec{0}$; the classical Jahn-Teller systems, one can consider small distortions around $\{\vec{R}^0\}$ in order to lift the degeneracy of the d degenerate eigenvalues of the electronic Hamiltonian $\hat{H}_{el}$. This leads to:

$$\langle \psi_j | \hat{H}_{el}(\{\vec{r}\})_{\{\vec{R}\}} | \psi_{j'} \rangle = E(\{\vec{R}^0\})\delta_{j=j'} + \underbrace{\sum_I \sum_\nu \langle \psi_j | \left[\frac{\partial \hat{H}_{el}}{\partial u_{I\nu}}\right]_{|\{\vec{R}^0\}} | \psi_{j'} \rangle\, u_{I\nu}}_{\hat{U}_{j,j'}^{\mathrm{JT}}} + \cdots \quad . \tag{2.14}$$

Here, $\hat{U}_{j,j'}^{JT}$ is a perturbation between the degenerate j and j' energy surfaces and named the Jahn-Teller potential. This potential does not only couple the energy surfaces but also couples electrons and lattice vibrations. Thus we can rewrite the Born-Oppenheimer approximation as follows:

$$\Psi(\{\vec{r}\};\{\vec{R}\}) = \sum_d \psi_d(\{\vec{r}\})_{\{\vec{R}\}}\, \phi_d(\{\vec{R}\}). \tag{2.15}$$

Then, considering the nuclei part of time-independent Schrödinger equation $\hat{\mathrm{H}} = \mathbf{E}\Psi$, one can obtain:

$$\hat{H}_{nucl}\phi_d(\{\vec{R}\}) = \left[\hat{T}_N + \hat{U}_N^{\mathrm{PH}}\right] \phi_d(\{\vec{R}\}) + \sum_{d'} \hat{U}_{d,d'}^{\mathrm{JT}}\, \phi_d(\{\vec{R}\}) = \mathbf{E}\, \phi_d(\{\vec{R}\}). \tag{2.16}$$

The ground state of equation 2.16 leads to a new structure $\{\tilde{\vec{R}}^0\}$ in which the electronic structure is no longer degenerate. Let's take a look on how this degeneracy breaking takes place for example in the ideal cubic LaMnO$_3$ (as shown in figure 2.7). LaMnO$_3$ has two degenerate Mn $3d^4$ configurations; three electrons in the t_{2g} orbitals and one electron in the e_g orbitals. According to the Jahn-Teller theorem, this degeneracy should be broken by some electronic instability. This instability can be brought by the normal modes Q_2 and Q_3 as illustrated in figure 2.17. One can calculate the Jahn-Teller potential $\hat{U}^{\mathrm{JT}}$ from the effect obtained due to the modes of Q_2 and Q_3 and also taking into account the ligand field contribution.

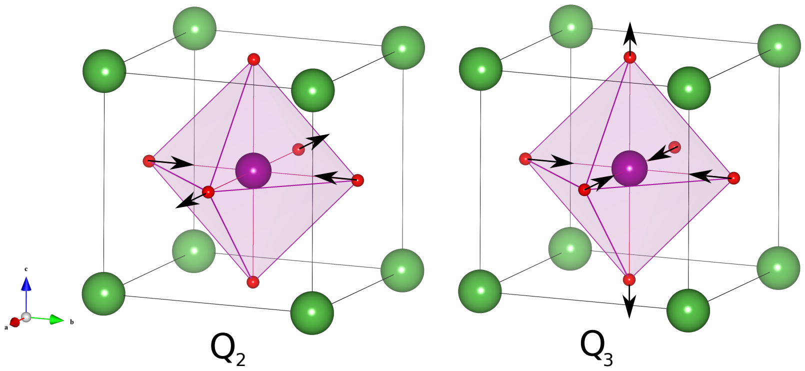

Fig. 2.17 The degenerate vibrational modes Q_2 and Q_3 in ideal cubic perovsktie $LaMnO_3$

When a tetragonal elongation along z takes place as shown in figure 2.18, the electronic ground state degeneracy is broken by the stabilization of the d orbitals with a z component (d_{z^2} in e_g level and d_{yz}, d_{xz} in t_{2g} level) while the d orbitals without a z component are higher in energy ($d_{x^2-y^2}$ in e_g level and d_{xy} in t_{2g} level).

On the other hand, when tetragonal compression along z takes place as shown in figure 2.19 the electronic ground state degeneracy is broken by the stabilization of the d orbitals without a z component ($d_{x^2-y^2}$ in e_g level and d_{xy} in t_{2g} level) while the orbitals with a z component are higher in energy (d_{z^2} in e_g level and d_{yz}, d_{xz} in t_{2g} level).

As a general rule, when there is an odd number of electrons in the e_g level the atomic ground state is doubly degenerated and thus Jahn-Teller effect takes place. In the case of $LaMnO_3$, which is a high-spin d^4, there is one electron in the e_g orbitals, thus the Jahn-Teller distortion occurs and lifts the orbital degeneracy, leading to an orbital ordering.

2.2.3 Effective Magnetic Interactions and Hopping Integrals

In the study of the manganites, it is vital to understand the magnetic interactions that can occur between the manganese ions. For this purpose, we will recall the mechanism at play in the effective exchange interactions between two Mn ions, resulting from direct interactions or interactions through $2p$ orbitals of the oxygen atoms.

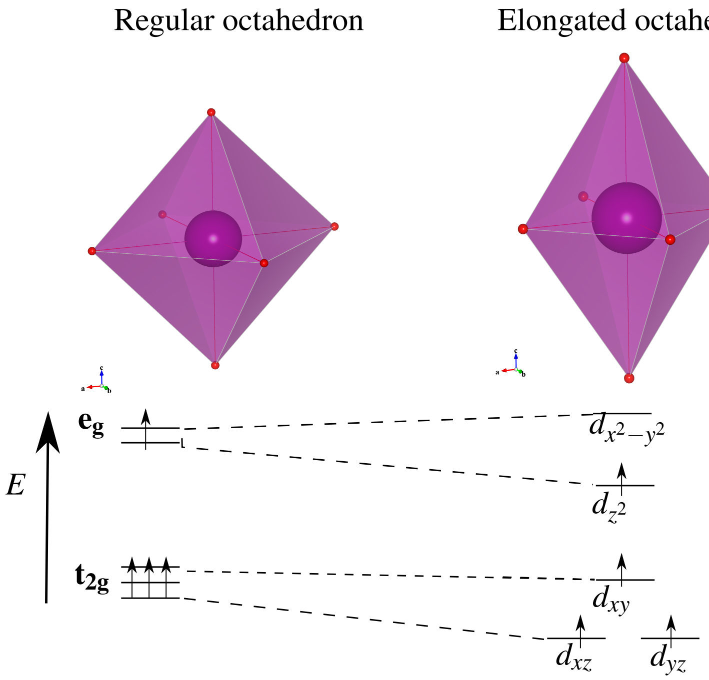

Fig. 2.18 Crystal-field splitting of five-fold degenerate atomic $3d$ levels into lower t_{2g} (triply degenerate) and higher e_g (doubly degenerate) levels. Jahn–Teller tetragonal distortion (elongation) of MnO_6 octahedron further lifts each degeneracy.

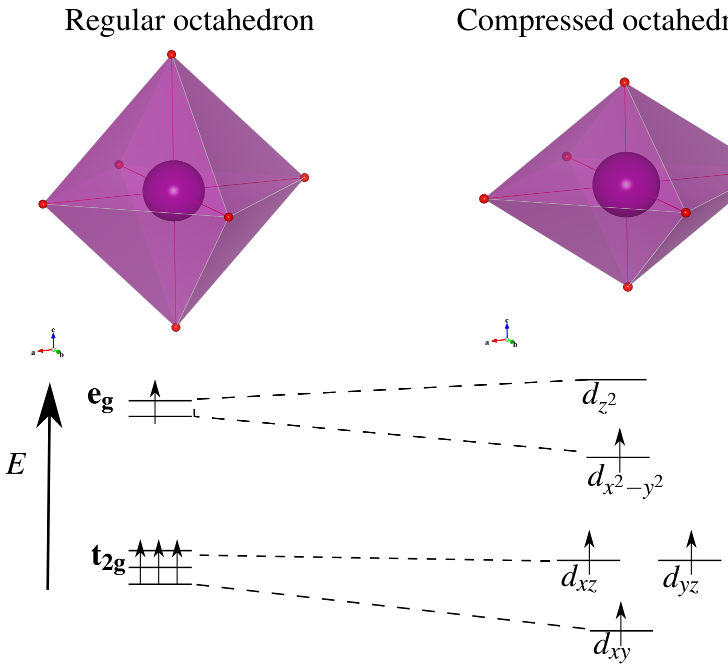

Fig. 2.19 Crystal-field splitting of five-fold degenerate atomic $3d$ levels into lower t_{2g} (triply degenerate) and higher e_g (doubly degenerate) levels. Jahn–Teller tetragonal distortion (compression) of MnO_6 octahedron further lifts each degeneracy.

In the present case, magnetic interactions take place locally between neighbouring atoms with open shells. They are short-range interactions between two bodies (atoms). They are the parameters of an effective Hamiltonian such as the Spin-Heisenberg model.

2.2.3.1 Coulomb repulsion in a 2-electrons-2-sites system

Let us start with a system with open d shells. We can build up a simple 2-electrons-2-sites system: one electron on each site. Let us call these sites A and B and the orbitals considered in these sites are d orbitals. From now on, we will call the d orbital at site A as orbital a and the d orbital at site B as orbital b. For generality purposes, in the case of a transition metal-oxide system, we can further consider two magnetic sites with one d orbital on each, and add the p orbitals of the anions located in between the two cation sites. We will presume that the p orbitals are doubly occupied and non magnetic. First, we focus on the Coulomb term of the two-electrons Hamiltonian. The Coulomb repulsion of the two-electrons Hamiltonian is given by $\hat{V}_{ee} = \frac{1}{|\vec{r}_1-\vec{r}_2}|$. Here, $\vec{r}_1$ and $\vec{r}_2$ are the position vectors of the electrons. The possible states of the system under our consideration can be schematically seen in figure 2.20. The states are (a) $|\uparrow,\uparrow\rangle$, (b) $|\downarrow,\downarrow\rangle$, (c) $|\uparrow,\downarrow\rangle$ and (d) $|\downarrow,\uparrow\rangle$. The energy of an electron in the orbital a or b is respectively given by ε_a or ε_b. ε_a and ε_b can be expressed by using the Fock operator as following

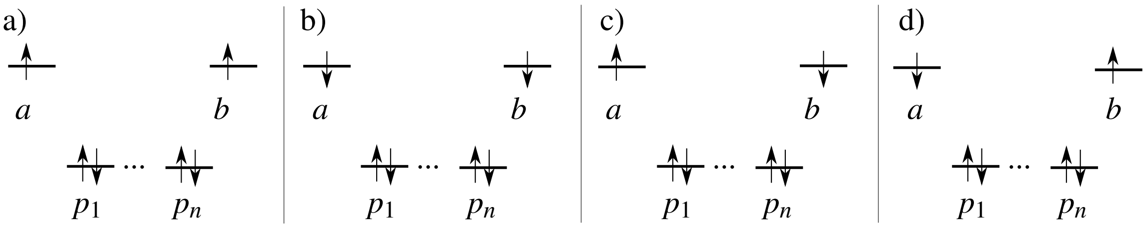

Fig. 2.20 The degenerate states of $\hat{H}_{el}$ are (a) $|\uparrow,\uparrow\rangle$, (b) $|\downarrow,\downarrow\rangle$, (c) $|\uparrow,\downarrow\rangle$ and (d) $|\downarrow,\uparrow\rangle$.

$$\varepsilon_a = \langle \varphi_a | \hat{T}_{ee} + \hat{V}_{eN} + \sum_{\substack{\text{other} \\ \text{occ. orb.}}} (2\hat{U}_0 - \hat{J}_0) | \varphi_a \rangle$$

and

$$\varepsilon_b = \langle \varphi_b | \hat{T}_{ee} + \hat{V}_{eN} + \sum_{\substack{\text{other} \\ \text{occ. orb.}}} (2\hat{U}_o - \hat{J}_o) | \varphi_b \rangle$$

where φ_a and φ_b are the one-electron wave functions corresponding to the orbitals a and b, $\hat{U}_o$ is the Coulomb operator and $\hat{J}_o$ is the exchange operator. They are given by the following formulae[1]:

$$\hat{U}_o|\varphi(\vec{r}_1)\rangle = \varphi(\vec{r}_1)\int d^3r_2\,\frac{|\varphi_o(\vec{r}_2)|^2}{|\vec{r}_1-\vec{r}_2|}$$

and

$$\hat{J}_o|\varphi(\vec{r}_1)\rangle = \varphi_o(\vec{r}_1)\int d^3r_2\,\frac{\varphi_o^*(\vec{r}_2)\varphi(\vec{r}_2)}{|\vec{r}_1-\vec{r}_2|}.$$

Considering the spins σ and σ', the two-electrons Slater determinant allows us to write the states of figure 2.20:

$$\begin{aligned}
\psi_{a,\sigma;b,\sigma'}(\vec{r}_1,s_1;\vec{r}_2,s_2) &= \frac{1}{\sqrt{2}}\begin{vmatrix}\varphi_a(\vec{r}_1)\sigma(s_1) & \varphi_a(\vec{r}_2)\sigma(s_2)\\ \varphi_b(\vec{r}_1)\sigma'(s_1) & \varphi_b(\vec{r}_2)\sigma'(s_2)\end{vmatrix}\\
&= \frac{1}{\sqrt{2}}\left(\varphi_a(\vec{r}_1)\varphi_b(\vec{r}_2)\sigma(s_1)\sigma'(s_2)-\varphi_b(\vec{r}_1)\varphi_a(\vec{r}_2)\sigma'(s_1)\sigma(s_2)\right)\\
&= |\varphi_a^{\sigma}\varphi_b^{\sigma'}\rangle
\end{aligned}$$

We can calculate the matrix elements of the $\hat{V}_{ee}$ by simply calculating $\langle\psi_{a,\sigma;b,\sigma'}|\frac{1}{|\vec{r}_1-\vec{r}_2|}|\psi_{a,\sigma;b,\sigma'}\rangle$ and $\langle\psi_{a,\sigma;b,\sigma'}|\frac{1}{|\vec{r}_1-\vec{r}_2|}|\psi_{a,\sigma';b,\sigma}\rangle$. When both electrons have the same spin ($\sigma=\sigma'$), i.e. for the $\psi_{\uparrow\uparrow}=|\uparrow,\uparrow\rangle$ and $\psi_{\downarrow\downarrow}=|\downarrow,\downarrow\rangle$, we have

$$\langle\psi_{a,\sigma;b,\sigma}|\frac{1}{|\vec{r}_1-\vec{r}_2|}|\psi_{a,\sigma;b,\sigma}\rangle = U_{ab}-J_{ab}$$

where U_{ab} is the Coulomb repulsion integral and has the form

$$U_{ab}=\int d^3r_1\int d^3r_2\frac{|\varphi_a(\vec{r}_1)|^2|\varphi_b(\vec{r}_2)|^2}{|\vec{r}_1-\vec{r}_2|} \tag{2.17}$$

and J_{ab} is the exchange integral and has the form

$$J_{ab}=\int d^3r_1\int d^3r_2\frac{\varphi_a^*(\vec{r}_1)\varphi_b(\vec{r}_1)\varphi_b^*(\vec{r}_2)\varphi_a(\vec{r}_2)}{|\vec{r}_1-\vec{r}_2|} \tag{2.18}$$

In the case of opposite spins, i.e for the states $\psi_{\uparrow\downarrow}=|\uparrow,\downarrow\rangle$ and $\psi_{\downarrow\uparrow}=|\downarrow,\uparrow\rangle$, we have

$$\langle\psi_{a,\uparrow;b,\downarrow}|\frac{1}{|\vec{r}_1-\vec{r}_2|}|\psi_{a,\uparrow;b,\downarrow}\rangle = \langle\psi_{a,\downarrow;b,\uparrow}|\frac{1}{|\vec{r}_1-\vec{r}_2|}|\psi_{a,\downarrow;b,\uparrow}\rangle = U_{ab}$$

---

[1] We used the following the notation to go from function to bra-ket notation: $\varphi(\vec{r})=|\varphi(\vec{r})\rangle=\langle\vec{r}|\varphi\rangle$.

and

$$\langle \psi_{a,\uparrow;b,\downarrow} | \frac{1}{|\vec{r}_1 - \vec{r}_2|} | \psi_{a,\downarrow;b,\uparrow} \rangle = \langle \psi_{a,\downarrow;b,\uparrow} | \frac{1}{|\vec{r}_1 - \vec{r}_2|} | \psi_{a,\uparrow;b,\downarrow} \rangle = -J_{ab}.$$

if the orbitals are real. Thus, we can give the total electronic energy of the states given in figure 2.20:

- For the states a) & b): $E = E_o + \varepsilon_a + \varepsilon_b + U_{ab} - J_{ab}$
- For the states c) & d): $E = E_o + \varepsilon_a + \varepsilon_b + U_{ab}$

where E_o is the energy of the electrons of the occupied orbitals that is all electrons except the ones in orbitals a and b. In the basis of $\psi_{\uparrow\uparrow}$, $\psi_{\uparrow\downarrow}$, $\psi_{\downarrow\uparrow}$ and $\psi_{\downarrow\downarrow}$ we can write the Coulomb repulsion term as following:

$$V_{ee} = \begin{array}{cc} \begin{array}{cccc} \psi_{\uparrow\uparrow} & \psi_{\uparrow\downarrow} & \psi_{\downarrow\uparrow} & \psi_{\downarrow\downarrow} \end{array} & \\ \begin{pmatrix} U_{ab} - J_{ab} & 0 & 0 & 0 \\ 0 & U_{ab} & -J_{ab} & 0 \\ 0 & -J_{ab} & U_{ab} & 0 \\ 0 & 0 & 0 & U_{ab} - J_{ab} \end{pmatrix} & \begin{array}{c} \psi_{\uparrow\uparrow} \\ \psi_{\uparrow\downarrow} \\ \psi_{\downarrow\uparrow} \\ \psi_{\downarrow\downarrow} \end{array} \end{array} \tag{2.19}$$

Then the two-electrons Hamiltonian matrix can be written as:

$$H_{el} = E_o I + \begin{array}{cc} \begin{array}{cccc} \psi_{\uparrow\uparrow} & \psi_{\uparrow\downarrow} & \psi_{\downarrow\uparrow} & \psi_{\downarrow\downarrow} \end{array} & \\ \begin{pmatrix} \varepsilon_a + \varepsilon_b + U_{ab} - J_{ab} & 0 & 0 & 0 \\ 0 & \varepsilon_a + \varepsilon_b + U_{ab} & -J_{ab} & 0 \\ 0 & -J_{ab} & \varepsilon_a + \varepsilon_b + U_{ab} & 0 \\ 0 & 0 & 0 & \varepsilon_a + \varepsilon_b + U_{ab} - J_{ab} \end{pmatrix} & \begin{array}{c} \psi_{\uparrow\uparrow} \\ \psi_{\uparrow\downarrow} \\ \psi_{\downarrow\uparrow} \\ \psi_{\downarrow\downarrow} \end{array} \end{array} \tag{2.20}$$

Diagonalizing the matrix 2.20 gives us the energies and the corresponding eigenstates. The triplet states are $\psi_{\uparrow\uparrow}$, $\psi_{\downarrow\downarrow}$ and $(\psi_{\uparrow\downarrow} + \psi_{\downarrow\uparrow})/\sqrt{2}$ with the energy $\varepsilon_{\text{triplet}} = \varepsilon_a + \varepsilon_b + U_{ab} - J_{ab}$. The singlet state is $(\psi_{\uparrow\downarrow} - \psi_{\downarrow\uparrow})/\sqrt{2}$ with the energy $\varepsilon_{\text{singlet}} = \varepsilon_a + \varepsilon_b + U_{ab} + J_{ab}$. It is pretty much clear that $U_{ab} > 0$ but one can easily show that $J_{ab} > 0$. Moreover, it is also obvious that $\varepsilon_{\text{triplet}} - \varepsilon_{\text{singlet}} = -2J_{ab}$. Thus, if the many-body basis set was only the one which reduces to those four Slater determinants, then the triplet state would be the ground state, in this open-shell two electron-two orbital system. Let us take the limit case when the two sites are not spatially separated, which means that the system is equivalent to an one-site system of one atom with two orbitals. Then, the result above can be seen as the Hund's first rule: In a degenerated atomic shell, the ground state will have the maximum spin. However, when the two sites are at very large distance, like in H_2 at very large distance, the ground state is the singlet state due to the contribution of the other Slater determinants in the wave function expansion. Thus, one should use perturbation theory to introduce the effect of the non dominant configurations in the wave function and the off-diagonal part of the Fock operator. These other terms can reverse the order of the singlet and triplet states.

2.2.3.2 Including the off-diagonal terms of Fock operator

Anderson Superexchange a.k.a. Superexchange through Space

Now, let us consider the case in which two electrons of opposite spins occupy the same orbital in the open d shell environment given above (without taking into account the participation of the p orbitals at first), we have six possible states: $|\uparrow,\uparrow\rangle$, $|\downarrow,\downarrow\rangle$, $|\uparrow,\downarrow\rangle$, $|\downarrow,\uparrow\rangle$, $|\uparrow\downarrow,\cdot\rangle$ and $|\cdot,\uparrow\downarrow\rangle$. The first four states are named as "covalent states" whereas the last two are named as "ionic states". In order to build the Hamiltonian of such a system in the basis of these states, let us recall the operators of second quantization. The operator $c^{\dagger}_{\alpha\sigma}$ creates a spin-σ electron in orbital α, where $\alpha = a,b$. For example, $c^{\dagger}_{a\uparrow}|0\rangle$ creates a spin-up electron in the orbital a. Here, $|0\rangle$ denotes the system with no electrons. In order to annihilate this electron from its orbital, we introduce the operator $c_{\alpha\sigma}$. For example, $c_{a\uparrow}$ removes a spin-up electron from the orbital a, if there is a spin-up electron in orbital a, otherwise it returns 0. The operator $n_{\alpha\sigma} = c^{\dagger}_{\alpha\sigma}c_{\alpha\sigma}$ works as an observer. It returns 0 when there is no spin-σ electron in the orbital α whereas it returns 1 when there is an electron. This operator can be used to describe the on-site Coulomb repulsion operator acting on orbital σ by the formulation $n_{\alpha\uparrow}n_{\alpha\downarrow}$. We defined the Coulomb repulsion between two electrons in a d-orbital as U_{aa} and U_{bb}, for a and b orbitals, respectively, as in equation 2.17. Then, the off-site Coulomb repulsion U_{ab} between the occupied a and b orbitals can be also expressed by using $(n_{\alpha\uparrow} + n_{\alpha\downarrow})(n_{\alpha'\uparrow} + n_{\alpha'\downarrow})$. J_{ab} is the exchange term between the states $|\uparrow,\downarrow\rangle$ and $|\downarrow,\uparrow\rangle$ and J_{ab} is also the exchange term between the states $|\uparrow\downarrow,\cdot\rangle$ and $|\cdot,\uparrow\downarrow\rangle$ since we take the orbitals

a and b real. Finally, $-t_{dd}$ is the hopping between a and b orbitals.

$$
\begin{aligned}
\hat{H} = {} & \underbrace{\sum_{\sigma}(\varepsilon_a n_{a\sigma} + \varepsilon_b n_{b\sigma})}_{\text{(a)}} + \underbrace{U_{aa} n_{a\uparrow} n_{a\downarrow} + U_{bb} n_{b\uparrow} n_{b\downarrow}}_{\text{(b)}} + \underbrace{U_{ab}(n_{a\uparrow} n_{b\downarrow} + n_{a\downarrow} n_{b\uparrow})}_{\text{(c)}} \\
& + \underbrace{(U_{ab} - J_{ab})(n_{a\uparrow} n_{b\uparrow} + n_{a\downarrow} n_{b\downarrow})}_{\text{(d)}} + \underbrace{J_{ab}(c^{\dagger}_{a\uparrow} c^{\dagger}_{b\downarrow} c_{a\downarrow} c_{b\uparrow} + c^{\dagger}_{b\uparrow} c^{\dagger}_{a\downarrow} c_{b\downarrow} c_{a\uparrow})}_{\text{(e)}} \\
& + \underbrace{J_{ab}(c^{\dagger}_{a\uparrow} c^{\dagger}_{a\downarrow} c_{b\downarrow} c_{b\uparrow} + c^{\dagger}_{b\uparrow} c^{\dagger}_{b\downarrow} c_{a\downarrow} c_{a\uparrow})}_{\text{(f)}} \underbrace{- t_{dd} \sum_{\sigma}(c^{\dagger}_{a\sigma} c_{b\sigma} + c^{\dagger}_{b\sigma} c_{a\sigma})}_{\hat{W}=\text{perturbation}}
\end{aligned}
\tag{2.21}
$$

Here, the part (a) is for the energy to put an electron on each orbital, the part (b) is for on-site Coulomb energy when two electrons are on the same orbital a or b, the part (c) is the off-site Coulomb energy when two electrons are on each orbital a and b with opposite spins, the part (d) is the energy of one electron on each orbital a and b with same spins, the part (e) is the exchange energy between the states $|\uparrow,\downarrow\rangle$ and $|\downarrow,\uparrow\rangle$ and the part (f) is the exchange energy between the states $|\uparrow\downarrow,\cdot\rangle$ and $|\cdot,\uparrow\downarrow\rangle$

We can assume that each part that we just gave is much larger than the term that the hopping $-t_{dd}$ describes. Thus, one can split the Hamiltonian into two parts: $\hat{H}_0$ unperturbed Hamiltonian $((\text{a}) + (\text{b}) + (\text{c}) + (\text{d}) + (\text{e}) + (\text{f}))$ and $\hat{W}$ perturbation. As one can see, we can write the Hamiltonian by separating into unperturbed and perturbation parts; $\hat{H} = \hat{H}_0 + \hat{W}$. In the basis of the states $|\uparrow,\uparrow\rangle$, $|\downarrow,\downarrow\rangle$ $|\uparrow,\downarrow\rangle$, $|\downarrow,\uparrow\rangle$, $|\uparrow\downarrow,\cdot\rangle$ and $|\cdot,\uparrow\downarrow\rangle$, the unperturbed Hamiltonian matrix is as follows:

$$
H_0 = \begin{array}{cccccc}
|\uparrow,\uparrow\rangle & |\downarrow,\downarrow\rangle & |\uparrow,\downarrow\rangle & |\downarrow,\uparrow\rangle & |\uparrow\downarrow,\cdot\rangle & |\cdot,\uparrow\downarrow\rangle \\
\end{array}
$$

$$
H_0 = \begin{pmatrix}
\varepsilon_a + \varepsilon_b + U_{ab} - J_{ab} & 0 & 0 & 0 & 0 & 0 \\
0 & \varepsilon_a + \varepsilon_b + U_{ab} - J_{ab} & 0 & 0 & 0 & 0 \\
0 & 0 & \varepsilon_a + \varepsilon_b + U_{ab} & -J_{ab} & 0 & 0 \\
0 & 0 & -J_{ab} & \varepsilon_a + \varepsilon_b + U_{ab} & 0 & 0 \\
0 & 0 & 0 & 0 & 2\varepsilon_a + U_{aa} & J_{ab} \\
0 & 0 & 0 & 0 & J_{ab} & 2\varepsilon_b + U_{bb}
\end{pmatrix}
\tag{2.22}
$$

Considering $\varepsilon_a + \varepsilon_b$ as reference energy and defining $\Delta_{ab} = \varepsilon_a - \varepsilon_b$ the matrix given in 2.22 becomes as following:

$$H_0 = \begin{array}{c} \begin{array}{cccccc} |\uparrow,\uparrow\rangle & |\downarrow,\downarrow\rangle & |\uparrow,\downarrow\rangle & |\downarrow,\uparrow\rangle & |\uparrow\downarrow,\cdot\rangle & |\cdot,\uparrow\downarrow\rangle \end{array} \\ \begin{pmatrix} U_{ab} - J_{ab} & 0 & 0 & 0 & 0 & 0 \\ 0 & U_{ab} - J_{ab} & 0 & 0 & 0 & 0 \\ 0 & 0 & U_{ab} & -J_{ab} & 0 & 0 \\ 0 & 0 & -J_{ab} & U_{ab} & 0 & 0 \\ 0 & 0 & 0 & 0 & U_{aa} + \Delta_{ab} & J_{ab} \\ 0 & 0 & 0 & 0 & J_{ab} & U_{bb} - \Delta_{ab} \end{pmatrix} \end{array} \tag{2.23}$$

This unperturbed Hamiltonian has eigenenergies

$$\varepsilon_{1,2,3} = U_{ab} - J_{ab}, \quad \varepsilon_4 = U_{ab} + J_{ab}, \quad \varepsilon_{5,6} = \frac{U_{aa} + U_{bb}}{2} \pm \frac{\sqrt{(U_{aa} - U_{bb} + 2\Delta_{ab})^2 + 4J_{ab}^2}}{2}$$

with eigenstates

$$\begin{aligned} \psi_1 &= \psi_{\uparrow\uparrow} = |\uparrow,\uparrow\rangle \\ \psi_2 &= \psi_{\downarrow\downarrow} = |\downarrow,\downarrow\rangle \\ \psi_3 &= \frac{\psi_{\uparrow\downarrow} + \psi_{\downarrow\uparrow}}{\sqrt{2}} = \frac{|\uparrow,\downarrow\rangle + |\downarrow,\uparrow\rangle}{\sqrt{2}} \\ \psi_4 &= \frac{\psi_{\uparrow\downarrow} - \psi_{\downarrow\uparrow}}{\sqrt{2}} = \frac{|\uparrow,\downarrow\rangle - |\downarrow,\uparrow\rangle}{\sqrt{2}} \\ \psi_{5,6} &= \frac{\left(|\uparrow\downarrow,\cdot\rangle + \left(\frac{U_{bb} - U_{aa} - 2\Delta_{ab} \pm \sqrt{(U_{aa} - U_{bb} + 2\Delta_{ab})^2 + 4J_{ab}^2}}{2J_{ab}} \right) |\cdot,\uparrow\downarrow\rangle \right)}{\sqrt{1 + \left(\frac{U_{bb} - U_{aa} - 2\Delta_{ab} \pm \sqrt{(U_{aa-U_{bb}+2\Delta_{ab}})^2) + 4J_{ab}^2}}{2J_{ab}} \right)^2}}. \end{aligned}$$

Assuming that $\varepsilon_a = \varepsilon_b$, $U_{aa} = U_{bb} = U_d$ one has the eigenenergies:

$$\varepsilon_{1,2,3} = U_{ab} - J_{ab}, \quad \varepsilon_4 = U_{ab} + J_{ab}, \quad \varepsilon_{5,6} = \varepsilon_{\pm} = U_d \pm J_{ab}$$

$$
\begin{aligned}
\psi_1 &= \psi_{\uparrow\uparrow} = |\uparrow,\uparrow\rangle \\
\psi_2 &= \psi_{\downarrow\downarrow} = |\downarrow,\downarrow\rangle \\
\psi_3 &= \frac{\psi_{\uparrow\downarrow}+\psi_{\downarrow\uparrow}}{\sqrt{2}} = \frac{|\uparrow,\downarrow\rangle + |\downarrow,\uparrow\rangle}{\sqrt{2}} \\
\psi_4 &= \frac{\psi_{\uparrow\downarrow}-\psi_{\downarrow\uparrow}}{\sqrt{2}} = \frac{|\uparrow,\downarrow\rangle - |\downarrow,\uparrow\rangle}{\sqrt{2}} \\
\psi_{5,6} = \psi_{\text{ion}}^{\pm} &= \frac{|\uparrow\downarrow,\cdot\rangle \pm |\cdot,\uparrow\downarrow\rangle}{\sqrt{2}}.
\end{aligned}
$$

The first three states are the triplet covalent states. ψ_4 is the singlet covalent state. $\psi_5 = \psi_{\text{ion}}^{+}$ ($\varepsilon_5 = \varepsilon_+$) and $\psi_6 = \psi_{\text{ion}}^{-}$ ($\varepsilon_6 = \varepsilon_-$) are the ionic states.

Thus, the diagonalized unperturbed Hamiltonian is as follows:

$$
\tilde{H}_0 = \begin{array}{c} \\ \left(\begin{array}{cccccc} \psi_1 & \psi_2 & \psi_3 & \psi_4 & \psi_5 & \psi_6 \\ U_{ab}-J_{ab} & 0 & 0 & 0 & 0 & 0 \\ 0 & U_{ab}-J_{ab} & 0 & 0 & 0 & 0 \\ 0 & 0 & U_{ab}-J_{ab} & 0 & 0 & 0 \\ 0 & 0 & 0 & U_{ab}+J_{ab} & 0 & 0 \\ 0 & 0 & 0 & 0 & U_d+J_{ab} & 0 \\ 0 & 0 & 0 & 0 & 0 & U_d-J_{ab} \end{array}\right) \end{array} \begin{array}{c} \\ \psi_1 \\ \psi_2 \\ \psi_3 \\ \psi_4 \\ \psi_5 \\ \psi_6 \end{array} \qquad (2.24)
$$

Since $U > U_{ab}$, the ground states are the triplet states ψ_1, ψ_2 and ψ_3 with the energy $U_{ab} - J_{ab}$.

When we include the hopping and perturb the Hamiltonian, we encounter an exchange mechanism, which can be schematically seen in figure 2.21. This exchange mechanism is named as “Anderson superexchange” [60] or “Superexchange through space”. Here, moving an electron from one orbital to another orbital comes with the hopping $-t_{dd}$. By adding the hopping to the Hamiltonian, one can rewrite the complete Hamiltonian matrix ($\hat{H} = \hat{H}_0 + \hat{W}$)

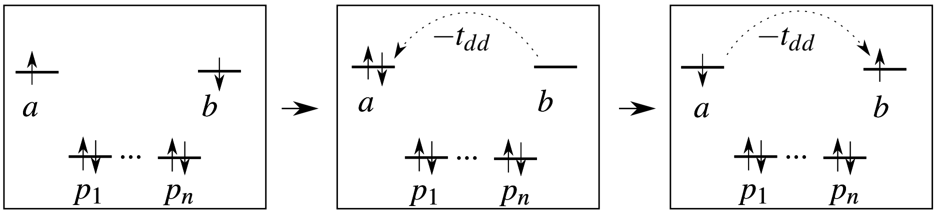

Fig. 2.21 Anderson superexchange a.k.a Superexchange “through space”

as the following in the basis set of $\{|\uparrow,\uparrow\rangle, |\downarrow,\downarrow\rangle, |\uparrow\downarrow\rangle, |\downarrow,\uparrow\rangle, |\uparrow\downarrow,\cdot\rangle, |\cdot,\uparrow\downarrow\rangle\}$:

$$
\begin{aligned}
H = & \begin{pmatrix}
U_{ab}-J_{ab} & 0 & 0 & 0 & 0 & 0 \\
0 & U_{ab}-J_{ab} & 0 & 0 & 0 & 0 \\
0 & 0 & U_{ab} & -J_{ab} & -t_{dd} & -t_{dd} \\
0 & 0 & -J_{ab} & U_{ab} & t_{dd} & t_{dd} \\
0 & 0 & -t_{dd} & t_{dd} & U_d & J_{ab} \\
0 & 0 & -t_{dd} & t_{dd} & J_{ab} & U_d
\end{pmatrix} \\
= & \underbrace{\begin{pmatrix}
U_{ab}-J_{ab} & 0 & 0 & 0 & 0 & 0 \\
0 & U_{ab}-J_{ab} & 0 & 0 & 0 & 0 \\
0 & 0 & U_{ab} & -J_{ab} & 0 & 0 \\
0 & 0 & -J_{ab} & U_{ab} & 0 & 0 \\
0 & 0 & 0 & 0 & U_d & J_{ab} \\
0 & 0 & 0 & 0 & J_{ab} & U_d
\end{pmatrix}}_{H_0} + \underbrace{\begin{pmatrix}
0 & 0 & 0 & 0 & 0 & 0 \\
0 & 0 & 0 & 0 & 0 & 0 \\
0 & 0 & 0 & 0 & -t_{dd} & -t_{dd} \\
0 & 0 & 0 & 0 & t_{dd} & t_{dd} \\
0 & 0 & -t_{dd} & t_{dd} & 0 & 0 \\
0 & 0 & -t_{dd} & t_{dd} & 0 & 0
\end{pmatrix}}_{W}
\end{aligned}
\tag{2.25}
$$

The Hamiltonian H in the basis set of the eigenstates of H_0 can be written as:

$$
\begin{aligned}
H = & \begin{array}{c} \begin{array}{cccccc} \psi_1 & \psi_2 & \psi_3 & \psi_4 & \psi_5 & \psi_6 \end{array} \\ \begin{pmatrix} U_{ab}-J_{ab} & 0 & 0 & 0 & 0 & 0 \\ 0 & U_{ab}-J_{ab} & 0 & 0 & 0 & 0 \\ 0 & 0 & U_{ab}-J_{ab} & 0 & 0 & 0 \\ 0 & 0 & 0 & U_{ab}+J_{ab} & -2t_{dd} & 0 \\ 0 & 0 & 0 & -2t_{dd} & U_d+J_{ab} & 0 \\ 0 & 0 & 0 & 0 & 0 & U_d-J_{ab} \end{pmatrix} \end{array} \\
= & \underbrace{\begin{pmatrix} U_{ab}-J_{ab} & 0 & 0 & 0 & 0 & 0 \\ 0 & U_{ab}-J_{ab} & 0 & 0 & 0 & 0 \\ 0 & 0 & U_{ab}-J_{ab} & 0 & 0 & 0 \\ 0 & 0 & 0 & U_{ab}+J_{ab} & 0 & 0 \\ 0 & 0 & 0 & 0 & U_d+J_{ab} & 0 \\ 0 & 0 & 0 & 0 & 0 & U_d-J_{ab} \end{pmatrix}}_{H_0} \\
+ & \underbrace{\begin{pmatrix} 0 & 0 & 0 & 0 & 0 & 0 \\ 0 & 0 & 0 & 0 & 0 & 0 \\ 0 & 0 & 0 & 0 & 0 & 0 \\ 0 & 0 & 0 & 0 & -2t_{dd} & 0 \\ 0 & 0 & 0 & -2t_{dd} & 0 & 0 \\ 0 & 0 & 0 & 0 & 0 & 0 \end{pmatrix}}_{W}
\end{aligned}
\tag{2.26}
$$

We will take into account $\hat{W}$ at the 2^{nd} order of perturbation theory to find the effective Hamiltonian. The low-energy states, i.e. the singlet and the triplet states, are the model space of our system. However, as one can see from the matrix $\tilde{W}$ the only hopping element appears between the singlet state ψ_4 and the ionic state $\psi_5 = \psi^+_{\text{ion}}$. Thus, applying the 2^{nd} perturbation theory on the triplet states does not give any correction to the energy of those states. However, one should correct the energy of the singlet state. Thus, we will apply 2^{nd} order perturbation on the model space.

2^{nd} order perturbation

At the 2^{nd} order perturbation, one can obtain the h_{ij} elements with the following formula;

$$h_{ij} = \sum_{\kappa} \frac{\langle \psi_i | \hat{T} | \psi_\kappa \rangle \langle \psi_\kappa | \hat{T} | \psi_j \rangle}{E^{(0)} - E^{(\psi_\kappa)}} \qquad \kappa \neq \text{model space} \tag{2.27}$$

where $E^{(\psi_\kappa)}$ is the energy of the state ψ_κ which is out of the model space. The indexes i and j correspond to the eigenstates of $\tilde{H}_0$. Thus, the correction to the energy of the singlet state ψ_4 is given as $-\frac{4t_{dd}^2}{U_d - U_{ab}}$ Thus, the corrected energy of the singlet state is given by

$$\varepsilon_{\text{singlet}} = U_{ab} + J_{ab} - \frac{4t_{dd}}{U_d - U_{ab}} \tag{2.28}$$

while the energy of the triplet states remains $\varepsilon_{\text{triplet}} = U_{ab} - J_{ab}$ Finally, we show that the singlet-triplet splitting (the effective exchange coupling) is

$$\varepsilon_{\text{triplet}} - \varepsilon_{\text{singlet}} - = J_{dd}^{\text{eff}} = \frac{4t_{dd}^2}{U_d - U_{ab}} - 2J_{ab}.$$

Here, $J_2^{\text{eff}} = \frac{4t_{dd}^2}{U_d - U_{ab}}$ is a 2^{nd} order term of the effective exchange coupling whereas $J_1^{\text{eff}} = -2J_{ab}$ is a 1^{st} order term. J_{dd}^{eff} is positive as long as $\frac{4t_{dd}^2}{U_d - U_{ab}} > 2J_{ab}$, which is the case except in very special conditions where the hopping integral is very small due to symmetry or distance reasons. Thus, the singlet state is the ground state and “Anderson Superexchange” or “Superexchange through space” results with antiferromagnetism.

Superexchange through Bridge

For the Anderson superexchange, it is crucial to have hopping between the d-orbitals. However, the d-orbitals are so localized that the hopping is non-negligible only between the orbitals on different atoms that are close to each other. In the case of transition metal oxides, transition metal cations (manganese ions in manganites) are separated by oxygen anions. Since $\mathrm{Mn}-\mathrm{Mn}$ distance is too large for the Anderson superexchange to be effective in most of the antiferromagnetic manganites, it is not possible to explain the antiferromagnetism in these compounds by means of Anderson superexchange. In such a situation we should take into account the 4^{th} order of the pertubation theory that involves a mechanism where hopping is done through a bridge orbital, for example through the oxygen p orbital. This mechanism is briefly called “superexchange through bridge” and can be seen in figure 2.22. Now for simplification we give the Coulomb repulsion between two electrons in a d-orbital as U_d and we neglect the Coulomb repulsion term between two electrons in p-orbitals. We also neglect

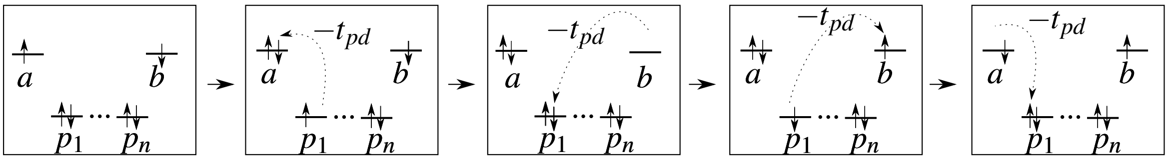

Fig. 2.22 Superexchange “through bridge”

the off-site Coulomb repulsion U_{ab} since we assume the distance between magnetic ions are large (for example Mn – Mn distance). The energy of an electron in a d or p orbital is given by ε_d or ε_p, respectively. $-t_{pd}$ is the hopping between p and d orbitals. The Hamiltonian for such a system is given by the following:

$$\begin{aligned}\hat{H} = \sum_{\sigma}\left(\varepsilon_d \sum_{\alpha=a,b} n_{\alpha\sigma} + \varepsilon_p n_{p\sigma}\right) + U_{ab}\sum_{\sigma}\left(\sum_{\alpha=a,b} n_{\alpha\sigma} n_{\alpha'\sigma'}\right) + U_d \sum_{\alpha=a,b} n_{\alpha\uparrow} n_{\alpha\downarrow} \\ + J_{ab}\sum_{\sigma}\left(\sum_{\alpha=a,b} c^{\dagger}_{\alpha\sigma} c^{\dagger}_{\alpha'\sigma'} c_{\alpha\sigma'} c_{\alpha'\sigma}\right) + J_{ab}\sum_{\sigma}\left(\sum_{\alpha=a,b} c^{\dagger}_{\alpha\sigma} c^{\dagger}_{\alpha\sigma'} c_{\alpha'\sigma'} c_{\alpha\sigma}\right) \\ -t_{pd}\sum_{\sigma}\left(\sum_{\alpha=a,b} c^{\dagger}_{\alpha\sigma} c_{p\sigma} + c^{\dagger}_{p\sigma} c_{\alpha\sigma}\right)\end{aligned} \tag{2.29}$$

Setting the reference energy to $2(\varepsilon_d + \varepsilon_p)$ and taking $\Delta_{pd} = \varepsilon_d - \varepsilon_p$ gives us the Hamiltonian matrix for antiparallel spins in d-orbitals:

$$H = \begin{array}{c} \begin{array}{ccccccccc} |b^{\downarrow} p_i^{\uparrow\downarrow} a^{\uparrow}\rangle & |b^{\uparrow} p_i^{\uparrow\downarrow} a^{\downarrow}\rangle & |b^{\downarrow} p_i^{\uparrow} a^{\uparrow\downarrow}\rangle & |b^{\uparrow\downarrow} p_i^{\downarrow} a^{\uparrow}\rangle & |b^{\uparrow} p_i^{\downarrow} a^{\uparrow\downarrow}\rangle & |b^{\uparrow\downarrow} p_i^{\uparrow} a^{\downarrow}\rangle & |p_i^{\uparrow\downarrow} a^{\uparrow\downarrow}\rangle & |b^{\uparrow\downarrow} p_i^{\uparrow\downarrow}\rangle & |b^{\uparrow\downarrow} a^{\uparrow\downarrow}\rangle \end{array} \\ \left(\begin{array}{cc|cccc|ccc} U_{ab} & -J_{ab} & t_{pd} & t_{pd} & 0 & 0 & 0 & 0 & 0 \\ -J_{ab} & U_{ab} & 0 & 0 & t_{pd} & t_{pd} & 0 & 0 & 0 \\ \hline t_{pd} & 0 & U_d+2U_{ab}+\Delta_{pd} & 0 & 0 & 0 & -t_{pd} & 0 & -t_{pd} \\ t_{pd} & 0 & 0 & U_d+2U_{ab}+\Delta_{pd} & 0 & 0 & 0 & -t_{pd} & -t_{pd} \\ 0 & t_{pd} & 0 & 0 & U_d+2U_{ab}+\Delta_{pd} & 0 & t_{pd} & 0 & t_{pd} \\ 0 & t_{pd} & 0 & 0 & 0 & U_d+2U_{ab}+\Delta_{pd} & 0 & t_{pd} & t_{pd} \\ \hline 0 & 0 & -t_{pd} & 0 & t_{pd} & 0 & U_d & J_{ab} & 0 \\ 0 & 0 & 0 & -t_{pd} & 0 & t_{pd} & J_{ab} & U_d & 0 \\ 0 & 0 & -t_{pd} & -t_{pd} & t_{pd} & t_{pd} & 0 & 0 & 2(U_d+2U_{ab}+\Delta_{pd}) \end{array}\right) \end{array} \tag{2.30}$$

with the basis set of the states which can be seen in figure 2.23 (left). Considering $\varepsilon_d > \varepsilon_p$ and noting that the high energy states are the ones with at least one doubly occupied d-orbital, $|b^{\downarrow} p_i^{\uparrow\downarrow} a^{\uparrow}\rangle$ and $|b^{\uparrow} p_i^{\uparrow\downarrow} a^{\downarrow}\rangle$ are the low-energy states while the rest of the states are high-energy states. One can apply the downfolding recursively to the Hamiltonian matrix given in 2.30.

Downfolding technique

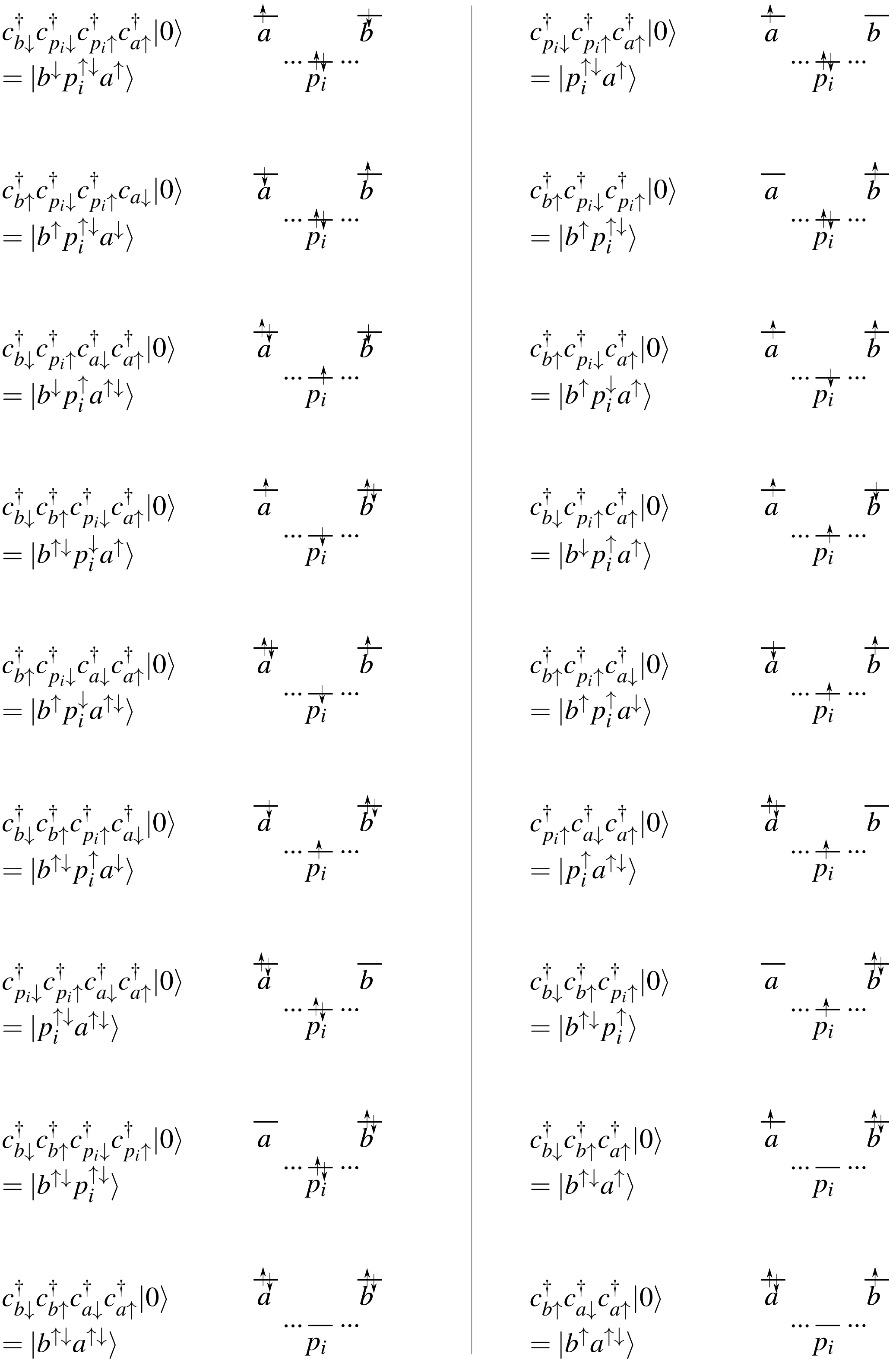

$$c^\dagger_{b\downarrow}c^\dagger_{p_i\downarrow}c^\dagger_{p_i\uparrow}c^\dagger_{a\uparrow}|0\rangle = |b^{\downarrow}p_i^{\uparrow\downarrow}a^{\uparrow}\rangle$$

$$c^\dagger_{b\uparrow}c^\dagger_{p_i\downarrow}c^\dagger_{p_i\uparrow}c_{a\downarrow}|0\rangle = |b^{\uparrow}p_i^{\uparrow\downarrow}a^{\downarrow}\rangle$$

$$c^\dagger_{b\downarrow}c^\dagger_{p_i\uparrow}c^\dagger_{a\downarrow}c^\dagger_{a\uparrow}|0\rangle = |b^{\downarrow}p_i^{\uparrow}a^{\uparrow\downarrow}\rangle$$

$$c^\dagger_{b\downarrow}c^\dagger_{b\uparrow}c^\dagger_{p_i\downarrow}c^\dagger_{a\uparrow}|0\rangle = |b^{\uparrow\downarrow}p_i^{\downarrow}a^{\uparrow}\rangle$$

$$c^\dagger_{b\uparrow}c^\dagger_{p_i\downarrow}c^\dagger_{a\downarrow}c^\dagger_{a\uparrow}|0\rangle = |b^{\uparrow}p_i^{\downarrow}a^{\uparrow\downarrow}\rangle$$

$$c^\dagger_{b\downarrow}c^\dagger_{b\uparrow}c^\dagger_{p_i\uparrow}c^\dagger_{a\downarrow}|0\rangle = |b^{\uparrow\downarrow}p_i^{\uparrow}a^{\downarrow}\rangle$$

$$c^\dagger_{p_i\downarrow}c^\dagger_{p_i\uparrow}c^\dagger_{a\downarrow}c^\dagger_{a\uparrow}|0\rangle = |p_i^{\uparrow\downarrow}a^{\uparrow\downarrow}\rangle$$

$$c^\dagger_{b\downarrow}c^\dagger_{b\uparrow}c^\dagger_{p_i\downarrow}c^\dagger_{p_i\uparrow}|0\rangle = |b^{\uparrow\downarrow}p_i^{\uparrow\downarrow}\rangle$$

$$c^\dagger_{b\downarrow}c^\dagger_{b\uparrow}c^\dagger_{a\downarrow}c^\dagger_{a\uparrow}|0\rangle = |b^{\uparrow\downarrow}a^{\uparrow\downarrow}\rangle$$

$$c^\dagger_{p_i\downarrow}c^\dagger_{p_i\uparrow}c^\dagger_{a\uparrow}|0\rangle = |p_i^{\uparrow\downarrow}a^{\uparrow}\rangle$$

$$c^\dagger_{b\uparrow}c^\dagger_{p_i\downarrow}c^\dagger_{p_i\uparrow}|0\rangle = |b^{\uparrow}p_i^{\uparrow\downarrow}\rangle$$

$$c^\dagger_{b\uparrow}c^\dagger_{p_i\downarrow}c^\dagger_{a\uparrow}|0\rangle = |b^{\uparrow}p_i^{\downarrow}a^{\uparrow}\rangle$$

$$c^\dagger_{b\downarrow}c^\dagger_{p_i\uparrow}c^\dagger_{a\uparrow}|0\rangle = |b^{\downarrow}p_i^{\uparrow}a^{\uparrow}\rangle$$

$$c^\dagger_{b\uparrow}c^\dagger_{p_i\uparrow}c^\dagger_{a\downarrow}|0\rangle = |b^{\uparrow}p_i^{\uparrow}a^{\downarrow}\rangle$$

$$c^\dagger_{p_i\uparrow}c^\dagger_{a\downarrow}c^\dagger_{a\uparrow}|0\rangle = |p_i^{\uparrow}a^{\uparrow\downarrow}\rangle$$

$$c^\dagger_{b\downarrow}c^\dagger_{b\uparrow}c^\dagger_{p_i\uparrow}|0\rangle = |b^{\uparrow\downarrow}p_i^{\uparrow}\rangle$$

$$c^\dagger_{b\downarrow}c^\dagger_{b\uparrow}c^\dagger_{a\uparrow}|0\rangle = |b^{\uparrow\downarrow}a^{\uparrow}\rangle$$

$$c^\dagger_{b\uparrow}c^\dagger_{a\downarrow}c^\dagger_{a\uparrow}|0\rangle = |b^{\uparrow}a^{\uparrow\downarrow}\rangle$$

Fig. 2.23 (Left) Basis set for the superexchange “through bridge” Hamiltonian given in 2.30 and (right) basis set for the effective hopping Hamiltonian given in 2.38

We can obtain the effective Hamiltonian by partitioning the Hilbert space into a reduced one. In this scenario, one considers the Hamiltonian matrix H in 2.30 as blocks of interest, such as low-energy states, high energy states. Thus, the Hamiltonian matrix H becomes as following; into blocks of low-energy states, high-energy states and transfer blocks matrices:

$$A = \begin{pmatrix} H_{00} & T_{01} \\ T_{10} & H_{11} \end{pmatrix} \quad \text{and} \quad B = \begin{pmatrix} H_{11} & T_{12} \\ T_{21} & H_{22} \end{pmatrix} \tag{2.31}$$

Then,

$$H = \begin{pmatrix} H_{00} & T_{01} & 0 \\ T_{10} & H_{11} & T_{12} \\ 0 & T_{21} & H_{22} \end{pmatrix} = \begin{pmatrix} H_{00} & \tilde{T}_{01} \\ \tilde{T}_{10} & B \end{pmatrix}. \tag{2.32}$$

Here, H_{00} is the Hamiltonian of the low-energy states, H_{11} and H_{22} are the Hamiltonian for the high energy states. T_{01} and T_{10} describe the transfer between the subspaces H_{00} and H_{11}. T_{12} and T_{21} describe the transfer between the subspaces H_{11} and H_{22}. Thus, now, one can partition the full system into low-energy states and project out the high-energy states. This process can be done by downfolding method where one can find the resolvent matrix of H by the following:

$$\begin{aligned} R(\varepsilon,H) &= (\varepsilon - H)^{-1} = \begin{pmatrix} \varepsilon - H_{00} & \tilde{T}_{01} \\ \tilde{T}_{10} & \varepsilon - B \end{pmatrix}^{-1} \\ &= \left(\varepsilon - (H_{00} + \tilde{T}_{01}(\varepsilon - B)^{-1}\tilde{T}_{10}\right)^{-1} \\ &= \left(\varepsilon - (H_{00} + \tilde{T}_{01} \begin{pmatrix} \varepsilon - H_{11} & T_{12} \\ T_{21} & \varepsilon - H_{22} \end{pmatrix}^{-1} \tilde{T}_{10}\right)^{-1} \\ &= \left(\varepsilon - \underbrace{(H_{00} + T_{01}(\varepsilon - H_{11} - T_{12}(\varepsilon - H_{22})^{-1}T_{21})^{-1})T_{10})}_{H_{\text{eff}}}\right)^{-1} \end{aligned} \tag{2.33}$$

Thus, the effective Hamiltonian can be given by setting $\varepsilon = 0$:

$$\begin{aligned}
H_{\text{eff}} &= H_{00} + T_{01}(\varepsilon - H_{11} - T_{12}(\varepsilon - H_{22})^{-1}T_{21})^{-1})T_{10} \\
&\sim H_{00} + T_{01}(-H_{11} - T_{12}(-H_{22})^{-1}T_{21})^{-1})T_{10} \\
&= \left(U_{ab} - J_{ab} - \frac{2t_{pd}^2}{U_d + 2U_{ab} + \Delta_{pd}}\right)\begin{pmatrix}1 & 0\\ 0 & 1\end{pmatrix} \\
&+ \left(J_{ab} - \frac{2t_{pd}^4}{(U_d + 2U_{ab} + \Delta_{pd})^2}\left(\frac{1}{U_d + J_{ab}} + \frac{1}{U_d + 2U_{ab} + \Delta_{pd}}\right)\right)\begin{pmatrix}1 & -1\\ -1 & 1\end{pmatrix}.
\end{aligned} \tag{2.34}$$

The eigenvalues and the corresponding eigenstates of the effective Hamiltonian given in 2.34 are as follows:

$$\begin{aligned}
\varepsilon_1 &= U_{ab} - J_{ab} - \frac{2t_{pd}^2}{U_d + 2U_{ab} + \Delta_{pd}} \\
\varepsilon_2 &= U_{ab} + J_{ab} - \frac{2t_{pd}^2}{U_d + 2U_{ab} + \Delta_{pd}} - \frac{4t_{pd}^4}{(U_d + 2U_{ab} + \Delta_{pd})^2}\left(\frac{1}{U_d + J_{ab}} + \frac{1}{U_d + 2U_{ab} + \Delta_{pd}}\right)
\end{aligned}$$

$$\begin{aligned}
\psi_1 &= \frac{|b^{\downarrow}p_i^{\uparrow\downarrow}a^{\uparrow}\rangle + |b^{\uparrow}p_i^{\uparrow\downarrow}a^{\downarrow}\rangle}{\sqrt{2}} \\
\psi_2 &= \frac{|b^{\downarrow}p_i^{\uparrow\downarrow}a^{\uparrow}\rangle - |b^{\uparrow}p_i^{\uparrow\downarrow}a^{\downarrow}\rangle}{\sqrt{2}}
\end{aligned}$$

Thus, one can obtain the effective exchange coupling by $\varepsilon_{\text{triplet}} - \varepsilon_{\text{singlet}} = \varepsilon_1 - \varepsilon_2$:

$$J_{pd}^{\text{eff}} = \frac{4t_{pd}^4}{(U_d + 2U_{ab} + \Delta_{pd})^2}\left(\frac{1}{U_d + J_{ab}} + \frac{1}{U_d + 2U_{ab} + \Delta_{pd}}\right) - 2J_{ab} \tag{2.35}$$

Here, $J_4^{\text{eff}} = \frac{4t_{pd}^4}{(U_d+2U_{ab}+\Delta_{pd})^2}\left(\frac{1}{U_d+2_{ab}+J_{ab}} + \frac{1}{U_d+\Delta_{pd}}\right)$ is a 4^{th} order term of the effective exchange coupling whereas $J_1^{\text{eff}} = -2J_{ab}$ is a 1^{st} order term. J_{pd}^{eff} is positive as long as

$$\frac{4t_{pd}^4}{(U_d + 2U_{ab} + \Delta_{pd})^2}\left(\frac{1}{U_d + 2U_{ab} + J_{ab}} + \frac{1}{U_d + \Delta_{pd}}\right) > 2J_{ab}$$

which is the case except very special conditions where the hopping integral is very small due to the symmetry reasons. Thus, ψ_2, the singlet state, is the ground state. The superexchange "through bridge" mechanism results with antiferromagnetism. The effective exchange coupling J_{pd}^{eff} exhibits the "superexchange through bridge" mechanism with four hopping steps as one can again see in figure 2.22. In order to generalize the superexchange through bridge mechanism explained above for a system with several open d shells, one has to sum up all the terms for all pairs of one electron on orbital *a* and one electron on orbital *b*. Of course, some of the terms will be zero due to symmetry.

Finally, we can give the effective exchange coupling with the contribution of 1^{st}, 2^{nd} and 4^{th} order terms:

$$\begin{aligned} J^{\text{eff}} &= J_1^{\text{eff}} + J_2^{\text{eff}} + J_4^{\text{eff}} \\ &= -2J_{ab} + \frac{4t_{dd}^2}{U_d - U_{ab}} + \frac{4t_{pd}^4}{(U_d + 2U_{ab} + \Delta_{pd})^2}\left(\frac{1}{U_d + 2U_{ab} + J_{ab}} + \frac{1}{U_d + 2U_{ab} + \Delta_{pd}}\right) \end{aligned}$$

Effective Hopping

Now we would like to talk about the case where there is only one electron for two *d*-orbitals. We consider the system of two open *d* shells separated with the bridge *p* orbitals. This time, there is only one electron on the *d* orbitals. Let us first assume that there is a direct hopping (1^{st} order perturbation) between the two *d*-orbitals *a* and *b*, the bridge orbitals do not participate the mechanism at this stage. This case can be schematically seen in figure 2.24. There are two possible states: $c^\dagger_{a\uparrow}|0\rangle = |\uparrow,\cdot\rangle$ and $c^\dagger_{b\uparrow}|0\rangle = |\cdot,\uparrow\rangle$. Using the Hamiltonian given in 2.21, setting $\varepsilon_a = \varepsilon_b$ as a reference energy, one can obtain the Hamiltonian matrix in the basis set of the states $|\uparrow,\cdot\rangle$ and $|\cdot,\uparrow\rangle$ for such mechanism:

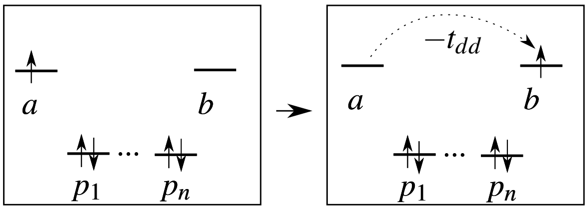

Fig. 2.24 Direct hopping

$$H = \begin{array}{cc} |\uparrow,\cdot\rangle & |\cdot,\uparrow\rangle & \\ \left(\begin{array}{c} 0 \\ -t_{dd} \end{array}\right. & \left.\begin{array}{c} -t_{dd} \\ 0 \end{array}\right) & \begin{array}{c} |\uparrow,\cdot\rangle \\ |\cdot,\uparrow\rangle \end{array} \end{array} \tag{2.36}$$

Diagonalizing this matrix gives us the eigenenergies and the corresponding eigenstates

$$\varepsilon_1 = -t_{dd}, \quad \psi_1 = \frac{|\uparrow,\cdot\rangle + |\cdot,\uparrow\rangle}{\sqrt{2}}$$

$$\varepsilon_2 = t_{dd}, \quad \psi_2 = \frac{|\uparrow,\cdot\rangle - |\cdot,\uparrow\rangle}{\sqrt{2}}$$

Taking $t_{dd} > 0$, ψ_1 is the ground state. Thus, the delocalization energy also known as the hopping energy is given by

$$\varepsilon_1 - \varepsilon_a = t_1^{\text{eff}} = -t_{dd}.$$

Now, let us consider the 2^{nd} order perturbation in which the bridge p-orbitals also can participate the hopping mechanism. The schematic representation of such a mechanism is given in figure 2.25.

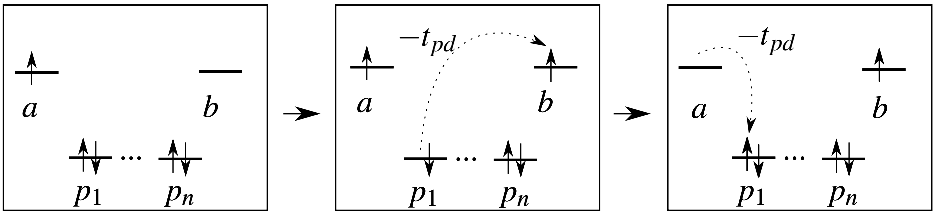

Fig. 2.25 Hopping through bridge

The Hamiltonian of such a system can be given by

$$\begin{aligned}\hat{H} = \sum_{\sigma}\left(\varepsilon_d \sum_{\alpha=a,b} n_{\alpha\sigma} + \varepsilon_p n_{p\sigma}\right) + U_{ab}\sum_{\sigma}\left(\sum_{\alpha=a,b} n_{\alpha\sigma} n_{\alpha'\sigma'}\right) + U_d \sum_{\alpha=a,b} n_{\alpha\uparrow} n_{\alpha\downarrow} \\ -t_{pd}\sum_{\sigma}\left(\sum_{\alpha=a,b}(c^{\dagger}_{\alpha\sigma} c_{p\sigma} + c^{\dagger}_{p\sigma} c_{\alpha\sigma})\right).\end{aligned} \tag{2.37}$$

Setting the reference energy as $\varepsilon_d + 2\varepsilon_p$ and taking $\Delta_{pd} = \varepsilon_d - \varepsilon_p$ and in the basis set of the states given in figure 2.23 (right), the Hamiltonian matrix for a system of 2-spin-up, 1 spin-down electrons can be given as follows:

$$H = \begin{array}{cc|ccccc|cc}
|p_i^{\uparrow\downarrow}a^{\uparrow}\rangle & |b^{\uparrow}p_i^{\uparrow\downarrow}\rangle & |b^{\uparrow}p_i^{\downarrow}a^{\uparrow}\rangle & |b^{\downarrow}p_i^{\uparrow}a^{\uparrow}\rangle & |b^{\uparrow}p_i^{\uparrow}a^{\downarrow}\rangle & |p_i^{\uparrow}a^{\uparrow\downarrow}\rangle & |b^{\uparrow\downarrow}p_i^{\uparrow}\rangle & |b^{\uparrow\downarrow}a^{\uparrow}\rangle & |b^{\uparrow}a^{\uparrow\downarrow}\rangle \\
0 & 0 & t_{pd} & -t_{pd} & 0 & t_{pd} & 0 & 0 & 0 \\
0 & 0 & -t_{pd} & 0 & t_{pd} & 0 & t_{pd} & 0 & 0 \\
\hline
t_{pd} & -t_{pd} & U_{ab}+\Delta_{pd} & 0 & 0 & 0 & 0 & t_{pd} & -t_{pd} \\
-t_{pd} & 0 & 0 & U_{ab}+\Delta_{pd} & 0 & 0 & 0 & -t_{pd} & 0 \\
0 & t_{pd} & 0 & 0 & U_{ab}+\Delta_{pd} & 0 & 0 & 0 & t_{pd} \\
t_{pd} & 0 & 0 & 0 & 0 & U_d+\Delta_{pd} & 0 & 0 & -t_{pd} \\
0 & t_{pd} & 0 & 0 & 0 & 0 & U_d+\Delta_{pd} & -t_{pd} & 0 \\
\hline
0 & 0 & t_{pd} & -t_{pd} & 0 & 0 & -t_{pd} & U_d+2\Delta_{pd} & 0 \\
0 & 0 & -t_{pd} & 0 & t_{pd} & -t_{pd} & 0 & 0 & U_d+2U_{ab}+2\Delta_{pd}
\end{array} \tag{2.38}$$

Let us obtain the effective Hamiltonian with both 2^{nd} order perturbation and downfolding the high-energy states.

1) 2^{nd} Order Perturbation

The ground states of the unperturbed H_0 of the Hamiltonian given 2.38 are $\psi_1 = c^{\dagger}_{p_i\downarrow}c^{\dagger}_{p_i\uparrow}c^{\dagger}_{a\uparrow}|0\rangle = |p_i^{\uparrow\downarrow}a^{\uparrow}\rangle$ and $\psi_2 = c^{\dagger}_{b\uparrow}c^{\dagger}_{p_i\downarrow}c^{\dagger}_{p_i\uparrow}|0\rangle = |b^{\uparrow}p_i^{\uparrow\downarrow}\rangle$. One can obtain the effective Hamiltonian in this basis set by using the formula given in 2.27:

$$H_{\text{eff}} = \begin{pmatrix} -\frac{2t_{pd}^2}{U_{ab}+\Delta_{pd}} - \frac{t_{pd}^2}{U_d+\Delta_{pd}} & \frac{t^2}{U_{ab}+\Delta_{pd}} \\ \frac{t^2}{U_{ab}+\Delta_{pd}} & -\frac{2t_{pd}^2}{U_{ab}+\Delta_{pd}} - \frac{t_{pd}^2}{U_d+\Delta_{pd}} \end{pmatrix} \tag{2.39}$$

Solving the eigenvalue problem of this Hamiltonian gives us the eigenstates

$$\varepsilon_1 = -\frac{t_{pd}^2}{U_{ab}+\Delta_{pd}} - \frac{t_{pd}^2}{U_d+\Delta_{pd}}, \quad \psi_1 = \frac{|p_i^{\uparrow\downarrow}a^{\uparrow}\rangle + |b^{\uparrow}p_i^{\uparrow\downarrow}\rangle}{\sqrt{2}}$$

$$\varepsilon_2 = -3\frac{t_{pd}^2}{U_{ab}+\Delta_{pd}} - \frac{t_{pd}^2}{U_d+\Delta_{pd}}, \quad \psi_2 = \frac{|p_i^{\uparrow\downarrow}a^{\uparrow}\rangle - |b^{\uparrow}p_i^{\uparrow\downarrow}\rangle}{\sqrt{2}}$$

If $t_{pd} > 0$, then ψ_2 is the ground state. Thus, the delocalization energy is given by

$$\varepsilon_1 - \varepsilon_2 = t_2^{\text{eff}} = 2\frac{t_{pd}^2}{\Delta_{pd}}.$$

2) Downfolding technique

We can also obtain the effective Hamiltonian by reducing the Hilbert space. Noting that high energy states are the states with at least one doubly occupied d-orbital, we can partition the Hamiltonian matrix given in 2.38 into blocks of low-energy states, high-energy states and transfer blocks matrices:

$$A = \begin{pmatrix} H_{00} & T_{01} \\ T_{10} & H_{11} \end{pmatrix} \quad \text{and} \quad B = \begin{pmatrix} H_{11} & T_{12} \\ T_{21} & H_{22} \end{pmatrix} \tag{2.40}$$

Then,

$$H = \begin{pmatrix} H_{00} & T_{01} & 0 \\ T_{10} & H_{11} & T_{12} \\ 0 & T_{21} & H_{22} \end{pmatrix} = \begin{pmatrix} H_{00} & \tilde{T}_{01} \\ \tilde{T}_{10} & B \end{pmatrix} \tag{2.41}$$

The resolvent matrix of H is given by the following:

$$\begin{aligned} R(\varepsilon, H) &= (\varepsilon - H)^{-1} = \begin{pmatrix} \varepsilon - H_{00} & \tilde{T}_{01} \\ \tilde{T}_{10} & \varepsilon - B \end{pmatrix}^{-1} \\ &= \left(\varepsilon - (H_{00} + \tilde{T}_{01}(\varepsilon - B)^{-1}\tilde{T}_{10}\right)^{-1} \\ &= \left(\varepsilon - (H_{00} + \tilde{T}_{01} \begin{pmatrix} \varepsilon - H_{11} & T_{12} \\ T_{21} & \varepsilon - H_{22} \end{pmatrix}^{-1} \tilde{T}_{10}\right)^{-1} \\ &= \left(\varepsilon - \underbrace{(H_{00} + T_{01}(\varepsilon - H_{11} - T_{12}(\varepsilon - H_{22})^{-1}T_{21})^{-1})T_{10})}_{H_{\text{eff}}}\right)^{-1} \end{aligned} \tag{2.42}$$

Thus, the approximation of the effective Hamiltonian can be given by setting $\varepsilon = 0$ and taking the limit when $U_d \to \infty$:

$$\begin{aligned} H_{\text{eff}} &= H_{00} + T_{01}(\varepsilon - H_{11} - T_{12}(\varepsilon - H_{22})^{-1}T_{21})^{-1})T_{10} \\ &\sim H_{00} + T_{01}(-H_{11} - T_{12}(-H_{22})^{-1}T_{21})^{-1})T_{10} \\ &= -\frac{2t_{pd}^2}{U_{ab} + \Delta_{pd}} \begin{pmatrix} 1 & -\frac{1}{2} \\ -\frac{1}{2} & 1 \end{pmatrix} \end{aligned} \tag{2.43}$$

Solving the eigenvalue problem of this Hamiltonian gives us the eigenstates

$$\varepsilon_1 = -\frac{t_{pd}^2}{U_{ab}+\Delta_{pd}}, \quad \psi_1 = \frac{|p_i^{\uparrow\downarrow}a^{\uparrow}\rangle + |b^{\uparrow}p_i^{\uparrow\downarrow}\rangle}{\sqrt{2}}$$

$$\varepsilon_2 = -3\frac{t_{pd}^2}{U_{ab}+\Delta_{pd}}, \quad \psi_2 = \frac{|p_i^{\uparrow\downarrow}a^{\uparrow}\rangle - |b^{\uparrow}p_i^{\uparrow\downarrow}\rangle}{\sqrt{2}}$$

If $t_{pd} > 0$, then ψ_2 is the ground state. Thus, the delocalization energy is given by

$$\varepsilon_1 - \varepsilon_2 = t_2^{\text{eff}} = 2\frac{t_{pd}^2}{\Delta_{pd}}.$$

We obtain the same delocalization energy as 2^{nd} order perturbation theory $t_2^{\text{eff}} = 2\frac{t_{pd}^2}{\Delta_{pd}}$. In order to generalize the effective hopping mechanism explained above for a system with several open d shells, one has to sum up all the terms for all pairs of one electron on the orbitals a and b. Naturally, some of the terms will be zero due to symmetry.

Finally, the effective hopping energy can be given by the contribution of both 1^{st} and 2^{nd} order terms:

$$t^{\text{eff}} = t_1^{\text{eff}} + t_2^{\text{eff}} = -2t_{dd} + 2\frac{t_{pd}^2}{\Delta_{pd}}$$

Due to the large distance between Mn ions in manganites (more generally metals in transition-metal oxides), one can expect the delocalization energy t_1^{eff} and the exchange coupling J_2^{eff} to be small as they include the terms consisting of t_{dd}. On the other hand, the terms t_2^{eff} and J_4^{eff}, i.e. the terms consisting of t_{pd}, are dominant if they are non-zero.

Double Exchange

In doped manganites with mixed valence, there are Mn^{3+} and Mn^{4+} ions separated by $2p$ orbitals of O^{2-}. In Mn^{4+} (d^3) ions, the t_{2g} orbitals are half-filled and the e_g orbitals are empty, whereas in Mn^{3+} (d^4) ions, the t_{2g} are still half-filled but there is one electron in the e_g level. While the nature of the occupied e_g orbital in Mn^{3+} is a question of symmetry and local energetics of the system (crystal field splitting, Jahn-Teller distortion etc.), one should note that delocalization is allowed between the e_g shells of the Mn^{3+} and the Mn^{4+} ions, for a ferromagnetic alignment. This mechanism is called “Double exchange” [15]. Let us try to explain how this double exchange mechanism takes place.

When there are Mn^{3+} and Mn^{4+} ions separated with $2p$ orbitals of O^{2-}, there are three terms in the energy of these two ions. The energy can be be written as:

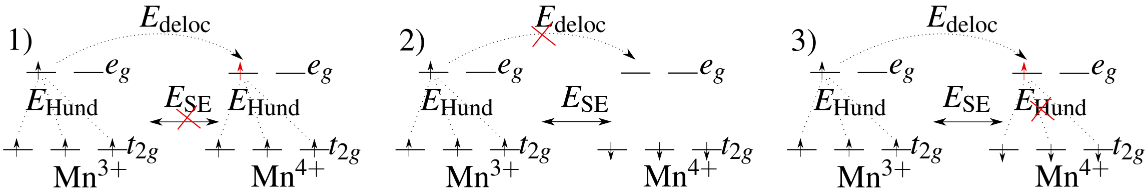

Fig. 2.26 Possible competing mechanisms in Mn^{3+}-Mn^{4+} environment 1) Frustrated superexchange 2) Frustrated delocalization 3) Frustrated Hund’s Exchange.

$$E = E_{\text{Hund}} + E_{\text{deloc}} + E_{\text{SE}} + K$$

where E_{Hund} is the Hund’s exchange energy within each ion, E_{deloc} is the e_g delocalization energy between the ions, E_{SE} is the superexchange energy, and K is the contribution of the other terms and it is a constant. Here, $E_{\text{Hund}} \propto J_H$, $E_{\text{deloc}} \propto t^{\text{eff}}$ and $E_{\text{SE}} \propto J^{\text{eff}}$. One cannot lower energy of all terms at the same time and has to frustrate one of them. Thus, depending on which pair is stabilized, three scenario can take place as follows:

1. $E_{\text{Hund}} + E_{\text{deloc}} \rightarrow$ “Frustrated Superexchange”: The system is ferromagnetic ordered Mn ions and one loses antiferromagnetic coupling between the ions.
2. $E_{\text{Hund}} + E_{\text{SE}} \rightarrow$ “Frustrated Delocalization”: The system is antiferromagnetic ordered Mn ions and one loses the delocalization energy between high spins.
3. $E_{\text{SE}} + E_{\text{deloc}} \rightarrow$ “Frustrated Hund’s exchange”: The delocalization of one e_g electron takes place and there exist an antiferromagnetic ordering of the spins in e_g and t_{2g} level. Thus, part of the electron ion each atom are not ferromagnetically aligned (atoms are not high spin anymore).

These three scenario can be schematically seen in figure 2.26[2] Among these three scenario, the first one takes place in $Mn^{3+} - O^{2-} - Mn^{4+}$ environment since the gain of energy that one gets with E_{Hund} and E_{deloc} is more than the one of E_{SE} (E_{Hund} is order of magnitude to eV, E_{deloc} is order of magnitude to 0.1 eV, E_{SE} is order of magnitude to

---

[2] The hopping of the one electron is given here schematically. In general, the hopping takes place through the oxygen $2p$ bridge orbitals in a mixed valence manganite.

0.01 eV.). Thus, because of the strong intra-atomic Hund's coupling, the transfer from Mn^{3+} and Mn^{4+} is energetically favourable only when the core spins (t_{2g}) of the Mn ions are aligned ferromagnetically. This explains why the double exchange mechanism leads to ferromagnetism despite the antiferromagnetic superexchange interactions. The double exchange mechanism explains also the correlation between the electrical conduction and ferromagnetism in doped manganites discovered by Jonker and Van Santen [12].

From the analysis above, one can point out the role of the allignment of the core t_{2g} spins in determining the e_g electron delocalization. The effective e_g hopping interaction between neighbouring magnetic sites i and j can be given by $t_{ij}^{\mathrm{eff}} = t_{ij}^{0} \cos(\theta_{ij}/2)$ [61, 62]. Here, t_{ij}^{0} is the intersite hopping interaction of the e_g electron between the neighbouring sites, i and j and θ_{ij} classical angle between the neighbouring core t_{2g} spins of sites i and j. Thus, when the t_{2g} spins are alligned parallel t_{ij}^{eff} is maximized (i.e. the case seen in figure 2.26 1)). This hopping maximization results an energy gain and reveals the ferromagnetic character of double exchange mechanism. On the other hand, when the t_{2g} spins are alligned antiparallel $t_{ij}^{\mathrm{eff}} = 0$ (i.e. the case seen in figure 2.26 2)).

The role of the geometry

In the effective hopping as well as exchange, the bond angle, i.e the angle of $\mathrm{Mn}-\mathrm{O}-\mathrm{Mn}$ plays a significant role. In an ideal octahedron environment the bond angle is 180°. In figure 2.27, one can see a representation of $\mathrm{Mn}-\mathrm{O}-\mathrm{Mn}$ angle, particularly the $d_{x^2-y^2} - p_x - d_{x^2-y^2}$ angle. Here, $180-\alpha$ is the angle between the two $d_{x^2-y^2}$ orbitals. The p-d transfer interaction will scale as $t_2^{\mathrm{eff}} \cos\alpha$ where t_2^{eff} is 2^{nd} order term of the effective hopping in the ideal cubic perovskite where the bond angle $\mathrm{Mn}-\mathrm{O}-\mathrm{Mn}$ is 180°. Thus, the 2^{nd} order

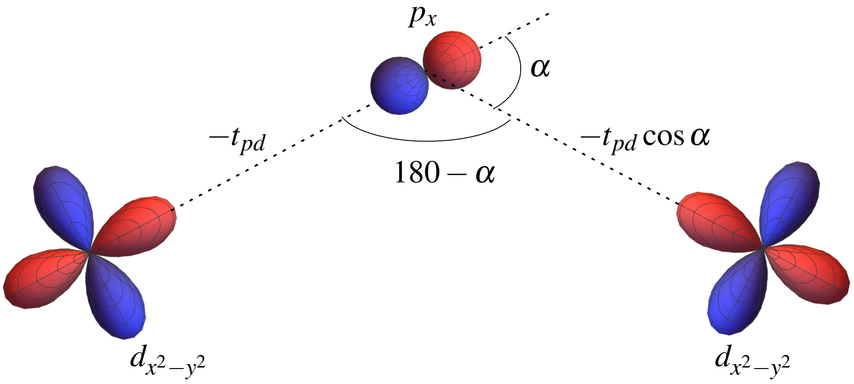

Fig. 2.27 A representation of the bond angle of $d_{x^2-y^2} - p_x - d_{x^2-y^2}$ in a distorted octahedron

term of the effective hopping is given by

$$t_2^{\text{eff}} \propto t_{pd}^2 \cos\alpha$$

whereas the 4^{th} order term of the effective superexchange coupling is given by

$$J_2^{\text{eff}} \propto t_{pd}^4 \cos^2\alpha.$$

One should note that the hopping energy is large for $d_{x^2-y^2} \rightarrow d_{x^2-y^2}$ in xy plane and $d_{z^2} \rightarrow d_{z^2}$ in the z direction.

2.2.4 Spin, Orbital and Charge Ordering

In perovskite manganites, different degrees of freedom can order: spin, electron and orbital. These orders are called magnetic, charge and orbital orders, respectively. Depending on the interactions at play, the spin of the electrons can allign in a particular pattern. This particular pattern is called spin ordering. Ferromagnetism is the result of parallel spin alignment, whereas antiferromagnetism occurs when spins are antiparallel to each other. In perovskites, antiferromagnetic spin ordering can take place in three different ways (limiting ourselves to first neighbours): (i) A-type antiferromagnetism; in-plane ferromagnetic spin ordering and out-of-plane antiferromagnetic ordering (ii) C-type antiferromagnetism; in-plane antiferromagnetic spin ordering and out-of-plane ferromagnetic spin ordering (iii) G-type antiferromagnetism; in-plane antiferromagnetic spin ordering and out-of-plane antiferromagnetic spin ordering. These different types of spin ordering of perovskite lattice is given schematictally in the figure 2.28.

The orbital ordering is a phenomenon where an orbital of a given degenerate shell is preferentially occupied and this preferential occupation leads to an ordered pattern. These preferential occupations usually results from the Jahn-Teller distortion, while the cooperativity between Jahn-Teller effects on the different atoms of the system results in the orbital ordering. Maezono et al. has studied the orbital ordering and spin ordering in undoped manganese oxides [63]. They obtained a theoretical phase diagram for spin/orbital ordering as a function of the antiferromagnetic interactions J_s between the t_{2g} electrons as illustrated in figure 2.29. For intermediate values of J_s, the system is A-type antiferromagnetic with G-type orbital ordered.

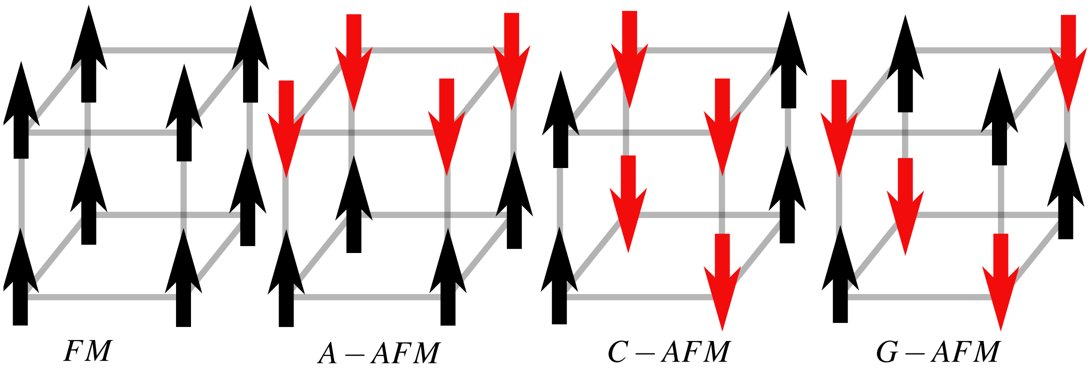

Fig. 2.28 Different type of spin arrangement of a lattice: Ferromagnetism (FM), A type antiferromagnetism ($A-AFM$), C type antiferromagnetism ($C-AFM$), G type antiferromagnetism ($G-AFM$)

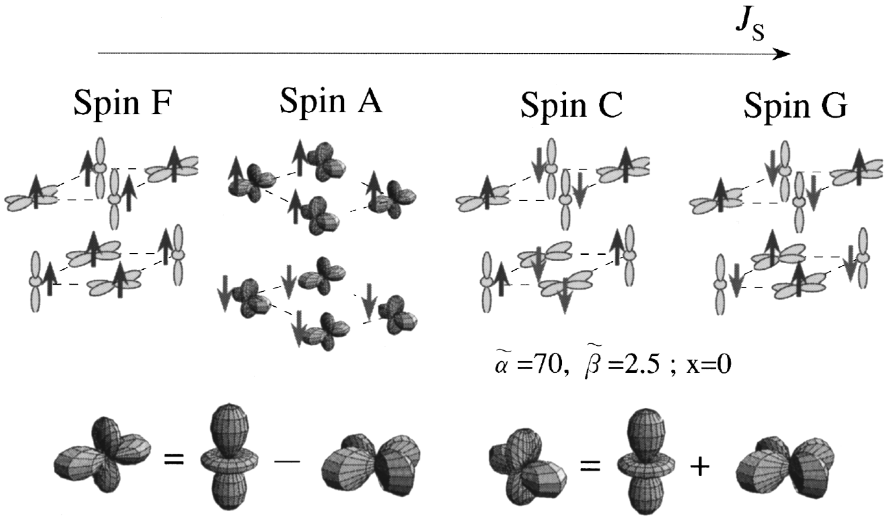

Fig. 2.29 Orbital structures of undoped manganites as a function of the J_s; antiferromagnetic interaction between core t_{2g} electrons. (Picture taken from reference [63])

Charge ordering in mixed-manganites is a periodic arrangement of the charges on the lattice and is only favoured for certain electron hole ratios, making it doping dependent. In particular, when the doping x is close to $x = 1/2$, the charge-ordering instability comes to the surface. Charge ordering is driven by Coulomb repulsion between nearest-neighbours atoms. In a charge ordered system, the electrical resistivity increases as the hopping of electrons is hindered. Chen and Cheong reported the first clear evidence of a charge ordering in $La_{0.5}Ca_{0.5}MnO_3$ [64]. In the case of $Nd_{1-x}Sr_xMnO_3$ given in figure 2.4, the ferromagnetic metallic (FM) phase state changes into the charge-ordered insulating (COI) below 160 K for $x = 1/2$. In figure 2.30, Tokura *et al.* [65] gave the spin, charge and orbital ordering patterns of the half-doped charge-exchange (CE) antiferromagnetic type manganites. One can see the equal distribution of Mn^{3+} and Mn^{4+} ions on the (001) plane of the orthorhombic lattice (*Pbnm* space group). At the same time, the e_g orbitals are also ordered in 1×2 superlattice on the same plane.

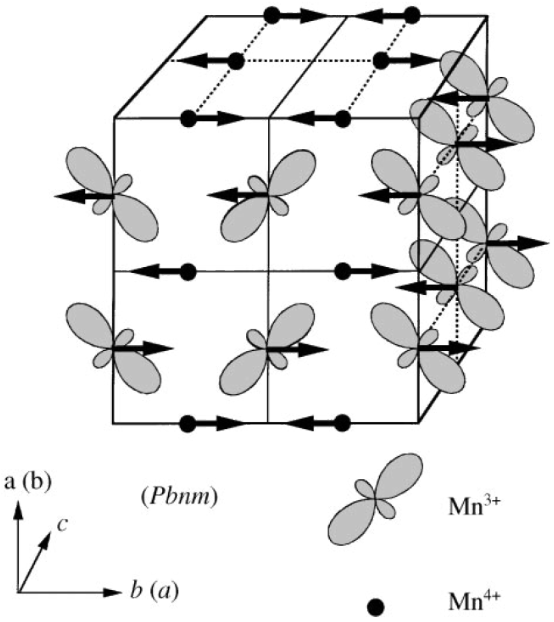

Fig. 2.30 Spin, charge, and orbital orderings of the CE AFM type observed for most of the $x = 1/2$ manganites. The e_g-orbital ordering is on Mn^{3+}. The Mn^{4+} sites are the closed circles. (Picture taken from reference [65])

2.3 Properties of Bulk LAMO vs LAMO Thin films

Until now, we have given the basic structural, electronic and magnetic properties of manganites. It is worth to mention once more that one can control and modify these properties by the deposition of the manganites in very thin films or in heterostructures. Thus, it is important to address some critical changes that the compound present when it is layered as thin films compared to its bulk form.

Studies on the structural characterization of thin films by several researchers show that there are differences in crystal symmetry (lattice parameters, symmetry group etc.) between the thin film and the bulk material due to the substrate-induced constraints. Electron microscopy techniques show that the manganite thin films can have a crystal structure, which is imposed by the lattice mismatch with the substrate. This crystal structure is different from that of the bulk manganites or thick films of the manganites. Thus, in addition to the structure differences, one can expect also changes in magnetic and transport properties in these compounds when they are deposited as thin films compared to their bulk forms. Now, let us briefly call some of the publications from literature for comparing the properties of bulk $\mathrm{La_{1-x}A_xMnO_3}$ and $\mathrm{La_{1-x}A_xMnO_3}$ thin films ($\mathrm{A = Ba, Sr, Ca}$).

In the study of bulk $\mathrm{La_{2/3}Ba_{1/3}MnO_3}$ samples and $\mathrm{La_{2/3}Ba_{1/3}MnO_3}$ thin films, Helmolt *et al.* noted that there a sharp cusp in the resistivity as a function of temperature in the bulk samples whereas the thin films show a broadening of the magnetic transition [66, 27]. In figure 2.31, one can see the resistivity against the temperature for both bulk samples and thin films. As-deposited thin films show a broader magnetic transition and their magnetoresistance is weaker temperature-dependent below 250 K. However, the annealing heat treatment increases the Curie temperature and results with a sharper transition as one can see on the right bottom in figure 2.31. Comparing the bulk samples and the annealed thin films, the differences probably arise from chemical disorder and oxygen deficiency [27].

Bibes *et al.* studied fully strained epitaxial thin films of $\mathrm{La_{2/3}Ca_{1/3}MnO_3}$ on the $\mathrm{SrTiO_3}$ [67]. They reported the lattice parameters for different films of the t film thickness $6 < t < 180$ nm. The a lattice parameter of LCMO is close to a lattice parameter of $\mathrm{SrTiO_3}$ within experimental error showing that the film is under strain. Aarts *et al.* also reported similar values of the c lattice parameters for the thin films of $\mathrm{La_{0.7}Ca_{0.3}MnO_3}$ on the $\mathrm{SrTiO_3}$ [68]. One can see the variation of the a and c lattice parameters of the $\mathrm{La_{2/3}Ca_{1/3}MnO_3}$ thin films with respect to the film thickness on the left in figure 2.32. Zandbergen *et al.* reported that the thin films ($\sim$ 6 nm) of $\mathrm{La_{0.73}Ca_{0.27}MnO_3}$ on a $\mathrm{SrTiO_3}$

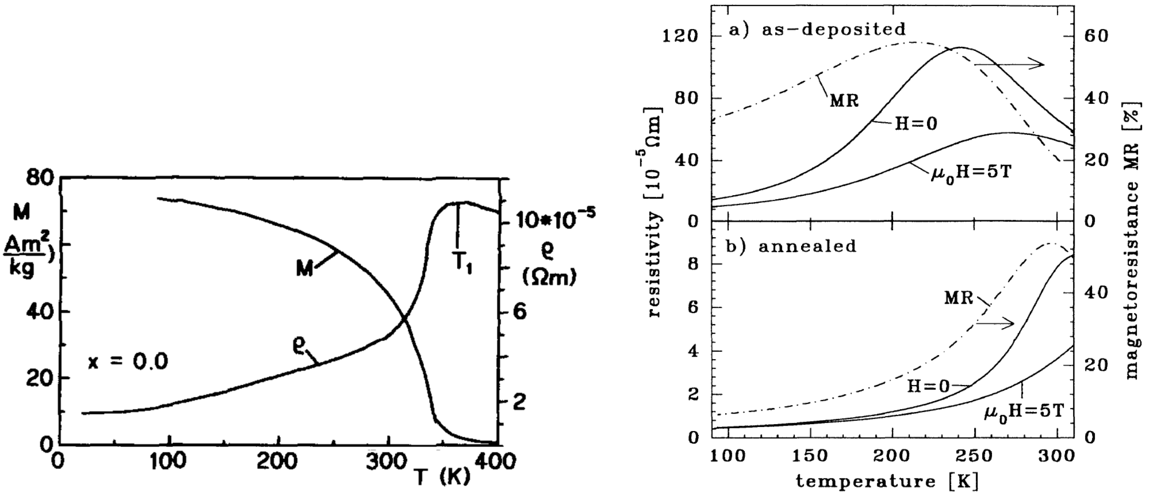

Fig. 2.31 The resistivity comparison of the bulk La$_{(2-x)/3}$Ba$_{(1+x)/3}$Mn$_{1-x}$Cu$_x$O$_3$ when $x = 0$ vs La$_{2/3}$Ba$_{1/3}$MnO$_3$ thin films. (Left) Picture adapted from the reference [66] and (right) picture taken from the reference [27]

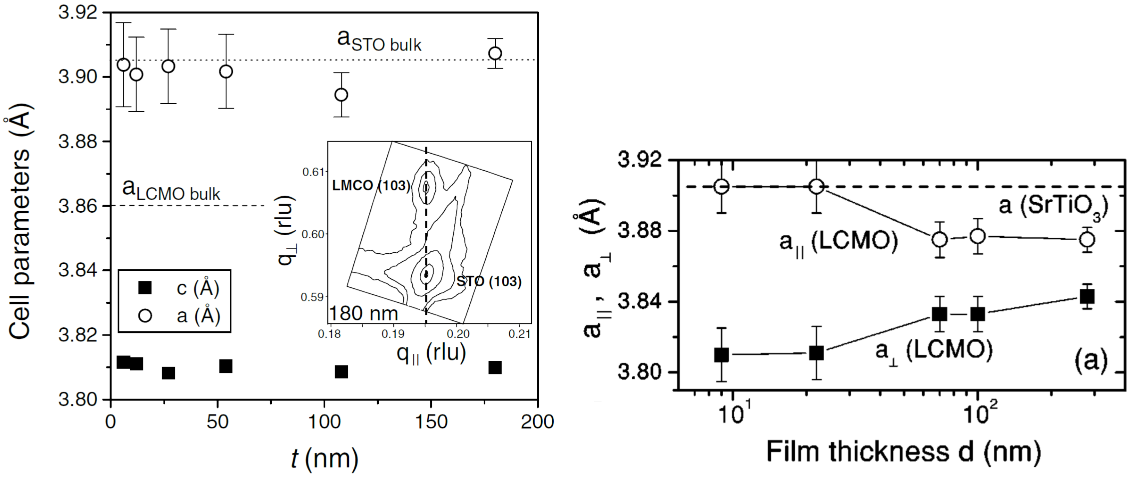

Fig. 2.32 (Left) The a and c parameters of the La$_{2/3}$Ca$_{1/3}$MnO$_3$ films on the SrTiO$_3$ vs t film thickness from the reference [67]. (Right) The in-plane ($a_{||}$) and out-of-plane ($a_{\perp}$) lattice parameter of the La$_{0.7}$Ca$_{0.3}$MnO$_3$ films on the SrTiO$_3$ vs d film thickness from the reference [69] ((Left) Picture taken from the reference [67] (Right) Picture adapted from the reference [69])

are ferromagnetically ordered-insulator around 150 K whereas the bulk or thicker films at this Ca doping exhibit an insulator-to-ferromagnetic metal transition [70]. Indeed, the film thickness plays a significant role in the properties of the thin films. When the film thickness is of the order of 100 nm, the films can behave bulk-like due to strain relaxation [69, 71]. One can see on the right in figure 2.32 that the in-plane lattice parameter of the films are not equal to the substrate in-plane lattice parameter when the thickness of the film increases. However, in very thin films (a few unit cell on a substrate), the physical properties can be quite different than the bulk or the thick films due to the induced in-plane epitaxial strain of the substrate [72, 73].

Magnetoresistance values in LCMO thin films are generally larger and occur at lower temperatures [28, 29, 68] than in the bulk samples [74]. It is also worth to remind again that the colossal magnetoresistance (CMR) of LCMO thin films: 127000% at 77 K, B = 6 T [28, 29].

It was also shown that by applying appropriate strains through substrate and alternated $BaTiO_3$ layers, the Curie temperature of both LSMO and LCMO ferromagnetic superlattices can be increased by more than an order of magnitude compared to the bulk [75]. In figure 2.33, one can see the magnetic measurements carried out in the temperature range 4-1000K. For

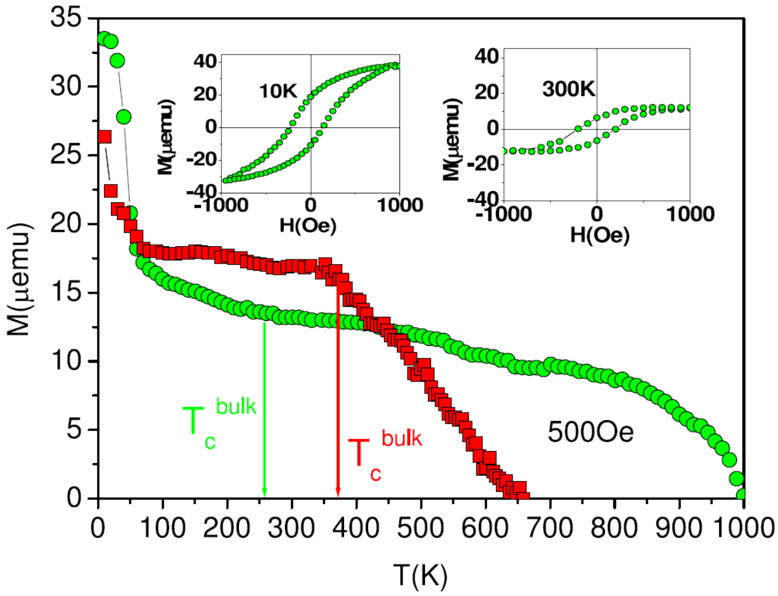

Fig. 2.33 Magnetization (500 Oerst- eds) for the $[(La_{2/3}Sr_{1/3}MnO_3)_3/(BaTiO_3)_3]_{25}$ (red squares) and $[(La_{2/3}Ca_{1/3}MnO_3)_4(BaTiO_3)_4]_{20}$ (green circles) superlattices. Hysteresis loops of the calcium superlattice, recorded at 10K and 300K, are presented in the inserts. The arrows mark the bulk Curie temperatures. (Picture taken from reference [75])

LCMO superlattices, the Curie temperature is measured about 1000 K whereas the Curie temperature of the LCMO bulk [76, 16] and thin films [29] is reported around 250-260 K. For LSMO superlattices, the Curie temperature is measured about 650 K whereas the Curie temperature of the LSMO bulk [77] or thin films [78] is about 370 K. This large increase of the Curie temperature is done through orbital ordering which is a result of the strains induced by the substate and alternated layers. In an ultrathin film environment, as the system will behave like a two-dimensional system, only in-plane magnetic interactions will determine the magnetic properties of the film. Thus, the Curie temperature of the ultrathin film can be maximized if one stabilizes in-plane magnetic orbital $d_{x^2-y^2}$ over out-of-plane d_{x^2} in the Mn^{3+} ions through Jahn-Teller distortion of the octahedra and maximizes the in-plane effective exchange of $d_{x^2-y^2}$ orbitals by preventing tilt of the MnO_6 [75]. On the other hand, at the interface of the manganite films and substrates it is observed that there is a strong supression of the magnetotransport properties due to the out-of-plane d_{x^2} orbital stabilization of the Mn^{3+} ions [72, 75, 79, 80]. This interfacial layer with supressed magnetic properties is named as “dead layer”.

The breakthrough of large increase in Curie temperature by strain and interface effects open new opportunities to control magnetic properties of the artificial heterostructures. During this thesis, we will focus on alternated manganite superlattices on a $SrTiO_3$ substrate and try to investigate the role of alternated layers in terms of the properties that they exhibit such as polarization of $BatiO_3$ and the role of antiferrodistortive motions of the manganite layers. We will also focus on the prevention of the formation of the dead layer by introducing manganite superlattices alternated with alkaline-earth oxides. As our study will be based on ab-initio calculation, we would like devote the next section to the technical background of density functional theory.

Chapter 3

Technical Details-Methods

Contents

3.1 Introduction

In this chapter we provide a brief overview of first-principles techniques used during this thesis. Ab-initio calculations for solids are based on the equations of quantum mechanics. In the first section of this chapter, we describe the quantum many-body problem and the Born-Oppenheimer approximation. In the second section, we present the basics of the Density Functional Theory. The exchange-correlation approximations are given in the third section. Basis sets to describe the wave functions are introduced in the fourth section. Finally, we give the computational details used in this thesis in the last section.

Let us first define some of the notations which will be used in this chapter:

- N is the total number of electrons,
- N_0 is the total number of nuclei,
- i is index of the i^{th} electron,
- I is index of the I^{th} the nucleus,
- $\vec{r}_i$ is the position vector of the i^{th} electron,
- $\vec{r}$ is the position vector of an electron,
- $\{\vec{r}\}$ is the ensemble of the position vectors of the electrons,
- $\vec{R}_I$ is the position vector of the I^{th} nucleus,
- $\vec{R}$ is the position vector of a nucleus,
- $\{\vec{R}\}$ is the ensemble of the position vectors of the nuclei,
- Z_I is the charge of the nucleus,
- M_I is the mass of the nucleus,
- m_{e} is the mass of an electron.
- σ is the spin.
- φ is the one-electron wave function
- Ψ, ψ, ϕ are the many-electron wave functions
- $\langle\hat{H}\rangle = \frac{\langle\psi|\hat{H}|\psi\rangle}{\langle\psi|\psi\rangle}$ is the expected value of the operator $\hat{H}$ in the wave function ψ.

3.2 Quantum Many-Body Problem

Quantum many-body problem is a general term for the investigation of the properties of microscopic physical systems that consist of large number of interacting particles. Quantum mechanics provides an accurate description for such systems.

3.2.1 Schrödinger Equation for many-body system

In quantum mechanics, the fundamental equation is the Schrödinger equation [81] which describes how the quantum state of a physical system evolves in time:

$$i\hbar\frac{d\Psi(\{\vec{r}\};\{\vec{R}\};t)}{dt} = \hat{\mathrm{H}}\Psi(\{\vec{r}\};\{\vec{R}\};t) \tag{3.1}$$

where i is the imaginary unit, $\hbar$ is the reduced Planck constant, Ψ is the wave or state function of the quantum system and $\hat{\mathrm{H}}$ is the Hamiltionian operator.

When the wave functions form stationary states one can describe these states by using the time-independent Schrödinger equation, that is;

$$\hat{\mathrm{H}}\Psi = \mathbf{E}\Psi \tag{3.2}$$

where $\mathbf{E}$ is the energy of the state Ψ. This equation is also called the energy eigenvalue equation and the wave function Ψ is the eigenfunction of $\hat{\mathrm{H}}$ corresponding to the eigenvalue $\mathbf{E}$.

3.2.2 Hamiltonian for a system of electrons and nuclei

The non-relativistic Hamiltonian for a system of N electrons and N_0 nuclei is given by the following equation:

$$\hat{\mathrm{H}} = -\frac{\hbar^2}{2m_\mathrm{e}}\sum_{i=1}^{N}\nabla_i^2 - \sum_{I=1}^{N_0}\frac{\hbar^2}{2M_I}\nabla_I^2 + \frac{e^2}{4\pi\varepsilon_0}\left[-\sum_{i=1}^{N}\sum_{I=1}^{N_0}\frac{Z_I}{|\vec{r}_i-\vec{R}_I|} + \frac{1}{2}\sum_{i\neq j}^{N}\frac{1}{|\vec{r}_i-\vec{r}_j|} + \frac{1}{2}\sum_{I\neq J}^{N_0}\frac{Z_I Z_J}{|\vec{R}_I-\vec{R}_J|}\right]. \tag{3.3}$$

Here, the first and second terms of the equation 3.3 correspond to the kinetic energy of the electrons and of the nuclei, respectively. The third term is the electron-nuclei Coulomb interaction. The fourth term is the electron-electron Coulomb interaction. Finally, the last term corresponds to the nuclei-nuclei interaction. By using simpler notations for each term we can rewrite the Hamiltonian in the following form:

$$\hat{\mathrm{H}}(\{\vec{R}\},\{\vec{r}\}) = \hat{T}_e(\{\vec{r}\}) + \hat{T}_N(\{\vec{R}\}) + \hat{V}_{eN}(\{\vec{R}\},\{\vec{r}\}) + \hat{V}_{ee}(\{\vec{r}\}) + \hat{V}_{NN}(\{\vec{R}\}) \tag{3.4}$$

where $\hat{T}_e$ and $\hat{T}_N$ are respectively kinetic energy operators for electrons and nuclei. $\hat{V}_{eN}$, $\hat{V}_{ee}$ and V_{NN} are the potential energy operators for electron-nuclei, electron-electron and nuclei-nuclei, respectively.

3.2.3 Born-Oppenheimer Approximation

Since the masses of nuclei are much larger than the mass of an electron, their velocity are rather small compared to electrons ones. One can thus predict the motion of the electrons to be immediate compared to the nuclei ones, and thus the nuclei to be at fixed positions when electrons move. Along this line, Max Born and Robert Oppenheimer assumed that one can separately treat the motion of atomic nuclei and electrons [82]. Within the Born-Oppenheimer approximation, the system wave function can be written as a simple product of an electron wave function ψ and a nuclei wave function ϕ:

$$\Psi(\{\vec{r}\};\{\vec{R}\}) = \psi(\{\vec{r}\})_{\{\vec{R}\}}\,\phi(\{\vec{R}\}).$$

At the same time, the non-relativistic Hamiltionian given in the equation 3.4 can be separated in a set of two independent equations describing the electronic movements and the nuclei ones;

$$\hat{H}_{el}(\{\vec{r}\})_{\{\vec{R}\}} = \hat{T}_e(\{\vec{r}\}) + \hat{V}_{eN}(\{\vec{r}\})_{\{\vec{R}\}} + \hat{V}_{ee}(\{\vec{r}\}) + V_{NN} \tag{3.5}$$

and

$$\hat{H}_{nucl}(\{\vec{R}\}) = \hat{T}_N(\{\vec{R}\}) + E(\{\vec{R}\}) \tag{3.6}$$

where $\hat{H}_{el}$ is electronic Hamiltonian and $\hat{H}_{nucl}$ is the nuclear one. Thus, the Schrödinger equation 3.2 splits into

$$\begin{aligned} \hat{H}_{el}\psi(\{\vec{r}\})_{\{\vec{R}\}} &= E(\{\vec{R}\})\,\psi(\{\vec{r}\})_{\{\vec{R}\}} \\ \hat{H}_{nucl}\phi(\{\vec{R}\}) &= \mathbf{E}\,\phi(\{\vec{R}\}). \end{aligned} \tag{3.7}$$

While $\hat{H}_{el}$ describes the electronic structure, $\hat{H}_{nucl}$ yields to the vibrational modes (phonons). In the electronic Hamiltonian, the electron-nuclei operator $\hat{V}_{eN}$ acts as a potential parametrized by the fixed nuclei positions. V_{NN} is a constant corresponding to nuclei-nuclei interactions. As far as the electron motion is concerned, it causes only a shift in the total energy. It can thus be neglected in solving the time-independent Schrödinger equation.

After solving the stationary time-independent electron Schrödinger equation for fixed nuclei positions, one can find the motion of the latter by solving the nuclei Schrödinger equation in which $E(\{\vec{R}\})$ is the electronic energy and acts as a potential for the nuclei equation. The eigenstates of the nuclear Hamiltonian around the equlibrium geometry will give access to the systems of vibrations (phonons) for a given electronic state. The equilibrium geometry is given by the minimization of the electronic energy with respect to the nuclei position. This procedure can be summarized schematically by

$$\min_{\{\vec{R}\}} \left[\min_{\psi} E[\{\vec{R}\}, \psi] \right] \tag{3.8}$$

where E is the ground-state the energy of the many-body system within the $\hat{H}_{el}\psi = E\psi$ eigenvalue problem. From now on, we will use the notation $\hat{H}$ to describe $\hat{H}_{el}$.

For the simplicity of the framework, we adopt the atomic units for the rest of this chapter. ($\hbar = m_\mathrm{e} = e = 4\pi/\varepsilon_0 = 1$)

3.3 Density Functional Theory: a way to solve the electronic structure

Density Functional Theory (DFT) is a computational method extensively used in quantum physics, quantum chemistry and material science. It was built by Hohenberg and Kohn [83] and Kohn and Sham [84] to treat the many-body electron-electron interactions. The basic idea of DFT rests in giving a special role to the one-body electronic density of the ground state of a quantum many-body system. Briefly, all ground state properties are to be considered to be unique functionals of the ground state density.

The one particle density, $n(\vec{r})$, is defined by N times of the measure of the probability for an electron to be present at any given point. The density is given by the expectation value of the the density operator $\hat{n}(\vec{r}) = \sum_{i=1}^{N} \sum_{\sigma_i} \delta(\vec{r} - \vec{r}_i)$. Here $\delta(\vec{r})$ is the Delta-Dirac function.

Thus, the one particle density is as follows:

$$n(\vec{r}) = \frac{\langle\psi|\hat{n}(\vec{r})|\psi\rangle}{\langle\psi|\psi\rangle} = N\frac{\sum_{\sigma_1}\cdots\sum_{\sigma_N}\int d\vec{r}_2\cdots\int d\vec{r}_N|\psi(\vec{r},\vec{r}_2,\vec{r}_3,\cdots,\vec{r}_N,\sigma_1,\sigma_2\cdots,\sigma_N)|^2}{\sum_{\sigma_1}\cdots\sum_{\sigma_N}\int d\vec{r}_1\int d\vec{r}_2\cdots\int d\vec{r}_N|\psi(\vec{r}_1,\vec{r}_2,\vec{r}_3,\cdots,\vec{r}_N\sigma_1\sigma_2\cdots\sigma_N)|^2}. \tag{3.9}$$

Taking the notation of $\hat{V}_{eN}$ as $\hat{V}_{\text{ext}}$ and naming it as external potential we express the external potential energy by means of an integral of density. The total energy for a state ψ is given by the expectation value of the Hamiltonian operator:

$$E = \frac{\langle\psi|\hat{H}|\psi\rangle}{\langle\psi|\psi\rangle} = \langle\hat{H}\rangle = \langle\hat{T}_e\rangle + \langle\hat{V}_{ee}\rangle + \int d\vec{r}V_{ext}(\vec{r})n(\vec{r}). \tag{3.10}$$

DFT consists of two fundamental theorems and the Kohn-Sham resolution principle. Let us take a clear look on these theorems first.

3.3.1 Hohenberg-Kohn Theorems

The idea of Hohenberg and Kohn is the basis of the formulation of the density functional theory as an exact theory of any many-body system of interacting particles in an external potential $\hat{V}_{\text{ext}}(\vec{r})$. The Hamiltonian is as follows,

$$\hat{H} = -\sum_{i=1}^{N}\nabla_i^2 + \sum_{i=1}^{N}\hat{V}_{\text{ext}}(\vec{r}_i) + \frac{1}{2}\sum_{i\neq j}^{N}\frac{1}{|\vec{r}_i - \vec{r}_j|}. \tag{3.11}$$

Theorem 1. *"For a given $\hat{V}_{ext}$ in an N electron system, only one ground state density $n_0(\vec{r})$ is associated to this potential. Moreover, if $n_0(\vec{r})$ is the ground state density of an N electron system, only one $\hat{V}_{ext}(\vec{r})$ can correspond to this density."*

Proof. The first part of the theorem is obvious. We will prove the second part by the method of proof of contradiction. First, we suppose that for an N electrons system there are two different external potentials, leading to the same ground state density $n_0(\vec{r})$, denoted $\hat{V}_{\text{ext}}^{(1)}(\vec{r})$ and $\hat{V}_{\text{ext}}^{(2)}(\vec{r})$ differing by more than a constant, i.e.

$$\hat{V}_{\text{ext}}^{(1)}(\vec{r}) \neq \hat{V}_{\text{ext}}^{(2)}(\vec{r}) + c$$

where c is a constant. Thus, there are two different hamiltonians, $\hat{H}^{(1)}$ and $\hat{H}^{(2)}$, which have two different ground state wave-functions, $|\psi^{(1)}\rangle$ and $|\psi^{(2)}\rangle$, which are assumed to have the same ground state density $n_0(\vec{r})$. Here we treat the case of non-degenarate ground states. Since $|\psi^{(2)}\rangle$ is not the ground state of $\hat{H}^{(1)}$, it follows that

$$E_0^{(1)} = \langle\psi^{(1)}|\hat{H}^{(1)}|\psi^{(1)}\rangle < \langle\psi^{(2)}|\hat{H}^{(1)}|\Psi^{(2)}\rangle \tag{3.12}$$

$$\begin{aligned} \Rightarrow \langle\psi^{(2)}|\hat{H}^{(1)}|\psi^{(2)}\rangle &= \langle\psi^{(2)}|\hat{H}^{(2)}|\psi^{(2)}\rangle + \langle\psi^{(2)}|\hat{H}^{(1)} - \hat{H}^{(2)}|\psi^{(2)}\rangle & (3.13)\\ &= E_0^{(2)} + \int d\vec{r}\Big[\hat{V}_{\text{ext}}^{(1)}(\vec{r}) - \hat{V}_{\text{ext}}^{(2)}(\vec{r})\Big]n_0(\vec{r}) & (3.14)\end{aligned}$$

$$\Rightarrow E_0^{(1)} < E_0^{(2)} + \int d\vec{r}\Big[\hat{V}_{\text{ext}}^{(1)}(\vec{r}) - \hat{V}_{\text{ext}}^{(2)}(\vec{r})\Big]n_0(\vec{r}) \tag{3.15}$$

Similarly, considering $|\psi^{(1)}\rangle$ is not the ground state of $\hat{H}^{(2)}$ gives us

$$E_0^{(2)} < E_0^{(1)} + \int d\vec{r}\Big[\hat{V}_{\text{ext}}^{(2)}(\vec{r}) - \hat{V}_{\text{ext}}^{(1)}(\vec{r})\Big]n_0(\vec{r}). \tag{3.16}$$

Summing the inequalities 3.15 and 3.16, we arrive at the contradictory inequality

$$E_0^{(1)} + E_0^{(2)} < E_0^{(1)} + E_0^{(2)}.$$

Therefore we simply show that there cannot be two different external potentials differing from each other by more than a constant leading to the same ground state density. Within this we have shown that $n_0(\vec{r}) \Rightarrow \hat{V}_{\text{ext}}$.

The reverse is more trivial. $\hat{V}_{\text{ext}}$ determines the Hamiltonian $\hat{H}$ for an N electrons system, which has one non-degenerate ground state wave-function ψ and accordingly one ground state density $n_0(\vec{r})$. □

Corollary 1. *Since the hamiltonian is fully determined by $\hat{V}_{ext}$ and N, except for a constant shift of the energy, it follows that the many-body wave-functions for all states (ground and excited) are determined by $n_0(\vec{r})$. Therefore, all properties of the system are completely determined given only the ground state density $n_0(\vec{r})$.*

Theorem 2. *"A universal functional for the ground state energy $E[n]$ can be defined in terms of the density. For any particular $\hat{V}_{ext}(\vec{r})$, the exact ground state energy of the system is the global minimum value of this functional, and the density $n(\vec{r})$ minimizing this functional is* *"the exact ground state density $n_0(\vec{r})$", provided with the fact that $n_0(\vec{r})$ is the density of an N electron system (N representability)."*

Proof. Since the density determines the external potential uniquely and the potential determines the ground state wave function uniquely, all the other observables of the system are also uniquely determined and can be described as functionals of $n(\vec{r})$. That means for instance that the total energy functional can be expressed as follows:

$$\begin{aligned} E_{\mathrm{HK}}[n] &= T[n] + E_{ee}[n] + \int d\vec{r}\,\hat{V}_{\mathrm{ext}}(\vec{r})\,n(\vec{r}) && (3.17) \\ &= F_{\mathrm{HK}}[n] + \int d\vec{r}\,\hat{V}_{\mathrm{ext}}(\vec{r})\,n(\vec{r}) && (3.18) \end{aligned}$$

where F_{HK} is the sum of the kinetic energy and electron-electron Coulomb energy. Since the form of these energies are the same for all systems F_{HK} is thus a universal functional of the density $n(\vec{r})$ and independent of the system.

Now let us take a system with the ground state density $n_0^{(1)}(\vec{r})$ corresponding to the external potential $\hat{V}_{\mathrm{ext}}^{(1)}(\vec{r})$. $E_{\mathrm{HK}}[n]$ can be formulated as the expectation value of the Hamiltonian in the ground state wavefunction $|\psi^{(1)}\rangle$

$$E_0^{(1)} = E_{\mathrm{HK}}[n_0^{(1)}] = \langle\psi^{(1)}|\hat{H}^{(1)}|\psi^{(1)}\rangle. \tag{3.19}$$

We consider another density $n^{(2)}(\vec{r})$ which corresponds to another wavefunction $|\psi^{(2)}\rangle$. So we can easily conclude that the energy $E^{(2)}$ of the wavefunction $|\psi^{(2)}\rangle$ with respect to the hamiltonian $\hat{H}^{(1)}$ is greater than $E_0^{(1)}$ by the following expression

$$E_0^{(1)} = \langle\psi^{(1)}|\hat{H}^{(1)}|\psi^{(1)}\rangle < \langle\psi^{(2)}|\hat{H}^{(1)}|\psi^{(2)}\rangle = E^{(2)}. \tag{3.20}$$

So, the energy given in the equations 3.17 evaluated for the ground state density $n_0(\vec{r})$ is lower than any energy for any other density $n(\vec{r})$. This proves the theorem. □

Corollary 2. *The functional $E[n]$ is sufficient to determine the exact ground state energy and density.*

In fact if we knew the functional $F_{\mathrm{HK}}[n]$ we could find the exact ground state density and energy by minimizing the total energy of the system. However, F_{HK} is unknown which leads us to use approximations. We will use the Kohn-Sham approximation to overcome this problem.

3.3.2 Kohn-Sham Ansatz

The basic principle of the Kohn and Sham ansatz lies down in replacing the many-body system by an auxiliary independent particle system, to find the ground state properties of the many-body system. Indeed, it is much easier to solve a non-interacting independent particle problem compared to an interacting many-body problem.

Kohn-Sham assumed that the exact ground state density of an interacting system can be written as the ground state density of a fictitious system of non-interacting particles. This assumption gives us the independent particle equations that can be solved numerically.

The Kohn-Sham ansatz consists of two main assumptions:

- By "non-interacting V-representability" we can represent the exact ground state density as the ground state density of an auxiliary system of non-interacting particles.
- We choose the Hamiltonian of the non-interacting system in a way to have the usual kinetic energy operator and an effective local potential $\hat{V}_{\text{eff}}(\vec{r})$ acting on an electron at point $\vec{r}$.

Let us define this auxiliary independent particle system. First, the Hamiltonian of this system is given by the following:

$$\hat{H}_{\text{aux}^\sigma} = -\frac{1}{2}\nabla^2 + \hat{V}^{\sigma}_{\text{eff}}(\vec{r}). \tag{3.21}$$

In a non-interacting independent electron system where $N = N^\uparrow + N^\downarrow$, the ground state ψ_0 has one electron in each of the N^σ orbitals φ_i^σ with the lowest eigenenergy ε_i^σ of Hamiltonian given in equation 3.21. The density of the such an auxiliary independent particle system is given by

$$n(\vec{r}) = \sum_\sigma n(\vec{r},\sigma) = \sum_\sigma \sum_{i=1}^{N^\sigma} |\varphi_i^\sigma(\vec{r})|^2, \tag{3.22}$$

The independent particle kinetic energy T_{KS} is

$$T_{\text{KS}} = \langle\psi|\hat{T}_{\text{KS}}|\psi\rangle = -\frac{1}{2}\sum_\sigma \sum_{i=1}^{N^\sigma} \langle\varphi_i^\sigma|\nabla^2|\varphi_i^\sigma\rangle \tag{3.23}$$

where ψ is now a non-interacting particle many-body wave function ($\psi = |\prod_i \varphi_i\rangle$). The Hartree energy, which is the classical Coulomb interaction energy of the electron density

$n(\vec{r})$ interacting with itself, is given as

$$E_{\text{Hartree}}[n] = \frac{1}{2}\int d\vec{r}d\vec{r}'\frac{n(\vec{r})n(\vec{r}')}{|\vec{r}-\vec{r}'|}. \tag{3.24}$$

We can formulate the total energy by rewriting E_{HK} the Hohenberg-Kohn expression given in 3.17 using the Kohn-Sham principle:

$$E_{\text{HK}} \simeq E_{\text{KS}} = T_{\text{KS}}[n] + \int d\vec{r}\hat{V}_{\text{ext}}(\vec{r})n(\vec{r}) + E_{\text{Hartree}}[n] + E_{\text{xc}}[n]. \tag{3.25}$$

E_{xc} is the exchange-correlation energy functional including Pauli Principle, correlated positions of electrons and the difference between the kinetic energy of the real system and the auxiliary Kohn-Sham one. It can be explicitly seen if we rewrite E_{xc} in terms of the Hohenberg-Kohn functional F_{HK}:

$$\begin{aligned} E_{\text{xc}}[n] &= F_{\text{HK}}[n] - (T_{\text{KS}}[n] + E_{\text{Hartree}}[n]) && (3.26)\\ &= T[n] - T_{\text{KS}}[n] + E_{\text{ee}}[n] - E_{\text{Hartree}}[n]. && (3.27)\end{aligned}$$

In fact, what is very remarkable about the exchange-correlation functional is that if we knew the exact value of E_{xc}, we could evaluate the exact ground state energy and density of the many-body system by simply solving Kohn-Sham equations for independent particles with this density.

Now it is time to introduce the Kohn-Sham variational equations and derive $\hat{H}_{\text{aux}} \simeq \hat{H}_{\text{KS}}$. We derive the variational functional over wavefunctions by Rayleigh-Ritz principle,

$$\forall i \quad , \quad \frac{\delta E_{\text{KS}}[n]}{\delta\varphi_i^*(\vec{r})} = \frac{\delta T_{\text{KS}}[n]}{\delta\varphi_i^*(\vec{r})} + \left[\frac{\delta E_{\text{ext}}[n]}{\delta n(\vec{r})} + \frac{\delta E_{\text{Hartree}}[n]}{\delta n(\vec{r})} + \frac{\delta E_{\text{xc}}[n]}{\delta n(\vec{r})}\right]\frac{\delta n(\vec{r})}{\delta\varphi_i^*(\vec{r})} \tag{3.28}$$

with the orthonormalized one electron wave functions (orbitals)

$$\langle\varphi_i|\varphi_j\rangle = \delta_{i,j}. \tag{3.29}$$

Now we have (for real orbitals)

$$\frac{\delta T_{\text{KS}}[n]}{\delta\varphi_i^*(\vec{r})} = -\frac{1}{2}\nabla^2\varphi_i(\vec{r}) \quad \text{and} \quad \frac{\delta n(\vec{r})}{\delta\varphi_i^*(\vec{r})} = \varphi_i(\vec{r}). \tag{3.30}$$

so we can construct the Kohn-Sham Schrödinger-like equations,

$$(\hat{H}_{\text{KS}} - \varepsilon_i)|\varphi_i(\vec{r})\rangle = 0, \tag{3.31}$$

where the $\hat{H}_{\text{KS}}$ is the mono-electronic effective Hamiltonian and ε_i are its eigenvalues. In Hartree atomic units,

$$\hat{H}_{\text{KS}} = -\frac{1}{2}\nabla^2 + \hat{v}_{\text{KS}}(\vec{r}), \tag{3.32}$$

with

$$\begin{aligned} \hat{v}_{\text{KS}}(\vec{r}) &= \frac{\delta E_{\text{ext}}[n]}{\delta n(\vec{r})} + \frac{\delta E_{\text{Hartree}}[n]}{\delta n(\vec{r})} + \frac{\delta E_{\text{xc}}[n]}{\delta n(\vec{r})} && (3.33) \\ &= \hat{v}_{\text{ext}}(\vec{r}) + \hat{v}_{\text{Hartree}}(\vec{r}) + \hat{v}_{\text{xc}}(\vec{r}). && (3.34) \end{aligned}$$

The Kohn-Sham Schrödinger-like equations equations 3.31 and 3.33 lead to the resulting density $n(\vec{r})$ and total energy E_{KS} given by 3.25. Here we must emphasize that these formulations are entirely independent of the approximation for the functional $E_{\text{xc}}[n]$.

Kohn-Sham ansatz allows us to replace the N interacting electrons Hamiltonian with an effective N non-interacting electrons Hamiltonians. Now the difficulty of the solution of an interacting system is only in the exchange-correlation functional. Thus, after we approximate this functional as accurately as possible, we can minimize the total energy of the many-body problem.

Since all the difficulty rests in the exchange-correlation functional it is vital to approximate this functional as accurately as possible. There have been different approaches to treat this functional over the years. Now we will give a brief introduction and description for the most common functionals such as local spin density approximation (LSDA) or generalized-gradient approximations (GGAs) and finally we will talk about hybrid functionals which are built using a combination of the exact exchange (from Hartree-Fock) and the effective exchange and correlation from LSDA and GGAs.

3.4 Exchange-Correlation Functionals

Using the Kohn-Sham ansatz the difficulty of the many-body problem is reduced to the approximation of the exchange-correlation functionals. The first, the simplest and the most widely used functional that we are about to explain is the local spin density approximation.

3.4.1 The local spin density approximation (LSDA)

The homogenous electron gas is the simplest model to represent the condensed matter. In this model, nuclei are replaced by a uniform positively charged background. In the homogeneous gas, all properties depend only on the electron and spin density. The LSDA approximation models the interacting systems using an energy functional extracted from the homogeneous electron gas. Indeed, the exchange-correlation energy is evaluated by an integral (over all space) on the exchange-correlation energy density at each point assumed to be the same as in a homogeneous electron gas.

$$\begin{aligned} E_{\mathrm{xc}}^{\mathrm{LSDA}}[n^{\uparrow},n^{\downarrow}] &= \int d^3r\, n(\vec{r})\varepsilon_{\mathrm{xc}}^{\mathrm{hom}}(n^{\uparrow}(\vec{r}),n^{\downarrow}(\vec{r})) && (3.35)\\ &= \int d^3r\, n(\vec{r})[\varepsilon_{\mathrm{x}}^{\mathrm{hom}}(n^{\uparrow}(\vec{r}),n^{\downarrow}(\vec{r}))+\varepsilon_{\mathrm{c}}^{\mathrm{hom}}(n^{\uparrow}(\vec{r}),n^{\downarrow}(\vec{r}))] && (3.36)\end{aligned}$$

where $n^{\uparrow}(\vec{r})$ and $n^{\downarrow}(\vec{r})$ stand for the density of the spin up and down electrons respectively. The expression of the exchange part of the homogeneous gas system is known;

$$\varepsilon_{\mathrm{x}}[n^{\uparrow},n^{\downarrow}] = -2^{1/3}\left(\frac{3}{4}\right)\left(\frac{3}{\pi}\right)^{1/3}\int d^3r\left[(n^{\uparrow})^{4/3}(\vec{r})+(n^{\downarrow})^{4/3}(\vec{r})\right] \tag{3.37}$$

whereas the correlation part is fitted on the curves obtained from Quantum Monte-Carlo calculations of the homogeneous electron gas electronic structure. Vosko *et al.* [85] and Perdew and Zunger [86] have introduced the most famous approaches for this functional.

The first disadvantage of LSDA lies down in the Hartree energy, which includes an electron-electron self interaction term that ought to be exactly cancelled by an exchange term. However, due to the local formulation of $\vec{v}_x$ in LSDA, this cancellation does not take place and a spurious self-interaction term remains. Even though the latter term is negligible for the homogeneous gas, it is large for the atoms. The second drawback is that band gaps are strongly underestimated. Many insulators such as CuO are found metallic within the LSDA scheme [87–89]. As a result, for metal/insulator interfaces, the Fermi Level of the metal is located in the conduction bands instead of the gap [56]. LSDA also underestimates the lattice constants, specifically for the ferroelectric materials [90]. Similarly, small deformations occurring in ferroelectric materials or Jahn-Teller systems are underestimated in LSDA.

3.4.2 Generalized-gradient approximations (GGAs)

The generalized-gradient approximations were introduced as an alternative for LSDA to improve the treatment of the non locality in quantum mechanics. Within this approach, the exchange and correlation functional not only depends on the density but also on the gradient of the density. So $E_{\mathrm{xc}}[n]$ is given as,

$$\begin{aligned} E_{\mathrm{xc}}^{\mathrm{GGA}}[n^{\uparrow},n^{\downarrow}] &= \int d^3r\, n(\vec{r})\, \varepsilon_{\mathrm{xc}}^{\mathrm{hom}}(n^{\uparrow}(\vec{r}),n^{\downarrow}(\vec{r}),|\nabla n^{\uparrow}|,|\nabla n^{\downarrow}|,\dots) && (3.38)\\ &= \int d^3r\, n(\vec{r})\, \varepsilon_{\mathrm{x}}^{\mathrm{hom}}(n) F_{\mathrm{xc}}(n^{\uparrow}(\vec{r}),n^{\downarrow}(\vec{r}),|\nabla n^{\uparrow}|,|\nabla n^{\downarrow}|,\dots) && (3.39) \end{aligned}$$

where F_{xc} is dimensionless and $\varepsilon_{\mathrm{x}}^{\mathrm{hom}}$ is the exchange energy of the unpolarized gas.

Though there are improvements in GGA compared to LSDA, GGA leads to some overestimations. Particularly, GGA-PBE proposed by Perdew, Burke and Ernzerhof [91] yields to supertetragonal structures for ferroelectric materials where LSDA has better results. As in LSDA, GGA functionals underestimate bandgaps. Due to this drawback, Wu and Cohen developed a recent GGA functional called GGA-WC [92] specifically designed for ferroelectric materials. GGA-WC tries to improve the estimations of the small deformations which are underestimated in LSDA.

3.4.3 Hybrid Functionals

The hybrid functionals are a set of approximations to the exchange-correlation energy functional in DFT that combines the exact exchange from the Hartree-Fock method with the exchange and correlation functional from LSDA or GGAs.

Since in terms of drawbacks LSDA and Hartree-Fock are the opposite of each other, (i.e. for instance band gaps are underestimated in LSDA whereas they are overestimated in

Hartree-Fock) this combination is expected to compensate failures of both approximations. Here, one should note that different hybrid functionals have been created by different mixing parameters.

Becke [93] proposed the simple half-half hybrid functional:

$$E_{\mathrm{xc}}^{\mathrm{hyb}} = \frac{1}{2}(E_{\mathrm{x}}^{0} + E_{\mathrm{xc}}^{\mathrm{LSDA}}) \tag{3.40}$$

where E_{x}^{0} is the exact exchange from Hartee-Fock method and $E_{\mathrm{xc}}^{\mathrm{LSDA}}$ is the LSDA exchange-correlation functional.

The most common hybrid functional B3LYP [94] is however, a much better mixing scheme. It was introduced by Becke [95] with mixing parameters fitted on large sets of experimental data ($A = 0.2$, $B = 0.9$ and $C = 0.81$),

$$E_{\mathrm{xc}}^{\mathrm{B3LYP}} = E_{\mathrm{x}}^{\mathrm{LSDA}} + A(E_{\mathrm{x}}^{0} - E_{\mathrm{x}}^{\mathrm{LSDA}}) + (1-A)B(E_{\mathrm{x}}^{\mathrm{GGA}} - E_{\mathrm{x}}^{\mathrm{LSDA}}) + E_{\mathrm{c}}^{\mathrm{LSDA}} + C(E_{\mathrm{x}}^{\mathrm{GGA}} - E_{\mathrm{c}}^{\mathrm{LSDA}}) \tag{3.41}$$

where the $E_{\mathrm{x}}^{\mathrm{LSDA}}$ and $E_{\mathrm{c}}^{\mathrm{LSDA}}$ are the exchange and correlation functionals within LSDA and $E_{\mathrm{x}}^{\mathrm{GGA}}$ and $E_{\mathrm{c}}^{\mathrm{GGA}}$ are respectively Becke's GGA exchange [96] and GGA correlation of Lee, Yan and Parr [97]. B3LYP is widely used for atomic and molecular calculations but its application to periodic systems are not always satisfactory. Indeed B3LYP estimates the lattice constants very well but it also overestimates the band gaps and slightly tetragonality. It does not reproduce the correct exchange-correlation energy for the free electron gas which is indeed a problem for metals [98].

B3PW, another hybrid functional, is composed of Becke's GGA exchange functional [96] with the GGA correlation functional of Perdew and Wang [99]. By setting the mixing parameters B and C to 1 in the equation 3.41, the B1 funcional of [100, 101] is given by:

$$E_{\mathrm{xc}}^{\mathrm{B1}} = E_{\mathrm{x}}^{\mathrm{GGA}} + A(E_{\mathrm{x}}^{0} - E_{\mathrm{x}}^{\mathrm{GGA}}) + E_{\mathrm{c}}^{\mathrm{GGA}}. \tag{3.42}$$

Becke suggested two different values 0.16 and 0.28 for A, depending on the choice of the GGA functional for the exchange $E_{\mathrm{x}}^{\mathrm{GGA}}$ and correlation $E_{\mathrm{c}}^{\mathrm{GGA}}$ [100].

B1WC, which we use during this thesis, is a combination of a B1 functional with the parameter A set to 0.16 and the Wu-Cohen GGA exchange-correlation functional [56]. It was specifically designed to properly treat both gaps and weak distortions. During this thesis, since we mainly studied metal/insulator interfaces, we thus needed to choose a functional that properly positions the metal Fermi level with respect to the insulator gap. In addition, a good treatment of the Jahn-Teller distortions present in the system is crucial in our calculations. Thus, the B1WC hybrid functional [56] was the best choice among all the possible functionals along these two criteria. On the other hand, it is known that B1WC underestimates the lattice constants about %1 compared to B3LYP functional and experiments. For example the lattice constant of $SrTiO_3$ (STO): $a_{\mathrm{STO}}^{\mathrm{B3LYP/exp}} = 3.905$ Å whereas $a_{\mathrm{STO}}^{\mathrm{B1WC}} = 3.88$ Å. However, since this underestimation is rather negligible we choose to work within B1WC as we want to define the band gaps and have the lattice distortions properly.

3.5 Basis Sets

After introducing the Born-Oppenheimer approximation, the DFT method and the exchange-correlation functionals, another step is left to solve the Kohn-Sham equations. Basis sets are needed to describe the wavefunctions, since Kohn-Sham equations are to be solved in a finite space.

In periodic systems, the quantum system is assumed to be represented by the repetition of a finite unit cell defined by unit vectors $\vec{a}_1, \vec{a}_2, \vec{a}_3$. The one-electron wave functions are expressed in the Bloch form as

$$\varphi_{n,\vec{k}}(\vec{r}) = \frac{1}{\sqrt{\Omega}} u_n(\vec{k},\vec{r}) e^{i\vec{k}\cdot\vec{r}}$$

where Ω is the volume of the unit cell and is equal to $\vec{a}_1 \cdot (\vec{a}_2 \times \vec{a}_3)$. Here, $u_n(\vec{k},\vec{r})$ is a lattice periodic function, $\vec{k}$ is a wave-vector of the reciprocal space and n is the energy band indice.

There are two main ways to construct a basis set to describe these functions: Plane-waves and Gaussian Orbitals.

3.5.1 Plane-Wave Basis Sets

In a plane-wave basis set, one rewrites the one-electron wave functions as

$$\varphi_{n,\vec{k}}(\vec{r}) = \frac{1}{\sqrt{\Omega}} \left(\sum_{\vec{G}} C_{n,\vec{k},\vec{G}} e^{i\vec{G}\cdot\vec{r}} \right) e^{i\vec{k}\cdot\vec{r}} \tag{3.43}$$

where $\vec{G}$ is a vector of reciprocal space. Since there is an infinite number of plane waves describing the Bloch functions in this Fourier expansion, one will approximate the equation 3.43 up to cut-off energy E_{cut}, that will reduce the plane wave expansion to a finite one:

$$\frac{\hbar^2}{2m}|\vec{k}+\vec{G}|^2 \leq E_{\text{cut}}.$$

The one-electron wave function will then be expressed in this finite plane wave basis set: $\{e^{i(\vec{k}+\vec{g})\cdot\vec{r}}, \frac{\hbar}{2m}|\vec{k}+\vec{G}|^2 \leq E_{\text{cut}}\}$.

3.5.2 Gaussian Orbitals

Linear combination of atomic orbitals (LCAO) is a method used to describe the orbitals (one-electron wave functions) of a system as a linear combination of local orbitals, centred on the different atoms:

$$\begin{aligned}\varphi_{n,\vec{k}}(\vec{r}) &= \sum_{\mu} a_{\mu,n}\phi_{\mu,\vec{k}}(\vec{r}) \\ \phi_{\mu,\vec{k}}(\vec{r}) &= \sum_{\vec{g}} \varphi_{\mu}(\vec{r}-\vec{A}_{\mu}-\vec{g})\, e^{i\vec{k}\cdot\vec{g}}\end{aligned} \tag{3.44}$$

where $\phi_{\mu,\vec{k}}(\vec{r})$ are Bloch functions defined in terms of local functions, i.e, local atomic orbitals $\varphi_{\mu}(\vec{r})$. Here, $\vec{g}$ is the real space Bravais lattice and $\sum_{\vec{g}}$ is extended to the set of all lattice vectors. $\vec{A}_{\mu}$ is the position of the nucleus in the zero reference cell ($\vec{g}=(0,0,0)$) on which φ_{μ} is centred.

The atomic orbitals of a given atom can be grouped into shells labelled by λ. All atomic orbitals with the same quantum numbers, s, n and l are grouped into the same shell. Thus, the atomic orbitals, φ_{μ} belonging to the same shell λ can be notated as φ_{λ}^{lm} and can be also expressed as linear combinations (normalized contractions) of normalized real solid harmonic Gaussian type functions $\gamma' = c\gamma$ where γ is the real solid harmonic Gaussian type function (primitive function) and c is the normalization coefficient:

$$\varphi_{\mu}(\vec{r}) = \varphi_{\lambda}^{\ell m}(\vec{r}) = N_{\lambda}\sum_{j} d_j^{\lambda} c_j^{\ell m}\gamma(\alpha_j^{\lambda};\vec{r}) = N_{\lambda}\sum_{j} d_j^{\lambda} c_j^{\ell m} X_{\ell}^{m}(\vec{r})G(\alpha_j^{\lambda};\vec{r}) \tag{3.45}$$

Here, j is the index running over the Gaussian type functions over the contraction where the d_j^{λ} is the contraction coefficient of the j-th primitive in the shell λ and N_{λ} is the normalization coefficient of atomic orbitals belonging to the shell λ. $G(\alpha_j;\vec{r}-\vec{A}_{\mu}-\vec{g})$ is the Gaussian function with the following formula;

$$G(\alpha_j;\vec{r}-\vec{A}_\mu-\vec{g}) = e^{-\alpha_j(\vec{r}-\vec{A}_\mu-\vec{g})^2}.$$

Finally, $X_l^m(\vec{r})$ is a real solid harmonic and is composed of the solid harmonic function Y_l^m as following:

$$X_\ell^{|m|}(\vec{r}) = \frac{Y_\ell^{|m|}(\vec{r})+Y_\ell^{-|m|}(\vec{r})}{2} \quad \text{and} \quad X_\ell^{-|m|}(\vec{r}) = \frac{Y_\ell^{|m|}(\vec{r})-Y_\ell^{-|m|}(\vec{r})}{2i}$$

with

$$Y_\ell^m(\vec{r}) = r^\ell P_\ell^{|m|}(\cos\Theta)e^{im\Phi}$$

where P_ℓ^m is the Legendre polynomial function characterized by the integers ℓ and m, such that $\ell \geq 0$ and $-\ell \leq m \leq \ell$.

3.6 Computational Details

All the results reported in this thesis are based on the theoretical techniques given in the previous sections. For the first-principle calculations we use the CRYSTAL code [57] which is an ab initio code based on density functional theory.

Since the compounds of our interest consist of metallic and insulating layers we choose to work with hybrid functionals in order to correctly localize the Fermi level of the metallic phase with respect to the insulator gap. The B1WC [102, 56] functional, is a good choice since it can describe accurately both the gaps amplitudes and the small structural distortions found in ferroelectric (as $BaTiO_3$) or Jahn-Teller systems (as $La_{2/3}Sr_{1/3}MnO_3$).

In all our calculations, we use effective core pseudopotentials (ECP) for the heavy atoms such as La and Sr atoms from reference [103, 104] and [105] respectively. The electrons in brackets are represented inside the pseudopotential in equations 3.46 and 3.47.

$$\text{La} : \left[1s^2 2s^2 2p^6 3s^2 3p^6 3d^{10}\right] 4s^2 4p^6 5s^2 4d^{10} 5p^6 6s^2 5d^1 \tag{3.46}$$

$$Sr : \left[1s^2 2s^2 2p^6 3s^2 3p^6 3d^{10}\right] 4s^2 4p^6 5s^2 \tag{3.47}$$

For the valence basis sets we use associated segmented basis set for La from reference [106]. For the valence basis set of Sr, we use Piskunov associated basis set [107] (3ζ quality).

Since Ba is a heavy atom, we used a small core effective pseudopotential. As in equations 3.46 and 3.47 the electrons treated in the core pseudopotential are in brackets.

$$\text{Ba} \;:\; \left[1s^2 2s^2 2p^6 3s^2 3p^6 4s^2 3d^{10} 4p^6 4d^{10}\right] 5s^2 5p^6 6s^2 \tag{3.48}$$

For Ba atom, we used the ECP from the reference [105]. Its associated basis set is found reference [107] and it is also of 3ζ quality.

For Pb, we used Hay-Wadt the large effective core pseudopotential [108].

$$\text{Pb} \;:\; \left[[\text{Xe}]4f^{14}5d^{10}\right] 6s^2 6p^2 \tag{3.49}$$

Its valence basis is set from reference [107]. The basis set is (3ζ).

All other atoms (Mn, Ti and O) are represented with an all-electron basis set. The basis set are of $2\zeta + P$ quality and can be found in references [109–112].

In all our calculations, we performed full geometry optimization under substrate imposed constrains; that is fixed in-plane lattice parameters (equal to the bulk $SrTiO_3$ substrate as found in a full geometry optimization under the same computational conditions: $a = b = a_{\text{STO}} = 3.88$ Å), and substrate in-plane symmetry operations ($P4mm$ space group) unless otherwise specified. Since a part of our study aims at investigating MnO_6 octahedra rotations we used a double unit cell ($\sqrt{2}a \times \sqrt{2}b$) in order to allow rotations. We introduced initial rotations manually by small atomic displacements and we let the structure to relax.

Another important point in our study is the La/Sr ionic disorder in $La_{2/3}Sr_{1/3}MnO_3$. In $LaMnO_3$, La has a formal charge of 3+, Mn a formal charge of 3+ and oxygen a 2− formal charge ($La^{3+}Mn^{3+}O_3^{2-}$). In $SrMnO_3$, Sr has a formal charge of 2+, Mn a formal charge of 4+ and oxygen again a 2− formal charge ($Sr^{2+}Mn^{4+}O_3^{2-}$). In order to treat the La/Sr ionic disorder we make full sets of calculations with all possible atomic orders. As fully La/Sr ordered systems can be expected to induce artefactual electronic localization effects we also defined average effective nuclear charges for La and Sr and redid all the calculations with these effective charges. We modelled the average effective nuclear charges for La and

Sr by using La^{3+} and Sr^{2+} in the correct proportions (In $La_{2/3}Sr_{1/3}MnO_3$, there is a mixed valence state for Mn $(La^{3+}_{2/3}Sr^{2+}_{1/3}Mn^{x}O^{2-}_{3}$. One can easily find that $x = 10/3$. By using this, one can find $La^{(3+\varepsilon_1)+}Mn^{10/3+}O^{2-}_{3}$ and $Sr^{(2+\varepsilon_2)+}Mn^{10/3+}O^{2-}_{3}$). Thus, the average nuclear charge is $29+\varepsilon_1$ for La and it is $10+\varepsilon_2$ for Sr since we used ECPs for La (29 electrons) and Sr (10 electrons). In addition, we also performed calculations using only La or Sr ECPs with average effective charges. Only the results seen in all the different calculations are presented, otherwise specified.

3.7 Parameters for the Results

In this section, we would like to define the parameters that we will use when presenting the results on the studied systems.

After the geometry optimization, we obtain the lattice parameters (a, b, c) in Å, Cartesian coordinates (x,y,z) in Å and the fractional $(\tilde{x},\tilde{y},\tilde{z}) = (x/a, y/b, z/c)$ of the system. In order to present the structural properties of the optimized geometry, we summarize our results with the help of following parameters.

Average Plane:

We calculate the average plane between cations and anions of each atomic plane by the following formula:

$$\tilde{z}_{\text{average plane}} = \frac{\tilde{z}_{\text{cation}} + \tilde{z}_{\text{anion}}}{2}$$

where $\tilde{z}_{\text{cation}}$ and $\tilde{z}_{\text{anion}}$ are the positions of the cation and anion in the $\vec{c}$ direction in fractional units for the same atomic plane.

Interplane distance:

Interplane distance is given by the difference of two consecutive z values of average planes; $\tilde{z}^{i+1}_{\text{average plane}} - \tilde{z}^{i}_{\text{average plane}}$. With this form, it is in the fractional units. In order to present it in Å, we multiply with the c lattice parameter of the system;

$$\text{interplane distance}_i = (\tilde{z}^{i+1}_{\text{average plane}} - \tilde{z}^{i}_{\text{average plane}}) \times c = z^{i+1}_{\text{average plane}} - z^{i}_{\text{average plane}}.$$

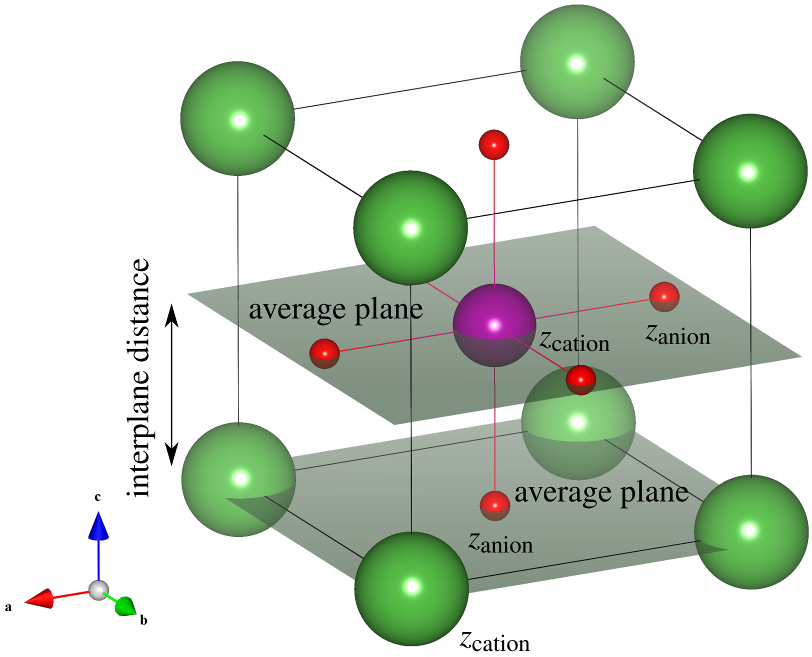

Fig. 3.1 Schematical representation of average plane and interplane distance for a ideal cubic perovskite $LaMnO_3$. La atoms are in the corners of the unit cell and presented as green. Mn atom is in the center of the unit cell and presented as purple. Oxygen atoms are at the face centres and presented as red.

One can see the representation of the average planes and interplane distance of a cubic perovskite $LaMnO_3$ in 4.3. In the figure, the bottom grey plane is the average plane of LaO and the top grey plane is the average plane of MnO_2. The interplane distance is the distance between these two average planes. As this system is an ideal cubic perovskite, the cations and anions of each plane has the same z-coordinate value; thus sit on the exact same plane: the average plane. However, in the case of lower symmetry systems (such as tetragonal symmetry), the z-coordinate of the cation and the anion of the same plane can differ, thus the average plane and interplane distance can give us clues about dimerization.

Rumpling:

The rumpling gives us the amplitude of the cationic/anionic displacement. It provides an estimation of the dipole moment, thus an estimation of the polarization in the system, since the average positions correspond to a non polar structure. The rumpling is calculated as;

$$\text{rumpling} = (\tilde{z}_{\text{cation}} - \tilde{z}_{\text{average plane}}) \times c = z_{\text{cation}} - z_{\text{average plane}}.$$

Mn-O distance ($\mathbf{d}_{\mathrm{Mn-O}}$):

We calculate the corresponding $\mathrm{Mn-O}$ distance in the $\vec{c}$ direction by following;

$$d_{\mathrm{Mn-O}} = (\tilde{z}_{\mathrm{Mn}} - \tilde{z}_{\mathrm{O}_1}) \times c \quad \text{or} \quad d_{\mathrm{Mn-O}} = (\tilde{z}_{\mathrm{O}_2} - \tilde{z}_{\mathrm{Mn}}) \times c$$

where Mn is manganese and O_1 and O_2 are the oxygen atoms as demonstrated in the figure 3.2.

Octahedron Thickness ($\mathbf{d}_{\mathrm{OO}}$):

We calculate the octahedron thickness of a unit cell ($\mathrm{O-Mn-O}$ distance in the $\vec{c}$ direction) by following;

$$d_{\mathrm{OO}} = (\tilde{z}_{\mathrm{O}_2} - \tilde{z}_{\mathrm{O}_1}) \times c$$

where O_1 and O_2 are the oxygen atoms as shown in the figure 3.2.

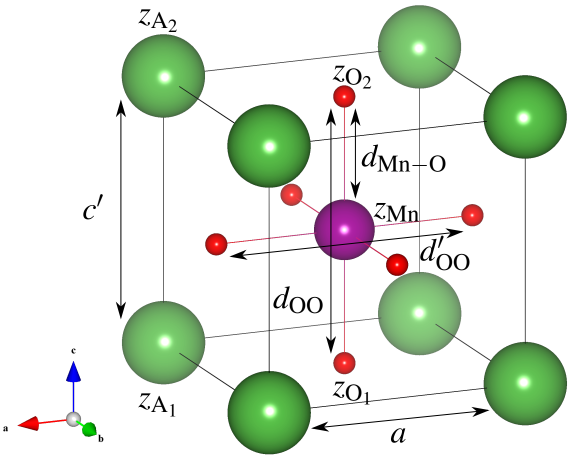

Fig. 3.2 Schematical representation of octahedron thickness and layer thickness for an ideal cubic perovskite $\mathrm{LaMnO_3}$.

Jahn-Teller distortion (JTd):

By using the octahedron thickness we can calculate the Jahn-Teller distortion (JTd) of the unit cell by

$$\mathrm{JTd} = d_{\mathrm{OO}}/a - 1$$

where a is the in-plane lattice parameter. When the Mn is in a regular octahedron environment $\mathrm{JTd} = 0$. Here, $d'_{\mathrm{OO}} = a$ in all calculations.

Layer Thickness (c′)

We also calculate the layer/unit cell thickness (cation-cation distance in the $\vec{c}$ direction) by following;

$$c' = (\tilde{z}_{A_2} - \tilde{z}_{A_1}) \times c$$

where A_1 and A_2 are the cations as displayed in the figure 3.2.

Tetragonality:

By using the layer thickness we can calculate the tetragonality of the unit cell by $c'/a - 1$ where a is the in-plane lattice parameter.

AFD motions:

In order to study of antiferrodistortive motions (AFD motions) of oxygens of the MnO_2 layer, one needs to double the unit cell in the $(\vec{a}, \vec{b})$ plane. Thus, the new cell parameters are as follows;

$$\vec{a'} = \vec{a} - \vec{b}, \quad \vec{b'} = \vec{a} + \vec{b}, \quad \vec{c}.$$

where $\vec{a}, \vec{b}, \vec{c}$ are the original unit cell parameters. The new unit cell is drawn within purple square in figure 3.3. We displace oxygen atoms of MnO_2 planes along $\vec{a}$ and $\vec{b}$ in the initial guess to give a push to the geometry optimization. After the geometry optimization, we check whether these atomic displacements are suppressed and the oxygen atoms come back to their symmetric positions or not. We can calculate the final optimized oxygen displacements by the following;

$$\mathrm{disp} = \sqrt{(\tilde{x} - \tilde{x}_0)^2 + (\tilde{y} - \tilde{y}_0)^2}$$

where $\tilde{x}_0$ and $\tilde{y}_0$ are the fractional in-plane coordinates of non-rotating oxygens atoms (O) and $\tilde{x}$ and $\tilde{y}$ are the fractional in-plane coordinates of rotating oxygens atoms (O′) of MnO_2. Finally, the angle of the rotation can be given by $\vartheta = \arctan \frac{\mathrm{disp}}{\mathrm{dist}_{\mathrm{Mn-O}}}$ where $\mathrm{dist}_{\mathrm{Mn-O}}$ is the in-plane distance between Mn and O in non-rotating octahedron.

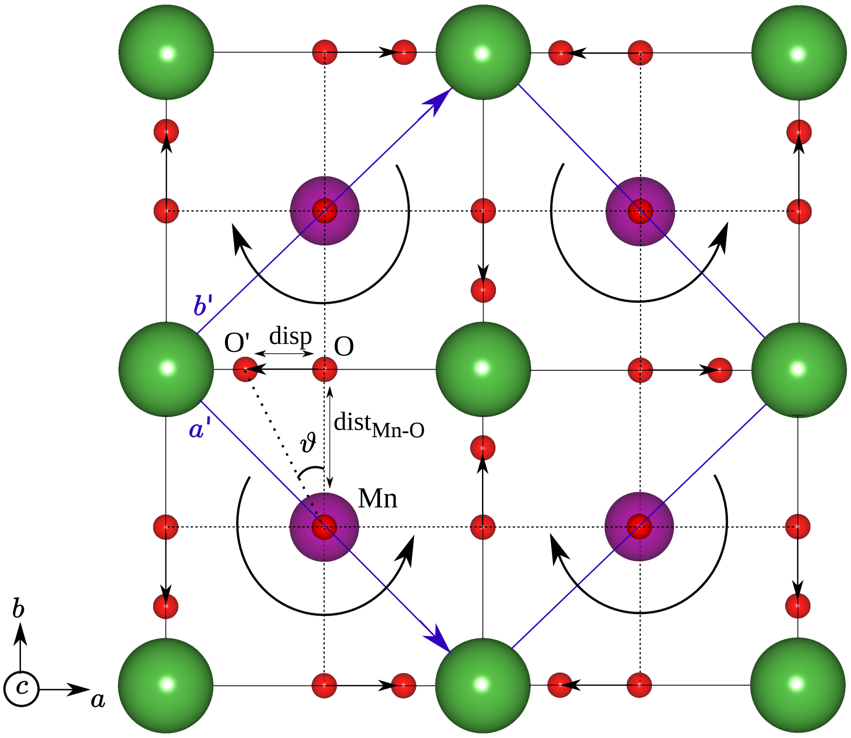

Fig. 3.3 Schematical representation of AFD motions of the oxygen atoms, as well as the octahedron, in the new unit cell $(\vec{a}', \vec{b}', c)$. The rotations are brought by the atomic displacement in the $(\vec{a}', \vec{b}')$ plane. The displacements are exaggerated for reading purposes. ϑ gives the angle of the rotation of octahedron.

Magnetic Moment:

We report the magnetic moment of each Mn in MnO_2 plane by extracting it from the Mulliken population analysis of $\alpha - \beta$ electrons.

Charge of a Plane:

We report the charge of each plane in the system studied by extracting it from the Mulliken population analysis of $\alpha + \beta$ electrons; for example for MnO_2,

$$\text{charge} = (Z_{\text{Mn}} - \tilde{Z}_{\text{Mn}}) + 2 \times (Z_{\text{O}} - \tilde{Z}_{\text{O}}) = (25 - \tilde{Z}_{\text{Mn}}) + 2 \times (8 - \tilde{Z}_{\text{O}})$$

where $\tilde{Z}_{\text{Mn}}$ and $\tilde{Z}_{\text{O}}$ are the computed number of $\alpha + \beta$ electrons of Mn and O and Z_{Mn} and Z_{O} are the atomic numbers of Mn and O.

The e_g Orbital Occupancy Ratio:

We report the e_g orbital occupancy ratio for each Mn atom ;

$$\eta_{e_g} = \eta_{x^2-y^2} / \eta_{z^2}$$

where $\eta_{x^2-y^2}$ is the occupancy of the orbital d_{x^2-y2} and η_{z^2} is the occupation number of the orbital d_{z^2}. The occupancies of the orbitals are generally obtained by the Mulliken population analysis of $\alpha - \beta$ electrons. In the case of the systems with AFD motions, in order to disentangle $t_{2g} - e_g$ mixing induced by the octahedron rotations, we need to take the x and y axes as the Mn local axes corresponding to the in-plane $\text{Mn} - \text{O}$ directions. Thus, in these cases, we calculate the density matrix of the d orbitals and extract real occupation numbers of the t_{2g} and e_g orbitals with the consideration of the in-plane rotations.

Total e_g Occupancy:

We also report the total e_g orbital occupancy for each Mn atom per octahedron as defined;

$$\text{tot}_{e_g} = \eta_{x^2-y^2} + \eta_{z^2}.$$

Delocalization of $3d_{z^2}$ on Ti:

We give the delocalization of the $3d_{z^2}$ electrons between $\mathrm{Mn}-\mathrm{Ti}$ at the interfaces. We extract this information by the Mulliken population analysis of $\alpha-\beta$ electrons of the $3d$-shell of Ti atoms at the interfaces. Indeed, in such a way we can measure the leak of the magnetic electrons on the Ti ions.

Polarization:

We also report the polarization of the systems in which we alternate manganite layers with buffer insulators such as $\mathrm{BaTiO_3}$ and $\mathrm{PbTiO_3}$. We calculate the polarization of the materials by using the following formula:

$$\vec{P} = \frac{|e|}{V} \sum Z_{\mathrm{ion}} \vec{r_{\mathrm{ion}}}$$

where V is the unit cell volume, Z^{ν}_{ion} are the Born-effective charges of each atom that we take from the Ref. [56] and $\vec{r^{\nu}}$ is the atomic displacement vector of the atom ν. For the latter, we take a hypothetical reference state with mirror symmetry planes ensuring there is no polarization in the system and we calculate the atomic displacement by subtracting atomic position from the reference positions.

Chapter 4

LMO-SMO Superlattices

Contents

4.1 Introduction

The aim of this chapter is to study the magnetic ground state of $\mathrm{LaMnO_3} - \mathrm{SrMnO_3}$ (LMO-SMO) superlattices by means of first-principle calculations. We will study the effect of strain by comparing different magnetic orderings for different thicknesses of ordered LMO-SMO superlattices. In first section we will report the study of $[(\mathrm{LaMnO_3})_1 - (\mathrm{SrMnO_3})_1]_1$. In the second section, we will increase the number of layers from 2 to 4 and report the study of $[(\mathrm{LaMnO_3})_1 - (\mathrm{SrMnO_3})_1]_2$ superlattice. Third section, we will study again a 4-layers system but with different cation ordering: $[(\mathrm{LaMnO_3})_2 - (\mathrm{SrMnO_3})_2]_1$. Fourth section will be dedicated to a 3-layers system; $[(\mathrm{LaMnO_3})_2 - (\mathrm{SrMnO_3})_1]_1$ and in the fifth section we will increase the number of layers from 3 to 6 layers; that is $[(\mathrm{LaMnO_3})_2 - (\mathrm{SrMnO_3})_1]_2$.

First, we have considered cubic perovskite structures of $\mathrm{LaMnO_3}$ and $\mathrm{SrMnO_3}$ and construct a tetragonal superlattice of them. The aim was to study the electronic and magnetic properties of this superlattice. The effect of epitaxial strain, which arises because of the lattice mismatch of the substrate and $\mathrm{LaMnO_3}$-$\mathrm{SrMnO_3}$ superlattice can be understood by the tetragonal distortion of the superlattice. This tetragonal distortion is evaluated by c/a ratio where c and a are the out-of-plane lattice and in-plane lattice parameters, respectively. The c/a ratio is determined by the linear relation $c - a_0 = -4\nu\,(a - a_0)$ [113], where a_0 is the hypothetical lattice constant of the superlattice under a strain-free condition. Here, ν is a Poisson ratio and it is around 0.3 for perovskite manganites [114]. Experimentally, a_0 value is the weighed average of the lattice constant of bulk $\mathrm{LaMnO_3}$ (3.936 Å) and bulk $\mathrm{SrMnO_3}$ (3.806 Å) [113, 115]. Thus, for example, a_0 of $[(\mathrm{LaMnO_3})_1 - (\mathrm{SrMnO_3})_1]_1$ superlattice is calculated as $\frac{1}{2}(3.936 + 3.806) = 3.871$ Å.

Previously, Nanda and Sathpathy[115] studied the effect of strain on the orbital ordering and magnetic structure of these superlattices by applying different c/a ratio and running total energy calculations. They interpreted their results in terms of a three-site Mn–O–Mn model.

According to their model, the orbital character of e_g electrons is determined by the strain. When the superlattice is under tensile strain ($c/a < 1$), the magnetic structure is A-type antiferromagnetic with preferential $d_{x^2-y^2}$ orbital occupancy. When there is lattice-matched structure, i.e. no strain ($c/a = 1$), the magnetic structure is ferromagnetic with equivalent e_g orbital occupancies. When the strain is compressive ($c/a < 1$), the magnetic structure is C-type antiferromagnetic with preferential d_{z^2} occupancy.

4.2 $[(\mathbf{LaMnO_3})_1 - (\mathbf{SrMnO_3})_1]_1$ Superlattice

First we start with the simplest case: $[(\mathrm{LaMnO_3})_1 - (\mathrm{SrMnO_3})_1]_1$. In figure 4.1 one can see the schematic representation of $[(\mathrm{LaMnO_3})_1 - (\mathrm{SrMnO_3})_1]_1$. Our first consideration was to study this superlattice deposited on $\mathrm{SrTiO_3}$ substrate. The substrate will impose its in-plane lattice parameter to the superlattice. The experimental a lattice parameter of $\mathrm{SrTiO_3}$ (STO) is found to be 3.905 Å. The optimized lattice parameter, however, is found to be 3.88 Å. During this study we tried both values for lattice parameters in our calculations in order to compare the results. We also studied strain-free environment for this superlattice in which the in-plane lattice parameters are free to relax. Thus, we were able to obtain hypothetical lattice parameters for the $\mathrm{LaMnO_3} - \mathrm{SrMnO_3}$ superlattice.

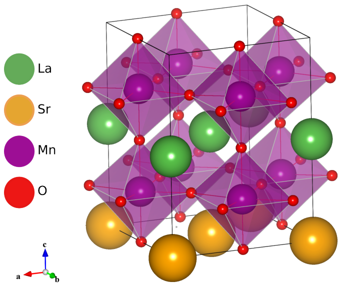

Fig. 4.1 Schematic picture for LMO-SMO superlattice

In figure 4.2 we report the energy difference of each magnetic configuration with the lowest state with respect to either optimized a lattice parameter or imposed a lattice parameter. The lowest energy is obtained for ferromagnetic ordering in the strain-free case. The C-type and G-type antiferromagnetic orderings are quite high in energy whereas ferromagnetic and A-type antiferromagnetic structures are close in energy in both $a = 3.88$ Å and $a = 3.905$ Å. Strain-free calculations show that ferromagnetic ordering desires contraction in-plane.

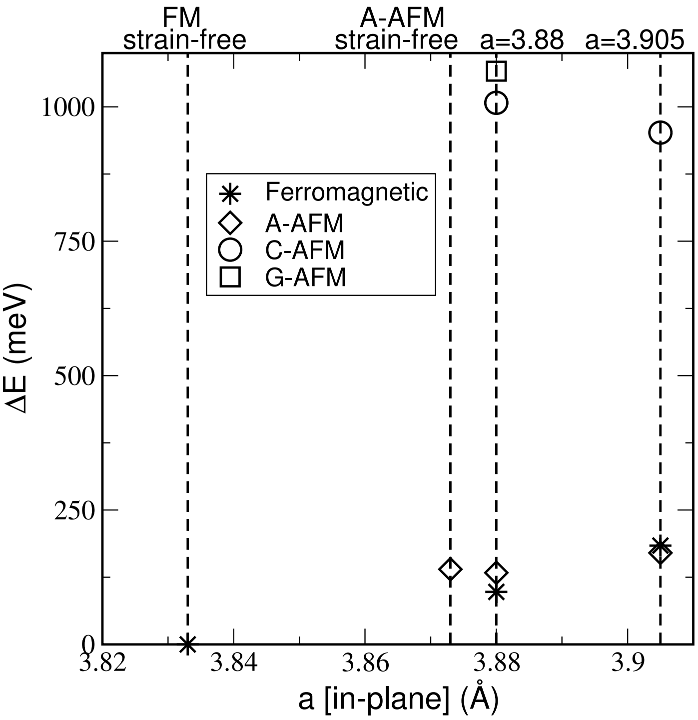

Fig. 4.2 Energy difference of each configuration with respect to the lowest energy ordering and geometry ($\Delta E = E - E_0$) vs. the imposed a in-plane lattice parameter. Here, E_0 is the lowest energy obtained for the ferromagnetic ordering in the strain-free case.

4.2.1 Strain-free conditions

First we consider an artificial strain-free environment by letting the in-plane lattice parameter to be optimized as well as c parameter. This calculation will give us the strain-free reference of the in-plane lattice parameter of LMO-SMO superlattices. We computed two magnetic configurations: ferromagnetic and A-type antiferromagnetic orderings. We found that the ferromagnetic configuration is lower in energy compared to antiferromagnetic one ($\Delta E = E_{\mathrm{A-AFM}} - E_{FM} \simeq 140$ meV for whole system). For the ferromagnetic LMO-SMO superlattice, the a lattice parameter is optimized at $a_{\mathrm{FM}} = 3.833$ Å. For A-type antiferromagnetic LMO-SMO superlattice, it is optimized at $a_{\mathrm{A-AFM}} = 3.873$ Å.

Ferromagnetic Ordering

In tables 4.1 and 4.2, we report the structural and magnetic properties of ferromagnetic LMO-SMO superlattice in strain-free environment. The parametrization of relevant quantities are as explained in details in Chapter 3, section 3.7. One can also get an aide from the figure 4.3 for visualizing the table 4.1. As we mentioned above, for ferromagnetic ordering, the a lattice parameter is optimized at $a_{\mathrm{FM}} = 3.833$Å. The c lattice parameter is optimized at $c_{\mathrm{FM}} = 7.714$

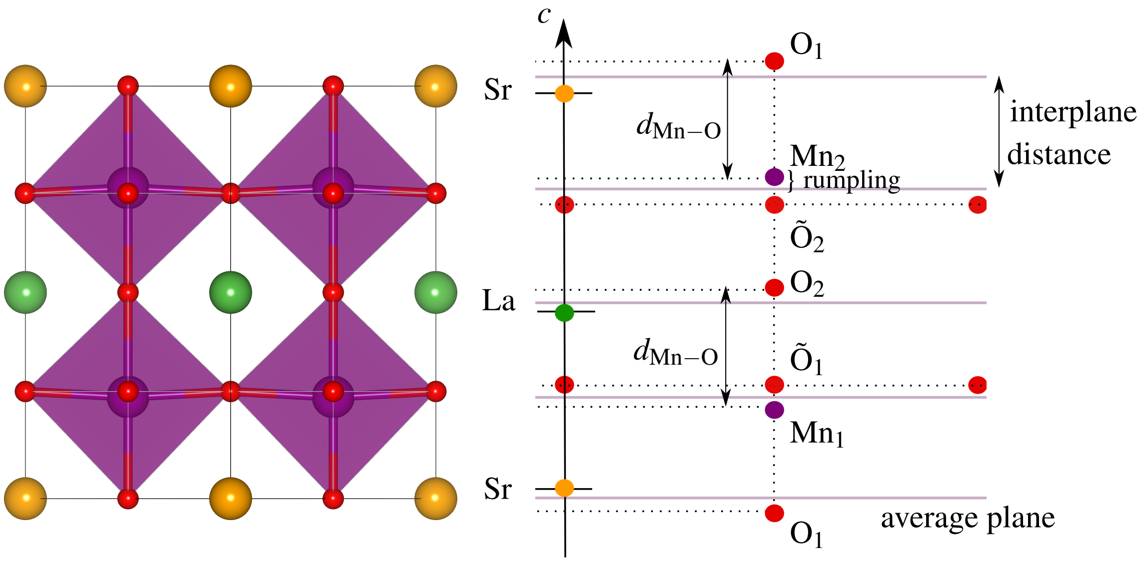

Fig. 4.3 Schematic picture defining the average planes and interplane distances, as well as rumpling. The oxygen atoms labelled as O_1 and O_2 belong to SrO and LaO planes, the oxygen atoms labelled as $\tilde{O}_1$ and $\tilde{O}_2$ belong to the first and second MnO_2 planes, respectively. The atomic displacements are exaggerated in the sketch for reading purposes.

Å. In table 4.1, first thing to comment is that the system doesn't have any polarization as we can see from the compensating the rumpling values of the MnO_2 planes. Next thing, by looking at the interplane distances one can easily see that the average MnO_2 planes are closer to the average LaO planes than to the SrO plane. (The average distance with the LaO is 1.904 Å and the average distance with SrO is 1.953 Å.) Another important result to mention is the $Mn-O$ distances in the $\vec{c}$ direction. The $d_{\mathrm{Mn-O}}$ between MnO_2 and LaO is 1.955 Å, while $d_{\mathrm{Mn-O}}$ between MnO_2 and SrO is 1.902 Å. The differences in the interplane distances and $d_{\mathrm{Mn-O}}$ are the sign of dimerization in the $\vec{c}$ direction. Indeeed, the $Mn-Mn$ distance in $\vec{c}$ direction ($d_{\mathrm{Mn-Mn}}$) changes depending on the plane that is sandwiched in between two Mn. When there is an Sr in the plane sandwiched it is $d_{\mathrm{Mn-Mn}}$ and when there is a La it is $d'_{\mathrm{Mn-Mn}}$. By simply summing up the corresponding Mn-O distances one can easily see that $d'_{\mathrm{Mn-Mn}} > d_{\mathrm{Mn-Mn}}$. This dimetrization is schematically drawn in figure 4.4.

	$\tilde{z}_{\text{average plane}}$	interplane distances (Å)	rumpling (Å)	$d_{\mathrm{Mn-O}}$(Å)
SrO	0.000		0	
		1.953		1.902
MnO_2	0.253		-0.051	
		1.904		1.955
LaO	0.500		0	
		1.904		1.955
MnO_2	0.747		0.051	
		1.953		1.902

Table 4.1 Table summarizing the structural properties of ferromagnetic $[(\mathrm{LaMnO_3})_1-(\mathrm{SrMnO_3})_1]_1$ superlattice in a strain-free environment. $a_{\mathrm{FM}} = 3.833$ Å. $c_{\mathrm{FM}} = 7.714$ Å.

In table 4.2, we can immediately see that the Mn-octahedron thickness (d_{OO}) and the layer thickness (c') are the same for the two layers so that the Jahn-Teller distortion (Jtd) and tetragonality ($c'/a-1$) values are the same as well. Both Jahn-Teller distortion and tetragonality values indicate very small elongation in the superlattice mono-layers. The magnetic moment of each Mn is the same. The e_g occupancy ratios are also the same in both octahedra. Finally, the e_g occupancy ratio shows that d_{z^2} is preferentially occupied over $d_{x^2-y^2}$ orbital though it is small. When we check the charges of the atomic planes in this table, we see that there is a global electron transfer from SrO at a lower level LaO planes toward MnO_2 ones.

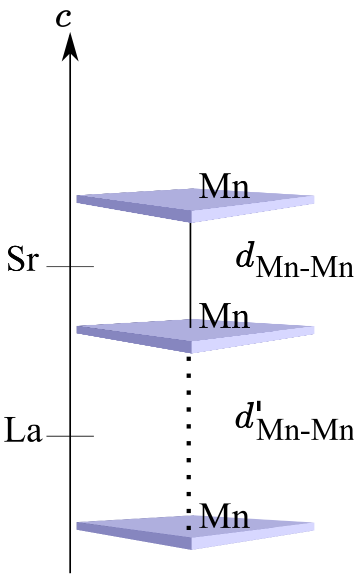

Fig. 4.4 Schematical representation of the dimerization in MnO$_2$ planes. $d'_{\text{Mn}-\text{Mn}}$ and $d_{\text{Mn}-\text{Mn}}$ are the Mn − Mn distances in $\vec{c}$ direction. $d'_{\text{Mn}-\text{Mn}} > d_{\text{Mn}-\text{Mn}}$

	d_{OO} (Å)	JTd	c' (Å)	$c'/a-1$	magnetic moment (μ_B)	$\frac{\eta_{x^2-y^2}}{\eta_{z^2}}$	total e_g	charge ($\lvert e\rvert$)
SrO								0.565
MnO$_2$	3.857	0.006	3.857	0.006	3.435	0.885	0.703	-0.833
LaO								1.100
MnO$_2$	3.857	0.006	3.857	0.006	3.434	0.885	0.703	-0.833

Table 4.2 Table summarizing the structural and magnetic properties of ferromagnetic [(LaMnO$_3$)$_1$ − (SrMnO$_3$)$_1$]$_1$ superlattice in a strain-free environment. $a_{\text{FM}} = 3.833$ Å. $c_{\text{FM}} = 7.714$ Å.

A-type Antiferromagnetic Ordering

In tables 4.3, 4.4 we report the results for A-type antiferromagnetic (ferromagnetic in plane, antiferromagnetic in $\vec{c}$ direction) ordered [(LMO)$_1$ − (SMO)$_1$]$_1$ superlattice in a strain-free environment. The a lattice parameter is optimized at $a_{\text{A-AFM}} = 3.873$ Å and the c lattice parameter is optimized at $c_{\text{A-AFM}} = 7.531$ Å. Thus, the first thing we can say is that, in a strain-free environment, the in-plane lattice parameter increases in A-type antiferromagnetic ordering compared to the ferromagnetic ordering ($a_{\text{A-AFM}} > a_{\text{FM}}$) while the out-of-plane lattice parameter decreases ($c_{\text{A}-\text{AFM}} < c_{\text{FM}}$). In table 4.3, one can see that $\tilde{z}_{\text{averageplane}}$ values are the same as for the ferromagnetic ordering, while the interplane distances are smaller than the ones in ferromagnetic ones. This is due to the overall contraction of the superlattice in $\vec{c}$ direction. However, the analysis of the interplane distances done for the FM ordering is valid for A-type antiferromagnetic ordering as well; the average MnO_2 planes are closer to the average LaO planes than to the average SrO planes. (The average distance with the LaO is 1.864 Å and the average distance with SrO is 1.905 Å.) The $d_{\text{Mn}-\text{O}}$ distances are overall smaller than the ones for the ferromagnetic ordering (the $d_{\text{Mn}-\text{O}}$ between MnO_2 and LaO is 1.911 Å, while is $d_{\text{Mn}-\text{O}}$ between MnO_2 and SrO is 1.859 Å) but there is also a interlayer dimerization. Finally, the rumpling values are decreased a little but again the system doesn't have any polarization.

	$\tilde{z}_{\text{average plane}}$	interplane distances (Å)	rumpling (Å)	$d_{\text{Mn}-\text{O}}$(Å)
SrO	0.000		-0.001	
		1.905		1.859
MnO_2	0.253		-0.046	
		1.864		1.911
LaO	0.500		0	
		1.864		1.911
MnO_2	0.747		0.046	
		1.905		1.859

Table 4.3 Table summarizing the structural properties of A-type antiferromagnetic $[(LaMnO_3)_1 - (SrMnO_3)_1]_1$ superlattice in a strain-free environment. $a_{\text{A}-\text{AFM}} = 3.873$ Å. $c_{\text{A}-\text{AFM}} = 7.539$ Å.

In table 4.4, one can see that the Mn-octahedra thickness and the layer thickness are more or less equal to each other for each mono-layer (around 3.77 Å). This value is less than the thickness value of ferromagnetic case. However, the JTd and $c'/a - 1$ values are five times larger than those of the ferromagnetic case. Both JTd and tetragonality indicate strong contraction in the superlattice octhedrons and mono-layers. As a consequence of the JTd value, the e_g occupancy ratio is higher than the one in the purely ferromagnetic case, and the d_{x-y^2} orbital is preferentially occupied over the d_{z^2} orbital. The magnetic moments of the Mn ions present alternated signs, because of the spin ordering. Their values are a little smaller than those of ferromagnetic case.

For comparing the relaxed lattice parameters of FM and A-AFM cases, one can take a look to the sketch given in Figure 4.5. Here, in the case of A-type AFM compared to FM,

	d_{OO} (Å)	JTd	c' (Å)	$c'/a-1$	magnetic moment (μ_B)	$\frac{\eta_{x^2-y^2}}{\eta_{z^2}}$	total e_g	charge ($\lvert e\rvert$)
SrO								0.609
MnO_2	3.770	-0.027	3.768	-0.027	3.374	2.045	0.67	-0.871
LaO								1.132
MnO_2	3.770	-0.027	3.771	-0.026	-3.374	2.045	-0.67	-0.871

Table 4.4 Table summarizing the structural and magnetic properties of A-type antiferromagnetic $[(\mathrm{LaMnO_3})_1-(\mathrm{SrMnO_3})_1]_1$ superlattice in a strain-free environment. $a_{\mathrm{A-AFM}} = 3.873$ Å. $c_{\mathrm{A-AFM}} = 7.539$ Å.

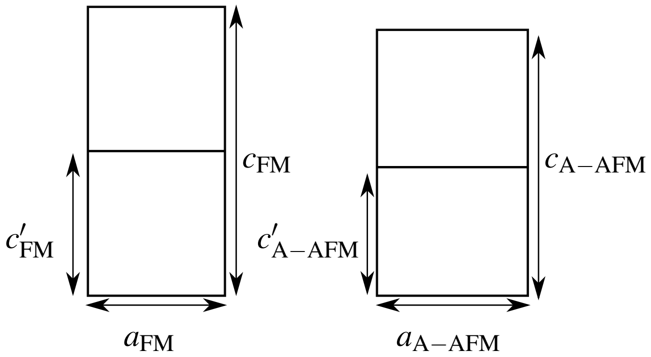

Fig. 4.5 Sketch for relaxed ferromagnetic and A-type antiferromagnetic $[(\mathrm{LMO})_1-(\mathrm{SMO})_1]_1$ superlattice lattice parameters. $a_{\mathrm{FM}} < a_{\mathrm{A-AFM}}$, $c_{\mathrm{FM}} > c_{\mathrm{A-AFM}}$ and $c'_{\mathrm{FM}} > c'_{\mathrm{A-AFM}}$

by taking into account the enlargement of the a lattice parameter and the reduction of the c lattice parameter, we can say that antiferromagnetism in $\vec{c}$ direction induces a contraction on the octahedra and layers along the $\vec{c}$ direction. The free energy of such a system can be given as

$$F = E_{\mathrm{elas}} + E_{\mathrm{deloc}} + E_{\mathrm{SX}} + E_{\mathrm{Hund}} \tag{4.1}$$

where E_{elas} is the elastic energy, E_{deloc} is the delocalization energy, E_{SX} is the superexchange energy and E_{Hund} is the Hund's energy.

When there is a ferromagnetic ordering in the system, the system will favor the in-plane delocalization. For this purpose, the a lattice parameter will decrease in the ferromagnetic ordering case. As a consequence, the in-plane delocalization t increases. The elastic energy enlarges the c lattice parameter in order to preserve the volume of the system. Naturally, the d_{OO} also increases and results with a positive JTd which is responsible of a weak dominance of d_{z^2} occupancy in the strain-free case.

When there is A-type antiferromagnetic ordering one can gain the superexchange energy compared to ferromagnetic solution. In order to favour the superexchange energy along the $\vec{c}$ direction the superlattice contracts in the $\vec{c}$ direction. On the other hand, elastic energy will still decrease the a lattice parameter but in order to preserve the volume this decrease will not be too much. The contraction in the $\vec{c}$ direction will result with a slightly dominant $d_{x^2-y^2}$ occupancy in the strain-free case.

4.2.2 Results with $a_{\mathrm{STO}} = 3.88$ Å

Now we look at a $[(\mathrm{LMO})_1 - (\mathrm{SMO})_1]_1$ superlattice deposited on a STO substrate. The imposed a lattice parameter is the one we optimized within our calculations; that is $a = 3.88$ Å. We computed different magnetic configurations: ferromagnetic, A-type antiferromagnetic, C-type antiferromagnetic and G-type antiferromagnetic. We found that the ferromagnetic ordering has the lowest energy. As the C-type antiferromagnetic and G-type antiferromagnetic configurations are way too high in energy we do no report their structural and magnetic properties here in this section. However, in section with imposed $a = 3.905$ Å, we will report the C-type antiferromagnetic configuration with the ferromagnetic and A-type antiferromagnetic configurations to have an idea. When $a = 3.88$ Å is imposed, the energy difference between the A-type antiferromagnetic ordering and the ferromagnetic ordering is found to be $\Delta E = E_{A-AFM} - E_{FM} \simeq 36$ meV for whole superlattice and 9 meV per manganite unit cell.

Ferromagnetic Ordering

In table 4.5 we report the structural results of the optimized geometry of $[(\mathrm{LMO})_1 - (\mathrm{SMO})_1]_1$ superlattice with imposed $a = 3.88$ Å when spins are ferromagnetically alligned. The c lattice parameter is optimized at $c_{\mathrm{FM}} = 7.617$ Å. The $\mathrm{MnO_2}$ planes have opposite rumplings, thus we can say that the system doesn't show any polarization. By looking at the interplane distances, one can easily see that the average $\mathrm{MnO_2}$ planes are closer to the average LaO planes than to the average SrO planes. The distance with the LaO is 1.876 Å and the distance with SrO is 1.932 Å. The $\mathrm{Mn-O}$ distance in the $\vec{c}$ direction also changes from one plane to another. The $d_{\mathrm{Mn-O}}$ between the $\mathrm{MnO_2}$ and LaO is 1.924 Å, while $d_{\mathrm{Mn-O}}$ is 1.884 Å between $\mathrm{MnO_2}$ and SrO. These two results are sign of a dimerization as we pointed out in the previous section. Though the interplane distances and the $\mathrm{Mn-O}$ distances decreased compared to the ferromagnetic strain-free case, the dimerization is still there and acts the same.

	$\tilde{z}_{\text{average plane}}$	interplane distances (Å)	rumpling (Å)	$d_{\text{Mn}-\text{O}}$(Å)
SrO	-0.127		0.000	
		1.932		1.884
MnO_2	0.127		-0.048	
		1.876		1.924
LaO	0.373		0.000	
		1.876		1.924
MnO_2	0.620		0.048	
		1.932		1.884

Table 4.5 Table summarizing the structural properties of ferromagnetic $[(\text{LaMnO}_3)_1 - (\text{SrMnO}_3)_1]_1$ superlattice on a SrTiO_3 substrate. The a lattice parameter is fixed at $a = 3.88$ Å. The c lattice parameter is optimized at $c_{\text{FM}} = 7.617$ Å.

In table 4.6, we give the results for the magnetic properties of the ferromagnetic ordered system. The Mn-magnetic moments are the same in each MnO_2 plane and this value is similar to the ferromagnetic-strain free case. We can immediately see that the Mn-octahedra thickness (d_{OO}) and the layer thickness (c') are the same in the two layers so that the Jahn-Teller distortion (JTd) and tetragonality are the same as well. Both Jahn-Teller distortion and tetragonality indicate that the superlattice mono-layers are contracted in the $\vec{c}$ direction and the e_g ratio shows that $d_{x^2-y^2}$ is preferentially occupied. This result is the opposite of the ferromagnetic strain-free case. When there is a strain due to the imposed a lattice parameter, the gain in the in-plane delocalization energy cannot take place by compressing the a lattice parameter. Thus, under the tensile strain, the system contracts in the $\vec{c}$ direction leading to a negative JTd which is associated to a dominant $d_{x^2-y^2}$ occupancy.

	d_{OO} (Å)	JTd	c' (Å)	$c'/a-1$	magnetic moment (μ_B)	$\frac{\eta_{x^2-y^2}}{\eta_{z^2}}$	total e_g	charge ($\lvert e \rvert$)
SrO								0.584
MnO_2	3.809	-0.018	3.808	-0.018	3.444	1.248	0.708	-0.854
LaO								1.125
MnO_2	3.809	-0.018	3.808	-0.018	3.444	1.248	0.708	-0.854

Table 4.6 Table summarizing the structural and magnetic properties of ferromagnetic $[(\text{LaMnO}_3)_1 - (\text{SrMnO}_3)_1]_1$ superlattice in a SrTiO_3 substrate. The a lattice parameter is fixed at $a = 3.88$ Å. The c lattice parameter is optimized at $c_{\text{FM}} = 7.617$ Å.

A-type Antiferromagnetic Ordering

In tables 4.7, 4.8 we report the structural and magnetic quantities for the A-type antiferromagnetic (ferromagnetic in plane, antiferromagnetic in $\vec{c}$ direction) ordered $[(\text{LMO})_1 - (\text{SMO})_1]_1$ superlattices. The c lattice parameter is optimized at $c_{\text{A-AFM}} = 7.531$ Å. It is worth to mention that this value is more or less the same as the c lattice parameter of the A-type antiferromagnetic system in strain-free environment ($c = 7.539$ Å). It is probably because of the very small mismatch between strain-free A-type antiferromagnetic in-plane lattice parameter ($a_{A-AFM} = 3.873$ Å) and the imposed in-plane lattice parameter ($a = 3.88$ Å). The mismatch is around 0.2%. Thus, we can expect to have about the same structural and magnetic properties with strain-free A-type antiferromagnetic case. Indeed, one can see from the corresponding tables that the strain-free (optimized at $a = 3.873$ Å) and strained A-type antiferromagnetic (fixed at $a = 3.88$ Å) cases show almost the same structural and magnetic properties. In comparison to the strained ferromagnetic case, the strained A-type antiferromagnetic system is indeed more contracted in $\vec{c}$ direction. This overall contraction in $\vec{c}$ direction also reflects on the interplane distances between average planes and $d_{\text{Mn-O}}$ distances, thus the same dimerization analysis is still valid. The rumpling in each plane is qualitatively the same with the strained ferromagnetic case.

	$\tilde{z}_{\text{average plane}}$	interplane distances (Å)	rumpling (Å)	$d_{\text{Mn-O}}$(Å)
SrO	0.040		0	
		1.904		1.858
MnO_2	0.293		-0.046	
		1.861		1.908
LaO	0.540		0	
		1.861		1.908
MnO_2	0.787		0.046	
		1.904		1.858

Table 4.7 Table summarizing the structural properties of A-type antiferromagnetic $[(\text{LaMnO}_3)_1 - (\text{SrMnO}_3)_1]_1$ superlattice in a $SrTiO_3$ substrate. The a lattice parameter is fixed at $a = 3.88$ Å. The c lattice parameter is optimized at $c_{\text{A-AFM}} = 7.531$ Å.

In table 4.8, one can see that the Mn-octahedra (d_{OO}) and layer (c') thicknesses are even smaller than those of strained ferromagnetic case. As a consequence of the larger negative JTd, the associated e_g ratio is higher than for the strained ferromagnetic case. As a conclusion, we can say that even if we have seen a contraction in the $\vec{c}$ direction in the strained ferromagnetic case, the contraction that we get from the strained A-type antiferromagnetic case is larger.

	d_{OO} (Å)	JTd	c' (Å)	$c'/a-1$	magnetic moment (μ_B)	$\frac{\eta_{x^2-y^2}}{\eta_{z^2}}$	total e_g	charge ($\lvert e\rvert$)
SrO								0.611
MnO_2	3.765	-0.030	3.764	-0.030	3.376	2.073	0.67	-0.873
LaO								1.135
MnO_2	3.765	-0.030	3.766	-0.030	-3.376	2.073	-0.67	-0.873

Table 4.8 Table summarizing the structural and magnetic properties of A-type antiferromagnetic $[(\mathrm{LaMnO_3})_1-(\mathrm{SrMnO_3})_1]_1$ superlattice in a $SrTiO_3$ substrate. The a lattice parameter is fixed at $a = 3.88$ Å. The c lattice parameter is optimized at $c_{\mathrm{A-AFM}} = 7.531$ Å.

4.2.3 Results with $a_{\mathrm{STO}} = 3.905$ Å

Now we look at a $[(\mathrm{LMO})_1-(\mathrm{SMO})_1]_1$ superlattice deposited on a substrate where the imposed a lattice parameter is the experimental STO one; that is $a = 3.905$ Å. We computed different magnetic configurations: ferromagnetic, A-type antiferromagnetic and C-type antiferromagnetic. We obtain the A-type antiferromagnetic ordering as the ground state when the a is fixed at 3.905 Å. The C-type antiferromagnetic ordering has a very large energy ($\Delta E = E_{C-AFM} - E_{A-AFM} = 782$ meV for whole superlattice). The energy difference between the A-type antiferromagnetic ordering and the ferromagnetic ordering is given by $\Delta E = E_{A-AFM} - E_{FM} \simeq -13$ meV for whole superlattice and -3 meV per manganite unit cell.

Ferromagnetic Ordering

In table 4.9, we report the structural results of the optimized geometry of $[(\mathrm{LMO})_1-(\mathrm{SMO})_1]_1$ superlattice with imposed $a = 3.905$ Å when spins are ferromagnetically alligned. The c lattice parameter is optimized at $c_{\mathrm{FM}} = 7.585$ Å. The structural and magnetic properties are qualitatively the same as for the ferromagentic case with imposed $a = 3.88$ Å , since in both cases the superlattice is under tensile strain. However, one should note that the overall contraction along $\vec{c}$ is a little bit larger in the $a = 3.905$ case than $a = 3.88$ Å case.

Naturally, this increase in overall contraction reflects in the other structural parameters such as interplane distances, $d_{\mathrm{Mn-O}}$, d_{OO} and etc. Nevertheless, the same analysis for the dimerization is again valid in this case.

	$\tilde{z}_{\text{average plane}}$	interplane distances (Å)	rumpling (Å)	$d_{\mathrm{Mn-O}}$(Å)
SrO	0.000		0	
		1.924		1.877
MnO_2	0.254		-0.047	
		1.868		1.915
LaO	0.500		0	
		1.868		1.915
MnO_2	0.746		0.047	
		1.925		1.877

Table 4.9 Table summarizing the structural properties of ferromagnetic $[(\mathrm{LaMnO_3})_1-(\mathrm{SrMnO_3})_1]_1$ superlattice in a $SrTiO_3$ substrate. The a lattice parameter is fixed at $a = 3.905$ Å. The c lattice parameter is optimized at $c_{\mathrm{FM}} = 7.585$ Å.

In table 4.10, we report the magnetic properties. The results are qualitatively similar to the ferromagnetic ordered case with the imposed $a = 3.88$ Å. As the overall contraction is increased in the $a = 3.905$ Å case, this reflects in the JTd and the associated the e_g occupancies but the physics does not change significantly from $a = 3.88$ Å case to $a = 3.905$ Å case when there is ferromagnetic ordering.

	d_{OO} (Å)	JTd	c' (Å)	$c'/a-1$	magnetic moment (μ_B)	$\frac{\eta_{x^2-y^2}}{\eta_{z^2}}$	total e_g	charge ($\lvert e\rvert$)
SrO								0.592
MnO_2	3.792	-0.029	3.793	-0.029	3.452	1.319	0.712	-0.863
LaO								1.135
MnO_2	3.792	-0.029	3.791	-0.029	3.452	1.319	0.712	-0.863

Table 4.10 Table summarizing the structural and magnetic properties of ferromagnetic $[(\mathrm{LaMnO_3})_1-(\mathrm{SrMnO_3})_1]_1$ superlattice in a $SrTiO_3$ substrate. The a lattice parameter is fixed at $a = 3.905$ Å. The c lattice parameter is optimized at $c_{\mathrm{FM}} = 7.585$ Å.

In figure 4.6, we report the total and partial densities of states for the $[(\mathrm{LMO})_1-(\mathrm{SMO})_1]_1$ superlattice in the ferromagnetic configuration. Mn atoms contribute to the electronic structure at the Fermi level. Mn t_{2g} states are below the Fermi level due to the crystal field splitting. At the Fermi level, Mn $e_g \uparrow$ states split into $d_{x^2-y^2}$ and d_{z^2}. Both orbitals are almost equally occupied (even though the e_g ratio shows preferential $d_{x^2-y^2}$ orbital occupancy the difference remains small). These partially occupied e_g orbitals lead to a ferromagnetic double exchange. In spin-down channel we can notice the gap at the Fermi level which is the sign of half-metallicity.

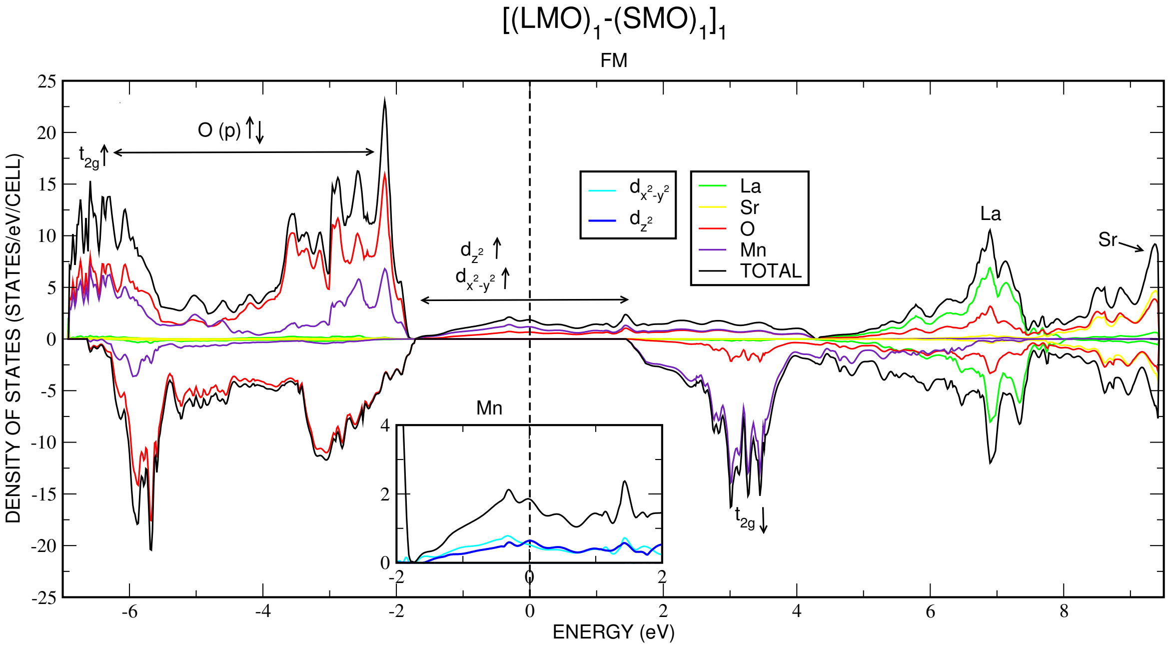

Fig. 4.6 Total and partial densities of states for the $[(\mathrm{LMO})_1-(\mathrm{SMO})_1]_1$ superlattice in ferromagnetic configuration. The symbols ↑ and ↓ are for the spin up and spin down states. The Mn $e_g \uparrow$ state at the Fermi level splits into $d_{x^2-y^2}$ and d_{z^2}. Both $d_{x^2-y^2}$ and d_{z^2} are more or less equally occupied.

A-type Antiferromagnetic Ordering

We give the results summarized in tables 4.11 and 4.12 for A-type antiferromagnetic ordering with imposed $a = 3.905$ Å. The c lattice parameter is optimized at $c_{A-AFM} = 7.500$ Å. The results in tables 4.11 and 4.12 are qualitatively similar to those of the A-type AFM ordering with imposed $a = 3.88$ Å. However, one must note that the overall contraction along the $\vec{c}$ increases in comparison to $a = 3.88$ Å case as the fixed a lattice parameter is larger than 3.88 Å. Let us remind that $a = 3.88$ Å is very close to the strain-free reference ($a = 3.873$ Å) for the A-type antiferromagnetic ordering. Thus, this effect can be attributed to the elastic energy that tends to keep the unit cell volume constant.

	$\tilde{z}_{\text{average plane}}$	interplane distances (Å)	rumpling (Å)	$d_{\text{Mn}-\text{O}}$(Å)
SrO	0.000		0	
		1.897		1.852
MnO_2	0.253		-0.045	
		1.853		1.898
LaO	0.500		0	
		1.852		1.898
MnO_2	0.747		0.046	
		1.898		1.852

Table 4.11 Table summarizing the structural properties of A-type antiferromagnetic $[(\text{LaMnO}_3)_1 - (\text{SrMnO}_3)_1]_1$ superlattice in a $SrTiO_3$ substrate. The a lattice parameter is fixed at $a = 3.905$ Å. The c lattice parameter is optimized at $c_{\text{A}-\text{FM}} = 7.500$ Å.

	d_{OO} (Å)	JTd	c' (Å)	$c'/a-1$	magnetic moment (μ_B)	$\frac{\eta_{x^2-y^2}}{\eta_{z^2}}$	total e_g	charge ($\lvert e \rvert$)
SrO								0.619
MnO_2	3.750	-0.040	3.752	-0.039	3.381	2.190	0.673	-0.882
LaO								1.145
MnO_2	3.750	-0.040	3.748	-0.040	-3.381	2.194	-0.674	-0.882

Table 4.12 Table summarizing the structural and magnetic properties of A-type antiferromagnetic $[(\text{LaMnO}_3)_1 - (\text{SrMnO}_3)_1]_1$ superlattice in a $SrTiO_3$ substrate. The a lattice parameter is fixed at $a = 3.905$ Å. The c lattice parameter is optimized at $c_{\text{A}-\text{AFM}} = 7.500$ Å.

In figure 4.7, we give the total and partial densities of states for the $[(\mathrm{LMO})_1-(\mathrm{SMO})_1]_1$ superlattice in the A-type antiferromagnetic configuration. Again, Mn atoms contribute to electronic structure at the Fermi level. Mn t_{2g} states are below the Fermi level due to crystal field splitting. At the Fermi level, Mn $e_g\uparrow$ states split into $d_{x^2-y^2}$ and d_{z^2}. Since the antiferromagnetism in the $\vec{c}$ direction enhances the contraction of Mn-octahedra in the $\vec{c}$ direction, the $d_{x^2-y^2}$ orbital occupancy is significantly larger than the one of d_{z^2}.

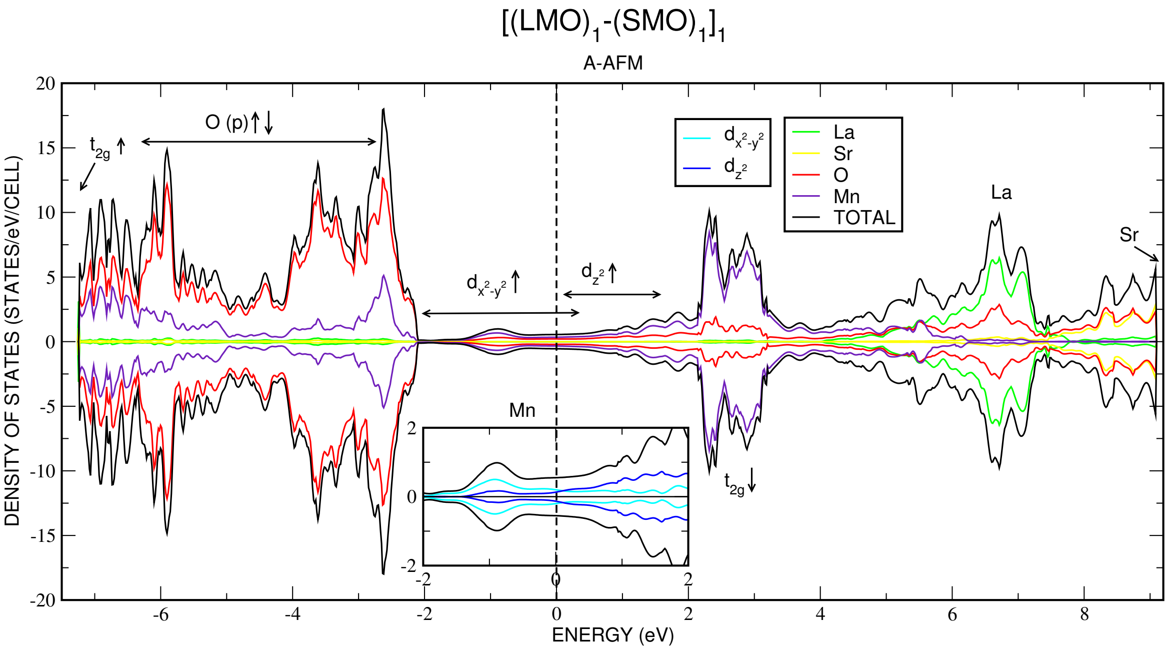

Fig. 4.7 Total and partial densities of states for the $[(\mathrm{LMO})_1-(\mathrm{SMO})_1]_1$ superlattice in A-type antiferromagnetic configuration. The symbols ↑ and ↓ are for the spin up and spin down states. The Mn $e_g\uparrow$ state at the Fermi level splits into $d_{x^2-y^2}$ and d_{z^2}. $d_{x^2-y^2}$ is occupied more than d_{z^2}.

C-type Antiferromagnetic Ordering

Though it is quite higher in energy compared to other magnetic configurations we also report C-type antiferromagnetic ordering; that is antiferromagnetic ordering in plane and ferromagnetic ordering in $\vec{c}$ direction. The results are summarized in table 4.13 and table 4.14. The c lattice parameter is optimized at $c_{\mathrm{C-AFM}} = 7.714$ Å which is larger than the c lattice parameters that are obtained for ferromagnetic and A-type antiferromagnetic superlattice with imposed $a = 3.905$ Å. This overall elongation in the $\vec{c}$ direction reflects on the interplane distances and the $d_{\mathrm{Mn-O}}$ as elongation as well. However, the main result on dimerization is still valid here too. The average $\mathrm{MnO_2}$ planes are closer to the average LaO planes than to the average SrO planes. The $\mathrm{Mn-O}$ distances (d_{Mn-O}) between MnO_2 and LaO planes (1.951 Å and 1.946 Å) is larger than the one of between MnO_2 and SrO (1.911 Å and 1.906 Å). From the rumpling values, we can again conclude that the system does not show any polarization.

	$\tilde{z}_{\text{average plane}}$	interplane distances (Å)	rumpling (Å)	$d_{\text{Mn-O}}$(Å)
SrO	0.000		0.001	
		1.959		1.911
MnO_2	0.254		-0.050	
		1.900		1.951
LaO	0.500		-0.001	
		1.898		1.946
MnO_2	0.746		0.050	
		1.957		1.906

Table 4.13 Table summarizing the structural properties of C-type antiferromagnetic $[(LaMnO_3)_1-(SrMnO_3)_1]_1$ superlattice in a $SrTiO_3$ substrate. The a lattice parameter is fixed at $a = 3.905$ Å. The c lattice parameter is optimized at $c_{\text{C-AFM}} = 7.714$ Å.

In table 4.14, we report the magnetic and related structural properties. The two Mn atoms of each plane has opposite signs in magnetic moment as we ordered C-type antiferromagnetism; that is antiferromagnetic in plane and ferromagnetic in the $\vec{c}$ direction. The charges of each plane is non-zero as we observed before in other calculations as well. The d_{OO} and c' values are close to each other so that the corresponding JTd and $c'/a-1$ are also close. We see the elongation in both d_{OO} and c' compared to ferromagnetic and A-type antiferromagnetic cases within $a = 3.905$ Å. However, what is remarkable in this table by looking at the JTd and the associated e_g occupancy ratio is that even though there is negative JTd, which is the sign of contraction in the $\vec{c}$ direction, the d_{z^2} orbital is preferentially occupied.

In figure 4.8, we can see the electronic structure of the C-type antiferromagnetic $[(\text{LMO})_1-(\text{SMO})_1]_1$ superlattice through the total and partial densities of states. One can see in the inset of Figure 4.8 that d_{z^2} is lower in energy and is more occupied whereas $d_{x^2-y^2}$ orbital is higher in energy and less occupied. The energy of the A-type antiferromagnetic configuration is lower than the energy of ferromagnetic configuration ($E_{\text{A-AFM}} - E_{FM} = -3$ meV per unit cell) when a is fixed at 3.905 Å, while it is the opposite ($E_{\text{A-AFM}} - E_{FM} = 9$ meV per unit cell) when a is fixed at 3.88 Å. However, the energy difference between these two magnetic configurations is quite small. This is smaller than room temperature ($k_BT \sim 25$ meV). This indicates that the magnetic ground state of $[(LaMnO_3)_1-(SrMnO_3)_1]_1$ superlattices

	d_{OO} (Å)	JTd	c' (Å)	$c'/a-1$	magnetic moment (μ_B)	$\frac{\eta_{x^2-y^2}}{\eta_{z^2}}$	total e_g	charge ($\lvert e\rvert$)
SrO								0.561
MnO_2	3.853	-0.013	3.857	-0.012	3.336 (-3.336)	0.321	0.617 (-0.617)	-0.837
LaO								1.111
MnO_2	3.861	-0.011	3.857	-0.012	3.320 (-3.320)	0.333	0.605 (-0.605)	-0.832

Table 4.14 Table summarizing the structural and magnetic properties of C-type antiferromagnetic $[(LaMnO_3)_1-(SrMnO_3)_1]_1$ superlattice in a $SrTiO_3$ substrate. The a lattice parameter is fixed at $a = 3.905$ Å. The c lattice parameter is optimized at $c_{C-AFM} = 7.714$ Å.

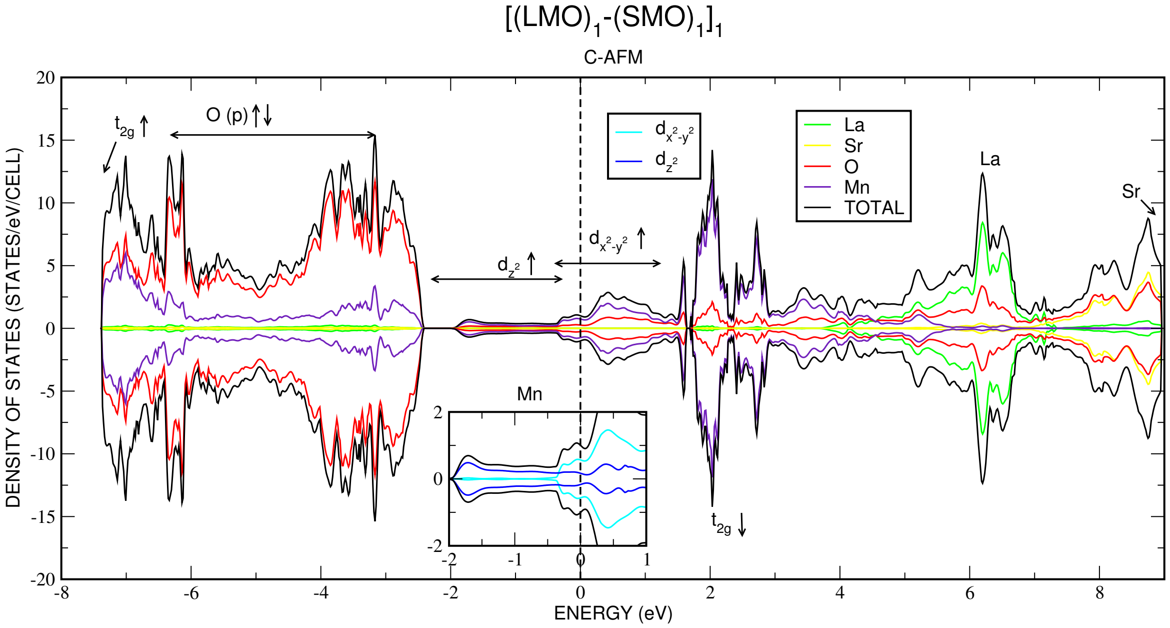

Fig. 4.8 Total and partial densities of states for the $[(LMO)_1-(SMO)_1]_1$ superlattice in C-type antiferromagnetic configuration. The symbols ↑ and ↓ are for the spin up and spin down states. The Mn $e_g\uparrow$ state at the Fermi level splits into $d_{x^2-y^2}$ and d_{z^2}. d_{z^2} is occupied more than $d_{x^2-y^2}$.

is quasi-degenerate in our calculations. In order to highlight this issue, we would like to check whether this comes from a size effect. Thus, we have increased the number of layers from 2 to 4. In addition, we will be able to check different magnetic configurations with by increasing the number of layers.

4.2.4 Analysis of Mn–Mn distances

Finally, we would like to summarize the Mn–Mn distances in each magnetic ordering for these superlattices. First, in table 4.15 we give the Mn–Mn distances for the superlattice in a strain-free environment and within imposed $a = 3.88$ Å and $a = 3.905$ Å. We see the dimerization in all cases.

	$d_{\mathrm{Mn-Mn}}$ (Å)					
	FM	A-AFM	FM	A-AFM	FM	A-AFM
	Strain-free	Strain-Free	$a = 3.88$ Å	$a = 3.88$ Å	$a = 3.905$ Å	$a = 3.905$ Å
MnO_2	↑	↓	↑	↓	↓	↑
SrO	3.804	3.718	3.768	3.716	3.754	3.704
MnO_2	↑	↑	↑	↑	↑	↑
LaO	3.91	3.822	3.848	3.816	3.83	3.796
MnO_2	↑	↓	↑	↓	↑	↓

Table 4.15 Table reporting the $d_{\mathrm{Mn-Mn}}$ values for strain-free, $a = 3.88$ Å and $a = 3.905$ Å for ferromagnetic, A-type antiferromagnetic cases. First line is visualized in red to point out it it is the repetition of the second MnO_2 plane due to periodicity.

4.3 $[(\mathbf{LaMnO_3})_1 - (\mathbf{SrMnO_3})_1]_2$ Superlattice

In this section, we double the size of the system with the same cationic order, $[(LaMnO_3)_1 - (SrMnO_3)_1]_2$, that allows us to study both size effects and different magnetic orderings. The schematic picture of such superlattices is given in figure 4.9. In such superlattice, other than the FM, A-AFM, C-AFM and G-AFM one can study the magnetic orderings such as ↑↑↓↓ ("uudd") and ↑↓↓↑ ("uddu"). Since we have seen in the 2-layers systems that the C-AFM and G-AFM are energetically too high, we didn't study them for the 4-layers systems. In figure 4.10 we gave the energy comparisons of each magnetic ordering with respect to the substrate on which the superlattice is deposited.

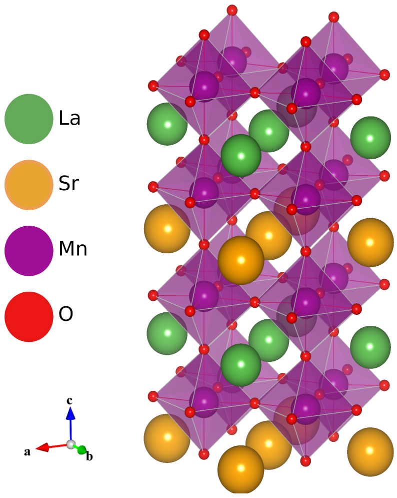

Fig. 4.9 Schematic picture for LMO-SMO superlattices

One can immediately notice that for both the substrate in-plane lattice parameter $a = 3.88$ Å and $a = 3.905$ Å, A-AFM is the ground state. In the 2-layers case, we got FM case as the ground state for $a = 3.88$ Å. This shows that we were not able to completely capture the real physics when the computed system had only 2-layers. What is also interesting here is that we managed to get an intermediate magnetic order between A-AFM and FM which is the "uudd" case. ‘

4.3.1 Strain-free conditions

As we did in previous section, we also study the superlattice in strain-free environment. We found that the ferromagnetic solution is lower in energy than the A-type antiferromagnetic one ($\Delta E = E_{\mathrm{A-AFM-FM}} - E_{\mathrm{FM}} \simeq 96$ meV for whole superlattice and 12 meV per manganite unit cell). The strain-free reference in-plane lattice parameter is optimized at $a_{\mathrm{FM}} = 3.836$ Å for the ferromagnetic ordering while it is optimized at $a_{\mathrm{A-AFM}} = 3.877$ Å for the A-type antiferromagnetic ordering. As one can see these values are consistent with strain-free values found for the two-layers system.

Ferromagnetic Ordering

In tables 4.16, 4.17, we report the structural and magnetic results for the ferromagnetic superlattice. The a lattice parameter is optimized at $a_{\mathrm{FM}} = 3.836$ Å. The c lattice parameter

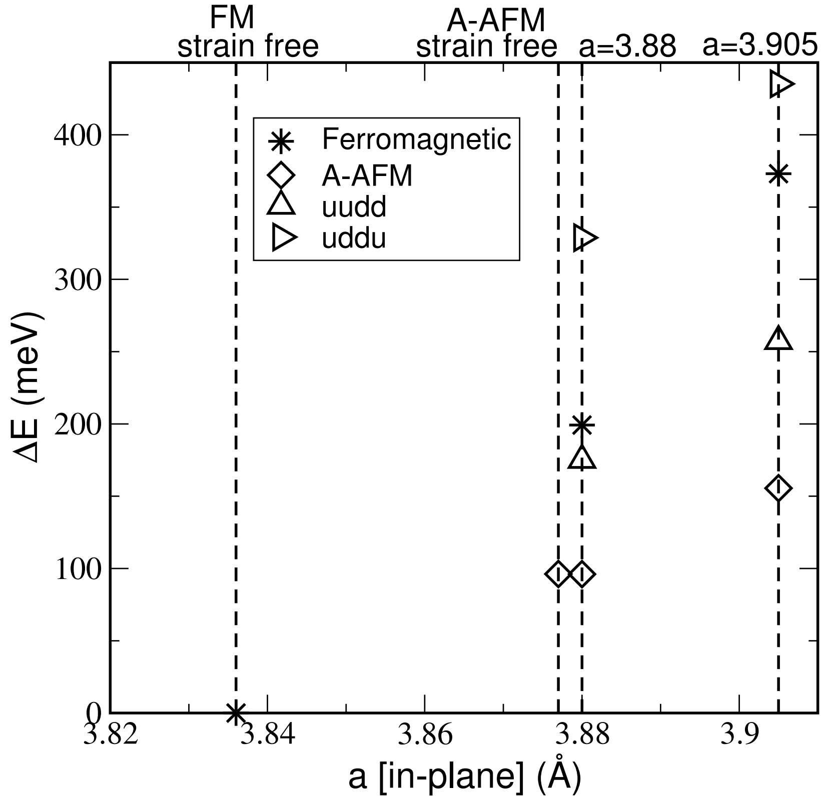

Fig. 4.10 Energy difference of each configuration with respect to the lowest energy ordering and geometry ($\Delta E = E - E_0$) vs. the imposed a in-plane lattice parameter. Here, E_0 is the lowest energy obtained for the ferromagnetic ordering in the strain-free case.

is optimized at $c_{\text{FM}} = 15.152$ Å. Though the in-plane lattice parameter is consistent with the strain-free two-layers ferromagnetic system ($a_{\text{FM}} = 3.836$ Å for four-layers and $a_{\text{FM}} = 3.833$ Å for two-layers), the c lattice parameter is smaller than twice of the c lattice parameter of the strain-free two-layers ferromagnetic system ($c_{\text{FM}} = 15.152$ Å for four-layers and $2 \times c_{\text{FM}} = 2 \times 7.714 = 15.428$ Å for two-layers doubled in $\vec{c}$ direction). This contraction in the $\vec{c}$ direction is reflected on the structural parameters of table 4.16. One can see that the interplane distances and the $d_{\text{Mn-O}}$ ones are qualitatively the same as for the strain-free two-layers ferromagnetic system but the values are smaller due to the overall contraction. The dimerization is kept.

	$\tilde{z}_{\text{average plane}}$	interplane distances (Å)	rumpling (Å)	$d_{\text{Mn-O}}$(Å)
SrO	0.000		0.001	
		1.919		1.870
MnO_2	0.127		-0.050	
		1.869		1.919
LaO	0.250		0	
		1.870		1.919
MnO_2	0.373		0.049	
		1.918		1.869
SrO	0.500		0	
		1.919		1.868
MnO_2	0.627		-0.050	
		1.869		1.919
LaO	0.750		0	
		1.870		1.920
MnO_2	0.873		0.050	
		1.919		1.869

Table 4.16 Table summarizing the structural properties of ferromagnetic $[(\text{LaMnO}_3)_1 - (\text{SrMnO}_3)_1]_2$ superlattice in a strain free environment. The a lattice parameter is optimized at $a_{\text{FM}} = 3.836$ Å. The c lattice parameter is optimized at $c_{\text{FM}} = 15.152$ Å.

In table 4.17, we report the magnetic and related structural results. The charges of each atomic plane are more or less the same as the ones in the strain-free two-layers ferromagnetic system. The Mn-magnetic moments of each MnO_2 plane are equal to each other and are also the same with strain-free two-layers ferromagnetic system. The main differences between strain-free four-layers ferromagnetic and strain-free two-layers ferromagnetic systems are in d_{OO} and c' of each layer and, corresponding JTd and tetragonality values. In strain-free four-layers ferromagnetic case, we see that the each layer and Mn-octahedra of each layer are equal to each other and are contracted (negative JTd and tetragonality). Previously, we have seen small elongation in Mn-octahedra of two-layers system with a slightly small dominant d_{z^2} occupancy. Now, in four-layers system, as we compress more in the $\vec{c}$ direction, the e_g ratio is closer to 1, indicating almost equal occupancies in $d_{x^2-y^2}$ and d_{z^2} orbitals.

	d_{OO} (Å)	JTd	c' (Å)	$c'/a-1$	magnetic moment (μ_B)	$\frac{\eta_{x^2-y^2}}{\eta_{z^2}}$	total e_g	charge ($\|e\|$)
SrO								0.563
MnO_2	3.789	-0.012	3.789	-0.012	3.435	0.939	0.704	-0.833
LaO								1.102
MnO_2	3.788	-0.012	3.784	-0.013	3.434	0.945	0.704	-0.834
SrO								0.564
MnO_2	3.787	-0.013	3.790	-0.012	3.431	0.950	0.702	-0.833
LaO								1.102
MnO_2	3.788	-0.012	3.788	-0.012	3.433	0.945	0.702	-0.833

Table 4.17 Table summarizing the structural and magnetic properties of ferromagnetic $[(LaMnO_3)_1-(SrMnO_3)_1]_2$ superlattice in a strain free environment. The a lattice parameter is optimized at $a_{FM} = 3.836$ Å. The c lattice parameter is optimized at $c_{FM} = 15.152$ Å.

A-type Antiferromagnetic Ordering

In tables 4.18, 4.19, we report the structural and magnetic properties of the strain-free four-layers A-type antiferromagnetic system. The a lattice parameter is optimized at $a_{A-AFM} = 3.877$ Å. The c lattice parameter is optimized at $c_{A-AFM} = 15.046$ Å. Both in-plane and out-of-plane lattice parameters are consistent with the strain-free two-layers ferromagnetic system ($a_{FM} = 3.836$ Å for four-layers and $a_{FM} = 3.833$ Å for two-layers, $c_{A-AFM} = 15.046$ Å for four-layers and $2 \times c_{A-AFM} = 2 \times 7.539 = 15.078$ Å for two-layers doubled in $\vec{c}$ direction). Relatively, the interplane distances between average planes and $Mn-O$ distances are consistent with the two-layers system.

In table 4.19, one can see the magnetic and related structural properties. The charges of each atomic plane is non-zero and the values are similar to those obtained in two-layers case. The Mn-magnetic moments have opposite signs in each plane and their values are similar to those of strain-free two-layers A-type antiferromagnetic case. The thickness of the layer and Mn-octahedra are the same in each and equal to each other. The values are similar to

	$\tilde{z}_{\text{average plane}}$	interplane distances (Å)	rumpling (Å)	$d_{\text{Mn}-\text{O}}$(Å)
SrO	0.000		0	
		1.902		1.855
MnO_2	0.126		-0.046	
		1.860		1.906
LaO	0.250		0	
		1.860		1.906
MnO_2	0.374		0.046	
		1.901		1.855
SrO	0.500		0	
		1.901		1.855
MnO_2	0.626		-0.046	
		1.860		1.906
LaO	0.750		0	
		1.860		1.906
MnO_2	0.874		0.046	
		1.901		1.855

Table 4.18 Table summarizing the structural properties of A-type antiferromagnetic $[(\text{LaMnO}_3)_1-(\text{SrMnO}_3)_1]_2$ superlattice in a strain free environment. The a lattice parameter is optimized at $a_{\text{A}-\text{AFM}} = 3.877$ Å. The c lattice parameter is optimized at $c_{\text{A}-\text{AFM}} = 15.046$ Å.

those obtained for the two-layers system. Similarly, the associated JTd and tetragonality are also the same. The corresponding e_g ratio shows the same tendency as two-layers system; a strongly dominant $d_{x^2-y^2}$ occupancy.

	d_{OO} (Å)	JTd	c' (Å)	$c'/a-1$	magnetic moment (μ_B)	$\frac{\eta_{x^2-y^2}}{\eta_{z^2}}$	total e_g	charge ($\lvert e \rvert$)
SrO								0.615
MnO_2	3.762	-0.030	3.763	-0.029	3.373	2.216	0.669	-0.875
LaO								1.136
MnO_2	3.762	-0.030	3.761	-0.030	-3.373	2.221	-0.67	-0.875
SrO								0.615
MnO_2	3.761	-0.030	3.762	-0.030	3.373	2.221	0.67	-0.875
LaO								1.136
MnO_2	3.762	-0.030	3.760	-0.030	-3.374	2.221	-0.67	-0.875

Table 4.19 Table summarizing the structural and magnetic properties of A-type antiferromagnetic $[(\mathrm{LaMnO}_3)_1-(\mathrm{SrMnO}_3)_1]_2$ superlattice in a strain free environment. The a lattice parameter is optimized at $a_{\mathrm{A-AFM}} = 3.877$ Å. The c lattice parameter is optimized at $c_{\mathrm{A-AFM}} = 15.046$ Å.

4.3.2 Results with $a_{\mathrm{STO}} = 3.88$ Å

Now we look at an $[(\mathrm{LMO})_1-(\mathrm{SMO})_1]_2$ superlattice deposited on STO substrate. The imposed a lattice parameter is the one that we optimized within our calculations; that is $a = 3.88$ Å. We computed different magnetic configurations: ferromagnetic, A-type antiferromagnetic "↑↑↓↓" and "↑↓↓↑ orderings. We have found the A-type antiferromagnetic ordering as the lowest energy ($E_{\mathrm{A-AFM}} - E_{\mathrm{FM}} = -103$ meV, $E_{\mathrm{A-AFM}} - E_{\mathrm{uudd}} \simeq -79$ meV, $E_{\mathrm{A-AFM}} - E_{\mathrm{uddu}} \simeq -233$ meV for whole superlattice).

Ferromagnetic Ordering

In table 4.20 we report the structural results of the optimized geometry of $[(\mathrm{LMO})_1-(\mathrm{SMO})_1]_2$ superlattice with imposed $a = 3.88$ Å when spins are ferromagnetically alligned. The c lattice parameter is optimized at $c_{\mathrm{FM}} = 15.258$ Å; this value is consistent with the c lattice parameter optimized for the strained two-layers ferromagnetic system ($c_{\mathrm{FM}} = 15.258$

Å for four-layers and $2 \times c_{\mathrm{FM}} = 2 \times 7.617 = 15.234$ Å for two-layers doubled in $\vec{c}$ direction). The structural properties are qualitatively the same with the strained two-layers ferromagnetic one. The values for interplane distances, rumplings and Mn – O distances are similar with the strained two-layers ferromagnetic ones. The same dimerization analysis is valid.

	$\tilde{z}_{\text{average plane}}$	interplane distances (Å)	rumpling (Å)	$d_{\mathrm{Mn-O}}$(Å)
SrO	-0.024		0	
		1.935		1.886
MnO_2	0.103		-0.048	
		1.880		1.928
LaO	0.226		0	
		1.880		1.928
MnO_2	0.350		0.048	
		1.934		1.886
SrO	0.476		0	
		1.935		1.886
MnO_2	0.603		-0.048	
		1.880		1.928
LaO	0.726		0	
		1.880		1.928
MnO_2	0.850		0.048	
		1.934		1.886

Table 4.20 Table summarizing the structural properties of ferromagnetic $[(\mathrm{LaMnO_3})_1 - (\mathrm{SrMnO_3})_1]_2$ superlattice in a $SrTiO_3$ substrate. The a lattice parameter is fixed at $a = 3.88$ Å. The c lattice parameter is optimized at $c_{\mathrm{FM}} = 15.258$ Å.

In the table 4.21, we report the magnetic and related structural properties. The results are qualitatively the same for the strained two-layers ferromagnetic superlattice. We observe negative JTd and related e_g occupancy ratio with slightly small dominance in $d_{x^2-y^2}$ occupancy. We again found an e_g occupancy ratio different from the one obtained for the strain-free four-layers ferromagnetic superlattice.

A-type Antiferromagnetic Ordering

In table 4.22 and 4.23, we summarize the results A-type antiferromagnetic $[(\mathrm{LMO})_1 - (\mathrm{SMO})_1]_2$ superlattice with imposed $a = 3.88$ Å. The results are qualitatively the same with A-type antiferromagnetic 2-layers superlattice.

	d_{OO} (Å)	JTd	c' (Å)	$c'/a-1$	magnetic moment (μ_B)	$\frac{\eta_{x^2-y^2}}{\eta_{z^2}}$	total e_g	charge ($\|e\|$)
SrO								0.580
MnO_2	3.815	-0.017	3.815	-0.017	3.447	1.152	0.71	-0.852
LaO								1.123
MnO_2	3.814	-0.017	3.815	-0.017	3.446	1.152	0.71	-0.852
SrO								0.581
MnO_2	3.814	-0.017	3.814	-0.017	3.447	1.152	0.71	-0.852
LaO								1.123
MnO_2	3.814	-0.017	3.814	-0.017	3.447	1.152	0.71	-0.852

Table 4.21 Table summarizing the structural and magnetic properties of ferromagnetic $[(LaMnO_3)_1-(SrMnO_3)_1]_2$ superlattice in a $SrTiO_3$ substrate. The a lattice parameter is fixed at $a = 3.88$ Å. The c lattice parameter is optimized at $c_{\text{FM}} = 15.258$ Å.

The c lattice parameter is optimized at $c_{\text{A-AFM}} = 15.039$ Å; this value is consistent with the c lattice parameter optimized for the strained two-layers A-type antiferromagnetic system ($c_{\text{FM}} = 15.258$ Å for four-layers and $2\times c_{\text{A-AFM}} = 2\times 7.531 = 15.062$ Å for two-layers doubled in $\vec{c}$ direction). The structural properties are qualitatively the same with the strained two-layers A-type antiferromagnetic one. The values for interplane distances, rumplings and $Mn-O$ distances are similar with the strained two-layers A-type antiferromagnetic ones. The same dimerization analysis is valid.

In the table 4.23, we report the magnetic and related structural properties. The results are qualitatively the same with strained two-layers A-type ferromagnetic superlattice. We observe negative JTd and related e_g occupancy ratio with large dominancy in $d_{x^2-y^2}$ occupancy. These result are also similar to the ones obtained for the strain-free four-layers A-type ferromagnetic superlattice.

↑↑↓↓ Ordering

Now we consider a different magnetic ordering where spins are alligned as ↑↑↓↓ ("uudd"). This magnetic configuration is found to be an intermediate phase between A-type antiferromagnetic and ferromagnetic phases ($E_{\text{A-AFM}} - E_{\text{FM}} = -103$ meV (-13 meV), $E_{\text{A-AFM}} - E_{\text{uudd}} \simeq -79$ meV (-10 meV) for whole superlattice (per unit cell)).

	$\tilde{z}_{\text{average plane}}$	interplane distances (Å)	rumpling (Å)	$d_{\text{Mn}-\text{O}}$(Å)
SrO	-0.007		0	
		1.901		1.855
MnO_2	0.119		-0.046	
		1.859		1.905
LaO	0.243		0	
		1.859		1.905
MnO_2	0.366		0.046	
		1.901		1.855
SrO	0.493		0	
		1.901		1.855
MnO_2	0.619		-0.046	
		1.859		1.905
LaO	0.743		0	
		1.859		1.905
MnO_2	0.866		0.046	
		1.901		1.855

Table 4.22 Table summarizing the structural properties of A-type antiferromagnetic $[(\text{LaMnO}_3)_1-(\text{SrMnO}_3)_1]_2$ superlattice in a $SrTiO_3$ substrate. The a lattice parameter is fixed at $a=3.88$ Å. The c lattice parameter is optimized at $c_{\text{A}-\text{AFM}}=15.039$ Å.

	d_{OO} (Å)	JTd	c' (Å)	$c'/a-1$	magnetic moment (μ_B)	$\frac{\eta_{x^2-y^2}}{\eta_{z^2}}$	total e_g	charge ($\lvert e\rvert$)
SrO								0.616
MnO_2	3.760	-0.031	3.760	-0.031	3.375	2.226	0.671	-0.877
LaO								1.138
MnO_2	3.760	-0.031	3.760	-0.031	-3.375	2.226	-0.671	-0.877
SrO								0.615
MnO_2	3.760	-0.031	3.760	-0.031	3.375	2.226	0.671	-0.877
LaO								1.138
MnO_2	3.760	-0.031	3.760	-0.031	-3.375	2.226	-0.671	0.877

Table 4.23 Table summarizing the structural and magnetic properties of A-type antiferromagnetic $[(\text{LaMnO}_3)_1-(\text{SrMnO}_3)_1]_2$ superlattice in a $SrTiO_3$ substrate. The a lattice parameter is fixed at $a=3.88$ Å. The c lattice parameter is optimized at $c_{\text{A}-\text{AFM}}=15.039$ Å.

In tables 4.24, 4.25 we summarize the results. The c lattice parameter is optimized as $c_{\text{uudd}} = 15.089$ Å; that is closer to $c_{\text{A-AFM}} = 15.039$ Å. When we analyse the interplane distances we see that the average MnO_2 planes are closer to LaO layers than SrO as we have seen previously in all cases. In fact the interplane distances, rumpling values and $\text{Mn}-\text{O}$ distances are very similar to those we obtained for A-type antiferromagnetic case.

	$\tilde{z}_{\text{average plane}}$	interplane distances (Å)	rumpling (Å)	$d_{\text{Mn}-\text{O}}$(Å)
SrO	0.005		0	
		1.906		1.858
MnO_2	0.131		-0.048	
		1.866		1.914
LaO	0.255		0	
		1.867		1.913
MnO_2	0.379		0.047	
		1.906		1.859
SrO	0.505		0	
		1.906		1.858
MnO_2	0.631		-0.047	
		1.867		1.914
LaO	0.755		0	
		1.866		1.914
MnO_2	0.879		0.047	
		1.906		1.859

Table 4.24 Table summarizing the structural properties of "↑↑↓↓" ordered $[(\text{LaMnO}_3)_1 - (\text{SrMnO}_3)_1]_2$ superlattice in a SrTiO_3 substrate. The a lattice parameter is fixed at $a = 3.88$ Å. The c lattice parameter is optimized at $c_{\text{uudd}} = 15.089$ Å.

In the table 4.25, we report the magnetic and related structural properties. The charges of each atomic plane are non-zero and they are more or less the same as in the case of A-type antiferomagnetic. The Mn-magnetic moment presents the spin ordering of the system: "↑↑↓↓". The other results are qualitatively the same as for the strained four-layers A-type ferromagnetic superlattice. We observe negative JTd and related e_g occupancy ratio with large dominance in $d_{x^2-y^2}$ occupancy. However, one must note that the dominant $d_{x^2-y^2}$ occupancy that one can get is larger in A-type antiferromagnetic case.

	d_{OO} (Å)	JTd	c' (Å)	$c'/a-1$	magnetic moment (μ_B)	$\frac{\eta_{x^2-y^2}}{\eta_{z^2}}$	total e_g	charge ($\lvert e\rvert$)
SrO								0.607
MnO_2	3.772	-0.028	3.772	-0.028	3.387	1.906	0.677	-0.869
LaO								1.132
MnO_2	3.772	-0.028	3.773	-0.028	3.387	1.901	0.676	-0.869
SrO								0.608
MnO_2	3.772	-0.028	3.772	-0.028	-3.385	1.906	-0.677	-0.869
LaO								1.132
MnO_2	3.772	-0.028	3.772	-0.028	-3.387	1.906	-0.677	-0.869

Table 4.25 Table summarizing the structural and magnetic properties of "↑↑↓↓" ordered $[(LaMnO_3)_1-(SrMnO_3)_1]_2$ superlattice in a $SrTiO_3$ substrate. The a lattice parameter is fixed at $a = 3.88$ Å. The c lattice parameter is optimized at $c_{\text{uudd}} = 15.089$ Å.

↑↓↓↑ Ordering

Another spin allignment which can be tested in such superlattice is ↑↓↓↑ ("uddu"). This configuration is energetically the highest. The structural results are given in tables 4.26. The c lattice parameter is optimized at $c_{\text{uddu}} = 15.133$ Å. Even though the values in interplane distances and $Mn-O$ distances change compared to the previous cases, the same dimerization is still valid here too.

In table 4.27, we give the magnetic and related structural properties. The charges of each atomic plane is non-zero and a little bit less than the ones we see in A-type antiferromagnetic and "↑↑↓↓" cases. The Mn-magnetic moment exhibit the spin ordering of the system: "↑↓↓↑". The other results are similar to A-type antiferromagnetic and "↑↑↓↓" cases. We observe negative JTd and the associated e_g occupancy ratio with dominant $d_{x^2-y^2}$ orbital. However, the e_g occupancy ratio is the smaller than A-type antiferromagnetic and "↑↑↓↓" cases.

4.3.3 Results with $a_{\text{STO}} = 3.905$ Å

Now we study the $[(LMO)_1-(SMO)_1]_2$ superlattice deposited on a substrate where the imposed a lattice parameter is the experimental STO one; that is $a = 3.905$ Å. We computed different magnetic configurations: ferromagnetic, A-type antiferromagnetic "↑↑↓↓" and "↑↓↓↑ orderings. We found that the A-type antiferromagnetic ordering has the lowest

	$\tilde{z}_{\text{average plane}}$	interplane distances (Å)	rumpling (Å)	$d_{\text{Mn}-\text{O}}$(Å)
SrO	-0.005		0	
		1.919		1.874
MnO_2	0.121		-0.045	
		1.865		1.910
LaO	0.245		0	
		1.864		1.909
MnO_2	0.368		0.045	
		1.919		1.874
SrO	0.495		0	
		1.919		1.874
MnO_2	0.621		-0.045	
		1.864		1.909
LaO	0.745		0	
		1.865		1.910
MnO_2	0.868		0.045	
		1.919		1.874

Table 4.26 Table summarizing the structural properties of "↑↓↓↑" ordered $[(LaMnO_3)_1 - (SrMnO_3)_1]_2$ superlattice in a $SrTiO_3$ substrate. The a lattice parameter is fixed at $a = 3.88$ Å. The c lattice parameter is optimized at $c_{\text{uddu}} = 15.133$ Å.

	d_{OO} (Å)	JTd	c' (Å)	$c'/a-1$	magnetic moment (μ_B)	$\frac{\eta_{x^2-y^2}}{\eta_{z^2}}$	total e_g	charge ($\lvert e \rvert$)
SrO								0.594
MnO_2	3.784	-0.025	3.784	-0.025	3.409	1.751	0.685	-0.862
LaO								1.129
MnO_2	3.783	-0.025	3.783	-0.025	-3.408	1.776	-0.683	-0.862
SrO								0.594
MnO_2	3.783	-0.025	3.783	-0.025	-3.407	1.776	-0.683	-0.862
LaO								1.129
MnO_2	3.784	-0.025	3.783	-0.025	3.409	1.751	0.685	-0.862

Table 4.27 Table summarizing the structural and magnetic properties of "↑↓↓↑" ordered $[(LaMnO_3)_1 - (SrMnO_3)_1]_2$ superlattice in a $SrTiO_3$ substrate. The a lattice parameter is fixed at $a = 3.88$ Å. The c lattice parameter is optimized at $c_{\text{uddu}} = 15.133$ Å.

energy ($E_{\mathrm{A-AFM}} - E_{\mathrm{FM}} = -218$ meV (-27 meV), $E_{\mathrm{A-AFM}} - E_{\mathrm{uudd}} \simeq -102$ meV (-13 meV), $E_{\mathrm{A-AFM}} - E_{\mathrm{uddu}} \simeq -280$ meV (35 meV) for whole superlattice (per unit cell)).

Ferromagnetic Ordering

In table 4.28 we report the structural results of the optimized geometry of $[(\mathrm{LMO})_1 - (\mathrm{SMO})_1]_2$ superlattice with imposed $a = 3.905$ Å when spins are ferromagnetically alligned. The c lattice parameter is optimized at $c_{\mathrm{FM}} = 15.152$ Å; this value is consistent with the c lattice parameter optimized for the strained two-layers ferromagnetic system ($c_{\mathrm{FM}} = 15.152$ Å for four-layers and $2 \times c_{\mathrm{FM}} = 2 \times 7.585 = 15.17$ Å for two-layers doubled in $\vec{c}$ direction). The structural properties are qualitatively the same with the strained two-layers ferromagnetic one. The values for interplane distances, rumplings and $\mathrm{Mn-O}$ distances are similar with the strained two-layers ferromagnetic ones. The same dimerization analysis is valid.

	$\tilde{z}_{\text{average plane}}$	interplane distances (Å)	rumpling (Å)	$d_{\mathrm{Mn-O}}$(Å)
SrO	0.000		0	
		1.922		1.876
MnO_2	0.127		-0.047	
		1.865		1.912
LaO	0.250		0	
		1.865		1.912
MnO_2	0.373		0.047	
		1.923		1.876
SrO	0.500		0	
		1.923		1.876
MnO_2	0.627		-0.047	
		1.865		1.912
LaO	0.750		0	
		1.865		1.912
MnO_2	0.873		0.047	
		1.923		1.876

Table 4.28 Table summarizing the structural properties of ferromagnetic $[(\mathrm{LaMnO_3})_1 - (\mathrm{SrMnO_3})_1]_2$ superlattice in a $SrTiO_3$ substrate. The a lattice parameter is fixed at $a = 3.905$ Å. The c lattice parameter is optimized at $c_{\mathrm{FM}} = 15.152$ Å.

In table 4.29, we report the magnetic and related structural properties. The results are qualitatively the same with strained two-layers ferromagnetic superlattice. We observe negative JTd and related e_g occupancy ratio with a dominant in $d_{x^2-y^2}$ occupancy (stronger than the one obtained for fixed $a = 3.88$ Å). These results are different than the ones obtained for strain-free four-layers ferromagnetic superlattice as well.

	d_{OO} (Å)	JTd	c' (Å)	$c'/a-1$	magnetic moment (μ_B)	$\frac{\eta_{x^2-y^2}}{\eta_{z^2}}$	total e_g	charge ($\|e\|$)
SrO								0.592
MnO$_2$	3.788	-0.030	3.788	-0.030	3.444	1.430	0.707	-0.863
LaO								1.136
MnO$_2$	3.788	-0.030	3.788	-0.030	3.445	1.430	0.707	-0.863
SrO								0.591
MnO$_2$	3.788	-0.030	3.788	-0.030	3.445	1.430	0.707	-0.863
LaO								1.136
MnO$_2$	3.789	-0.030	3.789	-0.030	3.444	1.430	0.707	-0.863

Table 4.29 Table summarizing the structural and magnetic properties of ferromagnetic $[(\mathrm{LaMnO_3})_1 - (\mathrm{SrMnO_3})_1]_2$ superlattice in a SrTiO$_3$ substrate. The a lattice parameter is fixed at $a = 3.905$ Å. The c lattice parameter is optimized at $c_{\mathrm{FM}} = 15.152$ Å.

A-type Antiferromagnetic Ordering

We report the results in table 4.30 and table 4.31 for A-type antiferromagnetic LMO-SMO superlattice with fixed $a = 3.88$ Å. The c lattice parameter is optimized as $c_{\mathrm{A-AFM}} = 14.980$ Å; this value is consistent with the c lattice parameter optimized for the strained two-layers A-type ferromagnetic system ($c_{\mathrm{A-AFM}} = 14.980$ Å for four-layers and $2 \times c_{\mathrm{A-AFM}} = 2 \times 7.500 = 15.00$ Å for two-layers doubled in $\vec{c}$ direction). The structural results are qualitatively the same with the A-type AFM ordered two-layers system superlattice with $a = 3.905$ Å.

In table 4.31, we report the magnetic and related structural properties. The results are qualitatively the same with strained two-layers ferromagnetic superlattice at fixed $a = 3.905$ Å. We observe negative JTd and related e_g occupancy ratio with a very dominant in $d_{x^2-y^2}$ occupancy (stronger than the one obtained for fixed $a = 3.88$ Å). We observe more contraction in the $\vec{c}$ direction, thus larger negative JTd and increase in the $d_{x^2-y^2}$ occupancy compared to strain-free four-layers A-type ferromagnetic superlattice.

	$\tilde{z}_{\text{average plane}}$	interplane distances (Å)	rumpling (Å)	$d_{\text{Mn-O}}$(Å)
SrO	-0.007		0	
		1.893		1.848
MnO_2	0.119		-0.046	
		1.852		1.897
LaO	0.243		0	
		1.852		1.897
MnO_2	0.366		0.046	
		1.893		1.848
SrO	0.493		0	
		1.894		1.848
MnO_2	0.619		-0.046	
		1.852		1.897
LaO	0.743		0	
		1.852		1.897
MnO_2	0.866		0.045	
		1.893		1.848

Table 4.30 Table summarizing the structural properties of A-type antiferromagnetic $[(\mathrm{LaMnO_3})_1 - (\mathrm{SrMnO_3})_1]_2$ superlattice in a $SrTiO_3$ substrate. The a lattice parameter is fixed at $a = 3.905$ Å. The c lattice parameter is optimized at $c_{\text{A-AFM}} = 14.980$ Å.

	d_{OO} (Å)	JTd	c' (Å)	$c'/a - 1$	magnetic moment (μ_B)	$\frac{\eta_{x^2-y^2}}{\eta_{z^2}}$	total e_g	charge ($\lvert e \rvert$)
SrO								0.623
MnO_2	3.745	-0.041	3.745	-0.041	3.38	2.353	0.674	-0.885
LaO								1.148
MnO_2	3.745	-0.041	3.745	-0.041	-3.38	2.353	-0.674	-0.885
SrO								0.623
MnO_2	3.745	-0.041	3.745	-0.041	3.38	2.353	0.674	-0.885
LaO								1.149
MnO_2	3.745	-0.041	3.745	-0.041	-3.38	2.353	-0.674	-0.885

Table 4.31 Table summarizing the structural and magnetic properties of A-type antiferromagnetic $[(\mathrm{LaMnO_3})_1 - (\mathrm{SrMnO_3})_1]_2$ superlattice in a $SrTiO_3$ substrate. The a lattice parameter is fixed at $a = 3.905$ Å. The c lattice parameter is optimized at $c_{\text{A-AFM}} = 14.980$ Å.

↑↑↓↓ and ↑↓↓↑ Orderings

We study also the two other magnetic orderings: "↑↑↓↓" and "↑↓↓↑". The results are given in tables 4.32, 4.33, 4.34, 4.35. The ”uudd“ state is again the intermediate phase between the A-type antiferromagnetic and ferromagnetic cases. The structural and magnetic properties of these configurations are qualitatively the same with the ones obtained for $a = 3.88$ Å.

	$\tilde{z}_{\text{average plane}}$	interplane distances (Å)	rumpling (Å)	$d_{\text{Mn}-\text{O}}$(Å)
SrO	0.000		0	
		1.899		1.852
MnO_2	0.126		-0.047	
		1.857		1.904
LaO	0.250		0	
		1.857		1.904
MnO_2	0.374		0.047	
		1.899		1.8530
SrO	0.500		0	
		1.900		1.853
MnO_2	0.626		-0.047	
		1.857		1.904
LaO	0.750		0	
		1.857		1.904
MnO_2	0.874		0.047	
		1.899		1.852

Table 4.32 Table summarizing the structural properties of "↑↑↓↓" ordered $[(\text{LaMnO}_3)_1 - (\text{SrMnO}_3)_1]_2$ superlattice in a $SrTiO_3$ substrate. The a lattice parameter is fixed at $a = 3.905$ Å. The c lattice parameter is optimized at $c_{\text{uudd}} = 15.027$ Å.

In four-layers system the energy of the A-type antiferromagnetic configuration is lower than the energy of ferromagnetic configuration ($E_{\text{A}-\text{AFM}} - E_{FM} = -13$ meV per unit cell when a is fixed at 3.905 Åand $E_{\text{A}-\text{AFM}} - E_{FM} = -27$ meV per unit cell) when a is fixed at 3.88 Å). Although the energy difference between these two magnetic configuration is higher than two-layers sysem they are still quite small (close to room temperature ($k_B T \sim 25$ meV). This indicates that the magnetic ground state $[(\text{LaMnO}_3)_1 - (\text{SrMnO}_3)_1]_2$ superlattices is quasi-degenerate in our calculations. However, compared to two-layers system, we managed to get the correct ground-state when $a = 3.88$ Å.

	d_{OO} (Å)	JTd	c' (Å)	$c'/a-1$	magnetic moment (μ_B)	$\frac{\eta_{x^2-y^2}}{\eta_{z^2}}$	total e_g	charge ($\lvert e \rvert$)
SrO								0.617
MnO_2	3.756	-0.038	3.756	-0.038	3.392	2.077	0.68	-0.879
LaO								1.141
MnO_2	3.757	-0.038	3.757	-0.038	3.392	2.077	0.68	-0.879
SrO								0.616
MnO_2	3.757	-0.038	3.757	-0.038	-3.392	2.077	-0.68	-0.879
LaO								1.141
MnO_2	3.756	-0.038	3.756	-0.038	-3.392	2.077	-0.68	-0.88

Table 4.33 Table summarizing the structural and magnetic properties of “↑↑↓↓” ordered $[(LaMnO_3)_1-(SrMnO_3)_1]_2$ superlattice in a $SrTiO_3$ substrate. The a lattice parameter is fixed at $a = 3.905$ Å. The c lattice parameter is optimized at $c_{\text{uudd}} = 15.027$ Å.

	$\tilde{z}_{\text{average plane}}$	interplane distances (Å)	rumpling (Å)	$d_{\text{Mn}-\text{O}}$(Å)
SrO	0.000		0	
		1.912		1.868
MnO_2	0.127		-0.044	
		1.854		1.898
LaO	0.250		0	
		1.853		1.898
MnO_2	0.373		0.044	
		1.913		1.868
SrO	0.500		0	
		1.911		1.868
MnO_2	0.627		-0.044	
		1.854		1.897
LaO	0.750		0	
		1.853		1.898
MnO_2	0.873		0.044	
		1.913		1.868

Table 4.34 Table summarizing the structural properties of “↑↓↓↑” ordered $[(LaMnO_3)_1-(SrMnO_3)_1]_2$ superlattice in a $SrTiO_3$ substrate. The a lattice parameter is fixed at $a = 3.905$ Å. The c lattice parameter is optimized at $c_{\text{uddu}} = 15.063$ Å.

	d_{OO} (Å)	JTd	c' (Å)	$c'/a-1$	magnetic moment (μ_B)	$\frac{\eta_{x^2-y^2}}{\eta_{z^2}}$	total e_g	charge ($\lvert e \rvert$)
SrO								0.599
MnO_2	3.766	-0.036	3.765	-0.036	3.414	1.899	0.687	-0.871
LaO								1.14
MnO_2	3.766	-0.036	3.766	-0.036	-3.414	1.899	-0.687	-0.869
SrO								0.599
MnO_2	3.766	-0.036	3.766	-0.036	-3.414	1.899	-0.687	-0.869
LaO								1.14
MnO_2	3.766	-0.036	3.766	-0.036	3.414	1.899	0.687	-0.869

Table 4.35 Table summarizing the structural and magnetic properties of "↑↓↓↑" ordered $[(LaMnO_3)_1-(SrMnO_3)_1]_2$ superlattice in a $SrTiO_3$ substrate. The a lattice parameter is fixed at $a = 3.905$ Å. The c lattice parameter is optimized at $c_{\mathrm{uddu}} = 15.063$ Å.

4.3.4 Analysis of Mn–Mn distances

Finally, we would like to summarize the Mn–Mn distances in each magnetic ordering for these superlattices. First, in table 4.36 we give the Mn–Mn distances for the superlattice in a strain-free environment and within imposed $a = 3.88$ Å. We see the same pattern in all the cases. This alternation between short and long distances is the sign of dimerization. In

	$d_{\mathrm{Mn-Mn}}$ (Å)					
	FM	A-AFM	FM	A-AFM	↑↑↓↓	↑↓↓↑
	Strain-free	Strain-Free	$a = 3.88$ Å	$a = 3.88$ Å	$a = 3.88$ Å	$a = 3.88$ Å
MnO_2	↑	↓	↑	↓	↓	↑
SrO	3.739	3.71	3.772	3.71	3.717	3.748
MnO_2	↑	↑	↑	↑	↑	↑
LaO	3.838	3.812	3.856	3.81	3.827	3.819
MnO_2	↑	↓	↑	↓	↑	↓
SrO	3.737	3.71	3.772	3.71	3.717	3.748
MnO_2	↑	↑	↑	↑	↓	↓
LaO	3.839	3.812	3.856	3.81	3.828	3.819
MnO_2	↑	↓	↑	↓	↓	↑

Table 4.36 Table reporting the $d_{\mathrm{Mn-Mn}}$ values for strain-free and $a = 3.88$ Å for ferromagnetic, A-type antiferromagnetic, "↑↑↓↓","↑↓↓↑", cases. First line is visualized in red to point out it it is the repetition of the fourth MnO_2 plane due to periodicity.

table 4.37 we give the Mn–Mn distances for the superlattice within imposed $a = 3.905$ Å. Again, we see the dimerization in the distances.

	$d_{\mathrm{Mn-Mn}}$ (Å)			
	FM	A-AFM	↑↑↓↓	↑↓↓↑
MnO_2	↑	↓	↓	↑
SrO	3.752	3.696	3.704	3.736
MnO_2	↑	↑	↑	↑
LaO	3.824	3.794	3.808	3.796
MnO_2	↑	↓	↑	↓
SrO	3.752	3.696	3.706	3.736
MnO_2	↑	↑	↓	↓
LaO	3.824	3.794	3.808	3.795
MnO_2	↑	↓	↓	↑

Table 4.37 Table reporting the $d_{\mathrm{Mn-Mn}}$ values for $a = 3.905$ Å for ferromagnetic, A-type antiferromagnetic, “↑↑↓↓”,“↑↓↓↑”, cases. First line is visualized in red to point out it it is the repetition of the fourth MnO_2 plane due to periodicity.

4.4 $[(\mathrm{LaMnO_3})_2-(\mathrm{SrMnO_3})_2]_1$ Superlattice

Until now, we studied one typical cation order regardless of the total number of layers of the superlattice: $[(\mathrm{LaMnO_3})_1-(\mathrm{SrMnO_3})_1]$. We devote this section to another cation ordered system: $(\mathrm{LaMnO_3})_2-(\mathrm{SrMnO_3})_2$. In the former superlattice, the $\mathrm{MnO_2}$ planes were only between SrO and LaO planes. However, in $(\mathrm{LaMnO_3})_2-(\mathrm{SrMnO_3})_2$ superlattice, $\mathrm{MnO_2}$ planes can also be in between either two SrO planes, or two LaO planes. The schematic picture of such superlattice is given in figure 4.11. We studied this superlattice in an artificial strain-free environment and on a substrate where the in-plane lattice parameter is imposed to $a = 3.88$ Å . The magnetic configuration that are investigated are again FM, A-AFM, "uudd" and "uddu". In figure 4.12, we gave energy comparisons of each magnetic ordering. Ferromagnetic configuration in a strain-free environment has the lowest energy.

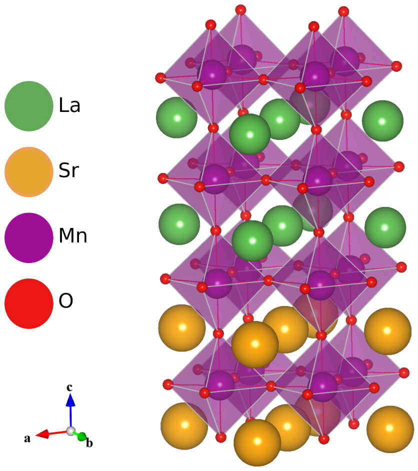

Fig. 4.11 Schematic picture for $(\mathrm{LMO})_2-(\mathrm{SMO})_2$ superlattices

4.4.1 Strain-free Conditions

We first study the superlattice in a strain-free environment. Thus, we can calculate the hypothetical in-plane lattice parameter of this superlattice with different spin alignments. We only took into account ferromagnetic and A-type antiferromagnetic cases. We found that the ferromagnetic ordering is lower in energy than the A-type antiferromagnetic one ($\Delta E = E_{\mathrm{A-AFM}} = E_{\mathrm{FM}} \simeq 226$ meV for whole superlattice, 28 meV per unit cell). The strain-free reference in-plane lattice parameter is optimized at $a_{\mathrm{FM}} = 3.828$ Å for the ferromagnetic ordering while it is optimized at $a_{\mathrm{A-AFM}} = 3.878$ Å for the A-type antiferromagnetic

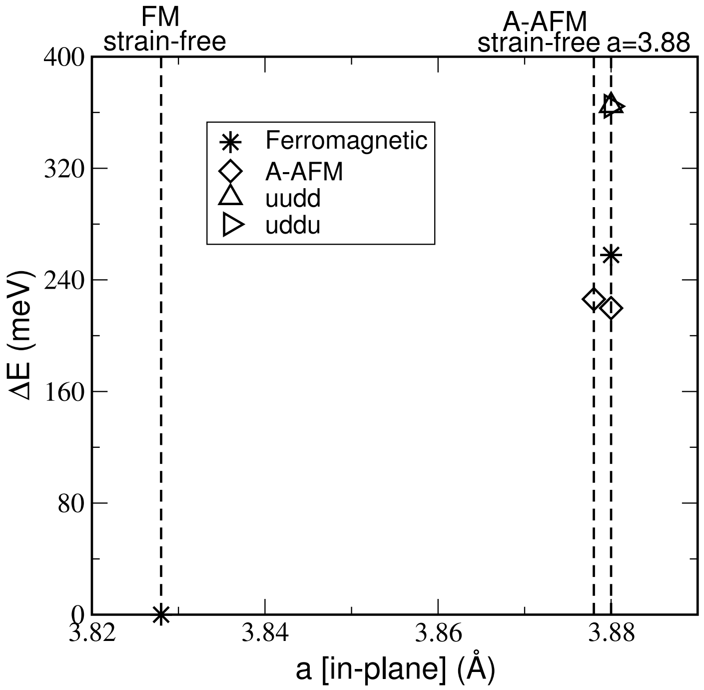

Fig. 4.12 Energy difference of each configuration with respect to the lowest energy ordering and geometry ($\Delta E = E - E_0$) vs. the imposed a in-plane lattice parameter. Here, E_0 is the lowest energy obtained for the ferromagnetic ordering in the strain-free case.

ordering. One can see that that $a_{\text{A-AFM}}$ is consistent with strain-free antiferromagnetic $[(\text{LMO})_1 - (\text{SMO})_1]_2$ superlattice while a_{FM} is smaller than the one of strain-free antiferromagnetic $[(\text{LMO})_1 - (\text{SMO})_1]_2$ superlattice.

Ferromagnetic Ordering

In table 4.38, 4.39, we report the structural and magnetic results of ferromagnetic superlattice. The a lattice parameter is optimized at $a_{\text{FM}} = 3.828$ Å. The c lattice parameter is optimized at $c_{\text{FM}} = 15.566$ Å. The in-plane lattice parameter ($a_{\text{FM}} = 3.828$ Å) is a bit smaller than the one obtained for strain-free ferromagnetic four layers $[(\text{LMO})_1 - (\text{SMO})_1]_2$ superlattice ($a_{\text{FM}} = 3.836$ Å). The optimized c lattice parameter ($c_{\text{FM}} = 15.566$ Å) is greater than the one obtained for strain-free ferromagnetic four layers $[(\text{LMO})_1 - (\text{SMO})_1]_2$ superlattice ($c_{\text{FM}} = 15.152$ Å) and greater than twice of the c lattice parameter of of the strain-free ferromagnetic two-layers ferromagnetic $[(\text{LMO})_1 - (\text{SMO})_1]_1$ superlattice ($2 \times c_{\text{FM}} = 2 \times 7.714 = 15.428$ Å). One can see in table 4.38 that the interplane distance and $d_{\text{Mn-O}}$ values are quite different than the previous systems because of the cation ordering. However, the average LaO planes are still closer to the average MnO_2 planes than the average SrO planes.

	$\tilde{z}_{\text{average plane}}$	interplane distances (Å)	rumpling (Å)	$d_{\text{Mn}-\text{O}}$(Å)
SrO	0.000		0.095	
		1.951		2.044
MnO_2	0.125		0.000	
		1.949		2.044
SrO	0.250		-0.094	
		2.002		1.815
MnO_2	0.379		-0.093	
		1.895		2.038
LaO	0.501		-0.050	
		1.937		1.886
MnO_2	0.618		0.000	
		1.937		1.887
LaO	0.745		0.050	
		1.895		2.037
MnO_2	0.871		0.092	
		2.000		1.814

Table 4.38 Table summarizing the structural properties of ferromagnetic $[(\text{LaMnO}_3)_2 - (\text{SrMnO}_3)_2]$ superlattice in a strain-free environment. The a lattice parameter is optimized at $a_{\text{FM}} = 3.828$ Å. The c lattice parameter is optimized at $c_{\text{FM}} = 15.566$ Å.

From magnetic properties given in the table 4.39, we notice that Mn-octahedra between two SrO layers has the largest thickness (4.089 Å) whereas the Mn-octahedra between two LaO layers has the smallest one (3.773 Å). In the former octahedra the d_{z^2} is preferentially occupied while in the latter $d_{x^2-y^2}$ is occupied. We notice that there is almost no Jahn-Teller distortion in the two other two Mn-octahedras between SrO and LaO layers. Thus, the e_g orbitals are more or less equally occupied in these layers. We also notice that tetragonality has exactly opposite behaviour compared to Jahn-Teller distortion. As we can see the relevant parameter to for the in-plane e_g orbital occupancy (i.e. $d_{x^2-y^2}$) is the Jahn-Teller distortion.

	d_{OO} (Å)	JTd	c' (Å)	$c'/a-1$	magnetic moment (μ_B)	$\frac{\eta_{x^2-y^2}}{\eta_{z^2}}$	total e_g	charge ($\|e\|$)
SrO								0.588
MnO_2	4.089	0.068	3.711	-0.031	3.572	0.353	0.805	-0.918
SrO								0.588
MnO_2	3.853	0.006	3.941	0.029	3.347	1.019	0.654	-0.798
LaO								1.082
MnO_2	3.773	-0.014	3.974	0.038	3.387	1.704	0.668	-0.820
LaO								1.081
MnO_2	3.851	0.006	3.940	0.029	3.345	1.022	0.653	-0.798

Table 4.39 Table summarizing the structural and magnetic properties of ferromagnetic $[(\mathrm{LaMnO_3})_2 - (\mathrm{SrMnO_3})_2]$ superlattice in a strain-free environment. The a lattice parameter is optimized at $a_{\mathrm{FM}} = 3.828$ Å. The c lattice parameter is optimized at $c_{\mathrm{FM}} = 15.566$ Å.

A-type Antiferromagnetic Ordering

We summarize the results for A-type antiferromagnetic strain-free $[(\mathrm{LaMnO_3})_2 - (\mathrm{SrMnO_3})_2]$ superlattice in the tables 4.40 and 4.41.The in-plane lattice parameter is optimized at $a_{\mathrm{A-AFM}} = 3.878$ Å. The c lattice parameter is optimized as $\mathrm{c_{A-AFM}} = 15.064$ Å. One can see in table 4.40 that the average LaO planes are still closer (around 1.833 Å) to the average MnO_2 planes than the average SrO planes (around 1.945 Å) when the MnO_2 plane is in between SrO and LaO but when the MnO_2 plane is sandwiched between only one type of plane then the average SrO planes are closer (1.842 Å) than the average LaO planes (around 1.911 Å). In the table 4.41, we see that all Mn-octahedras are contracted in c direction. Consequently, $d_{x^2-y^2}$ orbital is occupied more than d_{z^2} in all layers. The Mn-octahedras between SrO and LaO planes have the same Jahn-Teller distortion (-0.030) and e_g occupancy

	$\tilde{z}_{\text{average plane}}$	interplane distances (Å)	rumpling (Å)	$d_{\text{Mn}-\text{O}}$(Å)
SrO	0.003		0.051	
		1.842		1.894
MnO_2	0.125		0.000	
		1.842		1.895
SrO	0.247		-0.052	
		1.945		1.819
MnO_2	0.376		-0.074	
		1.833		1.945
LaO	0.498		-0.038	
		1.912		1.875
MnO_2	0.625		0.000	
		1.911		1.874
LaO	0.745		0.037	
		1.833		1.943
MnO_2	0.874		0.073	
		1.944		1.820

Table 4.40 Table summarizing the structural properties of A-type antiferromagnetic $[(\text{LaMnO}_3)_2-(\text{SrMnO}_3)_2]$ superlattice in a strain-free environment. The a lattice parameter is optimized at $a_{\text{A}-\text{AFM}} = 3.878$ Å. The c lattice parameter is optimized at $c_{\text{A}-\text{AFM}} = 15.064$ Å.

ratio (2.406). The Mn-octahedra in between two LaO planes is more contracted (JTd: -0.033) than the one in between two SrO planes (JTd: -0.023). Consequently, the e_g occupancy ratio is higher in the former (2.338) than the latter (1.873).

	d_{OO} (Å)	JTd	c' (Å)	$c'/a-1$	magnetic moment (μ_B)	$\frac{\eta_{x^2-y^2}}{\eta_{z^2}}$	total e_g	charge ($\lvert e \rvert$)
SrO								0.635
MnO_2	3.788	-0.023	3.582	-0.076	3.285	1.873	0.612	-0.872
SrO								0.545
MnO_2	3.764	-0.030	3.791	-0.023	-3.364	2.406	-0.671	-0.872
LaO								1.121
MnO_2	3.749	-0.033	3.899	0.005	3.452	2.338	0.721	-0.894
LaO								1.121
MnO_2	3.763	-0.030	3.940	-0.022	-3.364	2.406	-0.671	-0.872

Table 4.41 Table summarizing the structural and magnetic properties of A-type antiferromagnetic $[(LaMnO_3)_2-(SrMnO_3)_2]$ superlattice in a strain-free environment. The a lattice parameter is optimized at $a_{A-AFM} = 3.878$ Å. The c lattice parameter is optimized at $c_{A-AFM} = 15.064$ Å.

4.4.2 Results with $a_{STO} = 3.88$ Å

Now we take $[(LaMnO_3)_2-(SrMnO_3)_2]$ superlattice deposited on STO substrate where $a_{STO} = 3.88$ Å. We studied FM, A-AFM, "↑↑↓↓" and "↑↓↓↑" magnetic configurations in this superlattice. We found the A-type antiferromagnetic ordering as the lowest energy quite close to ferromagnetic ordering ($E_{A-AFM}-E_{FM} \simeq -38$ meV (-5 meV), $E_{A-AFM}-E_{uudd} \simeq -145$ meV (-18 meV), $E_{A-AFM}-E_{uddu} \simeq -145$ meV (-18 meV) for whole superlattice (per unit cell)).

Ferromagnetic Ordering

In tables 4.42 and 4.43, we report the results for ferromagnetic $[(LaMnO_3)_2-(SrMnO_3)_2]$ superlattice with imposed $a = 3.88$ Å. The c lattice parameter is optimized as $c_{FM} = 15.333$ Å; this value is smaller than the c lattice parameter optimized for the one of strain-free ferromagnetic $[(LaMnO_3)_2-(SrMnO_3)_2]$ superlattice ($c_{FM} = 15.566$ for the strain-free ferromagnetic $[(\mathrm{LaMnO_3})_2-(\mathrm{SrMnO_3})_2]$ superlattice). The average LaO planes are still closer (around 1.864 Å) to the average MnO_2 planes than the average SrO planes (around 1.983 Å) when the MnO_2 plane is in between SrO and LaO but when the MnO_2 plane is sandwiched between only one type of plane then the average SrO planes are closer (1.894 Å) than the average LaO planes (around 1.926 Å). In the table 4.43, one can see that the Mn-octahedra between two SrO layers is elongated (JTd: 0.012) whereas the rest of the Mn-octahedras are all contracted. In the elongated Mn-octahedra, as usual, the d_{z^2} is preferentially occupied. In the Mn-octahedra between two LaO layers, the $d_{x^2-y^2}$ occupancy is dominant. The e_g orbital occupancy is the same in the Mn-octahedras which are between SrO and LaO planes.

	$\tilde{z}_{\text{average plane}}$	interplane distances (Å)	rumpling (Å)	$d_{\text{Mn}-\text{O}}$(Å)
SrO	-0.007		0.069	
		1.894		1.963
MnO_2	0.117		0	
		1.894		1.963
SrO	0.240		-0.07	
		1.983		1.831
MnO_2	0.370		-0.083	
		1.864		1.991
LaO	0.491		-0.045	
		1.926		1.881
MnO_2	0.617		0	
		1.926		1.881
LaO	0.742		0.045	
		1.864		1.991
MnO_2	0.864		0.083	
		1.983		1.831

Table 4.42 Table summarizing the structural properties of ferromagnetic $[(\mathrm{LaMnO_3})_2-(\mathrm{SrMnO_3})_2]$ superlattice on a $SrTiO_3$ substrate. The a lattice parameter is fixed at $a = 3.88$ Å. The c lattice parameter is optimized at $c_{\text{FM}} = 15.333$ Å.

A-type antiferromagnetic Ordering

The results for the A-type antiferromagnetic ordered $(\mathrm{LaMnO_3})_2-(\mathrm{SrMnO_3})_2$ superlattice is given in the tables 4.44 and 4.45. The in-plane lattice parameter is imposed at $a_{\text{A}-\text{AFM}} = 3.88$ Å. The c lattice parameter is optimized as $c_{\text{A}-\text{AFM}} = 15.064$ Å. This is exactly same value

	d_{OO} (Å)	JTd	c' (Å)	$c'/a-1$	magnetic moment (μ_B)	$\frac{\eta_{x^2-y^2}}{\eta_{z^2}}$	total e_g	charge ($\|e\|$)
SrO								0.605
MnO_2	3.926	0.012	3.651	-0.059	3.464	0.646	0.721	-0.882
SrO								0.605
MnO_2	3.822	-0.015	3.870	-0.003	3.423	1.114	0.704	-0.839
LaO								1.105
MnO_2	3.763	-0.030	3.942	0.016	3.452	1.615	0.714	-0.861
LaO								1.105
MnO_2	3.822	-0.015	3.871	-0.002	3.424	1.114	0.704	-0.841

Table 4.43 Table summarizing the structural and magnetic properties of ferromagnetic $[(LaMnO_3)_2-(SrMnO_3)_2]$ superlattice in a $SrTiO_3$ substrate. The a lattice parameter is fixed at $a=3.88$ Å. The c lattice parameter is optimized at $c_{\mathrm{FM}}=15.333$ Å.

that we get for strain-free A-type antiferromagnetic $(LaMnO_3)_2-(SrMnO_3)_2$ superlattice. The average LaO planes are still closer (around 1.833 Å) to the average MnO_2 planes than the average SrO planes (around 1.944 Å) when the MnO_2 plane is in between SrO and LaO but when the MnO_2 plane is sandwiched between only one type of plane then the average SrO planes are closer (1.843 Å) than the average LaO planes (around 1.911 Å). This result is almost the same as the strain-free A-type antiferromagnetic ordering result. As one can see in the table 4.45, all Mn-octahedras are contracted in c direction when the spins are aligned antiparallel in $\vec{c}$ direction. Consequently, $d_{x^2-y^2}$ orbital is occupied more than d_{z^2} in all layers. Again, the e_g orbital occupancy is the same in the Mn-octahedras which are between SrO and LaO planes. The Mn-octahedra in between two LaO planes is more contracted than the one in between two SrO planes. Consequently, the former has higher e_g occupancy. In figure 4.13, we give total and partial densities of states for the $[(LMO)_2-(SMO)_2]$ superlattice in A-type antiferromagnetic configuration. At the down left, we present the total densities of states. Mn atoms contribute to electronic structure at the Fermi level. At the down right, we report the 3d orbitals of Mn atoms in each layer. Here, 1st Mn lies between two SrO layers while 3rd Mn is between two LaO layers. Both have their spins up. The 2nd and 4th Mn have their spins down. At the top panel, we report the 3d orbitals for each Mn more in details. We can clearly see that the $d_{x^2-y^2}$ orbital is more occupied than d_{z^2} in all layers.

	$\tilde{z}_{\text{average plane}}$	interplane distances (Å)	rumpling (Å)	$d_{\text{Mn}-\text{O}}$(Å)
SrO	-0.004		0.052	
		1.843		1.895
MnO_2	0.119		0	
		1.843		1.894
SrO	0.241		-0.051	
		1.944		1.819
MnO_2	0.370		-0.073	
		1.833		1.944
LaO	0.492		-0.037	
		1.911		1.874
MnO_2	0.619		0	
		1.912		1.874
LaO	0.746		0.037	
		1.833		1.944
MnO_2	0.867		0.073	
		1.945		1.819

Table 4.44 Table summarizing the structural properties of A-type antiferromagnetic $[(\text{LaMnO}_3)_2 - (\text{SrMnO}_3)_2]$ superlattice on a $SrTiO_3$ substrate. The a lattice parameter is fixed at $a = 3.88$ Å. The c lattice parameter is optimized at $c_{\text{A-AFM}} = 15.064$ Å.

	d_{OO} (Å)	JTd	c' (Å)	$c'/a-1$	magnetic moment (μ_B)	$\frac{\eta_{x^2-y^2}}{\eta_{z^2}}$	total e_g	charge ($\lvert e \rvert$)
SrO								0.634
MnO_2	3.789	-0.024	3.583	-0.076	3.287	1.878	0.613	-0.872
SrO								0.635
MnO_2	3.763	-0.030	3.790	-0.023	-3.366	2.394	-0.672	-0.819
LaO								1.121
MnO_2	3.748	-0.034	3.898	0.005	3.452	2.353	0.721	-0.896
LaO								1.121
MnO_2	3.763	-0.030	3.793	-0.023	-3.366	2.394	-0.672	-0.873

Table 4.45 Table summarizing the structural and magnetic properties of A-type antiferromagnetic $[(\text{LaMnO}_3)_2 - (\text{SrMnO}_3)_2]$ superlattice on a $SrTiO_3$ substrate. The a lattice parameter is fixed at $a = 3.88$ Å. The c lattice parameter is optimized at $c_{\text{A-AFM}} = 15.064$ Å.

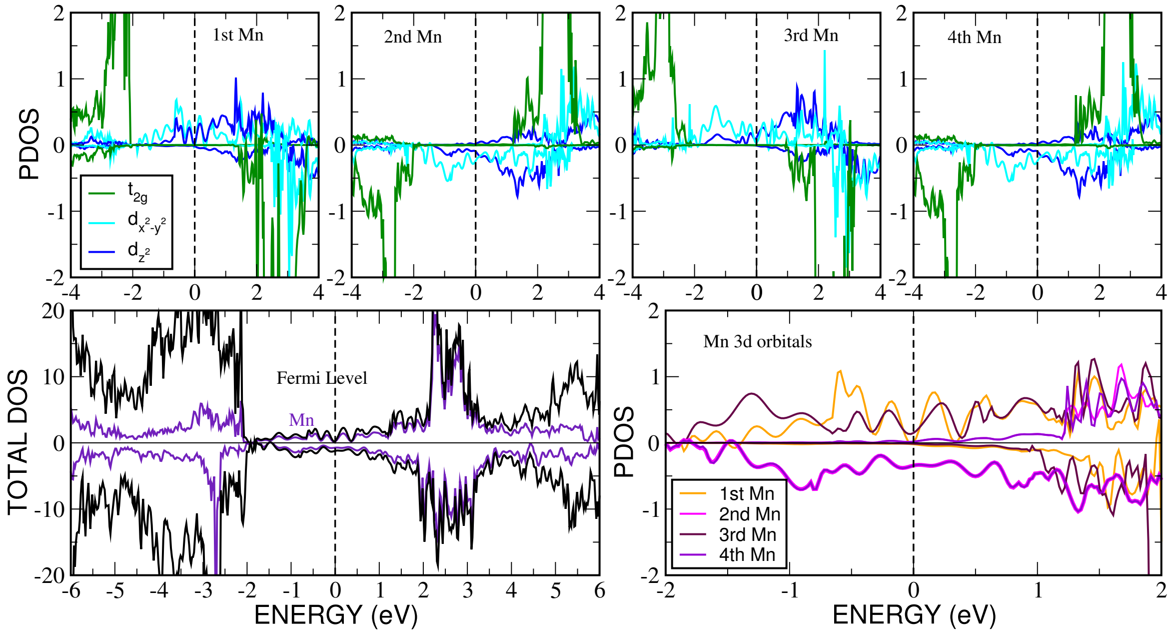

Fig. 4.13 Total and partial densities of states for the $(\mathrm{LMO})_2 - (\mathrm{SMO})_2)$ superlattice in A-type antiferromagnetic configuration. At the bottom panel, total density of states and Mn contribution is given.

“↑↑↓↓” and “↑↓↓↑” Orderings

The results for the “uudd” and “uddu magnetic configurations are qualitatively similar to the A-type antiferromagnetic ordered superlattice even though the structural parameters can change from one to another. The results given in the tables 4.47, 4.47 for “uudd” and in tables 4.47, 4.47 for “uddu”.

	$\tilde{z}_{\text{average plane}}$	interplane distances (Å)	rumpling (Å)	$d_{\text{Mn}-\text{O}}$(Å)
SrO	-0.005		0.057	
		1.851		1.906
MnO_2	0.117		-0.003	
		1.862		1.920
SrO	0.240		-0.055	
		1.963		1.833
MnO_2	0.370		-0.074	
		1.839		1.953
LaO	0.492		-0.040	
		1.916		1.874
MnO_2	0.618		-0.002	
		1.917		1.882
LaO	0.745		0.036	
		1.842		1.954
MnO_2	0.866		0.076	
		1.952		1.819

Table 4.46 Table summarizing the structural properties of "↑↑↓↓" ordered $[(\text{LaMnO}_3)_2 - (\text{SrMnO}_3)_2]$ superlattice on a $SrTiO_3$ substrate. The a lattice parameter is fixed at $a = 3.88$ Å. The c lattice parameter is optimized at $c_{\text{uudd}} = 15.141$ Å.

	d_{OO} (Å)	JTd	c' (Å)	$c'/a-1$	magnetic moment (μ_B)	$\frac{\eta_{x^2-y^2}}{\eta_{z^2}}$	total e_g	charge ($\|e\|$)
SrO								0.625
MnO_2	3.826	-0.014	3.601	-0.072	3.346	1.419	0.646	-0.869
LaO								0.615
MnO_2	3.786	-0.024	3.816	-0.016	3.403	1.775	0.691	-0.858
SrO								1.114
MnO_2	3.757	-0.032	3.909	0.007	-3.460	2.103	-0.723	-0.888
LaO								1.115
MnO_2	3.772	-0.028	3.815	-0.017	-3.355	2.108	-0.662	-0.856

Table 4.47 Table summarizing the structural and magnetic properties of "↑↑↓↓" ordered $[(\text{LaMnO}_3)_2 - (\text{SrMnO}_3)_2]$ superlattice on a $SrTiO_3$ substrate. The a lattice parameter is fixed at $a = 3.88$ Å. The c lattice parameter is optimized at $c_{\text{uudd}} = 15.141$ Å.

	$\tilde{z}_{\text{average plane}}$	interplane distances (Å)	rumpling (Å)	$d_{\text{Mn}-\text{O}}$(Å)
SrO	-0.004		0.056	
		1.862		1.920
MnO_2	0.119		0.002	
		1.852		1.906
SrO	0.241		-0.058	
		1.951		1.818
MnO_2	0.370		-0.076	
		1.842		1.954
LaO	0.492		-0.036	
		1.917		1.883
MnO_2	0.618		0.002	
		1.916		1.875
LaO	0.745		0.040	
		1.839		1.954
MnO_2	0.866		0.074	
		1.963		1.833

Table 4.48 Table summarizing the structural properties of "↑↓↓↑" ordered $[(\text{LaMnO}_3)_2-(\text{SrMnO}_3)_2]$ superlattice on a $SrTiO_3$ substrate. The a lattice parameter is fixed at $a = 3.88$ Å. The c lattice parameter is optimized at $c_{\text{uddu}} = 15.143$ Å.

	d_{OO} (Å)	JTd	c' (Å)	$c'/a-1$	magnetic moment (μ_B)	$\frac{\eta_{x^2-y^2}}{\eta_{z^2}}$	total e_g	charge ($\lvert e\rvert$)
SrO								0.615
MnO_2	3.826	-0.014	3.602	-0.072	3.347	1.419	0.646	-0.869
LaO								0.625
MnO_2	3.773	-0.028	3.813	-0.017	-3.355	2.108	0.646	-0.856
SrO								1.115
MnO_2	3.757	-0.032	3.910	0.008	-3.461	2.094	-0.724	-0.888
LaO								1.114
MnO_2	3.782	-0.024	3.818	-0.016	3.404	1.775	0.691	-0.857

Table 4.49 Table summarizing the structural and magnetic properties of "↑↓↓↑" ordered $[(\text{LaMnO}_3)_2-(\text{SrMnO}_3)_2]$ superlattice on a $SrTiO_3$ substrate. The a lattice parameter is fixed at $a = 3.88$ Å. The c lattice parameter is optimized at $c_{\text{uddu}} = 15.143$ Å.

4.4.3 Analysis of Mn–Mn distances

Finally, we would like to summarize the Mn–Mn distances in each magnetic ordering for these superlattices. First, in table 4.50 we give the Mn–Mn distances for the superlattice within imposed $a = 3.88$ Å. We see the same pattern in the distances for all magnetic orderings. This pattern is the sign of a tetramerization of the system.

	$d_{\mathrm{Mn-Mn}}$ (Å)					
	FM Strain-free	A-AFM Strain-Free	FM $a = 3.88$ Å	A-AFM $a = 3.88$ Å	↑↑↓↓ $a = 3.88$ Å	↑↓↓↑ $a = 3.88$ Å
MnO_2	↑	↓	↑	↓	↓	↑
SrO	3.858	3.714	3.794	3.714	3.725	3.753
MnO_2	↑	↑	↑	↑	↑	↑
SrO	3.859	3.714	3.794	3.713	3.753	3.724
MnO_2	↑	↓	↑	↓	↑	↓
LaO	3.924	3.82	3.872	3.818	3.827	3.837
MnO_2	↑	↑	↑	↑	↓	↓
LaO	3.924	3.817	3.872	3.818	3.836	3.829
MnO_2	↑	↓	↑	↓	↓	↑

Table 4.50 Table reporting the $d_{\mathrm{Mn-Mn}}$ values for strain-free and $a = 3.88$ Å for ferromagnetic, A-type antiferromagnetic, “↑↑↓↓”,“↑↓↓↑”, cases. First line is visualized in red to point out it it is the repetition of the fourth MnO_2 plane due to periodicity.

4.5 $[(\mathbf{LaMnO_3})_2-(\mathbf{SrMnO_3})_1]_1$ Superlattice

In this section, we focus on the $(\mathrm{LaMnO_3})_2-(\mathrm{SrMnO_3})_1$ superlattice. In figure 4.14, one can see the schematic representation of such superlattice. As we studied in previous sections, we also studied $(\mathrm{LaMnO_3})_2-(\mathrm{SrMnO_3})_1$ superlattice in a strain-free environment to determine its strain-free lattice parameters for ferromagnetic ordering. We also studied this superlattice on a STO superlattice where the in-plane lattice parameter is either imposed $a = 3.88$ or $a = 3.905$ Å. In such superlattice, other than FM and A-AFM one can also study the magnetic orderings such as "↑↑↓", "↑↓↓", "↓↑↑" and "↓↓↑". Though these magnetic orderings are expected to be higher in energy we studied them when a lattice parameter is imposed at 3.905 Å. In figure 4.15, we give the energy comparisons for different magnetic configuration with the lowest energy state with respect to a lattice parameter. The lowest energy is obtained for the ferromagnetic case in a strain-free environment.

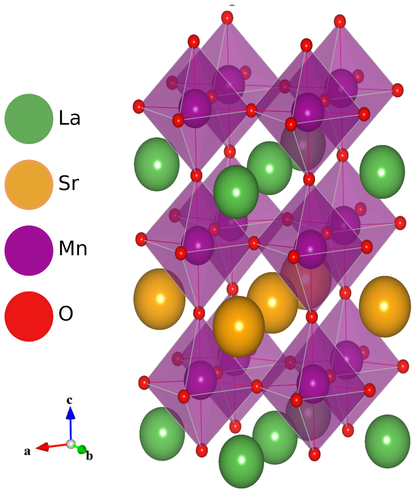

Fig. 4.14 Schematic picture for LMO-SMO superlattices

4.5.1 Strain-free conditions

We start to study the superlattice in a strain-free environment for ferromagnetic ordering. The strain-free reference in-plane lattice parameter is optimized at $a_{\mathrm{FM}} = 3.848$ Å for the ferromagnetic ordering.

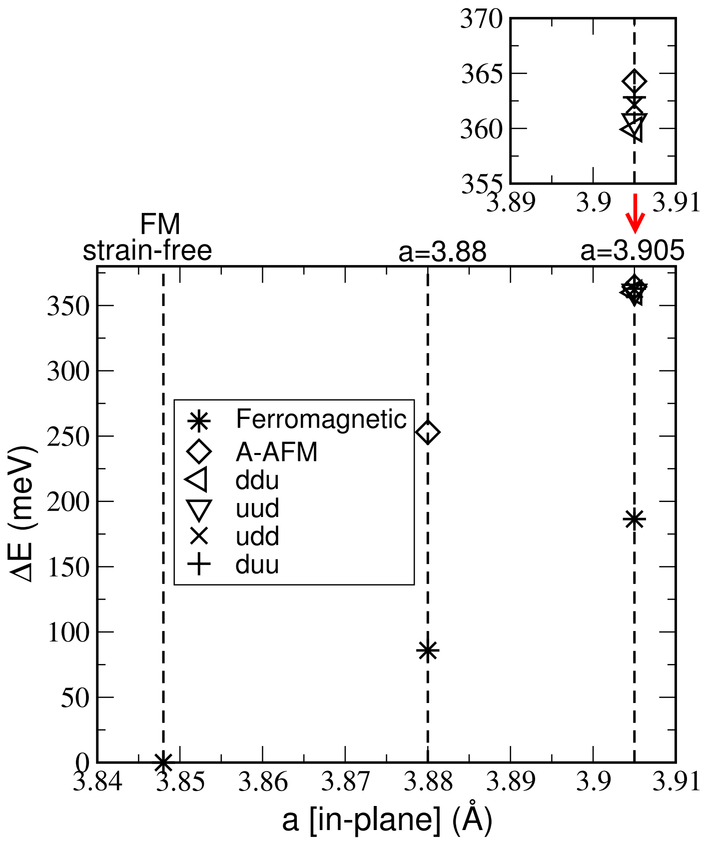

Fig. 4.15 Energy difference of each configuration with respect to the lowest energy ordering and geometry ($\Delta E = E - E_0$) vs. the imposed *a* in-plane lattice parameter. Here, E_0 is the lowest energy obtained for the ferromagnetic ordering in the strain-free case.

Ferromagnetic Ordering

In tables 4.51 and 4.52, we report the structural and magnetic properties of ferromagnetic $(\mathrm{LMO})_2 - (\mathrm{SMO})_1$ superlattice in strain-free environment. The a lattice parameter is optimized at $a_{\mathrm{FM}} = 3.848$ Å. The c lattice parameter is optimized at $c_{\mathrm{FM}} = 11.679$ Å. When we take a look at the interplane distances we again notice that the average LaO planes are closer to average $\mathrm{MnO_2}$ planes than average SrO planes. This is the reverse when we take a look at $d_{\mathrm{Mn-O}}$ values. The oxygen of SrO plane is closer to the Mn of $\mathrm{MnO_2}$ plane than the oxygen of LaO plane. However, there is a sign of spontanous symmetry breaking in these values. Indeed, in table 4.52, we notice that the Mn-octahedra has different thickness in each mono-layer. Although one can expect to have the same JTd ratio for the Mn-octahedras between the LaO and SrO planes we see that they have different values (JTd: 0.057 and -0.004). This spontaneous symmetry breaking happens in this 3-layers system in a strain-free environment for ferromagnetic ordering because the double-exchange mechanism favours to have delocalization in plane. Thus, when the lattice parameters are free to relax, the in-plane lattice parameter is as shortened as possible in order to maximize this in-plane delocalization. However, due to the elastic energy, the volume of the cell has to be preserved. Thus, one of Mn-octahedra between LaO and SrO planes is elongated (4.066 Å) along the $\vec{c}$ direction as a result.

	$\tilde{z}_{\text{average plane}}$	interplane distances (Å)	rumpling (Å)	$d_{\mathrm{Mn-O}}$(Å)
LaO	-0.002		0.067	
		1.935		2.071
$\mathrm{MnO_2}$	0.163		0.069	
		2.030		1.995
SrO	0.337		-0.034	
		1.952		1.852
$\mathrm{MnO_2}$	0.504		-0.066	
		1.888		1.982
LaO	0.666		-0.002	
		1.935		1.912
$\mathrm{MnO_2}$	0.832		0.000	
		1.939		1.868

Table 4.51 Table summarizing the structural properties of ferromagnetic $[(\mathrm{LaMnO_3})_2 - (\mathrm{SrMnO_3})_1]_1$ superlattice in a strain-free environment. The a lattice parameter is optimized at $a_{\mathrm{FM}} = 3.848$ Å. The c lattice parameter is optimized at $c_{\mathrm{FM}} = 11.679$ Å.

	d_{OO} (Å)	JTd	c' (Å)	$c'/a-1$	magnetic moment (μ_B)	$\frac{\eta_{x^2-y^2}}{\eta_{z^2}}$	total e_g	charge ($\|e\|$)
LaO								1.077
MnO_2	4.066	0.057	3.862	0.004	3.798	0.498	0.971	-0.971
SrO								0.532
MnO_2	3.834	-0.004	3.849	0.000	3.459	1.188	0.722	-0.854
LaO								1.070
MnO_2	3.779	-0.018	3.968	0.031	3.482	1.500	0.735	-0.854

Table 4.52 Table summarizing the structural and magnetic properties of ferromagnetic $[(\mathrm{LaMnO_3})_2-(\mathrm{SrMnO_3})_1]_1$ superlattice in a strain-free environment. The a lattice parameter is optimized at $a_{\mathrm{FM}}=3.848$ Å. The c lattice parameter is optimized at $c_{\mathrm{FM}}=11.679$ Å.

4.5.2 Results with $a_{\mathrm{STO}}=3.88$ Å

Now we look at the $[(\mathrm{LaMnO_3})_2-(\mathrm{SrMnO_3})_1]_1$ superlattice deposited on STO substrate. The imposed a lattice parameter is the one that we optimized within our calculations: $a=3.88$ Å. We computed two different magnetic orderings: ferromagnetic and A-type antiferromagnetic. We have found the ferromagnetic ordering as the lowest energy ($E_{\mathrm{A-AFM}}-E_{\mathrm{FM}}=$ 167 meV for the whole superlattice and 28 meV per unit cell).

Ferromagnetic Ordering

In table 4.53, we report the structural properties of the optimized geometry of $[(\mathrm{LaMnO_3})_2-(\mathrm{SrMnO_3})_1]_1$ superlattice with imposed $a=3.88$ Åwhen spins are ferromagnetically aligned. The c lattice parameter is optimized at $c_{\mathrm{FM}}=11.555$ Å. When we check the interplane distances for two layers where MnO_2 planes are sandwiched between LaO and SrO planes, we again see that the average LaO planes are closer to the average MnO_2 planes (around 1.883Å) than the average SrO planes (around 1.963 Å). When MnO_2 plane is only sandwiched between two LaO planes the interplane distance between the average LaO and MnO_2 planes is 1.930 Å.

In table 4.54, we report the magnetic and related structural properties. The results are very different than the ones of the strain-free $[(\mathrm{LaMnO_3})_2-(\mathrm{SrMnO_3})_1]_1$ ferromagnetic superlattice. There is no symmetry breaking in this case. The two Mn-octahedra that are between LaO and SrO planes have the equivalent JTd (0.001 and 0.002) and $c'/a-1$ values (-

	$\tilde{z}_{\text{average plane}}$	interplane distances (Å)	rumpling (Å)	$d_{\text{Mn-O}}$(Å)
LaO	-0.218		0.037	
		1.883		1.983
MnO_2	-0.055		0.063	
		1.963		1.899
SrO	0.115		0.001	
		1.965		1.904
MnO_2	0.285		-0.063	
		1.884		1.986
LaO	0.448		-0.039	
		1.930		1.891
MnO_2	0.615		0.000	
		1.930		1.892

Table 4.53 Table summarizing the structural properties of ferromagnetic $[(LaMnO_3)_2-(SrMnO_3)_1]_1$ superlattice on a $SrTiO_3$. The a lattice parameter is fixed at $a = 3.88$ Å. The c lattice parameter is optimized at $c_{FM} = 11.555$ Å.

0.018) with each other. In both of the Mn-octahedra, the e_g occupancy ratio shows that $d_{x^2-y^2}$ and d_{z^2} occupied more or less equivalently (0.924 and 0.903). The Mn-octahedra between two LaO planes is contracted the most (JTd: -0.025) with largest e_g occupancy ratio (1.415). In figure 4.16, we give the density of states of ferromagnetic $[(LaMnO_3)_2-(SrMnO_3)_1]_1$ superlattice with imposed $a = 3.88$ Å. One can see that in the 1st and 2nd manganese (between the planes LaO and SrO), $d_{x^2-y^2}$ and d_{z^2} are equivalently stabilized. In the 3rd Mn (between two LaO planes), $d_{x^2-y^2}$ orbital preferentially occupied.

	d_{OO} (Å)	JTd	c' (Å)	$c'/a-1$	magnetic moment (μ_B)	$\frac{\eta_{x^2-y^2}}{\eta_{z^2}}$	total e_g	charge ($\lvert e\rvert$)
LaO								1.089
MnO_2	3.882	0.001	3.810	-0.018	3.623	0.924	0.839	-0.919
SrO								0.555
MnO_2	3.890	0.002	3.810	-0.018	3.636	0.903	0.847	-0.924
LaO								1.09
MnO_2	3.783	-0.025	3.936	0.014	3.552	1.415	0.785	-0.893

Table 4.54 Table summarizing the structural and magnetic properties of ferromagnetic $[(LaMnO_3)_2-(SrMnO_3)_1]_1$ superlattice on a $SrTiO_3$. The a lattice parameter is fixed at $a = 3.88$ Å. The c lattice parameter is optimized at $c_{FM} = 11.555$ Å.

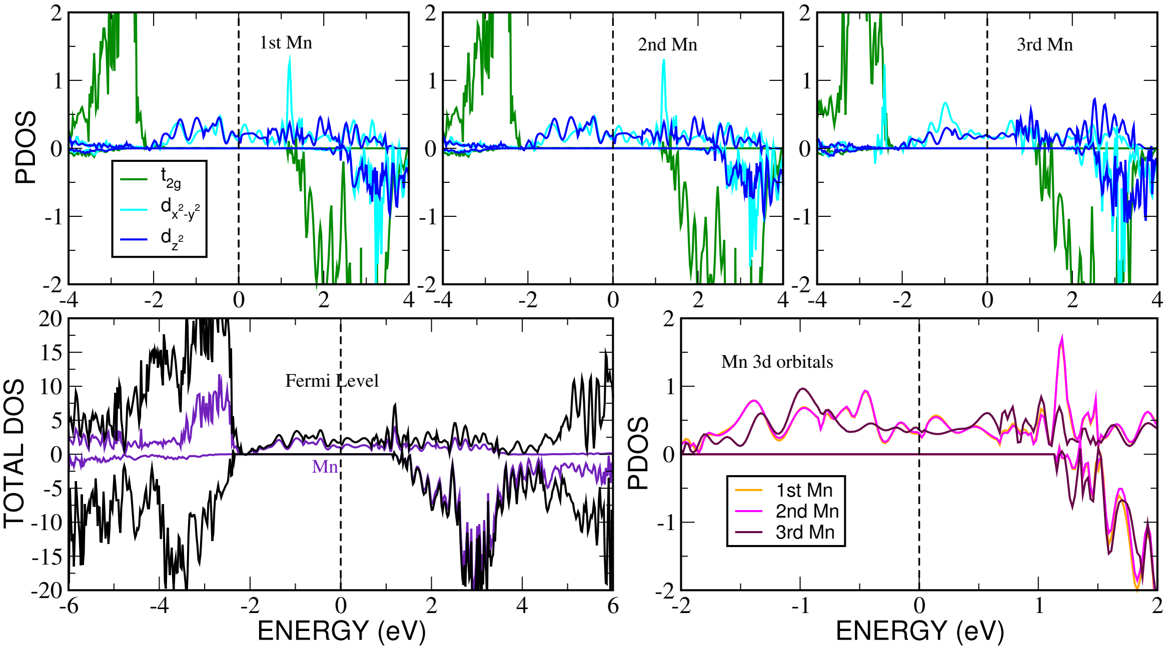

Fig. 4.16 Total and partial densities of states of $[(\mathrm{LaMnO_3})_2-(\mathrm{SrMnO_3})_1]_1$ superlattice on a $\mathrm{SrTiO_3}$ substrate where $a = 3.88$ Å.

A-type antiferromagnetic Ordering

In tables 4.55 and 4.56, we summarize the results of A-type antiferromagnetic $[(\mathrm{LaMnO_3})_2-(\mathrm{SrMnO_3})_1]_1$ superlattice with imposed $a = 3.88$ Å. The c lattice parameter is optimized at $c_{\mathrm{A-AFM}=11.585}$ Å. For two first layers where $\mathrm{MnO_2}$ planes are sandwiched between LaO and SrO planes, we see that antiferromagnetism in the $\vec{c}$ direction affects the symmetry in the interplane distances and $d_{\mathrm{Mn-O}}$ values (for example, the interplane distance between the average LaO and $\mathrm{MnO_2}$ planes are 1.924 and 1.851 Å whereas this value was around 1.883 Å in ferromagnetic ordering).

In table 4.56, we report the magnetic and related structural results of A-type antiferromagnetic $[(\mathrm{LaMnO_3})_2-(\mathrm{SrMnO_3})_1]_1$ superlattice with imposed $a = 3.88$ Å. The effect of antiferromagnetism in the $\vec{c}$ direction is again clear in the thickness of the Mn-octahedras between LaO and SrO planes. The first one is elongated (JTd: 0.051) with a dominant d_{z^2} occupancy, the second is contracted (JTd: -0.035) with a dominant $d_{x^2-y^2}$ occupancy. The Mn-octahedra between two LaO planes is also contracted (JTd: -0.030) with a dominant $d_{x^2-y^2}$ occupancy.

	$\tilde{z}_{\text{average plane}}$	interplane distances (Å)	rumpling (Å)	$d_{\text{Mn}-\text{O}}$(Å)
LaO	-0.226		0.072	
		1.924		2.068
MnO_2	-0.100		0.072	
		2.036		2.010
SrO	0.075		-0.046	
		1.922		1.813
MnO_2	0.241		-0.064	
		1.851		1.932
LaO	0.401		-0.017	
		1.923		1.910
MnO_2	0.567		0.005	
		1.929		1.853

Table 4.55 Table summarizing the structural properties of A-type ferromagnetic $[(\text{LaMnO}_3)_2 - (\text{SrMnO}_3)_1]_1$ superlattice on a SrTiO_3. The a lattice parameter is fixed at $a = 3.88$ Å. The c lattice parameter is optimized at $c_{\text{A}-\text{AFM}} = 11.585$ Å.

	d_{OO} (Å)	JTd	c' (Å)	$c'/a-1$	magnetic moment (μ_B)	$\frac{\eta_{x^2-y^2}}{\eta_{z^2}}$	total e_g	charge ($\lvert e\rvert$)
LaO								1.101
MnO_2	4.078	0.051	3.842	-0.010	3.833	0.438	1.004	-0.999
SrO								0.532
MnO_2	3.745	-0.035	3.802	-0.020	-3.281	2.764	-0.591	-0.851
LaO								1.097
MnO_2	3.763	-0.030	3.936	0.016	3.493	1.596	0.745	-0.878

Table 4.56 Table summarizing the structural and magnetic properties of A-type ferromagnetic $[(\text{LaMnO}_3)_2 - (\text{SrMnO}_3)_1]_1$ superlattice on a SrTiO_3. The a lattice parameter is fixed at $a = 3.88$ Å. The c lattice parameter is optimized at $c_{\text{A}-\text{AFM}} = 11.585$ Å.

4.5.3 Results with $a_{\mathrm{STO}} = 3.905$ Å

Now we study the $[(\mathrm{LaMnO_3})_2 - (\mathrm{SrMnO_3})_1]_1$ superlattice deposited on a substrate where the imposed a lattice parameter is the experimental one: $a = 3.905$ Å. We computer different magnetic orderings: ferromagnetic, A-type antiferromagnetic, "↑↑↓", "↑↓↓", "↓↑↑" and "↓↓↑" orderings. We have found ferromagnetic ordering as the lowest energy ($E_{\mathrm{A-AFM}} - E_{\mathrm{FM}} = 178$ meV (30 meV), $E_{\mathrm{A-AFM}} - E_{\mathrm{uud}} = 4$ meV (0.6 meV), $E_{\mathrm{A-AFM}} - E_{\mathrm{udd}} = 2$ meV (0.4 meV), $E_{\mathrm{A-AFM}} - E_{\mathrm{duu}} = 1$ meV (0.2 meV), $E_{\mathrm{A-AFM}} - E_{\mathrm{ddu}} = 4$ meV (0.7 meV) for the whole superlattice (per unit cell)). All other antiferromagnetic orderings are quasi-degenerate.

Ferromagnetic Ordering

In table 4.57, we report the structural properties of the optimized geometry for the $[(\mathrm{LaMnO_3})_2 - (\mathrm{SrMnO_3})_1]_1$ superlattice with imposed $a = 3.905$ Åwhen spins are ferromagnetically aligned. The c lattice parameter is optimized at $c_{\mathrm{FM}} = 11.508$ Å. When we check the interplane distances for two layers where $\mathrm{MnO_2}$ planes are sandwiched between LaO and SrO planes, we again see that the average LaO planes are closer to the average $\mathrm{MnO_2}$ planes (around 1.875Å) than the average SrO planes (around 1.957 Å). When $\mathrm{MnO_2}$ plane is only sandwiched between two LaO planes the interplane distance between the average LaO and $\mathrm{MnO_2}$ planes is 1.922 Å.

In table 4.58, we report the magnetic and related structural results of $[(\mathrm{LaMnO_3})_2 - (\mathrm{SrMnO_3})_1]_1$ superlattice with imposed $a = 3.905$ Å. The two Mn-octahedra that are between LaO and SrO planes have the equivalent JTd (-0.009 and -0.010) and $c'/a - 1$ values (-0.028) with each other. In both of the Mn-octahedra, the e_g occupancy ratio shows that $d_{x^2-y^2}$ and d_{z^2} occupied more or less equivalently (0.938 and 0.949). The Mn-octahedra between two LaO planes is contracted the most (JTd: -0.035) with largest e_g occupancy ratio (1.494).

A-type antiferromagnetic Ordering

We report the results in table 4.59 and table 4.60 for A-type antiferromagnetic $[(\mathrm{LaMnO_3})_2 - (\mathrm{SrMnO_3})_1]_1$ superlattice with fixed $a = 3.905$ Å. The c lattice parameter is optimized at $c_{\mathrm{A-AFM}} = 11.414$ Å.

For two first layers where $\mathrm{MnO_2}$ planes are sandwiched between LaO and SrO planes, we again see that antiferromagnetism in the $\vec{c}$ direction affects the symmetry in the interplane

	$\tilde{z}_{\text{average plane}}$	interplane distances (Å)	rumpling (Å)	$d_{\text{Mn-O}}$(Å)
LaO	0.000		0.038	
		1.875		1.974
MnO_2	0.163		0.062	
		1.957		1.897
SrO	0.333		-0.002	
		1.958		1.895
MnO_2	0.503		-0.062	
		1.873		1.973
LaO	0.666		-0.038	
		1.922		1.885
MnO_2	0.833		0.000	
		1.922		1.884

Table 4.57 Table summarizing the structural properties of ferromagnetic $[(\text{LaMnO}_3)_2 - (\text{SrMnO}_3)_1]_1$ superlattice on a SrTiO_3. The a lattice parameter is fixed at $a = 3.905$ Å. The c lattice parameter is optimized at $c_{\text{FM}} = 11.508$ Å.

	d_{OO} (Å)	JTd	c' (Å)	$c'/a - 1$	magnetic moment (μ_B)	$\frac{\eta_{x^2-y^2}}{\eta_{z^2}}$	total e_g	charge ($\|e\|$)
LaO								1.1
MnO_2	3.871	-0.009	3.794	-0.028	3.641	0.938	0.849	-0.932
SrO								0.563
MnO_2	3.867	-0.010	3.794	-0.028	3.634	0.949	0.844	-0.927
LaO								1.1
MnO_2	3.769	-0.035	3.920	0.004	3.559	1.494	0.788	-0.903

Table 4.58 Table summarizing the structural and magnetic properties of ferromagnetic $[(\text{LaMnO}_3)_2 - (\text{SrMnO}_3)_1]_1$ superlattice on a SrTiO_3. The a lattice parameter is fixed at $a = 3.905$ Å. The c lattice parameter is optimized at $c_{\text{FM}} = 11.508$ Å.

distances and $d_{\text{Mn}-\text{O}}$ values (for example, the interplane distance between the average LaO and MnO_2 planes are 1.856 and 1.832 Å whereas this value was around 1.875 Å in ferromagnetic ordering). The magnetic and related strucutral results are given in table 4.60.

	$\tilde{z}_{\text{average plane}}$	interplane distances (Å)	rumpling (Å)	$d_{\text{Mn}-\text{O}}$(Å)
LaO	0.001		0.034	
		1.856		1.949
MnO_2	0.164		0.059	
		1.957		1.916
SrO	0.336		-0.017	
		1.910		1.834
MnO_2	0.503		-0.058	
		1.832		1.906
LaO	0.663		-0.016	
		1.933		1.917
MnO_2	0.833		0.000	
		1.926		1.892

Table 4.59 Table summarizing the structural properties of A-type antiferromagnetic $[(LaMnO_3)_2 - (SrMnO_3)_1]_1$ superlattice on a $SrTiO_3$. The a lattice parameter is fixed at $a = 3.905$ Å. The c lattice parameter is optimized at $c_{\text{A}-\text{AFM}} = 11.414$ Å.

We see the effect of antiferromagnetism in the $\vec{c}$ direction in the two first layers where the Mn-octahedras are between LaO and SrO planes. They are both contracted but they have different Jahn-Teller distortion values (-0.010 and -0.042) and e_g occupancy ratios (1.005 and 2.964). The Mn-octahedra between two LaO planes is also contracted (JTd: -0.025) with a dominant $d_{x^2-y^2}$ occupancy as well.

"↑↑↓", "↑↓↓", "↓↑↑" and "↓↓↑" Orderings

We also study the magnetic orderings: "↑↑↓", "↑↓↓", "↓↑↑" and "↓↓↑". The results are given tables 4.61, 4.62, 4.63, 4.64, 4.65, 4.66, 4.67 and 4.68. The results in the "↑↓↓" and "↓↑↑" orderings are consistent with the A-type antiferromagnetic ordering because the spins of the manganese atoms of the two MnO_2 planes that are between LaO and SrO planes are antiparallel as it was in A-type antiferromagnetic ordering. On the other hand, in the "↑↑↓" and "↓↓↑" orderings, the spins in the MnO_2 planes between LaO and SrO planes are parallel. Thus, the results in these orderings are consistent with the ferromagnetic ordered superlattice.

	d_{OO} (Å)	JTd	c' (Å)	$c'/a-1$	magnetic moment (μ_B)	$\frac{\eta_{x^2-y^2}}{\eta_{z^2}}$	total e_g	charge ($\lvert e\rvert$)
LaO								1.118
MnO_2	3.865	-0.010	3.761	-0.037	3.659	1.005	0.874	-0.958
SrO								0.575
MnO_2	3.741	-0.042	3.745	-0.041	-3.372	2.964	-0.658	-0.905
LaO								1.105
MnO_2	3.809	-0.025	3.908	0.001	3.632	1.191	0.848	-0.936

Table 4.60 Table summarizing the structural and magnetic properties of A-type antiferromagnetic $[(\mathrm{LaMnO_3})_2 - (\mathrm{SrMnO_3})_1]_1$ superlattice on a $SrTiO_3$. The a lattice parameter is fixed at $a = 3.905$ Å. The c lattice parameter is optimized at $c_{\mathrm{A-AFM}} = 11.414$ Å.

	$\tilde{z}_{\text{average plane}}$	interplane distances (Å)	rumpling (Å)	$d_{\mathrm{Mn-O}}$(Å)
LaO	-0.001		0.044	
		1.872		1.977
MnO_2	0.163		0.060	
		1.951		1.891
SrO	0.333		-0.001	
		1.954		1.893
MnO_2	0.504		-0.060	
		1.871		1.978
LaO	0.667		-0.045	
		1.902		1.856
MnO_2	0.833		0.000	
		1.902		1.857

Table 4.61 Table summarizing the structural properties of "↑↑↓" ordered $[(\mathrm{LaMnO_3})_2 - (\mathrm{SrMnO_3})_1]_1$ superlattice on a $SrTiO_3$. The a lattice parameter is fixed at $a = 3.905$ Å. The c lattice parameter is optimized at $c_{\mathrm{uud}} = 11.452$ Å.

	d_{OO} (Å)	JTd	c' (Å)	$c'/a-1$	magnetic moment (μ_B)	$\frac{\eta_{x^2-y^2}}{\eta_{z^2}}$	total e_g	charge ($\lvert e\rvert$)
LaO								1.11
MnO_2	3.868	-0.009	3.776	-0.033	3.652	1.000	0.862	-0.946
SrO								0.569
MnO_2	3.871	-0.009	3.776	-0.033	3.656	0.989	0.865	-0.946
LaO								1.11
MnO_2	3.712	-0.049	3.900	-0.001	-3.399	3.194	-0.671	-0.899

Table 4.62 Table summarizing the structural and magnetic properties of “↑↑↓” ordered $[(\mathrm{LaMnO_3})_2-(\mathrm{SrMnO_3})_1]_1$ superlattice on a $SrTiO_3$. The a lattice parameter is fixed at $a = 3.905$ Å. The c lattice parameter is optimized at $c_{\mathrm{uud}} = 11.452$ Å.

	$\tilde{z}_{\text{average plane}}$	interplane distances (Å)	rumpling (Å)	$d_{\mathrm{Mn-O}}$(Å)
LaO	0.003		0.016	
		1.831		1.906
MnO_2	0.164		0.059	
		1.911		1.835
SrO	0.331		0.019	
		1.958		1.916
MnO_2	0.503		-0.059	
		1.855		1.948
LaO	0.665		-0.034	
		1.925		1.891
MnO_2	0.834		0.000	
		1.933		1.917

Table 4.63 Table summarizing the structural properties of “↑↓↓” ordered $[(\mathrm{LaMnO_3})_2-(\mathrm{SrMnO_3})_1]_1$ superlattice on a $SrTiO_3$. The a lattice parameter is fixed at $a = 3.905$ Å. The c lattice parameter is optimized at $c_{\mathrm{udd}} = 11.413$ Å.

	d_{OO} (Å)	JTd	c' (Å)	$c'/a-1$	magnetic moment (μ_B)	$\frac{\eta_{x^2-y^2}}{\eta_{z^2}}$	total e_g	charge ($\lvert e \rvert$)
LaO								1.105
MnO_2	3.740	-0.042	3.742	-0.042	3.372	2.940	0.658	-0.905
SrO								0.575
MnO_2	3.865	-0.010	3.762	-0.037	-3.66	1.007	1.004	-0.957
LaO								1.118
MnO_2	3.808	-0.025	3.908	0.001	-3.632	1.191	-0.848	-0.937

Table 4.64 Table summarizing the structural and magnetic properties of “↑↓↓” ordered $[(\mathrm{LaMnO_3})_2 - (\mathrm{SrMnO_3})_1]_1$ superlattice on a $\mathrm{SrTiO_3}$. The a lattice parameter is fixed at $a = 3.905$ Å. The c lattice parameter is optimized at $c_{\mathrm{udd}} = 11.413$ Å.

	$\tilde{z}_{\text{average plane}}$	interplane distances (Å)	rumpling (Å)	$d_{\mathrm{Mn-O}}$(Å)
LaO	0.004		0.016	
		1.831		1.907
MnO_2	0.164		0.059	
		1.912		1.834
SrO	0.331		0.019	
		1.959		1.918
MnO_2	0.503		-0.059	
		1.857		1.950
LaO	0.666		-0.034	
		1.925		1.891
MnO_2	0.834		0.000	
		1.933		1.916

Table 4.65 Table summarizing the structuralproperties of “↓↑↑” ordered $[(\mathrm{LaMnO_3})_2 - (\mathrm{SrMnO_3})_1]_1$ superlattice on a $\mathrm{SrTiO_3}$. The a lattice parameter is fixed at $a = 3.905$ Å. The c lattice parameter is optimized at $c_{\mathrm{duu}} = 11.416$ Å.

	d_{OO} (Å)	JTd	c' (Å)	$c'/a-1$	magnetic moment (μ_B)	$\frac{\eta_{x^2-y^2}}{\eta_{z^2}}$	total e_g	charge ($\lvert e \rvert$)
LaO								1.106
MnO_2	3.741	-0.042	3.743	-0.041	- 3.371	2.982	-0.657	-0.904
SrO								0.574
MnO_2	3.868	-0.009	3.764	-0.036	3.664	0.984	0.877	-0.958
LaO								1.118
MnO_2	3.807	-0.025	3.909	0.001	3.627	1.206	0.845	-0.934

Table 4.66 Table summarizing the structural and magnetic properties of "↓↑↑" ordered $[(\mathrm{LaMnO_3})_2 - (\mathrm{SrMnO_3})_1]_1$ superlattice on a $SrTiO_3$. The a lattice parameter is fixed at $a = 3.905$ Å. The c lattice parameter is optimized at $c_{\mathrm{duu}} = 11.416$ Å.

	$\tilde{z}_{\text{average plane}}$	interplane distances (Å)	rumpling (Å)	$d_{\mathrm{Mn-O}}$(Å)
LaO	-0.001		0.047	
		1.872		1.978
MnO_2	0.163		0.060	
		1.953		1.893
SrO	0.333		-0.001	
		1.953		1.892
MnO_2	0.504		-0.061	
		1.871		1.977
LaO	0.667		-0.047	
		1.902		1.856
MnO_2	0.833		0.000	
		1.903		1.857

Table 4.67 Table summarizing the structural properties of "↓↓↑" ordered $[(\mathrm{LaMnO_3})_2 - (\mathrm{SrMnO_3})_1]_1$ superlattice on a $SrTiO_3$. The a lattice parameter is fixed at $a = 3.905$ Å. The c lattice parameter is optimized at $c_{\mathrm{ddu}} = 11.453$ Å.

	d_{OO} (Å)	JTd	c' (Å)	$c'/a-1$	magnetic moment (μ_B)	$\frac{\eta_{x^2-y^2}}{\eta_{z^2}}$	total e_g	charge ($\lvert e\rvert$)
LaO								1.111
MnO_2	3.871	-0.009	3.781	-0.032	-3.656	0.991	-0.864	-0.946
SrO								0.568
MnO_2	3.869	-0.009	3.782	-0.032	-3.653	0.995	-0.862	-0.944
LaO								1.111
MnO_2	3.713	-0.049	3.891	0.004	3.399	3.214	0.67	-0.899

Table 4.68 Table summarizing the structural and magnetic properties of "↓↓↑" ordered $[(LaMnO_3)_2 - (SrMnO_3)_1]_1$ superlattice on a $SrTiO_3$. The a lattice parameter is fixed at $a = 3.905$ Å. The c lattice parameter is optimized at $c_{ddu} = 11.453$ Å.

4.5.4 Analysis of Mn–Mn distances

Finally, we would like to summarize the Mn–Mn distances in each magnetic ordering for these superlattices. First, in table 4.69 we give the Mn–Mn distances for the superlattice in a strain-free environment and within imposed $a = 3.88$ Å. Here, one can notice the spontaneous symmetry breaking in the strain-free case. The Mn–Mn distances when LaO is in between the MnO_2 layers are different in the 1st layer and in the 3rd one. When a is fixed to 3.88 Å, the symmetry is restored in the ferromagnetic ordering, however the symmetry remains broken in the A-type antiferromagnetic ordering. In table 4.70, we give the Mn–Mn distances within

	d_{Mn-Mn} (Å)		
	FM Strain-free	FM $a = 3.88$ Å	A-AFM $a = 3.88$ Å
MnO_2	↑	↑	↑
LaO	3.939	3.875	3.921
MnO_2	↑	↑	↑
SrO	3.847	3.803	3.823
MnO_2	↑	↑	↓
LaO	3.894	3.877	3.842
MnO_2	↑	↑	↑

Table 4.69 Table reporting the d_{Mn-Mn} values for strain free and $a = 3.88$ Å for ferromagnetic and A-type antiferromagnetic cases. First line is visualized in red to point out it it is the repetition of the third MnO_2 plane due to periodicity.

imposed $a = 3.905$ Å. One can see that Mn–Mn distances are symmetric for ferromagnetic, "↑↑↓" and "↓↓↑" where they are not for the rest of the orderings.

	$d_{\mathrm{Mn-Mn}}$ (Å)					
	FM	A-AFM	↑↑↓	↑↓↓	↓↑↑	↓↓↑
MnO_2	↑	↑	↓	↓	↑	↑
LaO	3.858	3.841	3.834	3.823	3.823	3.835
MnO_2	↑	↑	↑	↑	↓	↓
SrO	3.792	3.75	3.784	3.751	3.752	3.785
MnO_2	↑	↓	↑	↓	↑	↓
LaO	3.858	3.823	3.834	3.839	3.841	3.833
MnO_2	↑	↑	↓	↓	↑	↑

Table 4.70 Table reporting the $d_{\mathrm{Mn-Mn}}$ values for $a = 3.905$ Å for ferromagnetic, A-type antiferromagnetic, "↑↑↓","↑↓↓", "↓↑↑", "↓↓↑" cases. First line is visualized in red to point out it it is the repetition of the third MnO_2 plane due to periodicity.

4.6 $[(\mathbf{LaMnO_3})_2 - (\mathbf{SrMnO_3})_1]_2$ Superlattice

In this section, we double the size of the system with the same cation order of the previous section; that is $[(\mathrm{LaMnO_3})_2 - (\mathrm{SrMnO_3})_1]_2$. We studied the ferromagnetic ordering, A-type antiferromagnetic ordering, “↑↓↓↓↑↑” and “↑↓↓↓↑↑” orderings with imposed $a = 3.88$ Å. In figure 4.17, we give energy comparisons for different magnetic configurations with the lowest energy state. One can see that we obtain the ferromagnetic ordering as the lowest energy.

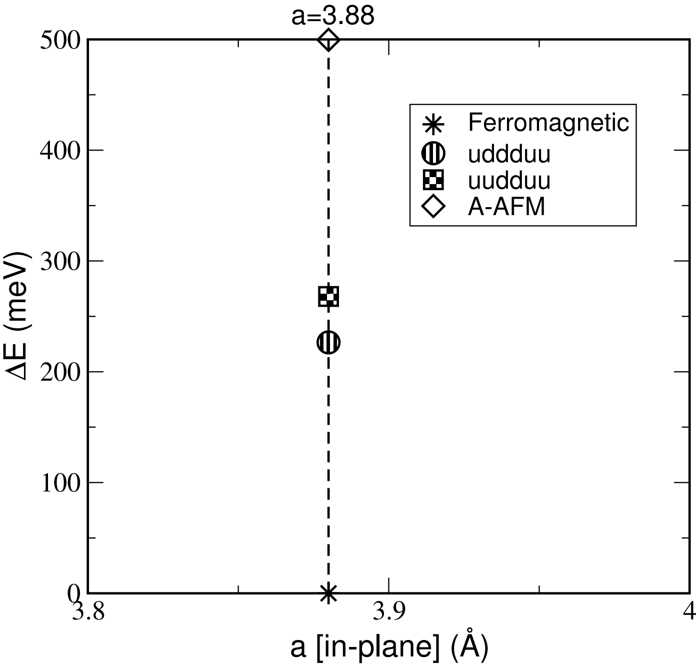

Fig. 4.17 Energy difference of each configuration with respect to the lowest energy ordering and geometry ($\Delta E = E - E_0$) vs. the imposed a in-plane lattice parameter. Here, E_0 is the lowest energy obtained for the ferromagnetic ordering when $a = 3.88$ Å.

4.6.1 Results with $a_{\mathrm{STO}} = 3.88$ Å

We studied this superlattice deposited on STO substrate. The imposed a lattice parameter is $a = 3.88$ Å. As we stated above, we found the ferromagnetic ordering as the lowest energy in our calculations ($E_{\mathrm{A-AFM}} - E_{\mathrm{FM}} = 726$ meV (61 meV), $E_{\mathrm{uddduu}} - E_{\mathrm{FM}} = 226$ meV (19 meV), $E_{\mathrm{uudduu}} - E_{\mathrm{FM}} = 268$ meV (22 meV) for the whole superlattice (per unit cell)).

Ferromagnetic Ordering

Now we look at the ferromagnetic $[(\text{LaMnO}_3)_2-(\text{SrMnO}_3)_1]_2$ superlattice with imposed $a=3.88$ Å. The c lattice parameter is optimized at $c_{\text{FM}}=23.120$ Å. In table 4.71, we give the structural properties of the optimized geometry. When we check the interplane distances for four layers where MnO_2 planes are sandwiched between LaO and SrO planes, we again see that the average LaO planes are closer to the average MnO_2 planes (around 1.881Å) than the average SrO planes (around 1.965 Å). When MnO_2 plane is only sandwiched between two LaO planes the interplane distance between the average LaO and MnO_2 planes is around 1.933 Å. This result is consistent with the ferromagnetic $[(\text{LaMnO}_3)_2-(\text{SrMnO}_3)_1]_1$ superlattice with imposed $a=3.88$ Å. In table 4.72, we report the magnetic and related structural properties. The four Mn-octahedra that are between LaO and SrO planes have the equivalent JTd (0.001, 0.000, 0.002 and 0.001) and $c'/a-1$ values (-0.018, -0.019, -0.018 and -0.017) with each other. In these Mn-octahedras, the e_g occupancy ratio shows that $d_{x^2-y^2}$ and d_{z^2} occupied more or less equivalently (0.925, 0.929, 0.901 and 0.909). The two Mn-octahedras between two LaO planes are contracted the most (JTd: -0.023) with largest e_g occupancy ratio (1.304).

A-type antiferromagnetic Ordering

We study at the A-type antiferromagnetic $[(\text{LaMnO}_3)_2-(\text{SrMnO}_3)_1]_2$ superlattice with imposed $a=3.88$ Å. The c lattice parameter is optimized at $c_{\text{A-AFM}}=22.999$ Å. In table 4.73, we give the structural properties of the optimized geometry. For the layers where MnO_2 planes are sandwiched between LaO and SrO planes, we see that antiferromagnetism in the $\vec{c}$ direction affects the symmetry in the interplane distances and $d_{\text{Mn-O}}$ values (for example, the interplane distance between the average LaO and MnO_2 planes are 1.949 and 1.851 Å whereas this value was around 1.881 Å in ferromagnetic ordering). Another point to remark is that since the number of layers is even in this superlattice there can be full antiferromagnetism in the $\vec{c}$ direction. Therefore, when we compare the results with A-type antiferromagnetic ordered $[(\text{LaMnO}_3)_2-(\text{SrMnO}_3)_1]_1$ superlattice where the number of layers are odd, even though the values of interplane distances for first half of $[(\text{LaMnO}_3)_2-(\text{SrMnO}_3)_1]_2$ superlattice are consistent, for the second half they do not exactly match.

In table 4.74, we report the magnetic and related structural properties.

	$\tilde{z}_{\text{average plane}}$	interplane distances (Å)	rumpling (Å)	$d_{\text{Mn}-\text{O}}$(Å)
LaO	0.000		0.037	
		1.881		1.980
MnO_2	0.081		0.063	
		1.965		1.902
SrO	0.166		0.000	
		1.964		1.901
MnO_2	0.251		-0.062	
		1.881		1.980
LaO	0.333		-0.037	
		1.933		1.896
MnO_2	0.416		0.000	
		1.933		1.896
LaO	0.500		0.037	
		1.882		1.983
MnO_2	0.581		0.063	
		1.967		1.905
SrO	0.666		-0.001	
		1.967		1.903
MnO_2	0.751		-0.063	
		1.881		1.982
LaO	0.833		-0.037	
		1.933		1.896
MnO_2	0.916		0.000	
		1.932		1.896

Table 4.71 Table summarizing the structural properties of ferromagnetic $[(\text{LaMnO}_3)_2-(\text{SrMnO}_3)_1]_2$ superlattice on a SrTiO_3. The a lattice parameter is fixed at $a = 3.88$ Å. The c lattice parameter is optimized at $c_{\text{FM}} = 23.120$ Å.

	d_{OO} (Å)	JTd	c' (Å)	$c'/a-1$	magnetic moment (μ_B)	$\frac{\eta_{x^2-y^2}}{\eta_{z^2}}$	total e_g	charge ($\|e\|$)
LaO								1.091
MnO_2	3.882	0.001	3.808	-0.018	3.63	0.925	0.843	-0.921
SrO								0.553
MnO_2	3.881	0.000	3.808	-0.019	3.628	0.929	0.841	-0.921
LaO								1.091
MnO_2	3.792	-0.023	3.940	0.015	3.555	1.304	0.788	-0.895
LaO								1.09
MnO_2	3.888	0.002	3.811	-0.018	3.634	0.901	0.846	-0.921
SrO								0.55
MnO_2	3.885	0.001	3.813	-0.017	3.629	0.909	0.842	-0.918
LaO								1.09
MnO_2	3.792	-0.023	3.940	0.015	3.55	1.304	0.788	-0.893

Table 4.72 Table summarizing the structural and magnetic properties of ferromagnetic $[(LaMnO_3)_2-(SrMnO_3)_1]_2$ superlattice on a $SrTiO_3$. The a lattice parameter is fixed at $a = 3.88$ Å. The c lattice parameter is optimized at $c_{FM} = 23.120$ Å.

The effect of full antiferromagnetism in the $\vec{c}$ direction is again clear in the thickness of the Mn-octahedras between LaO and SrO planes. The very 1st Mn octahedra between LaO and SrO planes is elongated (JTd: 0.073) with a dominant d_{z^2} occupancy, the 2nd Mn-octahera between LaO and SrO planes is contracted (JTd: -0.031) with a dominant $d_{x^2-y^2}$ occupancy. The 3rd Mn-octahedra between two LaO planes is also contracted (JTd: -0.034) with a dominant $d_{x^2-y^2}$ occupancy. Then, when the superlattice is repeated, the 4th Mn-octahedra is no longer elongated as the 1st one (JTd: -0.012). The JTd values of 5th and 6th Mn-octahera are consistent with the 2nd and 3rd ones.

"↑↓↓↓↑↑" Ordering

We study at the "↑↓↓↓↑↑" ordered $[(LaMnO_3)_2-(SrMnO_3)_1]_2$ superlattice with imposed $a = 3.88$ Å. The c lattice parameter is optimized at $c_{uddduu} = 23.084$ Å. In table 4.75, we give the structural properties of the optimized geometry. When we check the interplane distances for four layers where MnO_2 planes are sandwiched between LaO and SrO planes, we again see that the average LaO planes are closer to the average MnO_2 planes (around 1.847Å) than the average SrO planes (around 1.941 Å). When MnO_2 plane is only sandwiched between two LaO planes the interplane distance between the average LaO and MnO_2 planes is around

	$\tilde{z}_{\text{average plane}}$	interplane distances (Å)	rumpling (Å)	$d_{\text{Mn}-\text{O}}$(Å)
LaO	-0.004		0.096	
		1.949		2.125
MnO_2	0.081		0.079	
		2.062		2.039
SrO	0.170		-0.056	
		1.930		1.805
MnO_2	0.254		-0.069	
		1.851		1.956
LaO	0.335		-0.036	
		1.912		1.871
MnO_2	0.418		-0.004	
		1.903		1.878
LaO	0.501		0.029	
		1.861		1.946
MnO_2	0.581		0.056	
		1.937		1.887
SrO	0.666		-0.006	
		1.909		1.850
MnO_2	0.749		-0.053	
		1.852		1.911
LaO	0.829		-0.005	
		1.897		1.906
MnO_2	0.912		0.015	
		1.937		1.825

Table 4.73 Table summarizing the structural properties of A-type ferromagnetic $[(\mathrm{LaMnO_3})_2-(\mathrm{SrMnO_3})_1]_2$ superlattice on a $SrTiO_3$. The a lattice parameter is fixed at $a = 3.88$ Å. The c lattice parameter is optimized at $c_{\mathrm{A-AFM}} = 22.999$ Å.

	d_{OO} (Å)	JTd	c' (Å)	$c'/a-1$	magnetic moment (μ_B)	$\frac{\eta_{x^2-y^2}}{\eta_{z^2}}$	total e_g	charge ($\lvert e\rvert$)
LaO								1.089
MnO$_2$	4.164	0.073	3.856	-0.006	3.91	0.373	1.063	-1.036
SrO								0.522
MnO$_2$	3.761	-0.031	3.800	-0.021	-3.322	2.888	-0.622	-0.881
LaO								1.116
MnO$_2$	3.749	-0.034	3.880	0.000	3.486	2.692	0.742	-0.929
LaO								1.112
MnO$_2$	3.833	-0.012	3.764	-0.030	-3.566	1.282	-0.81	-0.929
SrO								0.586
MnO$_2$	3.761	-0.031	3.761	-0.031	3.381	2.323	0.668	-0.887
LaO								1.114
MnO$_2$	3.731	-0.038	3.939	0.015	-3.39	2.746	-0.663	-0.876

Table 4.74 Table summarizing the structural and magnetic properties of A-type ferromagnetic $[(\mathrm{LaMnO_3})_2-(\mathrm{SrMnO_3})_1]_2$ superlattice on a SrTiO$_3$. The a lattice parameter is fixed at $a=3.88$ Å. The c lattice parameter is optimized at $c_{\mathrm{A-AFM}}=22.999$ Å.

1.983 Å. This result is similar with the ferromagnetic $[(\mathrm{LaMnO_3})_2-(\mathrm{SrMnO_3})_1]_2$ superlattice with imposed $a=3.88$ Å because in this ordering, LaO planes are always in between ferromagnetically alligned Mn atoms and SrO planes are in between antiferromagnetically alligned Mn atoms.

In table 4.76, we report the magnetic and related structural properties. The 1st and 4th Mn-octahedra that are between LaO and SrO planes have the same JTd (-0.024) and e_g occupancy ratio (1.419). The 2nd and 5th Mn-octahedras between LaO and SrO planes are also contracted (JTd: -0.024) with e_g occupancy ratio (1.427). The 3rd and 6th Mn-octahedras that are between two LaO planes are elongated (JTd: 0.022) but they still have a dominant $d_{x^2-y^2}$ occupancy.

"↑↑↓↓↑↑" Ordering

We study at the "↑↑↓↓↑↑" ordered $[(\mathrm{LaMnO_3})_2-(\mathrm{SrMnO_3})_1]_2$ superlattice with imposed $a=3.88$ Å. The c lattice parameter is optimized at $c_{\mathrm{uudduu}}=23.039$ Å. In table 4.77, we give the structural properties of the optimized geometry. From the interplane distances and $d_{\mathrm{Mn-O}}$ there is no particular pattern.

	$\tilde{z}_{\text{average plane}}$	interplane distances (Å)	rumpling (Å)	$d_{\text{Mn}-\text{O}}$(Å)
LaO	0.003		-0.001	
		1.847		1.905
MnO_2	0.083		0.059	
		1.941		1.882
SrO	0.167		0.000	
		1.941		1.883
MnO_2	0.251		-0.058	
		1.847		1.905
LaO	0.331		0.000	
		1.983		1.984
MnO_2	0.417		0.000	
		1.983		1.984
LaO	0.503		-0.002	
		1.848		1.905
MnO_2	0.583		0.059	
		1.941		1.882
SrO	0.667		0.000	
		1.941		1.882
MnO_2	0.751		-0.058	
		1.847		1.905
LaO	0.831		0.001	
		1.983		1.984
MnO_2	0.917		0.000	
		1.983		1.984

Table 4.75 Table summarizing the structural properties of "↑↓↓↓↑↑" ordered $[(\text{LaMnO}_3)_2-(\text{SrMnO}_3)_1]_2$ superlattice on a SrTiO_3. The a lattice parameter is fixed at $a = 3.88$ Å. The c lattice parameter is optimized at $c_{\text{uddduu}} = 23.084$ Å.

	d_{OO} (Å)	JTd	c' (Å)	$c'/a-1$	magnetic moment (μ_B)	$\frac{\eta_{x^2-y^2}}{\eta_{z^2}}$	total e_g	charge ($\lvert e\rvert$)
LaO								1.088
MnO$_2$	3.787	-0.024	3.789	-0.023	3.45	1.419	0.716	-0.877
SrO								0.556
MnO$_2$	3.787	-0.024	3.789	-0.023	-3.454	1.427	-0.716	-0.879
LaO								1.088
MnO$_2$	3.968	0.023	3.964	0.022	-3.798	1.702	-0.97	-0.976
LaO								1.088
MnO$_2$	3.787	-0.024	3.789	-0.024	-3.449	1.419	-0.716	-0.877
SrO								0.556
MnO$_2$	3.787	-0.024	3.789	-0.024	3.45	1.427	0.716	-0.879
LaO								1.088
MnO$_2$	3.968	0.023	3.965	0.022	3.798	1.702	1.063	-0.976

Table 4.76 Table summarizing the structural and magnetic properties of "↑↓↓↓↑↑" ordered $[(\mathrm{LaMnO_3})_2-(\mathrm{SrMnO_3})_1]_2$ superlattice on a SrTiO$_3$. The a lattice parameter is fixed at $a = 3.88$ Å. The c lattice parameter is optimized at $c_{\mathrm{uddduu}} = 23.084$ Å.

In table 4.78, we report the magnetic and related structural properties. The 1st Mn-octahedra is elongated (JTd: 0.023) with a dominant d_{z^2} occupancy whereas all the rest of the Mn-octahedra are contracted with $d_{x^2-y^2}$ occupancy.

	$\tilde{z}_{\text{average plane}}$	interplane distances (Å)	rumpling (Å)	$d_{\text{Mn}-\text{O}}$(Å)
LaO	0.000		0.050	
		1.895		2.008
MnO_2	0.082		0.063	
		1.998		1.962
SrO	0.169		-0.027	
		1.945		1.855
MnO_2	0.253		-0.063	
		1.863		1.960
LaO	0.334		-0.034	
		1.940		1.903
MnO_2	0.418		-0.003	
		1.929		1.904
LaO	0.502		0.028	
		1.858		1.946
MnO_2	0.583		0.060	
		1.947		1.889
SrO	0.667		-0.001	
		1.929		1.870
MnO_2	0.751		-0.058	
		1.861		1.925
LaO	0.832		-0.013	
		1.932		1.930
MnO_2	0.916		0.005	
		1.943		1.888

Table 4.77 Table summarizing the structural properties of “↑↑↓↓↑↑” ordered $[(LaMnO_3)_2 - (SrMnO_3)_1]_2$ superlattice on a $SrTiO_3$. The a lattice parameter is fixed at $a = 3.88$ Å. The c lattice parameter is optimized at $c_{\text{uudduu}} = 23.039$ Å.

	d_{OO} (Å)	JTd	c' (Å)	$c'/a-1$	magnetic moment (μ_B)	$\frac{\eta_{x^2-y^2}}{\eta_{z^2}}$	total e_g	charge ($\lvert e\rvert$)
LaO								1.093
MnO_2	3.970	0.023	3.815	-0.017	3.755	0.679	0.935	-0.966
SrO								0.551
MnO_2	3.815	-0.017	3.801	-0.020	3.497	1.379	0.747	-0.895
LaO								1.082
MnO_2	3.807	-0.019	3.931	0.013	-3.568	1.251	-0.799	-0.906
LaO								1.107
MnO_2	3.834	-0.012	3.776	-0.027	-3.55	1.243	-0.794	-0.924
SrO								0.563
MnO_2	3.795	-0.022	3.772	-0.028	3.465	1.604	0.729	-0.894
LaO								1.097
MnO_2	3.818	-0.016	3.945	0.017	3.608	1.142	0.827	-0.91

Table 4.78 Table summarizing the structural and magnetic properties of "↑↑↓↓↑↑" ordered $[(\mathrm{LaMnO_3})_2-(\mathrm{SrMnO_3})_1]_2$ superlattice on a $SrTiO_3$. The a lattice parameter is fixed at $a = 3.88$ Å. The c lattice parameter is optimized at $c_{\mathrm{uudduu}} = 23.039$ Å.

4.6.2 Analysis of Mn–Mn distances

Finally, we would like to summarize the Mn–Mn distances in each magnetic ordering for these superlattices. First, in table 4.79 we give the Mn–Mn distances for the superlattice within imposed $a = 3.88$ Å. We see the cation symmetry in kept in the Mn-Mn distances in the ferromagnetic and "↑↓↓↓↑↑" orderings. Let us remind that these two spin orderings are respecting the cation one, while this is not the case for the other two spin orderings. Indeed, as could be expected in the A-type antiferromagnetic and "↑↑↓↓↑↑" orderings there is no symmetry in the Mn–Mn distances. This result points out that both cation and spin orderings play an important role on the lattice relaxation.

4.7 Conclusion

In this chapter, we studied the superlattices of the two undoped antiferromagnetic manganese oxides $LaMnO_3$ and $SrMnO_3$, i.e. $[\mathrm{LaMnO_3}]_\mathrm{n}-[\mathrm{SrMnO_3}]_\mathrm{m}$ superlattices. We investigated the magnetic ground state for different n and m values in strain-free environment and on a $SrTiO_3$ substrate with optimized and experimental a lattice parameter. We found that

	$d_{\mathrm{Mn-Mn}}$ (Å)			
	FM	A-FM	↑↓↓↓↑↑	↑↑↓↓↑↑
MnO_2	↑	↓	↑	↑
LaO	3.876	3.95	3.889	3.896
MnO_2	↑	↑	↑	↑
SrO	3.803	3.844	3.765	3.817
MnO_2	↑	↓	↓	↑
LaO	3.876	3.827	3.889	3.863
MnO_2	↑	↑	↓	↓
LaO	3.879	3.824	3.889	3.85
MnO_2	↑	↓	↓	↓
SrO	3.808	3.737	3.764	3.759
MnO_2	↑	↑	↑	↑
LaO	3.878	3.817	3.889	3.855
MnO_2	↑	↓	↑	↑

Table 4.79 Table reporting the $d_{\mathrm{Mn-Mn}}$ values for strain free and $a = 3.88$ Å for ferromagnetic, A-type antiferromagnetic, "↑↓↓↓↑↑", "↑↑↓↓↑↑" cases. First line is visualized in red to point out it it is the repetition of the third MnO_2 plane due to periodicity.

both the $[LaMnO_3]_1 - [SrMnO_3]_1$ and $[LaMnO_3]_2 - [SrMnO_3]_2$ superlattices are in a A-type antiferromagnetic state, whereas the $[LaMnO_3]_2 - [SrMnO_3]_1$ superlattice is ferromagnetic. These results are in full agreement with the experimental findings (B. Mercey private communication).

Chapter 5

BTO-LSMO Superlattices

Contents

5.1 Introduction

In chapter 4, we studied the $(\mathrm{LaMnO_3})_\mathrm{n} - (\mathrm{SrMnO_3})_\mathrm{p}$ superlattices. Our aim was to investigate these superlattices on different substrates with different magnetic orderings. We found that $(\mathrm{LaMnO_3})_1 - (\mathrm{SrMnO_3})_1$ superlattices on a $SrTiO_3$ substrate is A-type antiferromagnetic whereas $(\mathrm{LaMnO_3})_2 - (\mathrm{SrMnO_3})_1$ on a $SrTiO_3$ substrate if ferromagnetic.

In this chapter, we will combine the LSMO and LBMO compounds with alternated titanates such as $BaTiO_3$ (BTO), $PbTiO_3$ (PTO) and $SrTiO_3$ (STO) to study the effect of the alternated layer on the magnetic properties of the manganite part. In addition, we will take into account the antiferrodistortive motions (AFD) (*i.e* octahedra rotations) that take place in the manganite layers.

5.2 Alternated layers

As we mentioned earlier in Chapter 1, perovskite oxides form an important family of materials, exhibiting a wide variety of functional properties exploited in various devices. Artificial superlattices (SL) combining such compounds provides the opportunity not only to combine the intrinsic properties of the building layers, but also to induce totally new phenomena at their interfaces. Indeed, one can remind that at interfaces different degrees of freedom (charge, orbital, spin, lattice) may be coupled between the two materials, by the mean of effects such as symmetry breaking, charge transfer, strain engineering, etc. For instance, it was recently shown that such techniques enable the increase of Curie temperature by more than an order of magnitude in manganites $[\mathrm{BaTiO_3}]_\mathrm{n}[\mathrm{La_{2/3}A_{1/3}MnO_3}]_\mathrm{n}$ superlattices ($\mathrm{A} = \mathrm{Sr},\ \mathrm{Ca}$, $n = 3,4$) on a $\mathrm{SrTiO_3}$ substrate [75].

Since ferromagnetic materials with large Curie temperature are of great interest for technological applications in electronics and spintronics, the understanding of the degrees of freedom at play in the Curie temperature increase is of primary importance. Let us point out that this large increase of Curie temperature was observed in superlattices alternating very thin layers (a few mono-layers of each compounds) : Such lattices are not only dominated by interface effects but also by the interactions between the latters. Indeed the thickness of the layers is too small for the relaxation of the interface effects to take place before the occurence of the second interface. In other words the two interfaces are overlaping. In reference [75], the key role of the magnetic orbitals delocalization at the interface (charge transfer between layers), as well as the substrate and alternate layer tetragonal structure has been enlightened. The role of the $\mathrm{MnO_6}$ octahedra rotations and of the alternate layers properties, such as polarization, have however not been investigated while both are know to be of great importance. Indeed, octahedra rotations are known to be present in bulk manganites and coupled to the magnetic properties [116], as well as sensitive to the epitaxial strain imposed in thin films [117]. Similarly, Ismail-Beigi and coworkers showed that in polar / manganite interfaces, the polarization plays a key role [118–120].

The aim of this chapter is to investigate, using first principle calculations, the role of the octahedra rotations and alternated layer polarization in $[\mathrm{BaTiO_3}]_3[\mathrm{La_{2/3}A_{1/3}MnO_3}]_3$ superlattices with very thin layers (a few mono-layers) similar to those displaying a large increase of the Curie temperature in reference [75].

At this point let us remember that $\mathrm{La_{2/3}A_{1/3}MnO_3}$ (LSMO) is a ferromagnetic metal, thanks to the double exchange mechanism at play in the e_g sub-set of the Mn $3d$ orbitals.

The mixed valency of the Mn atoms ($\text{Mn}^{4+2/3}$ associated with a high spin configuration and a $t_{2g}^3 e_g^{2/3}$ atomic $3d$ configuration) allows a strong delocalisation between the latters (in-plane through their $d_{x^2-y^2}$ e_g-orbitals and out-of-plane through their d_{z^2} one), that combined with a large intra-atomic Hund's exchange overwhelms the antiferromagnetic coupling issued from the Mn–Mn super-exchange (double-exchange mechanism). In bulk LSMO, the rhombohedral structure insures an equal filling of the two e_g orbitals and an isotropic delocalization processes. In thin films, under tensile and quadratic strains, as in the present systems, this isotropic behavior is broken and Jahn-Teller distortions take place. In $[\text{BaTiO}_3]_\text{n}[\text{La}_{2/3}\text{A}_{1/3}\text{MnO}_3]_\text{n}$ superlattices, the distortion was shown to be mono-layer dependant, with interface elongated layers favoring d_{z^2} occupancy and central contracted layers favoring $d_{x^2-y^2}$ occupancy [75]. While the last one favors large in-plane delocalization and large T_c, the elongation at the interfaces are driven by small charge transfers at the interfaces (delocalization between Mn and Ti d_{z^2} orbitals) [79].

The systems studied in this chapter are pictured in figure 5.1. On the left in the figure, one can see the $[\text{BaTiO}_3]_3[\text{La}_{2/3}\text{Sr}_{1/3}\text{MnO}_3]_3$ (BTO-LSMO) superlattice. By construction,

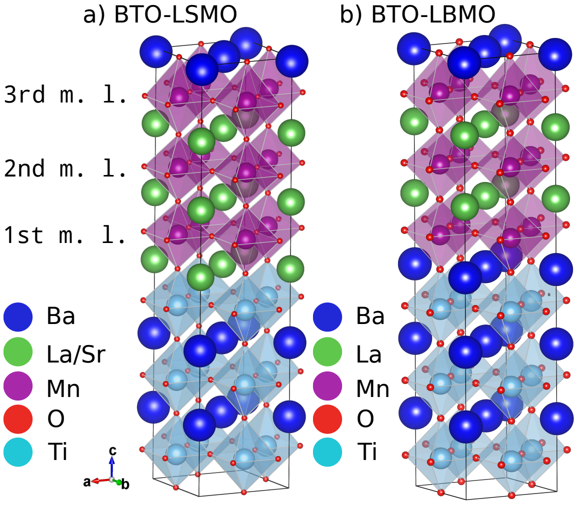

Fig. 5.1 Schematic representation of the unit cell used in the calculations: a) $[\text{BaTiO}_3]_3[\text{La}_{2/3}\text{Sr}_{1/3}\text{MnO}_3]_3$ (BTO-LSMO) superlattice b) $[\text{BaTiO}_3]_3[\text{La}_{2/3}\text{Ba}_{1/3}\text{MnO}_3]_3$ (BTO-LBMO) superlattice.

the $[\text{BaTiO}_3]_3[\text{La}_{2/3}\text{Sr}_{1/3}\text{MnO}_3]_3$ superlattice presents two different interfaces between the BaTiO_3 and the $\text{La}_{2/3}\text{Sr}_{1/3}\text{MnO}_3$ layers. One of them is (La/Sr)O/TiO_2 (the 1st LSMO mono-layer is attached to this interface). The other one is BaO/MnO_2 (the 3rd LSMO mono-layer is attached to this one). Thus, in order to clarify the role of this difference in the interfaces, we decided to also investigate a superlattice with equal interfaces between the two materials. Therefore, we also studied the $[\text{BaTiO}_3]_3[\text{La}_{2/3}\text{Ba}_{1/3}\text{MnO}_3]_3$ superlattice. One can see $[BaTiO_3]_3[La_{2/3}Ba_{1/3}MnO_3]_3$ (BTO-LBMO) superlattice on the right of the figure 5.1. In order to study symmetric interfaces (BaO/MnO_2) we did two different calculations: the first one without imposing the interface symmetry in the calculations and the second one with imposed mirror symmetry along z axis. Finally, we also investigated the role of the antiferrodistortive motions in the manganite layers.

5.2.1 Antiferrodistortive motions in BTO-LSMO

First we would like to study the release of AFD motions in the manganite layers of $[BaTiO_3]_3-[La_{2/3}Sr_{1/3}MnO_3]_3$ superlattice. Figure 5.2 reports the statistics found for the MnO_6 octahedra rotations, as a function of the different La/Sr ordering, as well as the induced stabilization energy. One sees immediately that the majority of the orderings are

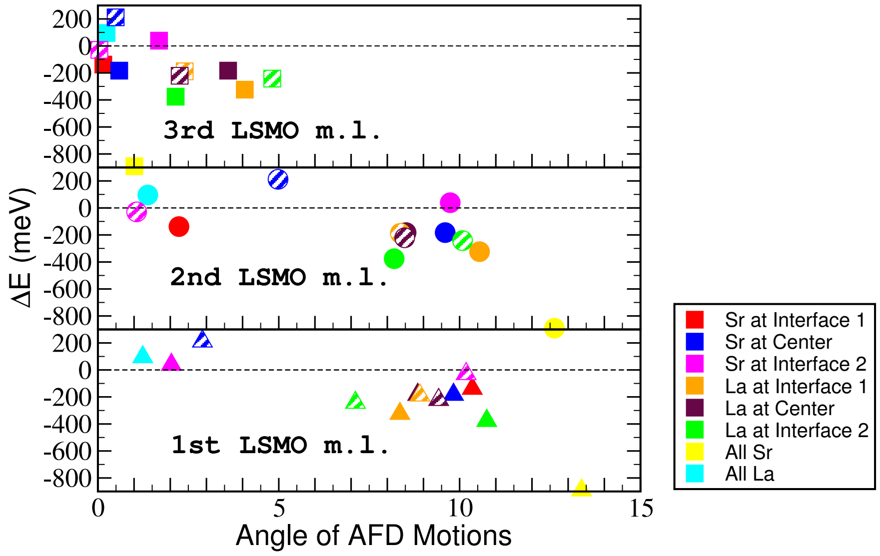

Fig. 5.2 Stabilization energy brought by the octahedra rotations in the $[BaTiO_3]_3[La_{2/3}Sr_{1/3}MnO_3]_3$ superlattice. The MnO_6 rotation angles are reported separately for each LSMO mono-layer (m.l.). The different colors correspond to different ordering of the La/Sr LSMO ions. The dashed symbols to real atoms and the filled ones to atoms with averaged effective nuclear charges.

stabilized by octahedra rotations.The stabilization energy brought by the octahedra rotations is in average of 187 meV for total system. The three LSMO mono-layers do not however behave in the same way. Two mono-layers exhibit rotations with a typical angle of 7° in average, while at one of the interfaces the rotations remain very weak; it is around $\sim 2°$ in average.

Figure 5.3 a) displays the MnO_6 octahedra rotations as a function of Jahn-Teller distortion, which is the main lattice degree of freedom for orbital order in manganites. The mono-layers that are on the right side of the dashed line show elongation in the $\vec{c}$ direction, whereas the mono-layers that are on the left side of the dashed line are contracted in the $\vec{c}$ direction. The calculations that we perform yield equivalent results and give the average layer behaviour of such superlattices: 1st and 2nd LSMO mono-layer Mn-octahedra are contracted whereas 3rd LSMO mono-layer Mn-octahedra is elongated. For AFD motion analysis, one can see the statistics fits into three clusters. The cluster identified with blue ellipse are the mono-layers showing Mn-octahedra elongation in the $\vec{c}$ direction and no/weak AFD motions (2° in average). They are essentially 3rd LSMO mono-layer at BaO/MnO_2 interface. The Mn-octahedra contracted mono-layers are grouped into red and orange circles. The cluster identified with red circle is for the mono-layers showing large AFD motions and they are essentially 1st LSMO mono-layer at (La/Sr)O/TiO_2 interface and a few of central mono-layer

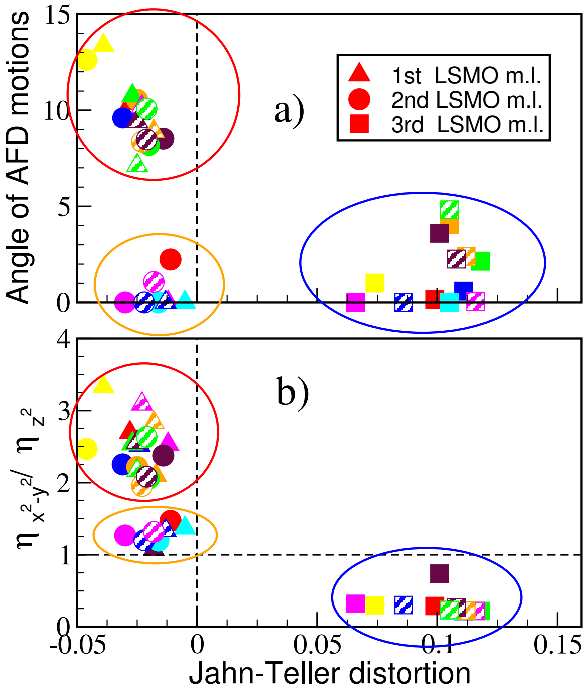

Fig. 5.3 Statistics of the MnO_6 rotation (top) and relative e_g orbital occupancy ratio (bottom) as a function of the Jahn-Teller distortion (JTd). The data fit into three clusters: The blue ellipse cluster stands for the mono-layers showing Mn-octahedra elongation in the $\vec{c}$ direction and no/weak AFD motions as well as dominant d_{z^2} orbital occupancy. The red circle cluster stands for the mono-layers showing Mn-octahedra contraction in the $\vec{c}$ direction and large AFD motions as well as dominant $d_{x^2-y^2}$ orbital occupancy. The orange ellipse cluster stands for the mono-layers showing Mn-octahedra contraction in the $\vec{c}$ direction and no/weak AFD motions as well as dominant $d_{x^2-y^2}$ orbital occupancy.

for some orderings. The orange cluster stands for the mono-layers showing no/weak AFD motions and they are essentially central (2nd) mono-layers. The difference in the amplitude of AFD motions exhibited by the red and orange clusters results from the dependence on the cation ordering of the system. In figure 5.3 b, we display the e_g occupancy ratio of the mono-layers against the Jahn-Teller distortion. The mono-layers under the dashed line show preferential d_{z^2} occupancy whereas the ones above the dashed line show $d_{x^2-y^2}$ occupancy. Again, the calculations yield to equivalent results for different ionic orderings: 1st and 2nd mono-layer Mn-octahedra are contracted with dominant $d_{x^2-y^2}$ orbital occupancy whereas the 3rd mono-layer Mn-octahedra is elongated with d_{z^2} occupancy. This correlation between JTd and preferential e_g orbital occupancy is fully expected from the theory. One can again fit the statistical data into three clusters in order to see the effect of the AFD motions on the the correlation of JTd vs the e_g occupancy ratio. In the blue ellipse cluster (elongated 3rd mono-layers with no/weak AFD motions), d_{z^2} is preferentially occupied over $d_{x^2-y^2}$ as mentioned. $d_{x^2-y^2}$ orbital is stabilized over d_{z^2} in the red cluster (contracted 1st mono-layers with large AFD motions) as well as in the orange one (contracted 2nd mono-layers with no/weak AFD motions). The contracted mono-layers with large AFD motions (the red circle cluster) have higher e_g occupancy ratio than the contracted mono-layers with no/small AFD motions (the orange circle cluster). One can conclude that the AFD motions are present only in contracted layers and they enhance the in-plane magnetic properties since it increases the $d_{x^2-y^2}$ orbital stabilization.

In order to see the impact of the released AFD motions in LSMO we report the comparison of the BTO-LSMO superlattices with and without AFD in figure 5.4 for one typical La/Sr ordering, (since the results for other cation orderings are qualitatively similar). At the top panel first we report the tetragonality $c/a-1$ ratio for each mono-layer (fig 5.4 a)). The c value is calculated as cation-cation distance. One can see that for both cases the first two mono-layers are contracted in $\vec{c}$ direction while the third layer is elongated but AFD motions tend to contract these layers a little bit less. In fact, the central layer is more or less cubic when the AFD motions are released.

Then (fig 5.4 b)), we report the Jahn-Teller distortion which gives similar results: for both cases the two first-mono layers are contracted while the 3rd mono-layer is elongated. After this, we report the MnO_2 rumpling (fig 5.5 c)). One sees that the AFD motions do affect neither the JTd nor the rumpling.

At the bottom panel, on the left (fig 5.4 d)), we give the e_g occupancy ratio, defined as $\eta_{x^2-y^2}/\eta_{z^2}$. First of all, for both cases we see that in the first two mono-layers $d_{x^2-y^2}$ is

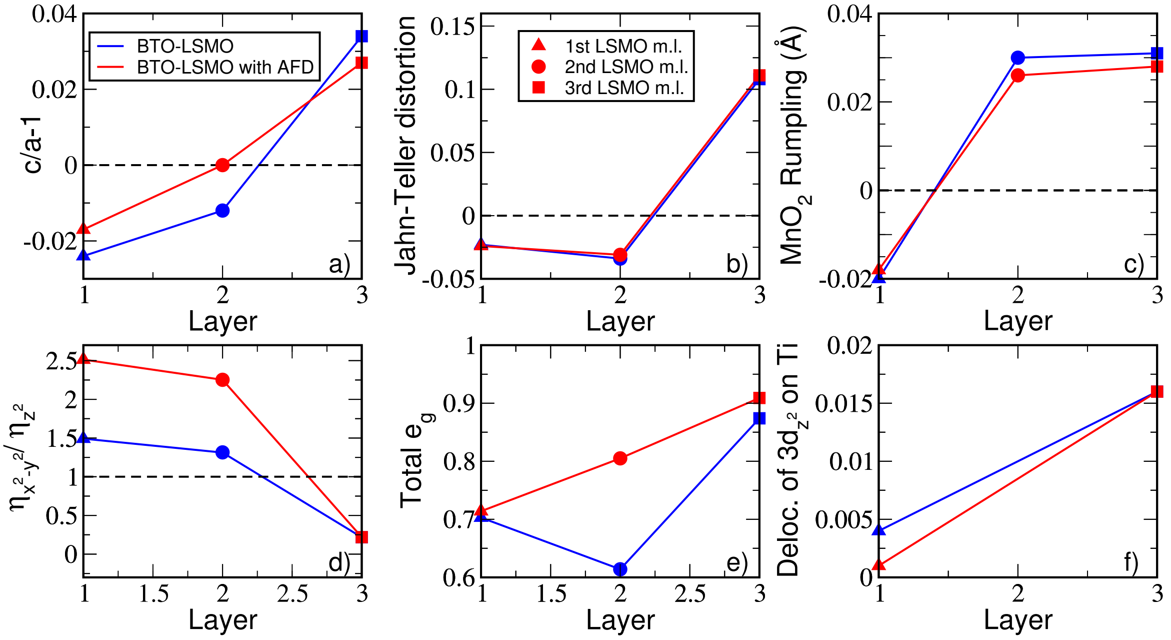

Fig. 5.4 Analysis of the $[BaTiO_3]_3[La_{2/3}Sr_{1/3}MnO_3]_3$ superlattice for the impact of antiferrodistortive (AFD) motions. The blue stands for the superlattice in which the AFD motions are not released, the red is for the superlattice where AFD motions are released. At the top panel from left to right, one finds the tetragonality $c/a-1$, Jahn-Teller distortion, MnO$_2$ rumpling in (Å). At the bottom panel from left to right, one finds the e_g occupancy ratio, total e_g occupancy and delocalization of $3d_{z^2}$ electrons on Ti at the interfaces. (Note: Real orbital occupation numbers are used for $\eta_{x^2-y^2}$ and η_{z^2}).

preferentially occupied, while d_{z^2} is preferred in the third mono-layer. However, we see that the ratio in the contracted layers increases strongly in the superlattice where the AFD motions are released. The ratio in the elongated layer does not change between the two calculations. These results tell us that the AFD motions enhance the in-plane magnetic properties in the contracted layers as it increases the in-plane e_g orbital, $d_{x^2-y^2}$, population.

On the second chart (fig 5.4 e)), we report the total e_g occupancies which is computed as $\eta_{x^2-y^2} + \eta_{z^2}$. Here we see a major difference for the central mono-layer. While the central layer is strongly depopulated if the AFD motions are not allowed, this depopulation is totally hindered by the AFD motions. It seems that the AFD motions compensate the depopulation in the central layer which is observed in previous calculations [75].

The last item at the bottom panel (fig 5.4 f)) is dedicated to the delocalization of $3d_{z^2}$ electrons between Mn and Ti at the interfaces. While there is no delocalization at the 1st mono-layer, there is a slight delocalization in the third mono-layer. This delocalization is however not affected by the AFD motions. One should remember that the mono-layer in which this delocalization is observed is elongated in $\vec{c}$ direction and thus do not present much AFD. In fact, it looks like AFD and interface delocalization are exclusive effects.

As a conclusion, one can say that the release of the AFD motions has little or no effects on JTd, rumpling and tetragonality, while it has a strong effect on the orbital occupations.

5.2.2 The effect of the interface: BTO-LBMO, a case with equivalent interfaces

Now in order to see the effect of the difference between the two interfaces, let us do the same AFD motion analysis in the $[BaTiO_3]_3[La_{2/3}Ba_{1/3}MnO_3]_3$ superlattice. The difference of this superlattice from $[BaTiO_3]_3[La_{2/3}Sr_{1/3}MnO_3]_3$ is that both interfaces are equivalent *i.e.* $BaO - MnO_2$ as one can see in figure 5.1 b. Let us note that there is only one cation order for $[BaTiO_3]_3[La_{2/3}Ba_{1/3}MnO_3]_3$ superlattice that make both interfaces equivalent, we thus focused our studies on this specific order. As we first focused on the AFD motions the symmetry group was kept to be as $P4mm$. However, in order to suppress the polarization in $BaTiO_3$ and study its effect we also considered the $P4/mmm$ space group of the $[BaTiO_3]_3[La_{2/3}Ba_{1/3}MnO_3]_3$ superlattice. In the $P4/mmm$ space group, there exists a mirror symmetry planes in the TiO_2 and MnO_2 central mono-layers of $BaTiO_3$ and

$La_{2/3}Ba_{1/3}MnO_3$. Let us first note that the stabilization energy brought by the Mn-octahedra rotations (in *P*4*mm* space group) is around 421 meV for the total system.

We report the comparison of the different BTO-LBMO superlattices in figure 5.5. Again,

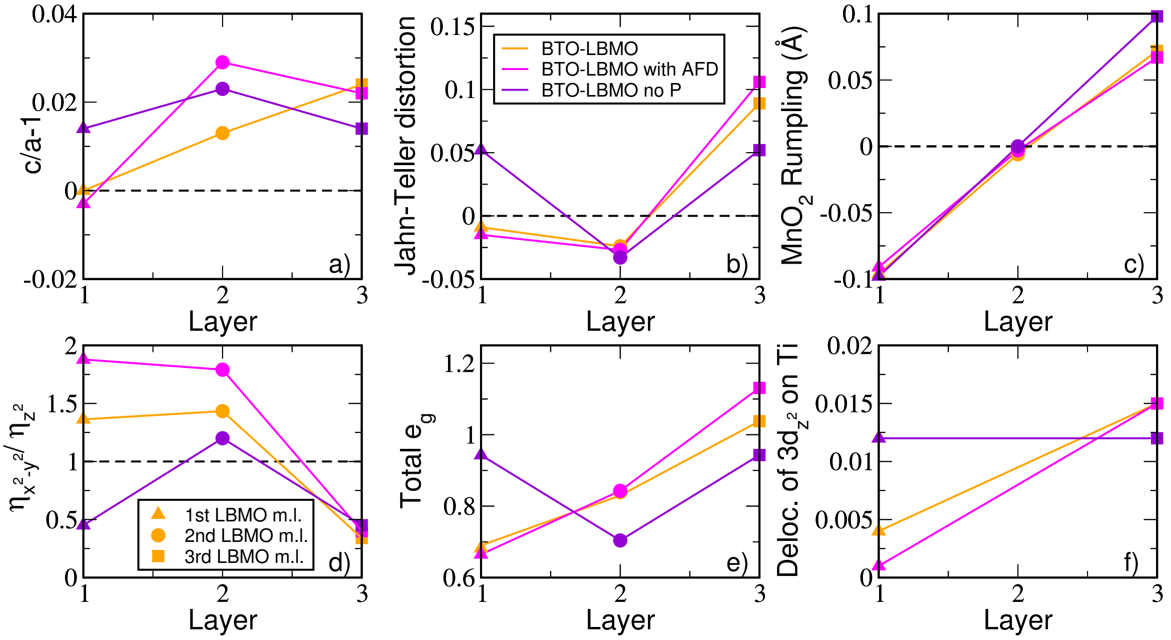

Fig. 5.5 Analysis of the $[BaTiO_3]_3[La_{2/3}Ba_{1/3}MnO_3]_3$ superlattice for the impact of antiferrodistortive (AFD) motions and polarization. The orange stands for the superlattice in which the AFD motions are not released (*P*4*mm* space group), the pink is for the superlattice where AFD motions are released (*P*4*mm* space group) and the purple is for the superlattice where the polarization in $BaTiO_3$ is supressed by imposing $P4/mmm$ symmetry. At the top panel from left to right, one finds the tetragonality $c/a-1$, the Jahn-Teller distortion, the MnO_2 rumpling in (Å). At the bottom panel from left to right, one finds the e_g occupancy ratio, total e_g occupancy and delocalization of $3d_{z^2}$ electrons on Ti at the interfaces. (Note: Mülliken populations are used for $\eta_{x^2-y^2}$ and η_{z^2}).

on the top panel, we first report the $c/a-1$ value (fig 5.5 a)). One can see that the values are slightly different than those of BTO-LSMO. In superlattices with *P*4*mm* symmetry group (the pink and orange symbols in figure 5.5), the first mono-layer is cubic (the $c/a-1$ is close to 0) whereas the central and 3rd mono-layers are elongated. The effect of the AFD is mainly on the central layer. The central layer is more elongated when the AFD motions are released. What is also striking is that even though the 1st and 3rd mono-layers present equivalent interfaces the $c/a-1$ values are not the same; showing a strong spontaneous symmetry breaking. This symmetry breaking arises from the direction of the polarization in the $BaTiO_3$. When we suppress the polarization in $BaTiO_3$ by imposing a $P4/mmm$ symmetry (the purple symbol in the figure 5.5), this spontaneous symmetry breaking disappears; both the 1st and

3rd mono-layers exhibit same tetragonality values. Within $P4/mmm$ symmetry, all three mono-layers are elongated.

Beside $c/a-1$ value (fig 5.5 b)), we give the Jahn-Teller distortion. In superlattices with $P4mm$ space group, with and without octahedra rotations, the first two Mn-octahedra are contracted and the 3rd one is again elongated as seen in BTO-LSMO superlattice. Again, in the 1st and the 3rd layers the Mn-octahedra do not have the same Jahn-Teller distortion, even if these two layers have the same interfaces. However, when there is $P4/mmm$ symmetry the 1st and 3rd Mn-octahedra have the same JTd values. Without polarization, the 1st and 3rd layers Mn-octahedra are elongated in $\vec{c}$ direction, whereas the central ones are contracted.

After this (fig 5.5 c)), we report the MnO_2 rumpling. For all cases, the results are qualitatively similar suggesting there is no polarization in LBMO, which is to be expected sinceLBMO is a conducting system. Both Jahn-Teller distortion and MnO_2 rumpling are not affected by the AFD motions.

At the bottom panel, on the left (fig 5.5 d)), we give the e_g occupancy ratio. First of all, within $P4mm$ symmetry, with and without AFD motions, we see that in the first two mono-layers $d_{x^2-y^2}$ is preferentially occupied while d_{z^2} is preferred in the third mono-layer. However, we see that the ratio in the contracted layers increases in superlattices where the AFD motions are released, (as seen in BTO-LSMO superlattice). The ratio in the elongated layer seems not to change as AFD motions are set on. This result again supports the idea that AFD motions enhance the in-plane magnetic properties, in the contracted layers, since it increases the $d_{x^2-y^2}$ orbital occupation (which is correlated with the in-plane magnetic properties). When the polarization is suppressed in $BaTiO_3$, the behaviour is not the same. d_{z^2} is preferentially occupied in the 1st and 3rd Mn-octahedra as it is expected from the Jahn-Teller distortion values of these octahedras in this superlattice. $d_{x^2-y^2}$ orbital is occupied in the central layer. Thus, the polarization seems to enhance the in-plane magnetic properties since $\eta_{x^2-y^2}$ occupancy is lower in non-polarized system. This issue will be studied in more details later.

Beside the e_g occupancy ratio, we report the total e_g occupancies (fig 5.5 e)). The results are qualitatively similar for the cases in $P4mm$ with and without octahedra rotations. The most populated layer is the elongated layer. Within $P4/mmm$, the populations are the same for the 1st and 3rd layer as it is expected. The central layer is the least populated when the polarization is killed.

The last item in the bottom panel (fig 5.5 f)) is the delocalization of $3d_{z^2}$ electrons between Mn-Ti at the interfaces. As one can see that there is no delocalization at the 1st mono-layer, whereas there is always a weak delocalization in the third mono-layer. One should again remember that the mono-layer in which this delocalization is observed is elongated in $\vec{c}$ direction. When the polarization is supressed, the delocalization is the same in both interfaces.

After the careful study of AFD motions one can conclude:

1. The AFD motions definitely exist in both BTO-LSMO and BTO-LBMO superlattices at least at low temperature.
2. These rotations take place only in mono-layers which are contracted in the $\vec{c}$ direction.
3. The amplitude of these rotations, however, is cation order dependent.
4. Though the Jahn-Teller distortion, which is the relevant structural parameter for the e_g occupancy ratio, does not change significantly as AFD set on, we saw that AFD motions slightly increase the e_g occupancy in the contracted octahedras, and strongly increase the $d_{x^2-y^2}$ vs. d_{z^2} occupancies ratio.
5. Layer contraction can globally decrease the total e_g occupancy.

By studying BTO-LBMO, we tried to highlight the role of the asymmetric interface of BTO-LSMO. However, what we have seen in BTO-LBMO is that even if the two interfaces are the same, they act in a similar way as the asymmetric interfaces in BTO-LSMO, and that a spontaneous symmetry breaking occurs in the manganite. This result suggests that the relevant parameter for the symmetry breaking here is not related to the interface asymmetry, but rather to a parameter related to the alternated layer that differentiate the two interfaces. The natural candidate is the polarization in $BaTiO_3$. By imposing the $P4/mmm$ symmetry and killing the polarization in $BaTiO_3$ we have seen that indeed the orientation of the polarization in $BaTiO_3$ determine the behaviour of the interface layers of the manganite.

5.2.3 The Role of the Polarization

We shall thus now enlarge our study to investigate the role of the polarization in the alternated layers of the manganite superlattices. For such a purpose we extend our compounds to

$[PbTiO_3]_3[La_{2/3}Sr_{1/3}MnO_3]_3$, since $PbTiO_3$ is known to exhibit larger polarization than $BaTiO_3$.

The results are summarized in figure 5.6. Again, at the top panel first we report $c/a-1$ ratio. In PTO-LSMO, all three mono-layers are contracted whereas in the BTO-LSMO only first two mono-layers are contracted. The amplitudes of the contractions in these two mono-layers are similar to the contraction in PTO-LSMO. In BTO-LBMO, the first mono-layer remains cubic and the last two mono-layers are elongated. In totally symmetric BTO-LBMO where BTO does not induce any polarization, all three mono-layers are elongated. The central one is a little bit more elongated than the two equal interfacial ones.

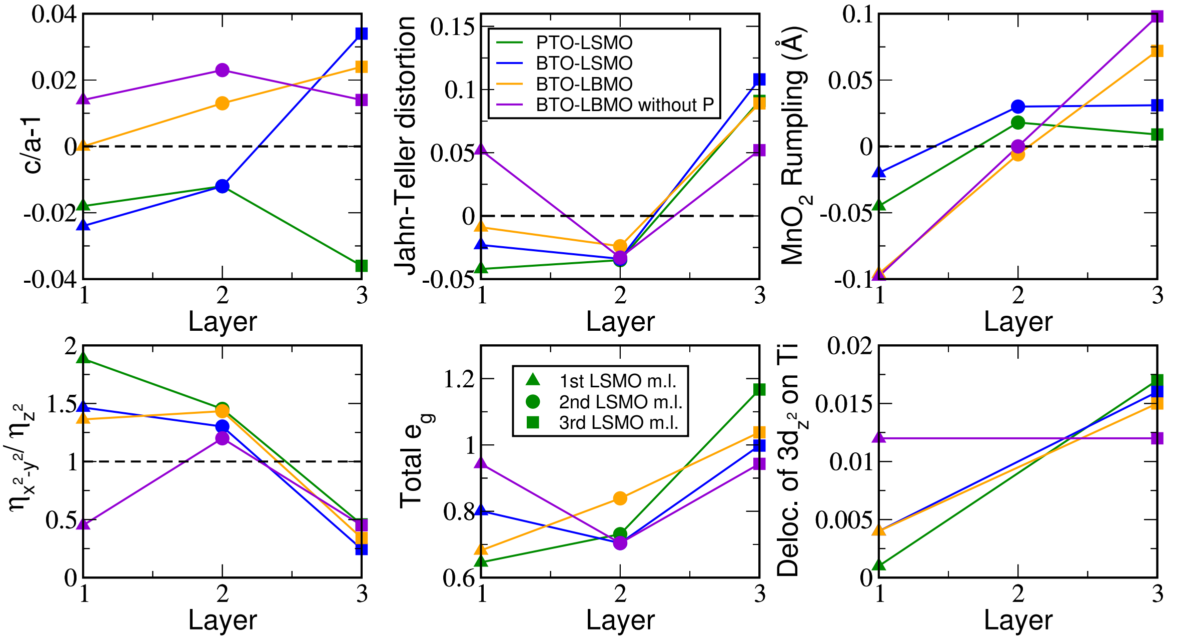

Fig. 5.6 Analysis of the effect of polarization in manganite superlattices. The green stands for $[PbTiO_3]_3[La_{2/3}Sr_{1/3}MnO_3]_3$ superlattice in *P*4*mm* space group. The blue stands for $[BaTiO_3]_3[La_{2/3}Sr_{1/3}MnO_3]_3$ superlattice. The orange stands $[BaTiO_3]_3[La_{2/3}Ba_{1/3}MnO_3]_3$ superlattice. The purple stands $[BaTiO_3]_3[La_{2/3}Ba_{1/3}MnO_3]_3$ superlattice in $P4/mmm$ where there is mirror symmetry planes to suppress the polarization in $BaTiO_3$. At the top panel from left to right, one finds the tetragonality $c/a-1$, Jahn-Teller distortion, MnO_2 rumpling in (Å). At the bottom panel from left to right, one finds the e_g occupancy ratio, total e_g occupancy and delocalization of $3d_{z^2}$ electrons on Ti at the interfaces. (Note: Mülliken populations are used for $\eta_{x^2-y^2}$ and η_{z^2}).

At the top panel on the second chart, we give the Jahn-Teller distortion. Except totally symmetric BTO-LBMO, the rest has similar pattern. First and central layers Mn-octahedra are contracted, whereas the 3rd mono-layer is elongated. In totally symmetric BTO-LBMO, two interfacial octahedras are equally elongated and central one is contracted.

The pattern of MnO_2 rumpling is qualitatively similar in PTO-LSMO and BTO-LSMO. For BTO-LBMO, the rumpling pattern is rather linear since it has symmetric interfaces but the values in two interfaces are not exactly the same. However, in totally symmetric BTO-LBMO the rumpling values of two interfacial layers compensate each other whereas there is no rumpling in the cenral one since there is a mirror symmetry plane.

At the bottom panel on the left, we give the e_g occupancy ratio. The fundemental results are as follows; except totally symmetric BTO-LBMO, the ratio pattern is the same for the rest of the systems, the two first mono-layers are preferentially $d_{x^2-y^2}$ populated where is 3rd mono-layer is d_{z^2} populated. For totally symmetric BTO-LBMO, d_{z^2} is more occupied at the interfaces and $d_{x^2-y^2}$ is more occupied in the central layer. All these results are coherent with the observed JTd.

On the right, we report the total e_g occupancy for each layer in the superlattice. In the totally symmetric BTO-LBMO, the interface layers have the same total e_g occupancy. For the rest of the systems, we can see that the 3rd layer Mn-octahedra are more populated than the other two layers. One should point out that a larger e_g population is systematically observed in elongated layers.

The last item at the bottom panel is the delocalization of the orbital $3d_{z^2}$ of the Mn on Ti. Except for the totally symmetric BTO-LBMO, one can see the pattern directly. The first mono-layer, which is contracted, doesn't exhibit much delocalization on Ti whereas the elongated layer is slightly delocalized on Ti. In totally symmetric BTO-LBMO, the two interface Mn-octahedra are elongated and there is a delocalization on Ti at both interfaces. This result directly confirms that the delocalization is directly correlated to the elongation at the interfaces.

We will now try to get some clear picture about what is exactly happening in these systems by specifically displaying parameters correlations. Thus, we first would like to report the e_g occupancy ratio as a function of the Jahn-Teller distortion as we did for AFD analysis. In figure 5.7 we give the e_g ratio with respect to Jahn-Teller distortion. In this picture we also added the results that we got for the released AFD motions as they are the true ground states for BTO-LSMO and BTO-LBMO superlattices. Their colour are kept the same as before: Red for BTO-LSMO with AFD and pink for BTO-LBMO with AFD. Here, one can clearly see the expected inverse proportionality between e_g ratio and Jahn-Teller parameter.

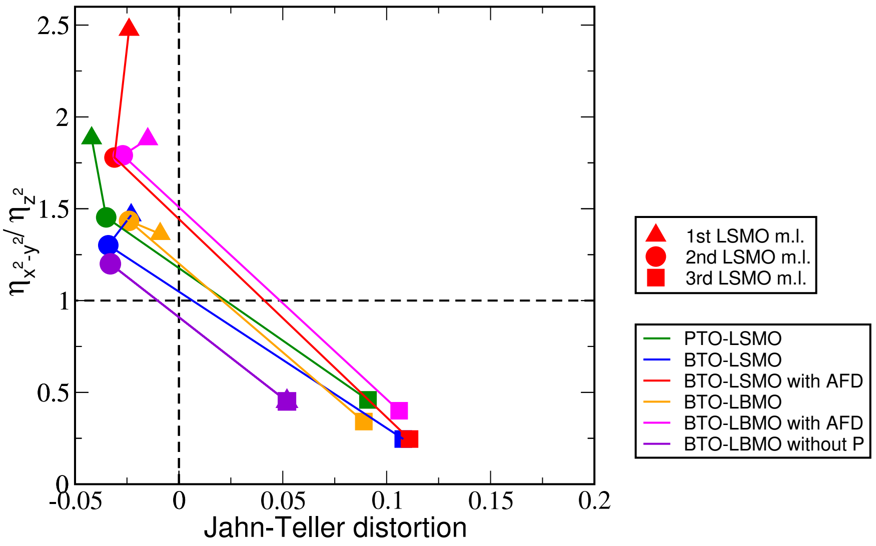

Fig. 5.7 Statistics of manganite superlattices with alternated titanates. The e_g orbital occupancy ratio as a function of Jahn-Teller distortion parameter. (Note: Mülliken populations are used for $\eta_{x^2-y^2}$ and η_{z^2}).

We also try to get a picture of the correlation between the e_g orbital occupancy ratio and MnO_2 rumpling. In figure 5.8 we summarized the e_g occupancy ratio as a function of MnO_2 rumpling. However, it is hard to get a clear relation by looking at this picture. This is most probably because the relevant rumpling parameter for the LSMO electronic structure is the TiO_2 rumpling of the alternating layer instead of the MnO_2 one. To clarify the role of the polarization in alternated layers on the manganite magnetic properties, we will analyse the alternated layer features. Thus, in figure 5.9 on the left, we give the Jahn-Teller distortion and the e_g orbital occupancy ratio of the LSMO mono-layers as a function of the TiO_2 rumpling. On the right, we give the TiO_2 rumpling in Å for each layer in each system. On the right, considering absolute values we see that the largest amplitude for the rumpling is for PTO-LSMO which is natural since it has the largest polarization. The two BTO-LSMO system with and without AFD motions come after that. They have more or less the same rumpling values. Then, BTO-LBMO with AFD motions has larger rumpling than BTO-LBMO without AFD motions. Here, we see that there is an effect of the manganite layer on the alternated layer polarization. The totally symmetric BTO-LBMO has of course no TiO_2 rumpling.

By looking at the left of the figure 5.9, one can see that the three mono-layers behave differently. For the 1st mono-layers, we observe the largest rumpling in the alternated titanates with the largest contraction in the Mn octahedra. As the rumpling decreases, the JTd parameter increases. For the 2nd mono-layers, the central layers, the TiO_2 rumpling does not

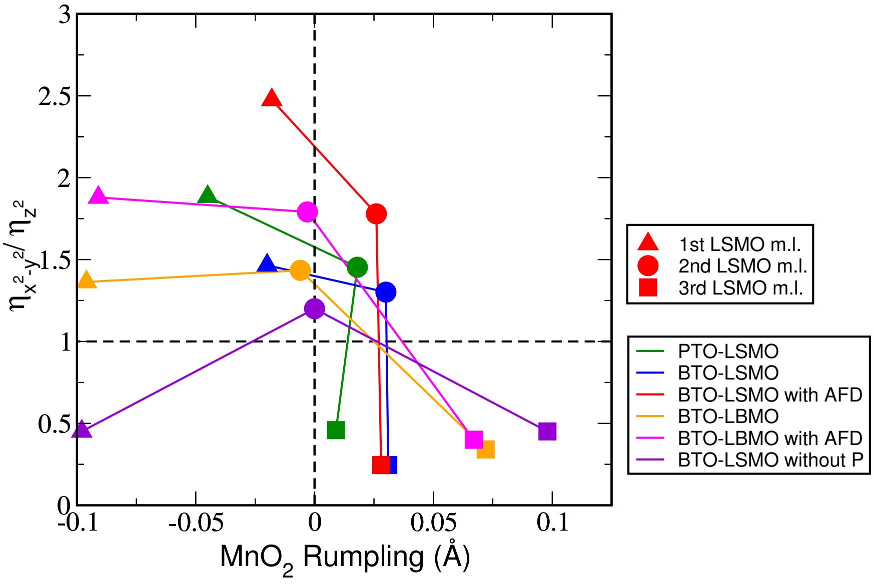

Fig. 5.8 Statistics of manganite superlattices with alternated titanates. The e_g orbital occupancy ratio as a function of MnO$_2$ rumpling in Å. (Note: Mülliken populations are used for $\eta_{x^2-y^2}$ and η_{z^2}).

significantly affect the Jahn Teller distortion. The 3rd mono-layers behave in a similar way. As a conclusion, the TiO$_2$ rumpling does not significantly affect the JT distortion except for the large decrease in JTd in the case of the totally symmetric BTO-LBMO. This is because the 1st mono-layer of the totally symmetric BTO-LBMO is elongated and that the total length of the BTO has to be preserved (volume conservation to minimize the elastic energy).

When we check the e_g ratio with respect to the TiO$_2$ rumpling, it is hard to say that the e_g ratio in PTO-LSMO (green) is enhanced with more TiO$_2$ rumpling, if we take into account the real ground states of BTO-LSMO (red) and BTO-LBMO (pink) (the ones which exhibit AFD motions). However, we should note here that we haven't released the AFD motions in PTO-LSMO. Thus, we might not be in the real ground state of PTO-LSMO, but if we compare PTO-LSMO with BTO-LSMO without AFD (blue) and BTO-LBMO without AFD (orange) it seems that e_g ratio is enhanced by the TiO$_2$ rumpling in the 1st mono-layer as it can predicted by the above analysis of JTd vs. TiO$_2$ rumpling for the 1st mono-layer. Comparing the cases with AFD (red and pink triangles), one can see that e_g ratio is enhanced when there is more TiO$_2$ rumpling. For the 2nd mono-layer (with and without AFD cases), the e_g ratio is not significantly affected by the rumpling, as can be predicted from the JTd vs. the TiO$_2$ rumpling for the 2nd mono-layer. This results holds for the e_g ratio of the 3rd mono-layer.

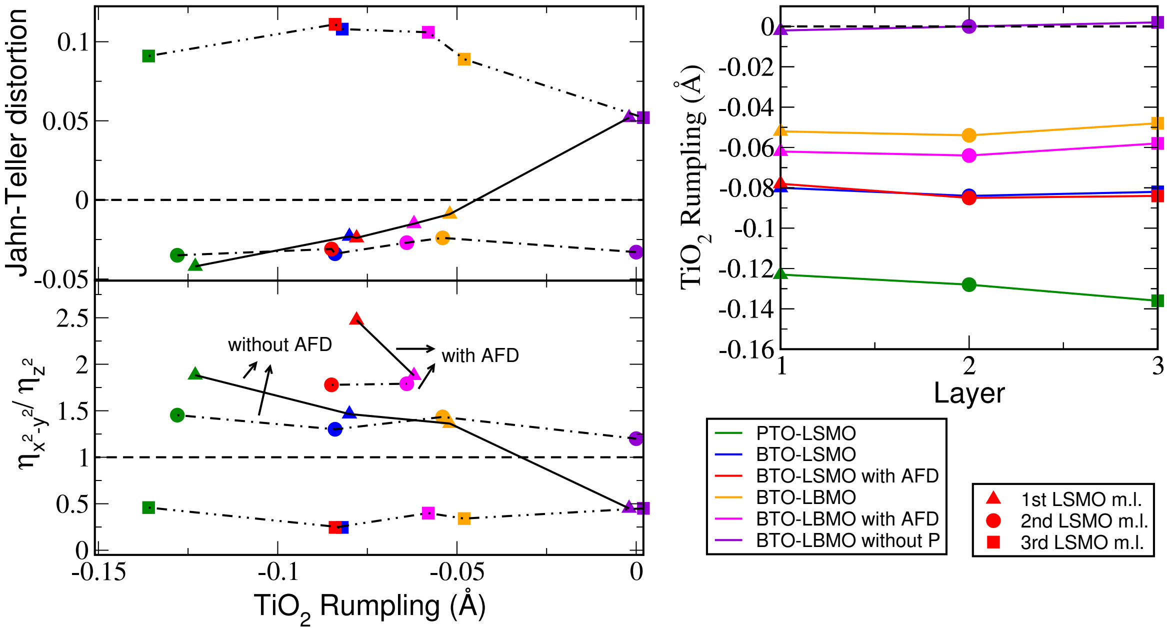

Fig. 5.9 Statistics of the effect of the TiO_2 rumpling in the alternated layers titanates on the manganite layer properties. On the left the Jahn-Teller distortion parameter, and the e_g orbital occupancy ratio given as a function of TiO_2 rumpling, on the right TiO_2 rumpling given for each layer. Lines are guide for the eyes. (Note: Mülliken populations are used for $\eta_{x^2-y^2}$ and η_{z^2}).

We can also compute the polarization in alternated layers by using the Born-effective charges as explained in the Chapter 3. Born effective charges are taken from reference [56]. In figure 5.10, we report the polarization of the alternated layer in each system. As stated before,

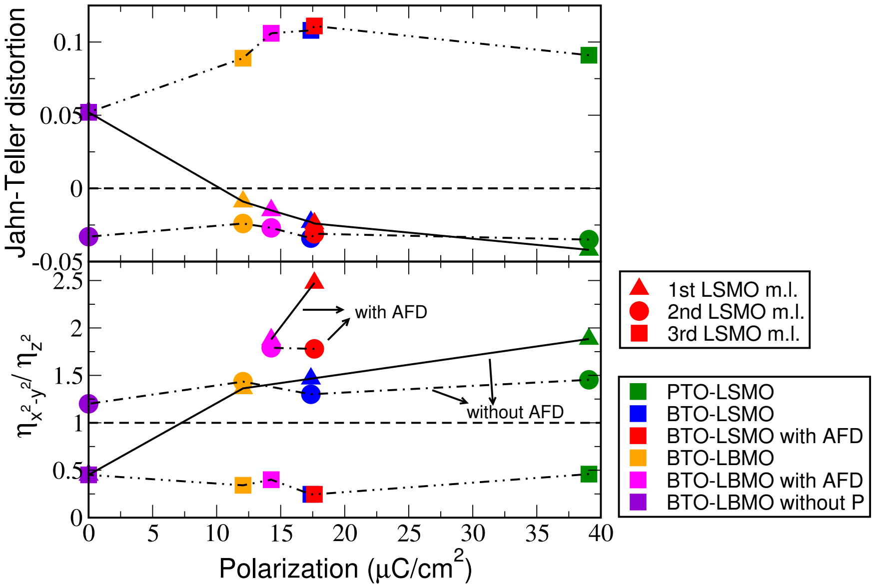

Fig. 5.10 Statistics of the amplitude of the polarization in the alternated titanates of the manganite superlattices with alternated layers. The Jahn-Teller distortion parameter and the e_g orbital occupancy ratio is given as a function of the the amplitude of the polarization. (Note: Mülliken populations are used for $\eta_{x^2-y^2}$ and η_{z^2}).

PTO has the largest polarization. The analysis we have done for the TiO_2 rumpling stands for the polarization as well. It seems that the more polarization the more contraction of the octahedra in the 1st mono-layers. In addition, with the consideration of the real ground states of BTO-LSMO and BTO-LBMO (with released octahedra rotations), polarization seems to improve the e_g ratio when we check the BTO-LSMO and BTO-LBMO 1st mono-layers (the red and pink triangles in the figure 5.10). In the 2nd mono-layers Mn-octahedra, the e_g ratio does not significantly change as the polarization changes. This is also the case when we include the AFD motions calculations (the red and pink circles). In the 3rd mono-layers Mn-octahedra, the amplitude of the polarization does not significantly affect the e_g ratio.

5.3 Conclusion

At the end of this study we can summarize the effects of the alternated layers in the manganite superlattices as follows:

1. The asymmetric or symmetric chemical nature of the interface is not a leading parameter for the electronic structure of the interface. Indeed, we have seen that the same type of spontaneous symmetry breaking that exists in BTO-LSMO superlattices also exists in BTO-LBMO superlattices, though the two interfaces in the latter are equivalent.

2. The orientation of the polarization that exists in the alternated layers is the parameter responsible for the spontaneous symmetry breaking in the interface manganite layers. The 1st mono-layer is contracted where the direction of the polarization is out-of-the the interface. The 3rd mono-layer is elongated where the direction of the polarization is into the interface. The possible different chemical nature of the interfaces plays a secondary role. As a result, we observe a delocalization of the $3d_{z^2}$ orbital of the Mn on the empty Ti ones in the 3rd mono-layer since it is elongated.

3. The amplitude of the polarization in the alternated layers only affect the 1st mono-layer of the manganite layers. When the amplitude increases, the contraction of Mn-octahedra of the 1st mono-layer increases, as well as the e_g ratio of this mono-layer.

The 2nd point is coherent with the paper of Ismail-Beigi and his co-workers [119]. Ismail-Beigi and his co-workers studied a non-periodic BTO-LSMO superlattice. In this superlattice, there is only one interface and the interface between the BTO and LSMO is composed of BaO/MnO_2 layers (there is vacuum at the end of the manganite layer). They pointed out the role of polarization in BTO by changing the direction of the polarization. In the accumulation state, where the direction of the polarization is out-of the interface layer, the interfacial BaO layer's oxygen is pushed toward to the interfacial Mn which results with JTd < 1. In the depletion state, where the direction of the polarization is into the interface layer, the BaO layer's oxygen is pushed away from the interfacial Mn which results JTd > 1. As the systems that we studied are periodic in first-principle calculations, the superlattice is repeated in the $\vec{c}$ direction, as well as the alternated layers. Thus, the polarization of the alternated layers can be into or out-of the interface. Thus, we can have both accumulation and depletion states in two different interfaces. The depletion takes place in the 3rd mono-layer (BaO/MnO_2 interface) the oxygen anion of the BaO layer is pushed away from the interfacial Mn resulting with an elongation in the 3rd mono-layer octahedra. The accumulation states takes place in the 1st mono-layer ($(La/Sr)O/TiO_2$ interface) the oxygen anion of the $(La/Sr)O$ layer is pushed toward the interfacial Mn resulting with a contraction in the 1st mono-layer octahedra. One can schematically see the role of the orientation of the polarization on the interfaces in both BTO-LSMO and BTO-LBMO superlattices in figure 5.11 and 5.12. The fact that there

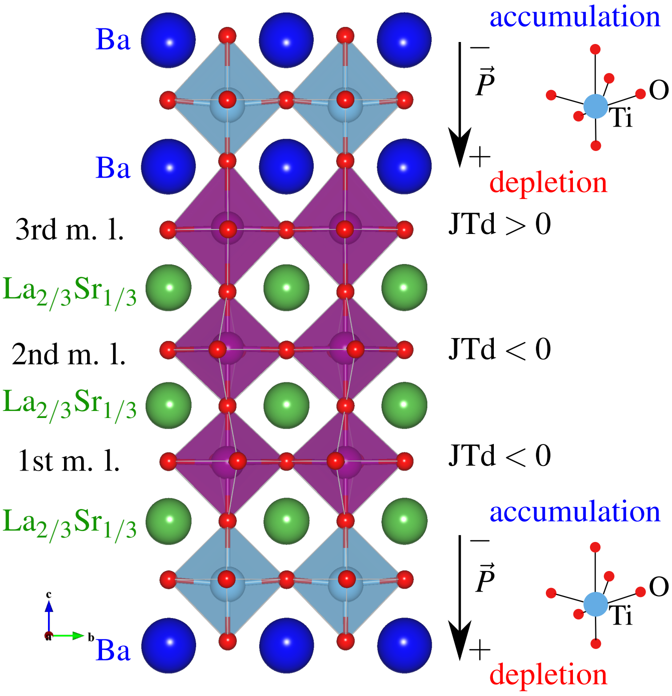

Fig. 5.11 Schematical representation of the orientation of the polarization in BTO-LSMO superlattice: the accumulation state where the polarization of alternate titanates is out-of the interface layer, the depletion state where the polarization of the alternate titanates is into the layer.

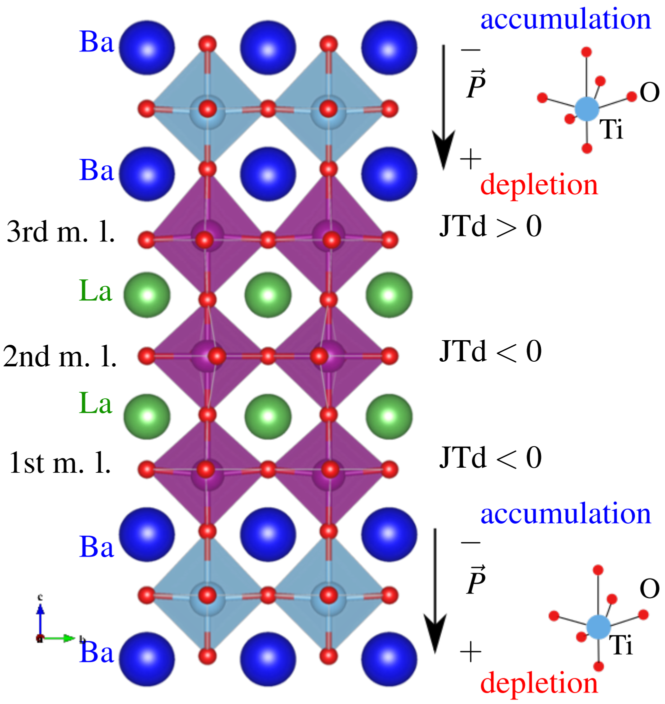

Fig. 5.12 Schematical representation of the orientation of the polarization in the BTO-LBMO superlattice: the accumulation state where the polarization of alternate titanates is out-of the interface layer, the depletion state where the polarization of the alternate titanates is into the layer.

exists one elongated and one contracted interface manganite mono-layers in BTO-LSMO superlattice is not a consequence of Ba proximity but the orientation of the polarization.

In this chapter, we also highlighted the role of the antiferrodistortive (AFD) motions in the manganite layer on the properties of the superlattices.:

1. The AFD motion are present at least at low temperature.
2. They only exist in the contracted mono-layers.
3. They do not affect the structural properties such as Jahn-Teller distortion or tetragonality.
4. However, even though they do not affect the Jahn-Teller distortion, which is the parameter responsible for the e_g orbital ordering, they do enhance the preferential $d_{x^2-Y^2}$ occupancy.
5. Thus, the AFD motions are expected to enhance the magnetic properties.

More general conclusions that we obtained through the study of BTO-LSMO superlattices are as follows:

1. The mono-layer contraction decreases the total e_g population.
2. The AFD motions and interface delocalization are exclusive effects.
3. The delocalization at the interfaces comes only in the elongated mono-layers.

As we stated before, at the 3rd mono-layer, where there is elongation, the d_{z^2} orbital is preferentially occupied and there is a delocalization of $3d_{z^2}$ electrons from Mn atoms to empty Ti d-shell. As a result, in this elongated layer the in-plane magnetic properties are expected to decrease. Our aim in the next chapter is to find a way to suppress this elongation and the correlated delocalization. For this purpose we will play on the alternated layers in order to prevent the delocalization.

Chapter 6

AO-LSMO Superlattices

Contents

6.1 Introduction

In the previous chapter, we studied the effect of the alternating layer polarization and AFD motions of manganite layers on the properties of $(\mathrm{BaTiO_3})_3/(\mathrm{La_{2/3}Sr_{1/3}MnO_3})_3$ superlattices. Indeed, we chose to work on these superlattices since they present the possibility to increase the Curie temperature by one order of magnitude compared to the bulk compound thanks to the orbital ordering triggered by the specific geometry around Mn ion [75]. We remind again that when manganite compounds such as $\mathrm{La_{2/3}Sr_{1/3}MnO_3}$ (LSMO) or $\mathrm{La_{2/3}Ca_{1/3}MnO_3}$ (LCMO) are built as a supperlattice with $\mathrm{BaTiO_3}$ alternating layers on a

$SrTiO_3$ substrate, the thickness of the LSMO mono-layers can be contracted or elongated. This geometric arrangements result in e_g orbital ordering (a mechanism to control which e_g orbital will be occupied). This result was the key point of such superlattices. Indeed, it is assumed that large $d_{x^2-y^2}$ orbital occupancy in such manganite superlattices induce high T_c and metallicity [75].

Unfortunately, a loss of magnetization and metalicity, also called "dead layer", is observed over a thickness of few unit cells at the interface of ferromagnetic manganites, such as $La_{2/3}Sr_{1/3}MnO_3$ (LSMO) or $La_{2/3}Ca_{1/3}MnO_3$ (LCMO), and most perovskite substrates or combined layers [121, 122]. Different hypotheses are considered to be the cause of this "dead layer" phenomenon:

1. Insulating state of the very thin manganite films is a result of homogeneous substrate strain [123],
2. Manganese e_g orbital reconstruction that may induce C-type antiferromagnetism [124, 125].
3. Electronic and/or chemical phase separation [126] related to structural inhomogeneities at the interface [127] or uncontrolled stoichiometry [128],
4. The weak delocalization of manganite Mn 3*d* electrons in the substrate Ti 3*d* empty orbitals at the interfaces [79].

For the 1st hypothesis, one must remember that a homogeneous substrate strain of the in-plane parameters does not relax for film thickness smaller than 1000 Å [126], whereas transport properties are significantly changed for films thinner than a few unit cells (3–4 on STO substrate [124, 122], 30 on $LaAlO_3$ substrate [124]). For the 2nd hypothesis, in very thin films [122], ferromagnetism is observed, in contradiction with the proposed C-type antiferromagnetic ordering resulting from orbital ordering. Since we would like to work with perfect interfaces, we will not consider the 3rd hypothesis and focus on the study of the 4th one where there is an enhanced d_{z^2} occupancy at the interface.

Let us explain briefly how the formation of a "dead layer" can take place at the interfaces in this hypothesis. The Mn d_{z^2} electrons can delocalize in the empty d_{z^2} orbitals of the substrate or of the alternating layer (typically $SrTiO_3$, $BaTiO_3$ or similar compounds). Even though this delocalization is weak (about one or two tenth of an electron [79]), at the interfaces this delocalization energetically favors the d_{z^2} orbital occupancy over the $d_{x^2-y^2}$

one. Thus, Jahn-Teller distortion of the MnO_6 octahedron takes place, favoring the elongation along the c directionn with a splitting of the e_g degeneracy [75] ($\varepsilon_{z^2} < \varepsilon_{x^2-y^2}$). The in-plane delocalization is thus hindered, at least by carrier density reduction. Consequently, the characteristics of the "dead layer" phenomenon appear, (reduced ferromagnetic spin arrangement and reduced conductivity [129, 122]). Such a Jahn-Teller distortion induces a small increase of the c lattice parameter [130, 79], that can be fully attributed to the delocalization mechanism at the interfaces, since strain effects tend to reduce c. Indeed, on a $SrTiO_3$ (STO) substrate, manganites such as LSMO or LCMO are under tensile strain ($a_{\text{STO}} = 3.905$ Å [131], $a_{\text{LSMO}} = 3.880$ Å [132], $a_{\text{LCMO}} = 3.86$Å [133] yielding a 0.65% tensile strain on LSMO and 1.15% on LCMO), known to favor a reduction of c lattice parameter.

In chapter 5, we have seen that such a delocalization takes place between the Mn $3d_{z^2}$ electrons in the Ti empty d_{z^2} orbitals of the alternated layers at the interface when the interfacial manganite mono-layer Mn-octahedra is elongated. The orientation of the polarization of the alternated layers, indeed, plays a role in such an elongation as we discussed in the previous chapter. However, suppressing the polarization in the alternated layers, as we studied in BTO-LBMO superlattice ($P4/mmm$ space), did suppress neither the elongation of manganite mono-layer at the interfaces nor the interface delocalization from the Mn to the Ti $3d_{z^2}$ orbitals. In this elongated manganite mono-layer, one can remember that we observed dominant d_{z^2} orbital population over d_{x^2} orbital. Thus, we expect to have reduced in-plane magnetic properties in this mono-layer. In order to prevent the formation of a such a layer, i.e. "dead layer", one thus needs to interface the manganite with an alternating layer material hindering the delocalization between the different layers.

The aim of this work was thus to find out whether the delocalization at the interfaces can explain the formation of the dead layer or not. For this purpose, we propose possible candidates for new alternating layers in manganite superlattices in which the delocalization at the interfaces are suppressed. In the next section, we will briefly discuss the requirements to fulfill for such alternating layers.

6.2 Possible compounds as alternating layers in manganite superlattices

As the hypothesis for the origin of the formation of a "dead layer" is the delocalization of d-shell between Mn and Ti atoms, one can suggest to use a compound with totally filled *d* shells as the alternating layers. Thus, the $BaSnO_3$ compound could be a good suggestion since Sn has totally filled d-shells. However, test calculations [134] on such heterostructures showed that there is a weak electron delocalization, from Sn filled d_{z^2} orbitals towards Mn partially occupied ones, very similar to what is observed in the calculations on $[BaTiO_3]_3 - [La_{2/3}Sr_{1/3}MnO_3]_3$ [75]. This delocalization results again in an increase of the Mn d_{z^2} orbital occupancy, and a Jahn-Teller distortion elongating the octahedra. One can thus expect such heterostructures to also exhibit a "dead layer" phenomenon.

Avoiding *d* orbitals in the alternating layers is another option to prevent this electron delocalization completely. So, we can set up our first requirement for such materials to be without *d* orbitals. The second requirement is to have a tetragonal or cubic structure. Indeed, in the manganite layers, it is crucial to prevent the rhombohedral distortion but rather favor a tetragonal distortion [75]. This tetragonal distortion, induced by the strain effect of the substrate and kept by alternating layers, should lead to the contraction of the mono-layers with favored the $d_{x^2-y^2}$ orbital occupancy and thus of the desired properties. At last but not least, after fulfilling these two requirements, the candidate compound must have a perfect epitaxy with the manganite layer.

We chose to test the alkaline-earth oxides, particularly the BaO compound, since it satisfies all the necessary conditions. Indeed, BaO has no d-shells as it doesn't have a transition metal in it. Moreover, the mismatch between BaO and LSMO is only of 0.7%, and between BaO and the STO substrate 0.3%. One can see the other alkaline-earth oxide lattice mismatch values with LSMO and STO in the table 6.1. We also need to mention that the epitaxy imposes for the BaO unit cell ($Fm\bar{3}m$ cubic group [135]) to be rotated in-plane by an angle of 45° [136, 137], compared to the manganite unit cell (this can be seen figure 6.1).

We thus studied, using first principle calculations, $[La_{2/3}Sr_{1/3}MnO_3]_n[BaO]_p$ superlattices, alternating a few unit cells of manganite and of simple Barium oxide. Superlattices with other alkaline-earth oxides (SrO, CaO and MgO) are also studied in order to see whether the results are resilient to a change in the alternating layer, despite their unrealistic strain values.

Compound	Space Group	a (Å)	Mismatch (%) STO substrate	LSMO bulk
BaO	$Fm\bar{3}m$	5.5391 [135]	0.3	0.7
SrO	$Fm\bar{3}m$	5.1615 [138]	-6.5	-6.2
CaO	$Fm\bar{3}m$	4.7990 [139]	-13.1	-12.8
MgO	$Fm\bar{3}m$	4.214 [140]	-23.7	-23.4

Table 6.1 Space Groups, lattice parameters and lattice mismatch of the different alkaline-earth simple oxides with the $SrTiO_3$ substrate [131, 141] and LSMO bulk [132, 142].

6.3 Results

6.3.1 Manganite thin films with simple BaO layers

We first studied the $[La_{2/3}Sr_{1/3}MnO_3]_3[BaO]_6$ superlattice in order to investigate its structural and magnetic properties. We computed our superlattice for all different cation models in order

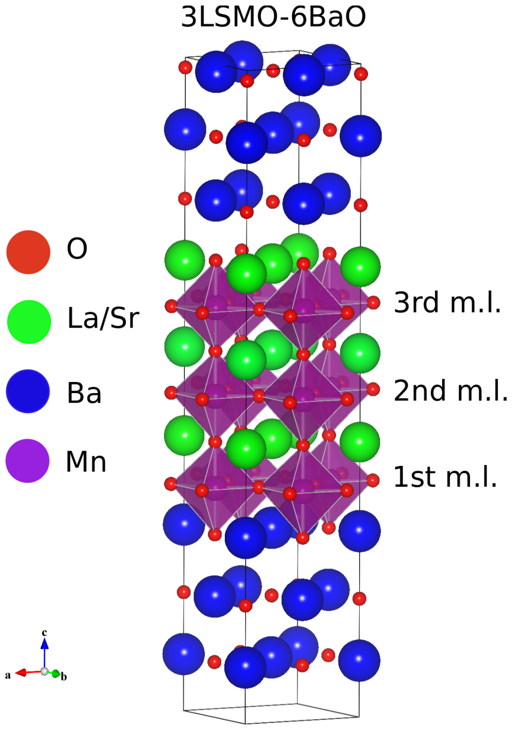

Fig. 6.1 (color online) Schematic representation of the $[La_{2/3}Sr_{1/3}MnO_3]_3[BaO]_6$ superlattice. m.l. stands for mono-layer.

to treat the manganite A-site cation disorder. As we mentioned in the technical details this elongated interface manganite layer we used ECPs with averaged effective nuclear charges in order to treat the average ions. We also tested the real charge cases in order to testify our results. We used a $\sqrt{2}a \times \sqrt{2}a \times c$ unit cell in order to allow octahedra rotations and in-plane antiferromagnetic (AFM) ordering. In figure 6.1 one can see the schematic representation of the superlattice studied. Here one should notice that the interfaces are non equivalent, since one corresponds to a (La/Sr,O)–(BaO) interface and the other to a (MnO_2)–(BaO) interface. We studied different magnetic orderings in our superlattices that is ferromagnetic (FM), A-type AFM (in-plane FM and out-of-plane AFM), C-type AFM (in-plane AFM and out-of-plane FM) and G-type AFM (in-plane and out-of-plane AFM), that can be seen in figure 6.2.

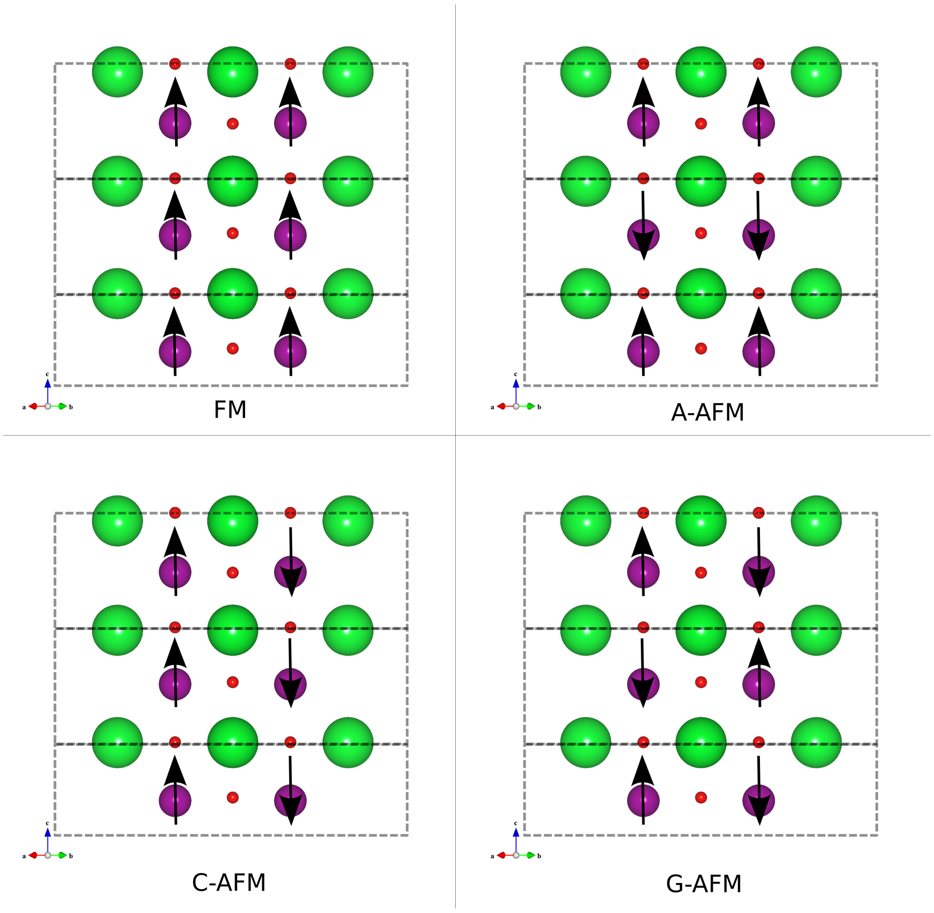

Fig. 6.2 Magnetic orderings studied in LSMO layers. Arrows indicate the spin directions. FM: ferromagnetic, A-AFM: A-type antiferromagnetic, C-AFM: C-type antiferromagnetic, G-AFM: G-type AFM antiferromagnetic ordering.

Our geometry optimization calculations showed us that the magnetic ground state always imposes FM in-plane order and a total net magnetic moment. The two out-of-plane magnetic arrangements (FM and A-AFM orders) are found quasi-degenerate within DFT error bars. Indeed, the energy difference per LSMO unit cell (or equivalently per Mn), between FM and A-type AFM orders, is in average 12 meV, with a mean deviation of 9 meV. One should mention that this is smaller than room temperature ($k_B T \sim 25$ meV). Cation ordering in LSMO determines whether the DFT ground state is the FM or the A-type AFM configuration. The two other magnetic configurations, in which there is in-plane AFM order, (C-AFM and G-AFM) are much higher in energy, ranging between 130 meV and 210 meV above the ground states.

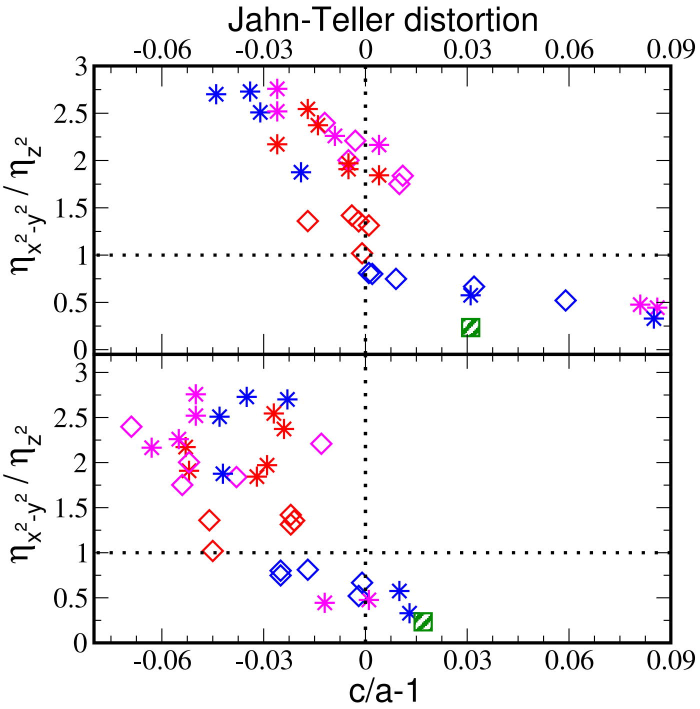

Fig. 6.3 $\eta(d_{x^2-y^2})/\eta(d_{z^2})$ ratio of the $d_{x^2-y^2}$ and d_{z^2} orbitals Mülliken occupancies in each mono-layer as a function of the Jahn-Teller distortion (JTd) and of the tetragonality parameter $c/a-1$. Red and pink symbols refer to the interfacial mono-layers, blue symbols to the central ones. Diamonds are for the FM order and stars for the A-type AFM one. The green dashed squares show the experimental values of LSMO over STO for 6 m.l. thin films exhibiting a dead layer. The Jahn-Teller distortion and c/a ratios are extracted from the cumulative displacements in Ref. [130] and the $\eta(d_{x^2-y^2})/\eta(d_{z^2})$ ratio is extracted from linear dichroism experiments of Ref. [124]. Bulk LSMO corresponds to the cross point between the dashed lines.

We report the statistics of both the Jahn-Teller distortion (JTd) (measured as $d_{OO}/a-1$, with d_{OO} the out-of-plane O-Mn-O distance) and c/a (c being the perovskite A-sites distances) as a function of the e_g orbitals Mülliken occupancies ratio in figure 6.3. The results are given for each LSMO mono-layers of the two quasi-degenerate ground states. We give the experimental values of Jahn-Teller distortion and $c/a-1$ values of 6 mono-layer LSMO over STO substrate from the reference [130]. We extracted Jahn-Teller distortion $c/a-1$ values from the cumulative displacements Δz of the atoms from the top TiO_2 layer of STO substrate given in Figure 4 of Ref [130]. We also give the experimental value of $\eta(x^2-y^2)/\eta(z^2)$ ratio of 6 mono-layer LSMO grown on STO from the reference [124]. Polarization-dependent X-ray absorption spectroscopy (XAS) helps to identify orbital occupation of transition-metal oxides. Linear Dichorism in XAS is the difference between X-ray absorption spectra taken with the polarization vector perpendicular and parallel to the crystal c-axis. One can use linear dicroism in L-edge XAS to identify the $3d$ orbital character of orbital-ordered compounds. Thus, we extracted the e_g occupancy ratio from the linear dicroism experiment results given in Figure 4 of Ref. [124] for 6 mono-layer LSMO over STO.

The main results are as follows: All three LSMO mono-layers are compressed along the $\vec{c}$ direction, except for the central layer in two AFM calculations. When we quantified the Jahn-Teller distortion of Mn-octahedra we saw that the Mn-octahedra of the interface mono-layers are contracted along the $\vec{c}$ direction whereas the Mn-octahedra of center mono-layer is elongated. The $d_{x^2-y^2}$ orbital occupancy is dominant in the contracted interfacial Mn-octahedras. This is the desired magnetic semi-metallic behavior. However, as one can expect, since the Mn-octahedra of the central mono-layer exhibits an elongation of the Mn-octahedra, the d_{z^2} orbiral is the preffered e_g orbital in this mono-layer. One must notice in figure 6.3 that there is dominant $d_{x^2-y^2}$ orbital occupancy for all mono-layers for a few calculations.

One can immediately remember from the previous chapter, where we studied $[La_{2/3}Sr_{1/3}MnO_3]_3[BaTiO_3]_3$ superlattices, that those results exhibit exact opposite behavior with these ones. In the $[La_{2/3}Sr_{1/3}MnO_3]_3[BaTiO_3]_3$ superlattices, one of the interface layers, into which the $BaTiO_3$ polarization directs, is elongated with a dominant d_{z^2} occupancy.

In table 6.2 and 6.3, we give the e_g spin populations and Mn magnetic moments per layer with associated structural properties of one typical cation ordering for FM and A-type AFM magnetic ordering. The cation ordering chosen is associated with the lowest energy for both FM and A-type AFM magnetic configurations.

LSMO mono-layer	e_g orb. $\eta_{x^2-y^2}$	spin pop. η_{z^2}	$\eta_{x^2-y^2}/\eta_{z^2}$	$c/a-1$	JTd	μ_{Mn}
1	**0.361**	0.266	1.357	-0.021	-0.002	3.343
2	0.368	**0.552**	0.667	-0.001	0.032	3.732
3	**0.597**	0.249	2.398	-0.069	-0.012	3.642

Table 6.2 Mülliken spin population of the Mn e_g orbitals, c/a ratio, JTd (Jahn-Teller distortion) and μ_{Mn} (Mn magnetic moment) in the ferromagnetic $[\mathrm{La}_{2/3}\mathrm{Sr}_{1/3}\mathrm{MnO}_3]_3[\mathrm{BaO}]_6$ ground state of one typical cation order.

LSMO mono-layer	e_g orb. $\eta_{x^2-y^2}$	spin pop. η_{z^2}	$\eta_{x^2-y^2}/\eta_{z^2}$	$c/a-1$	JTd	μ_{Mn}
1	**-0.394**	-0.166	2.373	-0.024	-0.014	3.26
2	0.256	**0.778**	0.329	-0.013	0.085	3.875
3	**-0.502**	-0.182	2.758	-0.050	-0.026	3.43

Table 6.3 Mülliken spin population of the Mn e_g orbitals, c/a ratio, JTd (Jahn-Teller distortion) and μ_{Mn} (Mn magnetic moment) in the A-type antiferromagnetic $[\mathrm{La}_{2/3}\mathrm{Sr}_{1/3}\mathrm{MnO}_3]_3[\mathrm{BaO}]_6$ ground state of one typical cation order.

One can see from these two tables that the behaviour is qualitatively similar. However, by looking at the e_g occupancy ratio one can notice that the $d_{x^2-y^2}$ orbital dominance (1st and 3rd m. l.) or d_{z^2} orbital dominance (2nd m. l.) is increased in the A-type AFM order compared to FM. Relatively, contraction in the 1st and 3rd mono-layer and elongation in the 2nd mono-layer are increased. The magnetic moment of Mn atom is qualitatively similar in each magnetic configuration.

These quasi-degenerate ground states (FM and A-type AFM orders) indicate that in real systems such superlattices may present one or the other spin arrangement as the ground state, according to the specific cation disorder. However one must keep in mind that at room temperature both FM and A-type AFM states have similar probabilities. Thus, we expect to have a net total magnetization even if the amplitude of this magnetization should be reduced. Moreover, the fact that this superlattice exhibit dominant $d_{x^2-y^2}$ orbital occupancy at the LSMO interfaces shows us that we reached our goal of controlling the e_g orbital occupancies.

6.3.2 The effect of the thickness of manganite layer: A test case of $(\mathrm{LSMO})_6-(\mathrm{BaO})_2$

Whether the previous section conclusion remains valid will be the focus of this section if one increases the size of the manganite layer. In order to check this point we increased the size of the LSMO layer to 6 mono-layers, and performed the geometry optimization calculations for one typical cation configuration. In figure 6.4, one can see the schematic representation of $[La_{2/3}Sr_{1/3}MnO_3]_6[BaO]_2$ superlattice. To keep the calculation to a reasonable size, we needed to simultaneously decrease the BaO layer thickness.

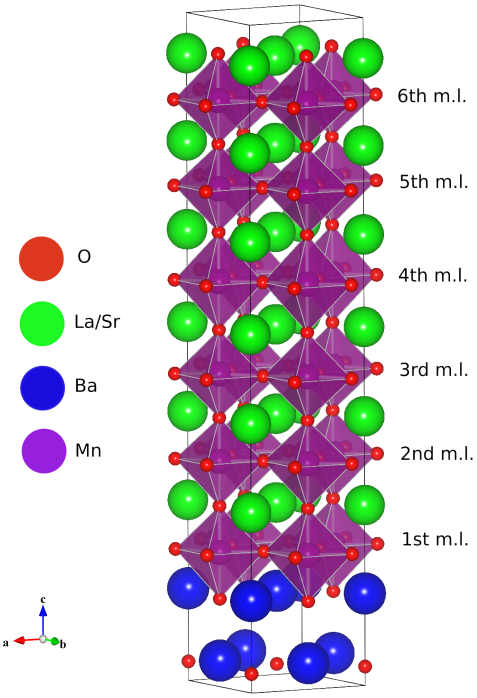

Fig. 6.4 (color online) Schematic representation of the $[La_{2/3}Sr_{1/3}MnO_3]_6[BaO]_2$ superlattice. m.l. stands for mono-layer.

We thus first checked whether such a reduction would affect the results. For this purpose we run test calculations on the preceding superlattice with only two mono-layers of BaO (i.e. on $[La_{2/3}Sr_{1/3}MnO_3]_3[BaO]_2$). The results for such a superlattice is summarized in the table 6.4. Even though the structural parameters, i.e. Jahn-Teller distortion parameter and tetragonality parameter, show different behaviour than those of $[La_{2/3}Sr_{1/3}MnO_3]_3[BaO]_6$, the e_g orbital spin populations as well as the e_g occupancy ratio and Mn magnetic moment

LSMO mono-layer	e_g orb. spin pop. $\eta_{x^2-y^2}$	η_{z^2}	$\eta_{x^2-y^2}/\eta_{x^2}$	$c/a-1$	JTd	μ_{Mn}
1	**0.395**	0.373	1.050	-0.026	0.022	3.536
2	0.375	**0.426**	0.892	-0.022	-0.009	3.573
3	**0.57**	0.27	2.024	-0.057	-0.011	3.627

Table 6.4 Mülliken spin population of the Mn e_g orbitals, c/a ratio, JTd (Jahn-Teller distortion) and μ_{Mn} (Mn magnetic moment) in the $[\mathrm{La}_{2/3}\mathrm{Sr}_{1/3}\mathrm{MnO}_3]_3[\mathrm{BaO}]_2$ ground state of one typical cation order.

showed similar behaviour. Thus, the 2-BaO mono-layers model is an appropriate choice for us to test the size of the manganite layer behaviour with a BaO alternated layer.

As there is a FM in-plane order in $[\mathrm{LSMO}]_3[\mathrm{BaO}]_6$ superlattices and the C-type and G-type AFM orders in $[\mathrm{LSMO}]_3[\mathrm{BaO}]_6$ superlattices are significantly higher in energy than the quasi-degenerate FM and A-type AFM, we only studied three different spin configurations for the $[\mathrm{La}_{2/3}\mathrm{Sr}_{1/3}\mathrm{MnO}_3]_6[\mathrm{BaO}]_2$ superlattices: FM order, A-type AFM and ↑↑↓↓↑↑ which can be seen in figure 6.5.

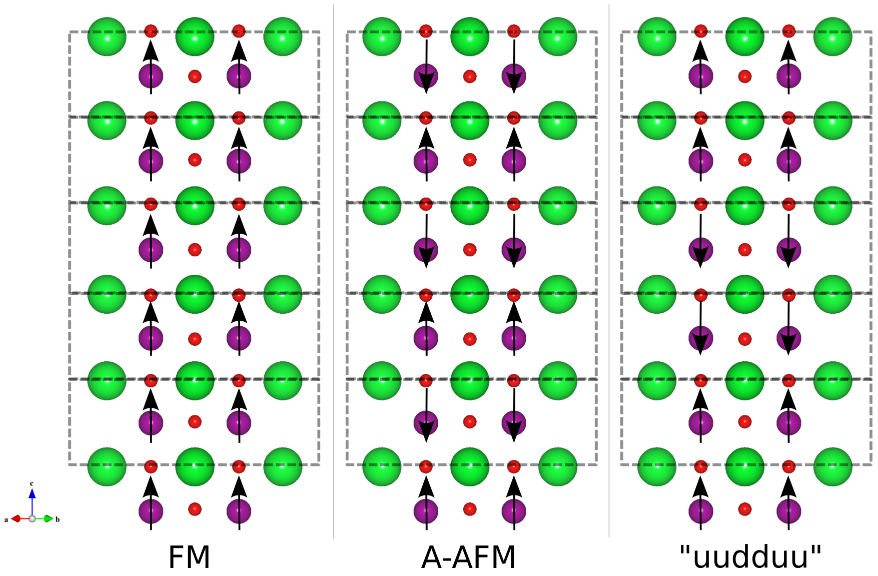

Fig. 6.5 Magnetic orderings studied in LSMO layers. Arrows indicate the spin directions. FM: ferromagnetic, A-AFM: A-type antiferromagnetic and “uudduu”: ↑↑↓↓↑↑ ordering.

Our calculations showed a ground-state with the ↑↑↓↓↑↑ pattern (“**uudduu**”) and a total net magnetization for the system. This ground state is again very close in energy to the FM state and the A-type AFM state. The latter does not however correspond to a full AFM state, since it exhibits a non null net total magnetization of about $1/10$ of an electron per Mn atom. The dominant e_g orbital occupancy in the different LSMO mono-layers is found qualitatively

Magnetic System	Net total magnetization per Mn atom
FM	3.67
↑↑↓↓↑↑	1.13
A-AFM	0.11

Table 6.5 Number of spin-up electrons, i.e. net total magnetization, per Mn atom for each magnetic configuration of $[La_{2/3}Sr_{1/3}MnO_3]_3[BaO]_2$ superlattice.

independent of the out-of–plane spin ordering (see tables 6.6, 6.7 and 6.8 for example).

LSMO mono-layer	e_g orb. spin pop. $\eta_{x^2-y^2}$	η_{z^2}	$\eta_{x^2-y^2}/\eta_{z^2}$	$c/a-1$	JTd	μ_{Mn}
1	**0.459**	0.319	1.439	-0.032	0.017	3.548
2	**0.467**	0.237	1.970	-0.028	-0.034	3.434
3	**-0.460**	-0.253	1.818	-0.021	-0.038	-3.449
4	-0.302	**-0.741**	0.408	0.013	0.070	-3.892
5	**0.480**	0.220	2.182	-0.027	-0.035	3.442
6	**0.501**	0.293	1.710	-0.043	-0.012	3.567

Table 6.6 Mülliken spin population of the Mn e_g orbitals, $c/a-1$ ratio, JTd (Jahn-Teller distortion) and μ_{Mn} (Mn magnetic moment) in the ↑↑↓↓↑↑ ordered $[La_{2/3}Sr_{1/3}MnO_3]_6[BaO]_2$ ground state of one typical cation order.

LSMO mono-layer	e_g orb. spin pop. $\eta_{x^2-y^2}$	η_{z^2}	$\eta_{x^2-y^2}/\eta_{z^2}$	$c/a-1$	JTd	μ_{Mn}
1	**0.452**	0.305	1.482	-0.031	0.014	3.52
2	**0.426**	0.311	1.370	-0.022	-0.025	3.484
3	**0.426**	0.328	1.299	-0.017	-0.026	3.511
4	0.385	**0.574**	0.671	0.004	0.033	3.788
5	**0.474**	0.342	1.386	-0.029	-0.020	3.594
6	**0.541**	0.258	2.097	-0.048	-0.014	3.572

Table 6.7 Mülliken spin population of the Mn e_g orbitals, $c/a-1$ ratio, JTd (Jahn-Teller distortion) and μ_{Mn} (Mn magnetic moment) in the ferromagnetic $[La_{2/3}Sr_{1/3}MnO_3]_6[BaO]_2$ of one typical cation order.

LSMO mono-layer	e_g orb. spin pop. $\eta_{x^2-y^2}$	 η_{z^2}	$\eta_{x^2-y^2}/\eta_{z^2}$	$c/a-1$	JTd	μ_{Mn}
1	**-0.492**	-0.261	1.885	-0.037	0.008	-3.509
2	**0.494**	0.2	2.470	-0.032	-0.038	3.412
3	**-0.426**	-0.165	2.933	-0.025	-0.044	-3.364
4	0.291	**0.771**	0.377	0.014	0.077	3.912
5	**-0.509**	-0.17	2.994	-0.031	-0.040	-3.407
6	**0.552**	0.213	2.592	-0.050	-0.021	3.516

Table 6.8 Mülliken spin population of the Mn e_g orbitals, $c/a-1$ ratio, JTd (Jahn-Teller distortion) and μ_{Mn} (Mn magnetic moment) in the A-type antiferromagnetic $[\mathrm{La}_{2/3}\mathrm{Sr}_{1/3}\mathrm{MnO}_3]_6[\mathrm{BaO}]_2$ of one typical cation order.

As in the $[\mathrm{LSMO}]_3[\mathrm{BaO}]_6$ calculations, the mono-layers at the interfaces are contracted and strongly dominated by the $d_{x^2-y^2}$ orbital occupancy. In fact only the inner most mono-layer is still elongated and dominated by d_{z^2} orbital occupancy. As can be seen in figure 6.6, the Mn magnetic moments and total e_g occupancies exhibit a strong correlation with the amplitude of the Jahn-Teller distortion. When the Mn-octahedra is elongated, there exist larger e_g population and naturally larger Mn magnetic moment. The Mn-octahedra in the

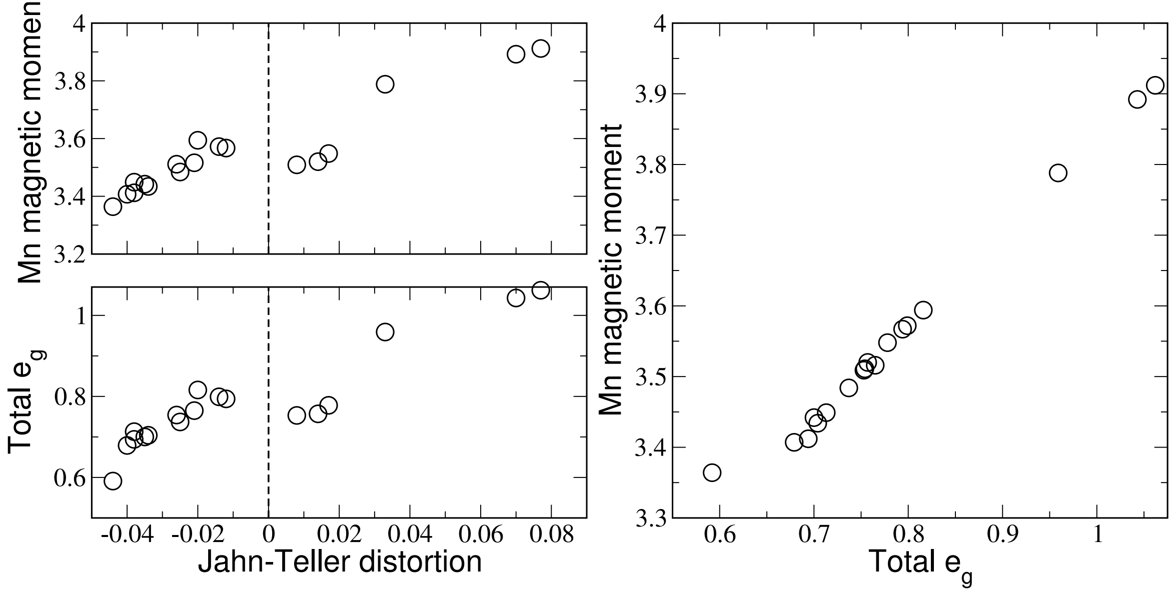

Fig. 6.6 The correlation between magnetic moment and total e_g population of each manganite mono-layer with the Jahn-Teller distortion of each manganite mono-layer in $[\mathrm{LSMO}]_6[\mathrm{BaO}]_2$ superlattices.

inner most mono-layer exhibit a strong elongation and the largest Mn magnetic moment as can be seen from the tables 6.6, 6.7 and 6.8. This specificity of the inner most mono-layer is responsible for the non-vanishing total magnetization in the A-type AFM state. These results show that, when increasing the thickness of the LSMO layer, one essentially increases the thickness of the interface layers and not of the central one. The former being contracted along $\vec{c}$ and dominated by $d_{x^2-y^2}$ orbital occupancy, it confirms that the use of BaO alternating layers allow the control of the $d_{x^2-y^2}$ vs d_{z^2} orbital occupancies at the LSMO interfaces.

6.3.3 Manganite thin films with different alkaline-earth oxides

In this section we will check whether this result is resilient to a change in the simple oxide and manganite compounds. We thus performed a set of calculations using BaO, SrO and MgO as alternating layers, and LSMO or LBMO as manganite layers ($[\mathrm{La}_{2/3}\mathrm{A}_{1/3}\mathrm{MnO}_3]_3[\mathrm{BO}]_6$), for a typical cation disorder model. Table 6.9 summarizes the e_g orbital occupancies, Mn magnetic moments and related structural properties for those calculations. One may notice that the $[\mathrm{LBMO}]_3[\mathrm{BaO}]_6$ and $[\mathrm{LSMO}]_3[\mathrm{SrO}]_6$ superlattices have in theory equivalent interfaces, unlike all the other superlattices we studied. One sees in table 6.9 that this symmetry is kept in the $[\mathrm{LSMO}]_3[\mathrm{SrO}]_6$ superlattice. Indeed, the two calculations with and without imposed symmetry yield equivalent results within errors bars. For the $[\mathrm{LBMO}]_3[\mathrm{BaO}]_6$ superlattice however, this is not the case. A spontaneous symmetry breaking occurs along the $\vec{c}$ axis, associated with a small energetic stabilization (37 meV $\simeq$ 430 K) per LBMO unit cell). This induces a symmetry breaking in the e_g orbitals occupancies as can be seen in table 6.9. Nevertheless, all manganite interface mono-layers are favoring a $d_{x^2-y^2}$ occupancy over a d_{z^2} one, as was the case for the $[\mathrm{LSMO}]_\mathrm{n}[\mathrm{BaO}]_\mathrm{p}$ compounds. The control of the orbital order at the interfaces thus seems to remain valid independently of the manganite compound and of the simple oxide chosen for the alternating layer.

6.3.4 Transport properties

We saw in the previous sections that the use of a simple oxide alternating layer allows to obtain the desired orbital ordering at the interfaces as well as the hindering of the delocalization at the interfaces. As one of our objectives was to improve the transport properties of the superlattices, we would like to present here the Boltzman transport (BoltzTrap) calculations carried out by our collaborator, Sébastien Lemal on our systems. He calculated the in-plane conductivity tensor $\sigma_{xx}(T,\mu) = \sigma_{yy}(T,\mu)$ at 300 K of the LSMO layers in of $[\mathrm{LSMO}]_\mathrm{n}[\mathrm{BaO}]_\mathrm{p}$

	LAMO	e_g orb.	spin pop.	$\eta_{x^2-y^2}/\eta_{z^2}$	$c/a-1$	JTd	μ_{Mn}
	mono-layer	$\eta_{x^2-y^2}$	η_{z^2}				
LBMO-BaO	1	**0.441**	0.284	1.553	-0.015	-0.001	3.479
	2	0.384	**0.538**	0.714	0.014	0.021	3.733
	3	**0.508**	0.263	1.932	-0.022	0.005	3.538
LBMO-BaO ($P4/mmm$)	1	**0.476**	0.265	1.796	-0.026	-0.002	3.5
	2	0.244	**0.655**	0.373	0.033	0.033	3.698
	3	**0.476**	0.265	1.796	-0.026	-0.002	3.5
LSMO-SrO	1	**0.478**	0.255	1.875	-0.062	-0.014	3.487
	2	0.399	**0.521**	0.766	0.010	0.007	3.728
	3	**0.479**	0.255	1.878	-0.064	-0.014	3.487
LSMO-SrO ($P4/mmm$)	1	**0.479**	0.252	1.901	-0.062	-0.014	3.484
	2	0.399	**0.528**	0.756	0.008	0.010	3.739
	3	**0.479**	0.252	1.901	-0.062	-0.014	3.484
LSMO-MgO	1	**0.352**	0.169	2.083	-0.077	-0.047	3.189
	2	0.234	**0.702**	0.333	0.016	0.061	3.75
	3	**0.596**	0.260	2.292	-0.107	-0.007	3.649
LBMO-MgO	1	**0.353**	0.166	2.127	-0.098	-0.054	3.186
	2	0.238	**0.695**	0.342	0.045	0.074	3.754
	3	**0.590**	0.321	1.838	-0.037	0.044	3.708

Table 6.9 Mülliken spin population of the Mn e_g orbitals in the $[\mathrm{La}_{2/3}\mathrm{A}_{1/3}\mathrm{MnO}_3]_3[\mathrm{BO}]_6$ ground state (A=Sr, Ba ; B=Ba, Sr, Mg). The shown example was chosen as the cation ordering associated with the lowest ground state energy.

and $[\mathrm{LSMO}]_3[\mathrm{BTO}]_3$ superlattices within the BoltzTrap code [143] (T is the temperature and μ is the chemical potential). These calculations rely on the previous first-principle results and are within constant relaxation time (CRTA). The results are presented in the figure 6.7. As we

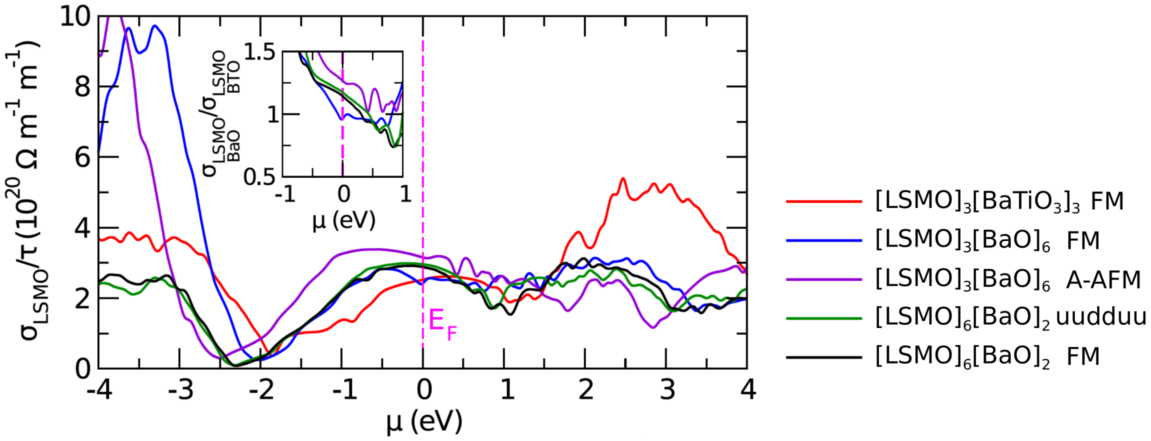

Fig. 6.7 Transport calculations on the $[\mathrm{LSMO}]_\mathrm{n}[\mathrm{BaO}]_\mathrm{p}$ and $[\mathrm{LSMO}]_3[\mathrm{BTO}]_3$ systems at 300 K.

can see from this figure there is not a significant evolution in the in-plane conductivity in the $[\mathrm{LSMO}]_3[\mathrm{BaO}]_6$ superlattice compared to FM $[\mathrm{LSMO}]_3[\mathrm{BTO}]_3$ superlattice. In the A-type AFM $[\mathrm{LSMO}]_3[\mathrm{BaO}]_3$ superlattice, we observe a small increase in the in-plane conductivity. In the $[\mathrm{LSMO}]_6[\mathrm{BaO}]_2$ superlattices, ferromagnetic and "↑↑↓↓↑↑" cases have similar spectral conductivities. The maximum LSMO conductivity obtained in these new superlattices is only $1.25\,\sigma_{xx}^{\mathrm{BTO-LSMO}}$. These results show that enhancing $d_{x^2-y^2}$ orbital occupancy is not necessarily enough to increase significantly the in-plane electrical conductivity. However, one should remind that our conductivity estimations are restricted to the CRTA, within which it has been recently shown (in $\mathrm{LaNiO_3}$ thin films) that such calculations underestimate the amplitude of the changes in conductivity compared to experimental measurements [144].

6.4 Conclusion

In summary, we may recall that thin films and superlattices of $[\mathrm{La}_{2/3}\mathrm{A}_{1/3}\mathrm{MnO}_3]$ (A=Sr, Ca) manganite compounds, over an $\mathrm{SrTiO_3}$ substrate, have been extensively studied in the hope to find a good material for electronic and spintronics applications. Indeed, on STO, the LSMO is under tensile strain, so one is entitled to expect that the elastic energy will favor a contraction of the mono-layers along the $\vec{c}$ direction. Due to the degeneracy of the e_g orbitals, such a contraction would have enhanced the occupation of the $d_{x^2-y^2}$ over the d_{z^2}

and thus the ferromagnetic and metallic behavior through the double exchange mechanism. Unfortunately the formation of a non-magnetic and insulating layer (called “dead layer”) at the interface prevents to reach this goal. One of the hypothesis to explain this “dead layer” supposed it originates in a weak delocalization of the Mn d_{z^2} orbitals in the empty Ti ones inducing a d_{z^2} dominant occupancy and a mono-layer extension along $\vec{c}$. The energy gain in this phenomenon overvalues the elastic energy loss of the LSMO volume increase.

We theoretically studied different possibilities to prevent the delocalization at the interface by using convenient alternating layers in the superlattices. Our first principle calculations showed that superlattices alternating manganite and alkaline-earth simple oxides efficiently prevent inter-layer delocalization, promote mono-layers contraction at the interfaces and a preferred $d_{x^2-y^2}$ occupancy over the d_{z^2} one. Our studies show that this result should hold for different manganite and alternating layer thicknesses. However, Boltzman transport calculations show that it marginally impacts the transport properties. The hypothesis of the origin of the dead layer in the e_g orbitals ordering should thus be questioned. Nevertheless, we succeeded in controlling the e_g orbital order and occupancies with appropriate alternating interface layers.

Conclusion

During this thesis, we studied theoretically manganite superlattices to investigate their structural and electronic properties by means of first-principle calculations. Our study is motivated by the interface effects that exist in perovskite oxides superlattices. Indeed, manganite thin films and superlattices have great potential for technological applications such as magnetic recording/memory technology. Perovskite oxides, with the formulation ABO_3, exhibit a wide variety of functional properties exploited in various technological applications. By combining such perovskites in superlattices, one can not only combine their intrinsic properties but also can induce totally new phenomena at their interfaces. Manganites are an important class of perovskite oxides which have been extensively studied due to their various exotic properties as we discussed in Chapter 2. Manganites, with the formulation $AMnO_3$ where *A* is an element or a solid solution of two or more elements, offer large varieties of systems with respect to the A site solid solution. The A-site generally is composed of one rare-earth trivalent element (R) and one divalent alkaline-earth element (D) ($A = R_{1-x}D_x$). Depending on the choice of R and D, manganites can display very rich phase diagrams of magnetic and electric phenomena with respect to doping concentration of D. In addition to this, giant and colossal magnetoresistance that a class of manganites show under the application of a magnetic field make them desirable for various devices. Intrinsic large Curie temperature is also another important feature that some manganites hold.

In this thesis, we chose to study in $La_{1-x}Sr_xMnO_3$ at the doping $x = 1/3$ deposited on $SrTiO_3$ substrate since it is a ferromagnetic metal and has a large Curie temperature ($T_c \simeq 370K$). We combined $La_{1-x}Sr_xMnO_3$ layers with different alternated insulator layers and studied structural and magnetic properties of such heterostructures by geometry optimizations within the Density Functional Theory (DFT) calculations. In Chapter 3, we gave the technical background of the DFT and our computational details.

We dedicated Chapter 4 to the study of $LaMnO_3 - SrMnO_3$ superlattices. We studied different magnetic orderings with different number of layers and cation orderings. Both strain-free superlattices and superlattices deposited on a $SrTiO_3$ substrate were studied by means of first-principle calculations. We found that $[LaMnO_3]_1 - [SrMnO_3]_1$ and $[LaMnO_3]_2 - [SrMnO_3]_2$ superlattices are A-type antiferromagnets, whereas the $[LaMnO_3]_2 - [SrMnO_3]_1$ superlattice is ferromagnetic.

In Chapter 5, we studied $[BaTiO_3]_3/[La_{2/3}Sr_{1/3}MnO_3]_3$ (BTO-LSMO) superlattice deposited on $SrTiO_3$ substrate by means of first-principle calculations. We did full geometry optimizations and investigated the electronic structures. Our study was motivated by the large increase in Curie temperature that is observed in this superlattices through orbital ordering compared to bulk LSMO. We studied the effect of the asymmetrical and symmetrical chemical nature of the interfaces, the effect of the polarization of the alternated layers, and the role of the antiferrodistortive motions of manganite layers on the electronic structure of these superlattices. Our findings in BTO-LSMO superlattices showed us that one interface mono-layer and central mono-layer Mn-octahedra are contracted along $\vec{c}$ direction (negative Jahn-Teller distortion) whereas the other interface mono-layer Mn-octahedra is elongated along $\vec{c}$ direction (positive Jahn-Teller distortion). This Jahn-Teller distortion is naturally followed by $d_{x^2-y^2}$ (d_{z^2}) orbital occupancy enhancement in the contracted (elongated) mono-layers Mn-octahedra. Since the LSMO layers are very thin (only a few unit cell) in BTO/LSMO superlattice, one thus expects that the in-plane magnetic properties are more important than the out-of magnetic properties. Therefore, preferential $d_{x^2-y^2}$ orbital occupancy maximize the in-plane magnetic properties of this superlattice. On the other hand, it is known that the elongated mono-layers with d_{z^2} orbital occupancy exhibit reduced magnetism and conductivity. In the elongated interface layer, we also observed a delocalization of the Mn-$3d$ electrons on the empty $3d_{z^2}$ orbital. First, we associated this symmetry breaking at the interfaces with the fact that BTO-LSMO has chemically asymmetric interfaces: (the interface attached to the contracted mono-layer: $(La/Sr)O/TiO_2$, the interface attached to the elongated mono-layer: BaO/MnO_2). Thus, we tried to work with symmetric (equivalent interfaces). To do this, we replaced $La_{2/3}Sr_{1/3}MnO_3$ (LSMO) with $La_{2/3}Ba_{1/3}MnO_3$ (LBMO) and worked in $[BaTiO_3]_3/[La_{2/3}Ba_{1/3}MnO_3]_3$ (BTO-LBMO) superlattice. In this new superlattice, we had only BaO/MnO_2-type of interfaces. However, we saw that there was still the same type of symmetry breaking in the interface Mn-octahedras in this new superlattice. We concluded at the end of this study that the asymmetric or symmetric chemical nature of the interface is not a leading parameter for the interface electronic structure. Thus, we changed our focus on the alternated layers possible impact on such a symmetry breaking. Indeed, $BaTiO_3$ is a ferroelectric insulator and it induces a spontaneous polarization in its layers. Supressing the polarization in $BaTiO_3$ layers in BTO-LBMO superlattice by imposing mirror symmetry planes in $\vec{c}$ direction helped us to suppress this spontaneous symmetry breaking in the interfaces of BTO-LBMO superlattice. In totally symmetric BTO-LBMO superlattice, both interface Mn-octahedra were elongated with dominant d_{z^2} occupancy and there were delocalization from Mn-3d orbitals to empty Ti 3d_{z^2} ones. Thus, we understood that the parameter responsible for the spontaneous symmetry breaking in the interface manganite layers is the orientation of the polarization. When the direction of polarization is out-of the interface manganite mono-layer, the interface manganite mono-layer Mn-octahedra is contracted with a dominant $d_{x^2-y^2}$ occupation. On the other hand, when it is into the interface manganite mono-layer Mn-octahedra, the latter is elongated with a dominant d_{z^2} occupation. We also observed a delocalization of the 3d_{z^2} orbital of the Mn on the empty Ti ones in the 3rd mono-layer when it is elongated. We wanted to investigate the role of polarization further and for this purpose, we decided to focus on the amplitude of the polarization. We studied the $[\mathrm{PbTiO_3}]_3/[\mathrm{La_{2/3}Sr_{1/3}MnO_3}]_3$ (PTO-LSMO) superlattice deposited on a $\mathrm{SrTiO_3}$ substrate since $\mathrm{PbTiO_3}$ induces larger polarization compared to $\mathrm{BaTiO_3}$ and compared our results with previous BTO-LSMO and BTO-LBMO superlattices. We saw that the amplitude of the polarization only affects the contracted interface Mn-octahedra. It enhances the contraction of this interface Mn-octahedra and the preferential occupancy of $d_{x^2-y^2}$ orbital. Next exploration was on the role of the antiferrodistortive (AFD) motions of the Mn-octahedra of LSMO layers. In order to realize the AFD motions, we first gave a initial guess by displacing the oxygen atoms of $\mathrm{MnO_2}$ planes along $\vec{a}$ and $\vec{b}$ directions. Then, we ran geometry optimization calculations to see whether these motions were kept or not. Through this study, we saw that the AFD motions are present at least at low temperature. These rotations do only exist in the contracted mono-layer Mn-octahedras. When we compared the results of rotating LSMO superlattices with the ones without rotations we saw that the Jahn-Teller distortion parameter was affected by the rotations. However, the rotations increased the preferential $d_{x^2-y^2}$ occupancy even though it didn't affect the Jahn-Teller distortion in the contracted Mn-octahedras. Thus, we concluded that these motions are expected to enhance the in-plane magnetic properties. We saw that the AFD motions and the delocalization of 3d_{z^2} from Mn–Ti at the elongated mono-layer Mn-octahedra are exclusive.

We dedicated Chapter 6 into the study of suppression of the elongated interface manganite layer that we observed in BTO-LSMO superlattice in Chapter 5. This elongated layer is named "dead layer" since it exhibits reduced magnetization and conductivity compared to the contracted LSMO mono-layers. We suggested that the delocalization of 3d electron of Mn to emtpy Ti 3d_{z^2} electrons at the interface can be a possible reason of this elongation and hindering magnetization. Thus, we wanted to find new alternated layers in order to suppress this delocalization. Within this line, we needed to work with a compound; (i) without d shells so that there cannot a delocalization take place at the interface, (ii) with a tetragonal or cubic structure so that tetragonal distortion can be favored in the manganite layers rather than rhombohedral one, (iii) having a perfect epitaxy with mangantite layers. Alkaline earth oxides fulfill all these three requirements. First, we studied $[BaO]_6/[La_{2/3}Sr_{1/3}MnO_3]_3$ (6[BaO]-3[LSMO]) superlattice deposited on $SrTiO_3$ substrate by means of first-principle calculations. We did full geometry optimizations and investigated the electronic structures for different magnetic orderings of LSMO layers. We found that ferromagnetic and A-type antiferromagnetic orderings are quasi-degenerate which implies that we have in-plane ferromagnetism in the BaO-LSMO superlattice. In both ground states, both interface LSMO mono-layers are contracted with dominant $d_{x^2-y^2}$ orbital occupancy whereas the central LSMO mono-layer is elongated with dominant d_{z^2} orbital occupancy. Thus, we successfully managed to kill the delocalization at the interface. In order to see if these results are also hold in thicker manganite layers, we studied $[BaO]_2/[La_{2/3}Sr_{1/3}MnO_3]_6$ (2[BaO]-6[LSMO]) superlattice. We decreased the number of BaO layers from 6 to 2 in order to have a feasible computational time but we first ran test calculation on $[BaO]_2/[La_{2/3}Sr_{1/3}MnO_3]_3$ (2[BaO]-6[LSMO]) superlattice in order to see if there is a change in results between 6[BaO]-3[LSMO] and 2[BaO]-6[LSMO] superlattices. Similar structural and magnetic properties are also observed in the latter. Thus, we continued our work in 2[BaO]-6[LSMO] superlattice without problem. We tested different magnetic orderings in 2[BaO]-6[LSMO] superlattice such as ferromagnetic, A-type antiferromagnetic and ↑↑↓↓↑↑ and we saw that ↑↑↓↓↑↑ is the lowest in energy but there is quasi-degeneracy with others at room temperature. The structure and magnetic properties are similar to those of 6[BaO]-3[LSMO]. Only the inner most central LSMO mono-layer is elongated with a dominant d_{z^2} orbital occupancy whereas the interface layers are contracted with a dominant $d_{x^2-y^2}$ orbital occupancy. In this superlattice, one essentially increases the thickness of the interface layers since the unit cells from the interface up to the inner most central layer are all contracted like the interface layer. After this study, we wanted to check whether our results are resilient to a change in the simple oxide and manganite compounds. Therefore, we took SrO and MgO as alternated layers (6 layers) and LBMO as manganite layer (3 layers) and performed set calculations with new superlattices. The results that we obtained for 6[BaO]-3[LSMO] superlattice are hold for these ones as well. In the study 6[BaO]-3[LBMO] and 6[SrO]-3[LSMO], we had the chance to study the effect of symmetric interfaces as we did before in BTO-LBMO superlattice. We saw that there is a spontanous symmetry breaking at the interfaces in 6[BaO]-3[LBMO] superlattice whereas there is no such symmetry breaking in 6[SrO]-3[LSMO]. This result is interesting and to be investigared further. Finally, Sébastian Lemal calculated the conductivity in these new superlattices by transport calculations in order to compare with BTO-LSMO superlattice. Unfortunately, although we managed to kill the elongation and delocalization at the interface and manage to favor $d_{x^2-y^2}$ over d_{z^2} orbital the maximum conductivity of this layer is not significantly improved compared to the dead layer present in BTO-LSMO $(1.25\,\sigma_{xx}^{\mathrm{BTO-LSMO}})$.

Future works can be dedicated to question the real reason behind the dead layer present in LSMO superlattices with alternated layers. Different alternated layers possibly hindering the delocalization at interface like fluorides such as potassium fluoride (KF) or bromides such as lithium bromide (LiBr) can be also tested to see if the conductivity is improved compared BTO-LSMO superlattice.

References

[1] M. K. Wu, J. R. Ashburn, C. J. Torng, P. H. Hor, R. L. Meng, L. Gao, Z. J. Huang, Y. Q. Wang, and C. W. Chu. Superconductivity at 93 k in a new mixed-phase y-ba-cu-o compound system at ambient pressure. *Phys. Rev. Lett.*, 58:908–910, Mar 1987.

[2] Hans Lüth. *Solid Surfaces, Interfaces and Thin Films*. Springer-Verlag Berlin Heidelberg, sixth edition edition, 2015.

[3] Milton Ohring. *Materials Science of Thin Films (Second Edition)*. Academic Press, San Diego, second edition edition, 2002.

[4] W Prellier, Ph Lecoeur, and B Mercey. Colossal-magnetoresistive manganite thin films. *Journal of Physics: Condensed Matter*, 13(48):R915, 2001.

[5] Pavlo Zubko, Stefano Gariglio, Marc Gabay, Philippe Ghosez, and Jean-Marc Triscone. Interface physics in complex oxide heterostructures. *Annual Review of Condensed Matter Physics*, 2:141–165, 2011.

[6] Eriko Ohshima, Yuko Saya, Masashi Nantoh, and Maki Kawai. Synthesis and magnetic property of the perovskite $\mathrm{bi}_{1-x}\mathrm{sr}_x\mathrm{mno}_3$ thin film. *Solid State Communications*, 116(2):73 – 76, 2000.

[7] Paul A. Salvador, Trong-Duc Doan, Bernard Mercey, and Bernard Raveau. Stabilization of ymno3 in a perovskite structure as a thin film. *Chemistry of Materials*, 10(10):2592–2595, 1998.

[8] C. Kwon, K.-C. Kim, M. C. Robson, J. Y. Gu, M. Rajeswari, T. Venkatesan, and R. . Desirable magnetotransport properties in doped mn-oxide-based superlattices. *Journal of Applied Physics*, 81(8):4950–4952, 1997.

[9] Yafeng Lu, J. Klein, C. Höfener, B. Wiedenhorst, J. B. Philipp, F. Herbstritt, A. Marx, L. Alff, and R. Gross. Magnetoresistance of coherently strained $\mathrm{la}_{2/3}\mathrm{ba}_{1/3}\mathrm{mno}_3/\mathrm{SrTiO}_3$ superlattices. *Phys. Rev. B*, 62:15806–15814, Dec 2000.

[10] Moon-Ho Jo, Neil D. Mathur, Jan E. Evetts, Mark G. Blamire, Manuel Bibes, and Josep Fontcuberta. Inhomogeneous transport in heteroepitaxial $\mathrm{la}_{0.7}\mathrm{ca}_{0.3}\mathrm{mno}_3/\mathrm{srtio}_3$ multilayers. *Applied Physics Letters*, 75(23):3689–3691, 1999.

[11] M. Izumi, T. Manako, Y. Konishi, M. Kawasaki, and Y. Tokura. $\mathrm{la}_{1-x}\mathrm{sr}_x\mathrm{mno}_3$ superlattices composed of ferromagnetic $x = 0.4$ and antiferromagnetic $x = 0.55$ layers. *Phys. Rev. B*, 61:12187–12195, May 2000.

[12] G.H. Jonker and J.H. Van Santen. Ferromagnetic compounds of manganese with perovskite structure. *Physica*, 16(3):337 – 349, 1950.

[13] J.H. Van Santen and G.H. Jonker. Electrical conductivity of ferromagnetic compounds of manganese with perovskite structure. *Physica*, 16(7):599 – 600, 1950.

[14] J. Volger. Further experimental investigations on some ferromagnetic oxidic compounds of manganese with perovskite structure. *Physica*, 20(1):49 – 66, 1954.

[15] Clarence Zener. Interaction between the d-shells in the transition metals. ii. ferromagnetic compounds of manganese with perovskite structure. *Phys. Rev.*, 82:403–405, May 1951.

[16] E. O. Wollan and W. C. Koehler. Neutron diffraction study of the magnetic properties of the series of perovskite-type compounds $[(1-x)\mathrm{La}, x\mathrm{Ca}]\mathrm{Mno}_3$. *Phys. Rev.*, 100:545–563, Oct 1955.

[17] G.H. Jonker. Magnetic compounds with perovskite structure iv conducting and non-conducting compounds. *Physica*, 22(6–12):707 – 722, 1956.

[18] C. W. Searle and S. T. Wang. Studies of the ionic ferromagnet (lapb)mno3. v. electric transport and ferromagnetic properties. *Canadian Journal of Physics*, 48(17):2023–2031, 1970.

[19] M. N. Baibich, J. M. Broto, A. Fert, F. Nguyen Van Dau, F. Petroff, P. Etienne, G. Creuzet, A. Friederich, and J. Chazelas. Giant magnetoresistance of (001)fe/(001)cr magnetic superlattices. *Phys. Rev. Lett.*, 61:2472–2475, Nov 1988.

[20] G. Binasch, P. Grünberg, F. Saurenbach, and W. Zinn. Enhanced magnetoresistance in layered magnetic structures with antiferromagnetic interlayer exchange. *Phys. Rev. B*, 39:4828–4830, Mar 1989.

[21] S. S. P. Parkin, Z. G. Li, and David J. Smith. Giant magnetoresistance in antiferromagnetic co/cu multilayers. *Applied Physics Letters*, 58(23):2710–2712, 1991.

[22] A. E. Berkowitz, J. R. Mitchell, M. J. Carey, A. P. Young, S. Zhang, F. E. Spada, F. T. Parker, A. Hutten, and G. Thomas. Giant magnetoresistance in heterogeneous cu-co alloys. *Phys. Rev. Lett.*, 68:3745–3748, Jun 1992.

[23] Eric E. Fullerton, M. J. Conover, J. E. Mattson, C. H. Sowers, and S. D. Bader. 150% magnetoresistance in sputtered fe/cr(100) superlattices. *Applied Physics Letters*, 63(12):1699–1701, 1993.

[24] L. H. Chen, S. Jin, T. H. Tiefel, and R. Ramesh. Creation of bulk, superlatticelike structure and giant magnetoresistance effect in a deformed cu-ni-fe alloy. *Applied Physics Letters*, 64(8):1039–1041, 1994.

[25] T. L. Hylton, K. R. Coffey, M. A. Parker, and J. K. Howard. Giant magnetoresistance at low fields in discontinuous nife-ag multilayer thin films. *Science*, 261(5124):1021–1024, 1993.

[26] R.M. Kusters, J. Singleton, D.A. Keen, R. McGreevy, and W. Hayes. Magnetoresistance measurements on the magnetic semiconductor nd0.5pb0.5mno3. *Physica B: Condensed Matter*, 155(1–3):362 – 365, 1989.

[27] R. von Helmolt, J. Wecker, B. Holzapfel, L. Schultz, and K. Samwer. Giant negative magnetoresistance in perovskitelike $la_{2/3}ba_{1/3}mno_x$ ferromagnetic films. *Phys. Rev. Lett.*, 71:2331–2333, Oct 1993.

[28] M. McCormack, S. Jin, T. H. Tiefel, R. M. Fleming, Julia M. Phillips, and R. Ramesh. Very large magnetoresistance in perovskite-like la-ca-mn-o thin films. *Applied Physics Letters*, 64(22):3045–3047, 1994.

[29] S. Jin, T. H. Tiefel, M. McCormack, R. A. Fastnacht, R. Ramesh, and L. H. Chen. Thousandfold change in resistivity in magnetoresistive la-ca-mn-o films. *Science*, 264(5157):413–415, 1994.

[30] Y Tokura and Y Tomioka. Colossal magnetoresistive manganites. *Journal of Magnetism and Magnetic Materials*, 200(1-3):1 – 23, 1999.

[31] S.M. Dunaevskii. Magnetic phase diagrams of manganites in the electron doping region. *Physics of the Solid State*, 46(2):193–212, 2004.

[32] Yoshinori Tokura, Akira Urushibara, Yutaka Moritomo, Takahisa Arima, Atsushi Asamitsu, Giyu Kido, and Nobuo Furukawa. Giant magnetotransport phenomena in filling-controlled kondo lattice system: La1-xsrxmno3. *Journal of the Physical Society of Japan*, 63(11):3931–3935, 1994.

[33] Farrel W. Lytle. X-ray diffractometry of low-temperature phase transformations in strontium titanate. *Journal of Applied Physics*, 35(7):2212–2215, 1964.

[34] P.G. Radaelli, M. Marezio, H.Y. Hwang, and S.-W. Cheong. Structural phase diagram of perovskite $A_{0.7}A'_{0.3}MnO_3$ (a= la, pr; a'= ca, sr, ba): A new *imma* allotype. *Journal of Solid State Chemistry*, 122(2):444 – 447, 1996.

[35] H. Y. Hwang, S-W. Cheong, P. G. Radaelli, M. Marezio, and B. Batlogg. Lattice effects on the magnetoresistance in doped $lamno_3$. *Phys. Rev. Lett.*, 75:914–917, Jul 1995.

[36] R. Mahesh, R. Mahendiran, A.K. Raychaudhuri, and C.N.R. Rao. Effect of the internal pressure due to the a-site cations on the giant magnetoresistance and related properties of doped rare earth manganates, ln1-xaxmno3 (ln = la, nd, gd, y; a = ca, sr, ba, pb). *Journal of Solid State Chemistry*, 120(1):204 – 207, 1995.

[37] Lide M. Rodriguez-Martinez and J. Paul Attfield. Cation disorder and size effects in magnetoresistive manganese oxide perovskites. *Phys. Rev. B*, 54:R15622–R15625, Dec 1996.

[38] F. Damay, C. Martin, A. Maignan, and B. Raveau. Cation disorder and size effects upon magnetic transitions in ln0.5a0.5mno3 manganites. *Journal of Applied Physics*, 82(12):6181–6185, 1997.

[39] C. Martin, A. Maignan, M. Hervieu, and B. Raveau. Magnetic phase diagrams of $L_{1-x}A_x$mno$_3$ manganites $(l = \mathrm{Pr,Sm};\ a = \mathrm{Ca,Sr})$. *Phys. Rev. B*, 60:12191–12199, Nov 1999.

[40] T. Terai, T. Sasaki, T. Kakeshita, T. Fukuda, T. Saburi, H. Kitagawa, K. Kindo, and M. Honda. Electronic and magnetic properties of $R_{0.5}A_{0.5}$mno$_3$ compounds ($r =$ Gd, dy, ho, er; $a =$ Sr, ca). *Phys. Rev. B*, 61:3488–3493, Feb 2000.

[41] S. M. Yusuf, K. R. Chakraborty, S. K. Paranjpe, R. Ganguly, P. K. Mishra, J. V. Yakhmi, and V. C. Sahni. Magnetic and electrical properties of $(\mathrm{la}_{1-x}\mathrm{dy}_x)_{0.7}\mathrm{ca}_{0.3}\mathrm{mno}_3$ perovskites. *Phys. Rev. B*, 68:104421, Sep 2003.

[42] H. L. Yakel. On the structures of some compounds of the perovskite type. *Acta Crystallographica*, 8(7):394–398, 1955.

[43] Jacqueline B.A.A. Elemans, B. Van Laar, K.R. Van Der Veen, and B.O. Loopstra. The crystallographic and magnetic structures of la1-xbaxmn1-xmexo3 (me = mn or ti). *Journal of Solid State Chemistry*, 3(2):238 – 242, 1971.

[44] K.R. Poeppelmeier, M.E. Leonowicz, J.C. Scanlon, J.M. Longo, and W.B. Yelon. Structure determination of $CaMnO_3$ and $CaMnO_{2.5}$ by x-ray and neutron methods. *Journal of Solid State Chemistry*, 45(1):71 – 79, 1982.

[45] K.R. Poeppelmeier, M.E. Leonowicz, and J.M. Longo. Camno2.5 and ca2mno3.5: New oxygen-defect perovskite-type oxides. *Journal of Solid State Chemistry*, 44(1):89 – 98, 1982.

[46] F Freyria Fava, Ph D'Arco, R Orlando, and R Dovesi. A quantum mechanical investigation of the electronic and magnetic properties of perovskite. *Journal of Physics: Condensed Matter*, 9(2):489, 1997.

[47] ‡ Lisbeth Rørmark, †, ‡ Anne Beate Mørch, † Kjell Wiik, ‡ Svein Stølen, , and † Tor Grande*. Enthalpies of oxidation of camno3-δ, ca2mno4-δ and srmno3-δ deduced redox properties. *Chemistry of Materials*, 13(11):4005–4013, 2001.

[48] J. Rodríguez-Carvajal, M. Hennion, F. Moussa, A. H. Moudden, L. Pinsard, and A. Revcolevschi. Neutron-diffraction study of the jahn-teller transition in stoichiometric lamno$_3$. *Phys. Rev. B*, 57:R3189–R3192, Feb 1998.

[49] Yasuhiko Syono, Syun iti Akimoto, and Kay Kohn. Structure relations of hexagonal perovskite-like compounds abx3 at high pressure. *Journal of the Physical Society of Japan*, 26(4):993–999, 1969.

[50] B.L. Chamberland, A.W. Sleight, and J.F. Weiher. Preparation and characterization of bamno3 and srmno3 polytypes. *Journal of Solid State Chemistry*, 1(3):506 – 511, 1970.

[51] T. Negas and R.S. Roth. Phase equilibria and structural relations in the system $BaMnO_{3-x}$. *Journal of Solid State Chemistry*, 3(3):323 – 339, 1971.

[52] Taki Negas and Robert S. Roth. The system $SrMnO_{3-x}$. *Journal of Solid State Chemistry*, 1(3):409 – 418, 1970.

[53] T. Negas. The $SrMnO_{3-x}Mn_3O_4$ system. *Journal of Solid State Chemistry*, 7(1):85 – 88, 1973.

[54] P.D. Battle, T.C. Gibb, and C.W. Jones. The structural and magnetic properties of srmno3: A reinvestigation. *Journal of Solid State Chemistry*, 74(1):60 – 66, 1988.

[55] E. Pavarini, E. Koch, J. van den Vrink, and G. Sawazky. Quantum materials: Experiments and theory. Modeling and Simulation 6, 2016.

[56] D. I. Bilc, R. Orlando, R. Shaltaf, G. M. Rignanese, J. Iniguez, and Ph. Ghosez. *Phys. Rev. B*, 77:165107, 2008.

[57] R. Dovesi, V. R. Saunders, C. Roetti, C. M. Zicovich-Wilson R. Orlando, F. Pascale, B. Civalleri, N. M. Harrison K. Doll, I. J. Bush, P. D'Arco, and M. Llunell, 2009. CRYSTAL09 User's Manual.

[58] H. A. Jahn and E. Teller. Stability of polyatomic molecules in degenerate electronic states. i. orbital degeneracy. *Proceedings of the Royal Society of London A: Mathematical, Physical and Engineering Sciences*, 161(905):220–235, 1937.

[59] E. Pavarini, E. Koch, J. van den Vrink, and G. Sawazky. Correlated electrons: from models to materials. Modeling and Simulation 2, 2012.

[60] P. W. Anderson. Antiferromagnetism. theory of superexchange interaction. *Phys. Rev.*, 79:350–356, Jul 1950.

[61] P. W. Anderson and H. Hasegawa. Considerations on double exchange. *Phys. Rev.*, 100:675–681, Oct 1955.

[62] P. G. de Gennes. Effects of double exchange in magnetic crystals. *Phys. Rev.*, 118:141–154, Apr 1960.

[63] Ryo Maezono, Sumio Ishihara, and Naoto Nagaosa. Phase diagram of manganese oxides. *Phys. Rev. B*, 58:11583–11596, Nov 1998.

[64] C. H. Chen and S-W. Cheong. Commensurate to incommensurate charge ordering and its real-space images in $la_{0.5}ca_{0.5}mno_3$. *Phys. Rev. Lett.*, 76:4042–4045, May 1996.

[65] Y Tokura and Y Tomioka. Colossal magnetoresistive manganites. *Journal of Magnetism and Magnetic Materials*, 200(1–3):1 – 23, 1999.

[66] R. von Helmolt, L. Haupt, K. Bärner, and U. Sondermann. Metal-semiconductor-transition and spin-glass properties of $la_{(2-x)/3}ba_{(1+x)/3}mn_{1-x}cu_xo_3$. *Solid State Communications*, 82(9):693 – 696, 1992.

[67] M. Bibes, Ll. Balcells, S. Valencia, J. Fontcuberta, M. Wojcik, E. Jedryka, and S. Nadolski. Nanoscale multiphase separation at $la_{2/3}ca_{1/3}mno_3/srtio_3$ interfaces. *Phys. Rev. Lett.*, 87:067210, Jul 2001.

[68] J. Aarts, S. Freisem, R. Hendrikx, and H. W. Zandbergen. Disorder effects in epitaxial thin films of (la,ca)mno3. *Applied Physics Letters*, 72(23):2975–2977, 1998.

[69] M. Ziese, H. C. Semmelhack, and K. H. Han. Strain-induced orbital ordering in thin $\mathrm{la}_{0.7}\mathrm{ca}_{0.3}\mathrm{mno}_3$ films on srtio_3. *Phys. Rev. B*, 68:134444, Oct 2003.

[70] H. W. Zandbergen, S. Freisem, T. Nojima, and J. Aarts. Magnetoresistance and atomic structure of ultrathin films of $\mathrm{la}_{0.73}\mathrm{ca}_{0.27}\mathrm{mno}_3$ on srtio_3. *Phys. Rev. B*, 60:10259–10262, Oct 1999.

[71] I. C. Infante, F. Sánchez, J. Fontcuberta, M. Wojcik, E. Jedryka, S. Estradé, F. Peiró, J. Arbiol, V. Laukhin, and J. P. Espinós. Elastic and orbital effects on thickness-dependent properties of manganite thin films. *Phys. Rev. B*, 76:224415, Dec 2007.

[72] A. Tebano, C. Aruta, S. Sanna, P. G. Medaglia, G. Balestrino, A. A. Sidorenko, R. De Renzi, G. Ghiringhelli, L. Braicovich, V. Bisogni, and N. B. Brookes. Evidence of orbital reconstruction at interfaces in ultrathin $\mathrm{la}_{0.67}\mathrm{sr}_{0.33}\mathrm{mno}_3$ films. *Phys. Rev. Lett.*, 100:137401, Apr 2008.

[73] M. Huijben, L. W. Martin, Y.-H. Chu, M. B. Holcomb, P. Yu, G. Rijnders, D. H. A. Blank, and R. Ramesh. Critical thickness and orbital ordering in ultrathin $\mathrm{la}_{0.7}\mathrm{sr}_{0.3}\mathrm{mno}_3$ films. *Phys. Rev. B*, 78:094413, Sep 2008.

[74] R. Mahesh, R. Mahendiran, A.K. Raychaudhuri, and C.N.R. Rao. Giant magnetoresistance in bulk samples of $\mathrm{la}_{1-x}\mathrm{a}_x\mathrm{mno}_3$ (a = sr or ca). *Journal of Solid State Chemistry*, 114(1):297 – 299, 1995.

[75] Aymeric Sadoc, Bernard Mercey, Charles Simon, Dominique Grebille, Wilfrid Prellier, and Marie-Bernadette Lepetit. Large increase of the curie temperature by orbital ordering control. *Phys. Rev. Lett.*, 104:046804, Jan 2010.

[76] P. Schiffer, A. P. Ramirez, W. Bao, and S-W. Cheong. Low temperature magnetoresistance and the magnetic phase diagram of $\mathrm{la}_{1-x}\mathrm{ca}_x\mathrm{mno}_3$. *Phys. Rev. Lett.*, 75:3336–3339, Oct 1995.

[77] A. Urushibara, Y. Moritomo, T. Arima, A. Asamitsu, G. Kido, and Y. Tokura. Insulator-metal transition and giant magnetoresistance in $\mathrm{la}_{1-x}\mathrm{sr}_x\mathrm{mno}_3$. *Phys. Rev. B*, 51:14103–14109, May 1995.

[78] H. L. Ju, C. Kwon, Qi Li, R. L. Greene, and T. Venkatesan. Giant magnetoresistance in $\mathrm{la}_{1-x}\mathrm{sr}_x\mathrm{mno}_z$ films near room temperature. *Applied Physics Letters*, 65(16):2108–2110, 1994.

[79] Marie-Bernadette Lepetit, Bernard Mercey, and Charles Simon. Interface effects in perovskite thin films. *Phys. Rev. Lett.*, 108:087202, Feb 2012.

[80] A. Tebano, A. Orsini, P. G. Medaglia, D. Di Castro, G. Balestrino, B. Freelon, A. Bostwick, Young Jun Chang, G. Gaines, E. Rotenberg, and N. L. Saini. Preferential occupation of interface bands in $\mathrm{la}_{2/3}\mathrm{sr}_{1/3}\mathrm{mno}_3$ films as seen via angle-resolved photoemission. *Phys. Rev. B*, 82:214407, Dec 2010.

[81] E. Schrödinger. *Physical Review*, 28 (6):1049, 1926.

[82] M. Born and J. R. Oppenheimer. *Annalen der Physik*, 84:457, 1927.

[83] P. Hohenberg and W. Kohn. *Phys. Rev.*, 136:B864, 1964.

[84] W. Kohn and L. J. Sham. *Phys. Rev.*, 140:A1133, 1965.

[85] S. H. Vosko, L. Wilk, and M. Nusair. *Can. J. Phys.*, 58:1200, 1980.

[86] J. P. Perdew and A. Zunger. *Phys. Rev. B*, 23:5048, 1981.

[87] K. Terakura, T. Oguchi, A. R. Williams, and J. Kübler. Band theory of insulating transition-metal monoxides: Band-structure calculations. *Phys. Rev. B*, 30:4734–4747, Oct 1984.

[88] M. Grioni, M. T. Czyzyk, F. M. F. de Groot, J. C. Fuggle, and B. E. Watts. Unoccupied electronic states of cuo: An oxygen 1 s x-ray-absorption spectroscopy investigation. *Phys. Rev. B*, 39:4886–4890, Mar 1989.

[89] W. Y. Ching, Yong-Nian Xu, and K. W. Wong. Ground-state and optical properties of cu_2o and cuo crystals. *Phys. Rev. B*, 40:7684–7695, Oct 1989.

[90] K. M. Rabe and Ph. Ghosez. *Modern Ferroelectrics*. Springer-Verlag, Berlin, 2007.

[91] J. P. Perdew, K. Burke, and M. Ernzerhof. *Phys. Rev. Letters*, 77:3865, 1996.

[92] Z. Wu and R. E. Cohen. *Phys. Rev. B*, 73:235116, 2006.

[93] A. D. Becke. *J. Chem. Phys.*, 98:1372, 1993.

[94] A. D. Becke. *J. Chem, Phys.*, 98:5648, 1993.

[95] A. D. Becke. *J. Chem. Phys.*, 98:5648, 1993.

[96] A. D. Becke. *Phys. Rev. A*, 38:3098, 1988.

[97] R. G. Parrand C. Lee, W. Yang. *Phys. Rev. B*, 37:785, 1988.

[98] Joachim Paier, Martijn Marsman, and Georg Kresse. Why does the b3lyp hybrid functional fail for metals? *The Journal of Chemical Physics*, 127(2), 2007.

[99] J. P. Perdew. *Electronic Structure of Solids*. Akademie, Berlin, 1991.

[100] R. Dovesi, R. Orlando, B. Civalleri, C. Roetti, V. R. Saunders, and C. M. Zicovich-Wilson. *Z. Kristallogr.*, 220:571, 2005.

[101] A. D. Becke. *J. Chem. Phys.*, 104:1040, 1996.

[102] Niall J. English P. Garc ía Fernández, S. Ghosh and J. A. Aramburu. *Phys. Rev. B*, 86:144107, 2012.

[103] M. Dolg, H. Stoll, A. Savin, and H. Preuss. *Theor. Chim. Acta*, 75:173, 1989.

[104] M. Dolg, H. Stoll, and H. Preuss. *Theor. Chim. Acta*, 85:441, 1993.

[105] P.J. Hay and W.R. Wadt. *J. Chem. Phys.*, 82:284, 1985.

[106] X. Cao and M. Dolg. *J. Molec. Struct. (Theochem)*, 581:139, 2002.

[107] S. Piskunov, E. Heifets, R. I. Eglitis, and G. Borstel. *Comp. Mat. Science*, 29:165, 2004.

[108] P.J. Hay and W.R. Wadt. *J. Chem. Phys.*, 82:270, 1985.

[109] M. D. Towler, N. L. Allan, N. M. Harrison, V. R. Saunders, W. C. Mackrodt, and E. Aprà. *Ab initio* study of mno and nio. *Phys. Rev. B*, 50:5041–5054, Aug 1994.

[110] T. Bredow, P. Heitjans, and M. Wilkening. *Phys. Rev. B*, 70:115111, 2004.

[111] F. Cora. *Mol. Phys.*, 103:2483, 2005.

[112] T. Bredow, K. Jug, and R. A. Evarestov. *B. Solid State Phys.*, 243:R10, 2006.

[113] Hiroyuki Yamada, M. Kawasaki, T. Lottermoser, T. Arima, and Y. Tokura. $\mathrm{lamno}_3/\mathrm{srmno}_3$ interfaces with coupled charge-spin-orbital modulation. *Applied Physics Letters*, 89(5):052506, 2006.

[114] Yoshinori Konishi, Zhong Fang, Makoto Izumi, Takashi Manako, Masahiro Kasai, Hideki Kuwahara, Masashi Kawasaki, Kiyoyuki Terakura, and Yoshinori Tokura. Orbital-state-mediated phase-control of manganites. *Journal of the Physical Society of Japan*, 68(12):3790–3793, 1999.

[115] B. R. K. Nanda and Sashi Satpathy. Effects of strain on orbital ordering and magnetism at perovskite oxide interfaces: $\mathrm{lamno}_3/\mathrm{srmno}_3$. *Phys. Rev. B*, 78:054427, Aug 2008.

[116] Pablo Garcia-Fernandez, Jose Antonio Aramburu, and Miguel Moreno. Influence of magnetic ordering on structural instabilities in insulating perovskites. *Phys. Rev. B*, 83:174406, May 2011.

[117] A. Vailionis, H. Boschker, W. Siemons, E. P. Houwman, D. H. A. Blank, G. Rijnders, and G. Koster. Misfit strain accommodation in epitaxial $ab\mathrm{o}_3$ perovskites: Lattice rotations and lattice modulations. *Phys. Rev. B*, 83:064101, Feb 2011.

[118] Hanghui Chen and Sohrab Ismail-Beigi. Ferroelectric control of magnetization in $\mathrm{la}_{1-x}\mathrm{sr}_x\mathrm{mno}_3$ manganites: A first-principles study. *Phys. Rev. B*, 86:024433, Jul 2012.

[119] Hanghui Chen, Qiao Qiao, Matthew S. J. Marshall, Alexandru B. Georgescu, Ahmet Gulec, Patrick J. Phillips, Robert F. Klie, Frederick J. Walker, Charles H. Ahn, and Sohrab Ismail-Beigi. Reversible modulation of orbital occupations via an interface-induced polar state in metallic manganites. *Nano Lett.*, 14:4965, 2014.

[120] Steven R. Spurgeon, Prasanna V. Balachandran, Despoina M. Kepaptsoglou, Anoop R. Damodaran, J. Karthik, Siamak Nejati, Lewys Jones, Haile Ambaye, Valeria Lauter, Quentin M. Ramasse, Kenneth K. S. Lau, Lane W. Martin, James M. Rondinelli, and Mitra L. Taheri. Polarization screening-induced magnetic phase gradients at complex oxide interfaces. *Nature Communications*, 6:6735 EP –, Apr 2015. Article.

[121] Hiroyuki Yamada, Yoshihiro Ogawa, Yuji Ishii, Hiroshi Sato, Masashi Kawasaki, Hiroshi Akoh, and Yoshinori Tokura. Engineered interface of magnetic oxides. *Science*, 305(5684):646–648, 2004.

[122] M. Huijben, L. W. Martin, Y.-H. Chu, M. B. Holcomb, P. Yu, G. Rijnders, D. H. A. Blank, and R. Ramesh. Critical thickness and orbital ordering in ultrathin $la_{0.7}sr_{0.3}mno_3$ films. *Phys. Rev. B*, 78:094413, Sep 2008.

[123] M. Ziese, H. C. Semmelhack, and K. H. Han. Strain-induced orbital ordering in thin $la_{0.7}ca_{0.3}mno_3$ films on $srtio_3$. *Phys. Rev. B*, 68:134444, Oct 2003.

[124] A. Tebano, C. Aruta, S. Sanna, P. G. Medaglia, G. Balestrino, A. A. Sidorenko, R. De Renzi, G. Ghiringhelli, L. Braicovich, V. Bisogni, and N. B. Brookes. Evidence of orbital reconstruction at interfaces in ultrathin $la_{0.67}sr_{0.33}mno_3$ films. *Phys. Rev. Lett.*, 100:137401, Apr 2008.

[125] A. Tebano, A. Orsini, P. G. Medaglia, D. Di Castro, G. Balestrino, B. Freelon, A. Bostwick, Young Jun Chang, G. Gaines, E. Rotenberg, and N. L. Saini. Preferential occupation of interface bands in $la_{2/3}sr_{1/3}mno_3$ films as seen via angle-resolved photoemission. *Phys. Rev. B*, 82:214407, Dec 2010.

[126] I. C. Infante, F. Sánchez, J. Fontcuberta, M. Wojcik, E. Jedryka, S. Estradé, F. Peiró, J. Arbiol, V. Laukhin, and J. P. Espinós. Elastic and orbital effects on thickness-dependent properties of manganite thin films. *Phys. Rev. B*, 76:224415, Dec 2007.

[127] M. Bibes, Ll. Balcells, S. Valencia, J. Fontcuberta, M. Wojcik, E. Jedryka, and S. Nadolski. Nanoscale multiphase separation at $la_{2/3}ca_{1/3}mno_3/srtio_3$ interfaces. *Phys. Rev. Lett.*, 87:067210, Jul 2001.

[128] Julia A. Mundy, Yasuyuki Hikita, Takeaki Hidaka, Takeaki Yajima, Takuya Higuchi, Harold Y. Hwang, David A. Muller, and Lena F. Kourkoutis. Visualizing the interfacial evolution from charge compensation to metallic screening across the manganite metalâ??insulator transition. *Nature Communications*, 5:3464 EP –, Mar 2014. Article.

[129] I. Pallecchi, L. Pellegrino, E. Bellingeri, A. S. Siri, D. Marré, A. Tebano, and G. Balestrino. Field effect in manganite ultrathin films: Magnetotransport and localization mechanisms. *Phys. Rev. B*, 78:024411, Jul 2008.

[130] R. Herger, P. R. Willmott, C. M. Schlepütz, M. Björck, S. A. Pauli, D. Martoccia, B. D. Patterson, D. Kumah, R. Clarke, Y. Yacoby, and M. Döbeli. Structure determination of monolayer-by-monolayer grown $la_{1-x}sr_xmno_3$ thin films and the onset of magnetoresistance. *Phys. Rev. B*, 77:085401, Feb 2008.

[131] R. J. Nelmes, G. M. Meyer, and J. Hutton. Thermal motion in srtio3 at room temperature: Anharmonic or disordered? *Ferroelectrics*, 21(1):461–462, 1978.

[132] L. Pinsard, J. Rodríguez-Carvajal, and A. Revcolevschi. Structural phase diagram of $la_{1-x}sr_xmno_3$ for low sr doping. *Journal of Alloys and Compounds*, 262:152 – 156, 1997.

[133] J Blasco, J García, J M de Teresa, M R Ibarra, P A Algarabel, and C Marquina. A systematic study of structural, magnetic and electrical properties of perovskites. *Journal of Physics: Condensed Matter*, 8(40):7427, 1996.

[134] Marie-Bernadette Lepetit. Private Communication.

[135] Robert J. Zollweg. X-ray lattice constant of barium oxide. *Phys. Rev.*, 100:671–673, Oct 1955.

[136] Javier Junquera, Magali Zimmer, Pablo Ordejón, and Philippe Ghosez. First-principles calculation of the band offset at bao/batio$_3$ and sro/srtio$_3$ interfaces. *Phys. Rev. B*, 67:155327, Apr 2003.

[137] Eric Bousquet, Javier Junquera, and Philippe Ghosez. First-principles study of competing ferroelectric and antiferroelectric instabilities in batio$_3$/BaO superlattices. *Phys. Rev. B*, 82:045426, Jul 2010.

[138] J. Bashir, Rao Tahir A. Khan, N. M. Butt, and G. Heger. Thermal atomic displacement parameters of sro. *Powder Diffraction*, 17(3):222–224, 009 2002.

[139] William Primak, Herman Kaufman, and Roland Ward. X-ray diffraction studies of systems involved in the preparation of alkaline earth sulfide and selenide phosphors. *Journal of the American Chemical Society*, 70(6):2043–2046, 1948.

[140] V. G. Tsirelson, A. S. Avilov, Yu. A. Abramov, E. L. Belokoneva, R. Kitaneh, and D. Feil. X-ray and Electron Diffraction Study of MgO. *Acta Crystallographica Section B*, 54(1):8–17, Feb 1998.

[141] Helen D Megaw. Crystal structure of double oxides of the perovskite type. *Proceedings of the Physical Society*, 58(3):340, 1946.

[142] P. G. Radaelli, G. Iannone, M. Marezio, H. Y. Hwang, S-W. Cheong, J. D. Jorgensen, and D. N. Argyriou. Structural effects on the magnetic and transport properties of perovskite $A_{1-x}A'_x$mno$_3$ ($x = 0.25$, 0.30). *Phys. Rev. B*, 56:8265–8276, Oct 1997.

[143] G. K. H. Madsen and D. J. Singh. BoltzTraP. A code for calculating band-structure dependent quantities. *Computer Physics Communications*, 175:67–71, July 2006.

[144] Jennifer Fowlie, Marta Gibert, Giulio Tieri, Alexandre Gloter, Jorge Íñiguez, Alessio Filippetti, Sara Catalano, Stefano Gariglio, Alexander Schober, Mael Guennou, Jens Kreisel, Odile Stéphan, and Jean-Marc Triscone. Conductivity and local structure of lanio3 thin films. *Advanced Materials*, 29(18):1605197–n/a, 2017. 1605197.

List of figures

List of tables